UNIVERSITY OF CALIFORNIA

Santa Barbara

Phase-equilibria modeling of magma mixing:

Petrogenetic case studies featuring the Magma Chamber Simulator

A dissertation submitted in partial satisfaction of the requirements for the degree

Doctor of Philosophy in Earth Science

by

Melissa Ashley Scruggs

Committee in charge:

Professor Frank J. Spera, Co-Chair

Professor Matthew Rioux, Co-Chair

Professor Roberta Rudnick, Co-Chair

March 2022

The dissertation of Melissa Ashley Scruggs is approved.

_____
Roberta Rudnick, Committee Co-Chair

_____
Matthew Rioux, Committee Co-Chair

_____
Frank J. Spera, Committee Co-Chair

December 2021

Phase-equilibria modeling of magma mixing:

Petrogenetic case studies featuring the Magma Chamber Simulator

by

Melissa Ashley Scruggs

DEDICATION

To my daughter Korin, who has been with me every step of the way. I love you to the moon and back—I'm so proud of the young woman you've become and am excited to see how far you'll soar.

ACKNOWLEDGEMENTS

Thank you to my advisors, Dr. Frank J. Spera and Dr. Matthew Rioux, for their invaluable instruction, mentorship, and guidance along the path to becoming a better scientist and researcher. Thank you to Dr. Roberta L. Rudnick for her tutelage and the opportunity to work with a true icon of geochemistry, and to Drs. Keith Putirka and Jeanine Ash for their unparalleled mentorship in navigating the waters to becoming an independent researcher. To Dr. Wendy Bohon, Dr. Janine Krippner, Mika McKinnon, Dr. Jazmin Scarlett, and Alyssa Kaess, thank you a million times over for being the outstanding role models that you are—the world is a better place because of your talented scientific storytelling. I'm in awe of and inspired by each of you every single day. To Dr. Leigh Anne Riedman, Dr. Val Finlayson, and Laura Hollister, thank you for being wonderful friends and role models—I hope one day that everybody will recognize what astonishing scientists and teachers you are. To my dear friends, Treva Watters, Alaina and Drew Tudman, Alex Ptylak, (soon-to-be Dr.) Elizabeth Erickson, Addison Sani, Dr. Allison Price, and Dr. Anne Billingsley, to my daughter Korin, and to my best friend and husband Jeff Rash, thank you for standing by me through thick and thin. Your unconditional love and support has meant the absolute world to me; I owe you so much. Please know that this dissertation is as much yours as it is mine.

VITA OF MELISSA ASHLEY SCRUGGS

December 2021

EDUCATION

Bachelor of Science in Geology, University of Missouri, Kansas City, May 2011

Master of Science in Geology, California State University, Fresno, August 2014

Doctor of Philosophy in Earth Science, University of California, Santa Barbara, December 2021

PROFESSIONAL EMPLOYMENT

2020-2021: Teaching Associate, Department of Earth Science, University of California, Santa Barbara

2015-2020: Teaching Assistant, Department of Earth Science, University of California, Santa Barbara

2015 & 2016: Summer Teaching Associate, Department of Earth Science, University of California, Santa Barbara

2013-2014: Adjunct Instructor, Lecturer, Math Science & Engineering Division, Fresno City College

2013-2014: Research Assistant, Earth & Environmental Science Department, California State University Fresno

2012-2014: Tutor, Athletics Department, California State University Fresno

2011-2014: Teaching Assistant, Earth & Environmental Science Department, California State University Fresno

PUBLICATIONS

Bohrson, Wendy A., Spera, Frank J., Heinonen, Jussi S., Brown, Guy A., **Scruggs, Melissa**, Adams, Jenna, Takach, Marie, and Zeff, Garrett. (2020) Diagnosing open-system magmatic processes using the Magma Chamber Simulator (MCS): Part I – Major elements and phase equilibria. *Contributions to Mineralogy and Petrology*, 175, 104. doi: 10.1007/s00410-020-01722-z.

Heinonen, Jussi S., Bohrson, Wendy A., Spera, Frank J., Brown, Guy A., **Scruggs, Melissa A.**, and Adams, Jenna. (2020) Diagnosing open-system magmatic processes using the Magma Chamber Simulator (MCS): Part II – trace elements and isotopes. *Contributions to Mineralogy and Petrology*, 175, 105. doi: 10.1007/s00410-020-01718-9.

Scruggs, Melissa A. & Putirka, Keith D. (2018) Eruption Triggering by Partial Crystallization of Mafic Enclaves at Chaos Crags, Lassen Volcanic Center, California. *American Mineralogist*, 103, 1575-1590.

Spera, Frank & **Scruggs, Melissa**. (2016) Fractional Crystallization and Assimilation. In *Encyclopedia of Geochemistry: a Comprehensive Reference Source on the Chemistry of the Earth*. William M. White, ed. doi: 10.1007/978-3-319-39193-9_285-1.

AWARDS

June 2020, UCSB Science Line Award
June 2018, UCSB Dept. of Earth Science Preston Cloud Award
June 2017, UCSB Dept. of Earth Science Harry Glicken Award
2016-2017, UCSB Graduate Equity Fellowship Award
April 2016, PSAAPG Coast Geological Society Scholarship
August 2015, CSUF College of Math & Science Most Outstanding Thesis Award
2014 – 2015, UCSB Graduate Student Fellowship
2013 – 2014, Ibrahim M. Abou-Ghorra Scholarship
2012 – 2014, CSUF Graduate Equity Fellowship Award
2012 – 2013, Frederick D. Trauger Scholarship
May 2011, Departmental Honors, UMKC Geoscience Department
May 2011, Latin Honors, *Magna Cum Laude*, UMKC College of Arts & Sciences
2010 – 2011, Norman Royal Book Award Recipient
2010 – 2011, AEG / ACSE Undergraduate Scholarship Award Recipient
2009 – 2010, MODNR Environmental Education Scholarship Recipient
2009 – 2010, TWA Environmental Award Scholarship Recipient
2009 – 2010, UMKC Geosciences Award Scholarship Recipient

FIELDS OF STUDY

Major Field: Volcanology, Petrology, Mineralogy, Geology

Studies in Igneous Petrology and Magma Dynamics with Professor Frank J. Spera

Studies in Open-System Magmatic Differentiation Processes with Professor Frank J. Spera

Studies in Igneous Petrology and Geochemistry with Professor Matthew Rioux

ABSTRACT

Phase-equilibria modeling of magma mixing:

Petrogenetic case studies featuring the Magma Chamber Simulator

by

Melissa Ashley Scruggs

In the last 40 years or so, there has been a renaissance regarding the commonality and importance of magma bodies as open systems, where energy and mass are exchanged between a magma body and its surroundings over its lifetime. Paralleling this has been the advancement of computing technologies and significant developments in the fields of petrology and petrochemistry, resulting in a plethora of phase-equilibria modeling options available to the modern day igneous petrologist. This dissertation demonstrates how the additional constraints imposed by considering phase-equilibria when examining variations in major oxide, trace element, and isotope compositions can provide further insight into the different magmatic processes at play in an active volcanic system. This dissertation consists of four chapters: 1) software development and packaging of *MCS-PhaseEQ*, a phase-equilibria modeling program with application to the major element systematics of open magmatic systems; 2) software development and packaging of *MCS-Traces*, a trace element and isotope systematics calculator for open magmatic systems, to be used in conjunction with *MCS-Traces*; 3) A case study of Kilauea Volcano, where *MCS-PhaseEQ* is used to address questions of magma identity, magma volumes, and the petrogenetic processes required to produce the evolved

lavas erupted during the January 1997 Episode 54 fissure eruption; and 4) A case study of Chaos Crags, where *MCS-PhaseEQ* and *MCS-Traces* are used to resolve seemingly conflicting geochemical signatures of Chaos Crags mafic enclaves.

Chapters 1 and 2 present a user-friendly, refined software package for the Magma Chamber Simulator (MCS; see Bohrson *et al.* 2014)—a rigorous, energy- and mass-constrained thermodynamic model for evaluating the relative contributions of different magmatic processes in complex, open systems. MCS updates include a new, streamlined user interface, comprehensive data production and visualization, the ability to simulate up to 30 recharge events, a suite of online tutorials and new case studies, the addition of stoping as a method of assimilation, and the application of trace element and isotope calculations to *MCS-PhaseEQ* model outputs to track changes in geochemical compositions during mixing, assimilation, and crystallization. The case studies presented herein demonstrate the importance of examining variations in trace element and isotope compositions—in addition to major oxide and mineral compositions and relationships—as they record geochemical signatures that might be otherwise obfuscated if only the major oxide compositions of a magma are investigated.

Chapter 3 presents an investigation of the petrogenetic origin of unusually evolved lavas erupted at a mantle-plume fed, intraplate ocean-island basalt volcano. Chapter 3 examines whether the geochemical and petrological signatures of low-MgO lavas erupted along the East Rift Zone of Kilauea Volcano on 30-31 January 1997 (Episode 54) can be explained by mixing between juvenile basaltic magmas and partially crystalline material from earlier eruptions, and also whether calculated mixing proportions are consistent with GPS-based geodetic inversions of ground deformation and intrusion growth. Open-system phase-equilibria

thermodynamic models were used to constrain the composition, degree of differentiation, and thermodynamic state of the rift-stored, two Pyx-Pl saturated low-MgO magma body immediately preceding its mixing with high-MgO recharge and degassed drainback magmas, shortly before disruptive fissure activity within Napau Crater began. Mixing models constructed using the Magma Chamber Simulator reproduce the mineralogy and compositions of Episode 54 lavas within uncertainties, and suggest that the identity of the low-MgO magma body may be either variably differentiated remnants of un-erupted magmas intruded into Napau Crater in October 1968, or another spatially and compositionally similar magma body. Fissure A-E lavas can be replicated by a 43:57 mixture of mafic magmas with a low-MgO magma produced by ~23% fractionation of the 1968 intrusion. Fissure F lavas are reproduced by a 40:60 mixture of the same mafic recharge with a more evolved magma produced by ~35% fractionation of the 1968 intrusion. The resultant mineral assemblages and compositions suggest that this rift-stored magma body was ~40-50% crystalline at the time of mixing, and likely compositionally stratified. Phase-equilibria model results corroborate field and geochemical relationships indicating that sub-edificial intrusions at intraplate shield volcanoes crystallize and evolve, only to be remobilized later by mafic recharge magma—and also demonstrate that the pre-eruptive conditions of an intrusive body may be recovered by examining mineral compositions within mixed lavas. Discrepancies between the geodetically-consistent mixing proportions and those used in our mixing models highlight the uneven and complex nature of incomplete mixing on shorter, more localized scales reflected in erupted lavas, whereas geodetically-determined mixing proportions may reflect large-scale contributions to an entire, un-erupted intrusive body.

Chapter 4 affirms the importance of including phase-equilibria constrained trace element and isotopic calculations when evaluating the petrogenesis of mafic enclaves. This chapter presents new trace element and $^{87}Sr/^{86}Sr$ and $^{143}Nd/^{144}Nd$ isotope data for mafic enclaves and host lavas of the ~1100 BP eruption of Chaos Crags (a series of six lava domes in the Lassen Volcanic Center, Northern California), which documents the contamination of mafic endmember magmas by anatectic melts derived by low degrees of partial melting of a Sierra Nevada granitoid (*sensu lato*) wallrock at mid-crustal depths, *prior* to their later mixing with a rhyodacitic mush that dominated the system at shallow depth. Enclaves whose isotopic signatures suggest higher extents of contamination are found in the latter half of the eruptive sequence (Domes D-F), consistent with a meltback of the conduit walls during the latter stages of magma ascent, after significant wallrock heating. The contamination event is followed by recharge of now-variably contaminated mafic magmas into the shallow-level rhyodacitic magma body. This two-stage petrogenetic sequence of Assimilation and Fractional Crystallization (AFC) followed by Recharge (R) reproduces the isotopic trends, and closely approximates the mineralogical, trace element and major oxide compositions of Chaos Crags mafic enclaves. The results of our study allow for a more nuanced and quantified temporal view of magmatic evolution for this system and serve as a reminder of the importance and spatially heterogeneous pattern of upper crustal assimilation processes in volcanic arc lavas when mafic magmas ascend through thick sections of older and colder 'granitoid' crust.

TABLE OF CONTENTS

I. Diagnosing Open-System Magmatic Processes Using the Magma Chamber Simulator (MCS): Part I - Major Elements and Phase Equilibria

A. Introduction

Studies of igneous rocks provide evidence that magmas evolve as open systems where exchange of matter and energy occurs at a range of spatial and temporal scales. Since the 1950's, improvements in geochemical instrumentation have enabled high precision analyses of igneous products (e.g., melts and fluid inclusions, single crystals, populations of crystals) at increasingly smaller spatial and temporal scales. These analytical advancements have led to many new insights into the complexities of how magmas evolve and aggregate. To fully utilize the enormous potential afforded by such data sets, a parallel advancement in computational modeling is a logical complement.

Trace element and isotopic models of open system magma processes have evolved from earlier studies that focused on mass balance (e.g., Taylor, 1980; DePaolo, 1981 and others) to those that incorporated mass and energy balance in the context of open system evolution (e.g., Spera & Bohrson, 2001; Bohrson & Spera, 2001, and references therein). Thermodynamic modeling has also progressed in important ways, and present-day models such as the family of rhyolite-MELTS models (Ghiorso & Sack 1995; Asimow & Ghiorso, 1998; Gualda *et al.* 2012; Ghiorso & Gualda 2015), pMELTS (Ghiorso et al. 2002) and THERMOCALC (e.g., Powell & Holland, 1988, Powell & Holland, 1994, Powell *et al*., 1998) provide tools for documenting mineral-melt-fluid phase equilibria in differentiating magmatic systems. In this contribution, we present the Magma Chamber Simulator (MCS; Bohrson *et al*., 2014) as a versatile computational tool for the igneous petrologist/geochemist. MCS utilizes the MELTS

family of models to combine thermodynamic constraints on melt-solid-fluid equilibria with mass and energy conservation for a composite open magma undergoing magma mixing via recharge, crustal assimilation via wallrock partial melting and stoping, and fractional crystallization. Model output includes compositional, isotopic, mass, and thermal data on all melts, solids, and fluid in each subsystem.

MCS is a forward modeling tool (discussion of both forward and inverse modeling in geochemistry may be found in Albarede, 1995) that can serve in several ways to elucidate the evolution of magmatic systems. Forward modeling helps to understand how variations in the values of specific parameters (e.g., pressure, parental magma composition, wallrock initial temperature, number and mass of recharge events) affect the course of magmatic system evolution. This approach enables one to obtain an intuitive understanding of open system magmatic processes, including a basis for concluding which variables have the largest effect. Forward modeling is also useful when attempting to model a particular natural system. In this case, one can adjust input parameters in order to best reproduce petrological and geochemical data from a particular suite of igneous rocks. Understanding the sensitivity of the solution to input parameters is especially important when modeling natural systems because the investigator is often confronted with significant uncertainties.

The use of MCS to both build intuition and to model data from individual volcanic or plutonic systems addresses a range of goals in the study of igneous rocks. Among the questions that can be addressed by MCS are: how does the balance of mantle and crust change with time in a particular magmatic system; are there systematic differences in mantle versus crustal input in different tectonic settings (e.g., Cox & Hawkesworth 1984; Asmerom *et al*. 1991; Moore *et al*. 2018); what influences where magma storage zones form (shallow versus

middle versus deep crust, e.g., Walker *et al.* 1993; Mangiacapra *et al.* 2008; Becerril *et al.* 2013; Weber & Castro 2017); what conditions favor large versus small magma bodies; and what processes and/or conditions modeled by MCS influence magma bodies to erupt (e.g., Tepley *et al*. 2000; Tepley *et al*. 2013; Wark *et al*. 2007; Scruggs & Putirka 2018, Ubide & Kamber 2018)?

In this contribution, we provide an overview of the design of the major element and phase equilibria part of the code (MCS-PhaseEQ); the trace element and isotope part of MCS (MCS-Traces) will be discussed in a companion paper (Heinonen *et al*., 2020). We also highlight the utility of forward modeling by providing a comparison of cases that illustrate the petrologic and geochemical consequences of five recharge, assimilation, stoping, fractional crystallization (RASFC) scenarios (FC, R_2FC, AFC, S_2FC, and R_2AFC where the subscript defines the number of "events"). The results of these models provide perspective on how melt + crystals + fluid in a crustal magma system may evolve in response to different combinations of open-system processes. Presentation of these models also serves to illustrate the rich array of results that MCS produces and how these results may be used to distinguish different open system scenarios (e.g., presence or absence or magma recharge, stoping versus assimilation of anatectic melt). In the companion paper, trace element and isotopic characteristics for these same five cases are presented along with the theory and code logistics for MCS-Traces. Examples of the use of MCS in studies of natural systems are given elsewhere (e.g., Borisova *et al*. 2017; Takach, 2018, Heinonen *et al*., 2019).

B. Design of the Magma Chamber Simulator

1. What is the Magma Chamber Simulator?

The Magma Chamber Simulator is a thermodynamic model that quantifies the evolution of an open composite magmatic system composed of four subsystems: resident magma, cumulate reservoir, wallrock, and distinct recharge reservoirs. These subsystems interact by exchange of matter and energy following the constraints imposed by local thermodynamic equilibrium, as described below. MCS models simultaneous fractional crystallization, contamination by partial melt assimilation ("AFC" in the MCS jargon) and stoping (S, SFC in the MCS jargon), and magma mixing by recharge.

In MCS, the resident Magma subsystem (M), initially a finite mass of melt in a well-defined thermodynamic state, is coupled to its host Wallrock (WR) via a diabatic and semi-permeable boundary. During AFC processes, sensible (melt cooling) and latent heat (formation of cumulates by fractional crystallization, FC) flows across the M-WR boundary, heating up and potentially partially melting wallrock. If partial melt forms and the melt fraction in wallrock exceeds a rheologically-determined, user-specified critical threshold (or FmZero), this anatectic melt thoroughly mixes and equilibrates with melt in the M subsystem (called M melt for brevity). Crystals that form in response to AFC become part of a cumulate reservoir that is thermally connected to but chemically isolated from M melt. The extent of matter transfer between WR and M is governed by key parameters connected to ambient geological conditions and initial bulk compositions (Tables 1 and 2, e.g., is WR cold or warm, wet or dry, gabbroic or granitic)? In addition to contamination of M melt by wallrock partial melt, contamination can occur by the process of stoping (S). In MCS, stoped wallrock is added

en masse to M melt, and the contaminated system comes to a new equilibrium state at a new thermodynamically-controlled temperature. The stoping event may cause crystalline solids or a fluid to precipitate, and naturally, the contaminated M melt assumes a different bulk composition. A final process that MCS accounts for is magma mixing by recharge (R). During R, a finite mass of internally equilibrated recharge magma, in a well-defined thermodynamic state, is added to M melt, and the new mixture attains chemical potential equilibrium. This operation is computationally identical to the stoping operation. The user-defined condition that triggers an R or S event is either a specified M melt temperature or a temperature decrement from the last S or R event. The current version of MCS allows a total of up to thirty distinct events of the S or R type. For more information about the theoretical underpinnings of MCS, the reader is directed to Bohrson *et al*. (2014).

2. How does the Magma Chamber Simulator Computer Code Work?

The MCS calculations are undertaken in two parts: (1) *MCS-PhaseEQ*: the major element and phase equilibria computation of the RASFC evolution, and (2) *MCS-Traces*: the trace element and isotopic (Sr, Nd, Hf, Pb, Os, and O) consequences of the RASFC scenario from output of *MCS-PhaseEQ*. This bipartite structure recognizes that robust trace element/isotopic calculations are necessarily built upon an accurate major element solution that quantifies phase abundances, compositions, and temperatures, a researcher may iterate in step (1) by comparing observables with predicted results before investing effort into trace element and isotopic modeling. Conversely, because of the bipartite structure, a researcher can run multiple trace element and isotopic ratio calculations using, for example, different initial trace element compositions and/or mineral-melt, mineral-fluid partition coefficients for M, WR, S and R utilizing the same part (1) RASFC solution. Feedback to *MCS-PhaseEQ* for different trace

element concentrations and isotopic ratios is not required because major phase stability is not typically sensitive to trace elements. The bipartite approach maintains maximal flexibility in the pursuit of a 'best-fit' model and aids in understanding the sensitivity of a full solution (phase equilibria, trace elements and isotope) to the initial conditions and parameters.

MCS-PhaseEQ is the union between a computational thermodynamic engine and an executive brain (Bohrson *et al*., 2014). The executive brain is built with Microsoft's Visual Basic programming language; a snapshot of the user interface of the current version is presented in Fig. 1. The brain is responsible for implementing the particular R_nAS_nFC scenario specified by the user by (1) sending instructions to the chosen rhyolite- or pMELTS engine, (2) performing additional internal calculations based on values returned from rhyolite- or pMELTS, (3) making the conditional and complex sequential executive decisions required to carry out the user-defined R_nAS_nFC petrological scenario, (4) producing a variety of real-time and archived graphical and numerical output, and (5) archiving input and output in a systematic manner enabling a synoptic view of the results. Several separate tools are available from the MCS website to mine and utilize the output for various purposes.

The thermodynamic engine implemented in the *MCS-PhaseEQ* is one of the rhyolite- or pMELTS codes currently available. These are enumerated as pMELTS, and rhyolite-MELTS versions 1.0.2, 1.1.0, or 1.2.0 (Ghiorso & Sack 1995; Asimow & Ghiorso, 1998; Ghiorso *et al*. 2002; Gualda *et al*. 2012; Ghiorso & Gualda 2015; http://melts.ofm-research.org/). A centerpiece of rhyolite- or pMELTS is a thermodynamic model for the dependence of Gibbs free energy of silicate liquids as a function of melt composition, temperature (roughly 1000-2000 K), and pressure (roughly 0-3 GPa). For numerical calculations, the laws of thermodynamics, which are adhered to in rhyolite- and pMELTS are not sufficient, must be

adjoined with the thermodynamic properties of the materials composing the composite system.

3. More about Critical Design Features of Magma Chamber Simulator

MCS was designed as a thermodynamic model that has built-in assumptions about the ways in which the subsystems interact. Like all models, the design of MCS leads to limitations in its application to natural systems and to developing a framework for understanding how RASFC processes, in all their complexity. In this section, we enumerate key aspects of the design features of MCS and highlight limitations in its use.

First and perhaps foremost, as noted, MCS is a *thermodynamic* model that, while allowing for open system behavior, assumes local thermodynamic equilibrium. There are no compositional, pressure, temperature or other gradients within wallrock, magma or recharge reservoirs. Because MCS is a thermodynamic and *not* a transport model, thorough and complete homogenization is assumed when magmas mix, blocks are stoped, or partial melts are assimilated. Heat and matter are instantaneously exchanged between wallrock, magma (melt + cumulates) and recharge/stoping subsystems, and each subsystem is therefore characterized by a uniform temperature in each "step" of a simulation. Enthalpy is conserved, and thus the temperature of the M melt and cumulate subsystems is affected not only by temperature decrements imposed by user-defined cooling (see below), but also by adjustments required by addition of hotter or colder recharge magma or wallrock stoped blocks or anatectic melt.

In MCS, no absolute timescale is defined. However, an MCS 'arrow of time' (i.e., sequence of events) is defined by a user-specified RASFC scenario. Output archives an

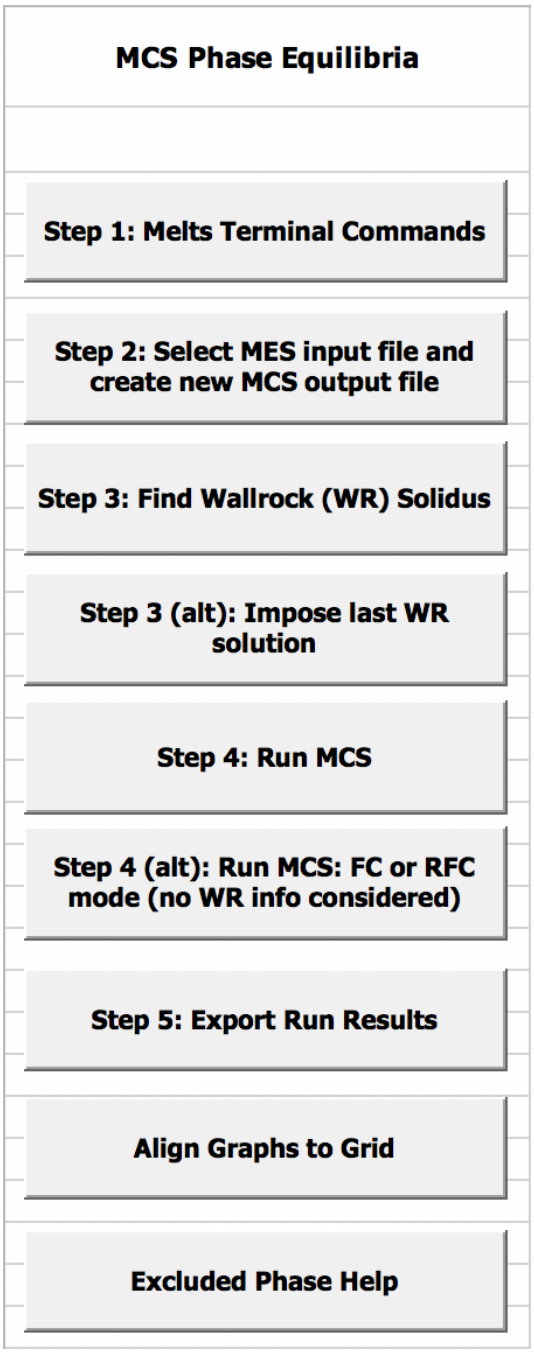

Figure 1. Command functions in the phase equilibria/major element interface of MCS-PhaseEQ. Step 1 initiates MCS communication with rhyolite- or pMELTS. Step 2 involves choosing an output file name and input MES file from those available. Step 3 is a preliminary calculation that prepares the WR subsystem by computing a solidus or near solidus thermodynamic state for wallrock for eventual coupling with the M subsystem, a requirement for AFC scenarios. Step 4 launches and runs the MCS-PhaseEQ simulation. Step 5 involves exporting the simulation results to an Excel workbook (see Online Resource 6). The other steps provide enhanced capability for running MCS, and these are detailed on the MCS website.

Table 1: System Variables and Compositions of Parent Magma, Recharge Magmas, Wallrock and Stoped Blocks for Five MCS Simulations

System Variables		
Pressure (GPa)	0.1	
Percolation Threshold	0.1	
fO_2 (during simulation)	none/absent	
Compositions		
Oxide in Wt.%	Parental (Resident) and Recharge Magma Composition	Wallrock & Stoped Block Composition
SiO_2	49.38	64.53
TiO_2	1.73	0.62
Al_2O_3	13.79	14.92
Fe_2O_3	1.83*	1.30**
Cr_2O_3	0.00	0.00
FeO	8.73	3.71
MnO	0.18	0.10
MgO	7.82	2.40
NiO	0.00	0.00
CoO	0.00	0.00
CaO	12.09	3.48
Na_2O	2.12	3.17
K_2O	0.23	2.71
P_2O_5	0.15	0.15
H_2O	1.96	1.94
CO_2	0.000	0.97

* For the parent magma, Fe^{+2}/Fe^{+3} was calculated at FMQ at 1129° C and at 0.1 GPa after adding ~2 wt.% of H_2O. Following this fO_2 calculation, the magma composition was normalized to 100%. See text for additional discussion.

** For the WR, Fe^{+2}/Fe^{+3} was calculated at FMQ at 740° C and at 0.1 GPa after adding ~2 wt.% of H_2O and ~1 wt.% of CO_2; Following this fO_2 calculation, the WR composition was normalized to 100%. See text for additional discussion.

Table 2: Initial Conditions for Five MCS Simulations

	FC	R_2FC	AFC	S_2FC	R_2AFC
Magma Liquidus Temperature (°C)	1129	1129	1129	1129	1129
Temperature Decrement (°C)	5	5	5	5	5
Magma Initial Mass (expressed as mass units, m.u.)	100	100	100	100	100
Hard Stop Temperature (°C)[a]	900	900	800	900	800
Wallrock Find Solidus Start Temperature (°C)[b]	880	880	880	880	880
Wallrock Find Solidus End Temperature (°C)[b]	700	700	700	700	700
Wallrock Find Solidus Temperature Decrement (°C)[b]	5	5	5	5	5
Wallrock Initial Temperature (°C)	100	100	700	100	700
Wallrock Initial Mass (m.u.)	200	200	200	200	200
Recharge/Stope Event 1: Mass (m.u.)		75		17	75
Recharge/Stope Event 1: Temperature of Recharge/Stoped Block When Recharge/Stoping Occurs (°C)[c]		1130		760	1130
Recharge/Stope Event 1: Temperature of Magma When Recharge/Stoping Occurs (°C)[d]		1050		1015	1050
Recharge/Stope Event 2: Mass (m.u.)		75		38	75
Recharge/Stope Event 2: Temperature of Recharge/Stoped Blocked When Recharge/Stoping Occurs (°C)[c]		1080		795	1080
Recharge/Stope Event 2: Temperature of Magma When Recharge/Stoping Occurs (°C)[d]		1000		908	1000

[a]Hard stop temperature is temperature at which simulation ends, if this temperature is achieved prior to wallrock and magma reaching thermal equilibrium.

[b]These parameters represent the starting and ending temperatures and the temperature decrement that are used in the wallrock find solidus routine of MCS. See http://mcs.geol.ucsb.edu for more information.

[c]This represents the temperature of the recharge magma/stoped block when it enters the M melt.

[d]This represents the temperature of the resident magma (M melt and cumulates) when the recharge/stoping event occurs. Note that the temperature at which recharge actually occurs (e.g., ~1049°C for R1 in R_2FC case) differs slightly from that reported in the input (1050°C) because the recharge event occurs in the step after that target temperature is reached.

evolutionary record of melt composition, cumulate petrology, anatectic melt composition, wallrock residual mineralogy, and pre-mixing state of stoped blocks and recharge magmas. Quantification of timescales can be approximated using simple scaling arguments based on observed features such as mineral zoning and magma mixing times (e.g., Oldenburg *et al.* 1989; Costa *et al*. 2008; Spera *et al.* 2016) in consort with MCS results. A critic might object to the purely thermodynamic approach noting that many irreversible processes with concomitant entropy production (heat conduction and convection, chemical diffusion, transport of momentum by the action of viscosity) surely come into play during the evolution of magmatic systems. We would not argue against this vantage. However, experience shows that local equilibrium is indeed often attained in high-temperature petrologic systems. Both the existence of a host of useful geothermometers, geobarometers, and geohygrometers (e.g., Putirka 2008, 2017; Wade *et al*. 2008; Coogan *et al*. 2014; Neave & Putirka 2017) and the consistency of laboratory experiments with observed features in natural magmatic systems (e.g., Bowen 1928; Yoder & Tilley 1962; Grove *et al*. 1992; Villiger *et al*. 2007) support the notion that a thermodynamic approach has validity and can be used to provide a useful 'reference frame' with which transport considerations can be contemplated. Development of an open system magmatic system model that simultaneously incorporates transport phenomena at macroscopic to molecular scales and embraces the assumption of local thermodynamic equilibrium, when appropriate and valid for three-dimensional representations, lies in the future.

The thermodynamic solutions provided by MCS are dependent on the quality of the thermodynamic data that underpins rhyolite- or pMELTS. These data include the standard state properties of all phases, activity-composition relations for all crystalline solutions

defined by end-members with known standard state properties, the mixing properties of H_2O-CO_2 supercritical fluids, and the Gibbs excess free energy model for silicate liquids. The latter gives the excess Gibbs energy of silicate melt as a function of composition, temperature, and pressure for multicomponent silicate melt. Any thermodynamic model is no better than the data and basic assumptions upon which it is based. The MELTS thermodynamic database, while robust, has its limitations. For example, the activity-composition relations for garnet, trioctahedral mica, and amphibole family phases are reasonable but imperfect. Hence in volcanic and plutonic rocks where these phases are modally abundant, the predictions of system evolution are more uncertain. The coverage in p-T space for which the rhyolite- and pMELTS engines are optimized is roughly 1000-2000 K and 0 to 3 GPa, limiting modeling to the outer ~100 km of Earth and deeper on smaller bodies such as the Moon, Mars, Venus, Mercury and the asteroids. Fortunately, this coverage is sufficient for a great variety of igneous environments that may be modeled with MCS.

Finally, we list additional design features that are critical for the MCS user to appreciate: (1) MCS is an isobaric model, and therefore the composite system is defined by a single pressure (e.g., Table 1); (2) during assimilation, anatectic melt is transferred between wallrock and M melt. A fluid phase and solids are not; they remain as a part of the wallrock subsystem; (3) the criterion that a threshold fraction of melt be attained in wallrock before partial melt is added to and equilibrated with resident melt is informed by the rheological properties of crystal-liquid mixtures (Lesher & Spera 2015); however, the mass of partial melt added from wallrock is simply the difference between the evolving local melt fraction in wallrock and this user-defined threshold value. There is no Darcy percolation *per se*. Transport details justifying melt extraction dynamics are given elsewhere (Spera & Bohrson 2001; Bohrson *et al.* 2014);

(4) wallrock temperature is uniform throughout the entire wallrock mass; (5) the output of MCS includes mass, thermal, and compositional information for melt, solids and fluid phase for all subsystems; the user must be astute when comparing (e.g.,) melt compositions in MCS with whole-rock compositions from an igneous suite, as magmas (and their solidified equivalents) can be complex combinations of melt, crystals and fluid phase.

A complete description of the MCS along with the code (both PC and Mac versions), examples, tutorials, and related tools may be found at https://mcs.geol.ucsb.edu, the MCS website. One of the related tools, the MCS Visualizer, operates on the output produced by the *MCS-PhaseEQ* code to generate an animated portrayal of a simulation, and the Cumulate Calculator compiles the compositional information of the incremental and bulk cumulate and residual wallrock composition for any MCS simulation; the Cumulate Calculator is particularly useful to track compositional model data relevant to intrusive environments. The Visualizer and Cumulate Calculator are not described here; details may be found on the MCS website. The MCS is continuously being developed so the reader is referred to the website for news and the most up-to-date version available.

C. Comparison of Closed (Fractional Crystallization) and Open-System Magma Evolution Illustrated by MCS

We present five *MCS-PhaseEQ* simulations that compare the melt composition and phase equilibria evolution of a magma body undergoing fractional crystallization (FC), recharge (two events)-fractional crystallization (R_2FC), assimilation-fractional crystallization (AFC), fractional crystallization accompanied by assimilation through stoping (two events) (S_2FC), and recharge (two events)-assimilation-fractional crystallization (R_2AFC). We provide

detailed comparisons of temperatures, masses, and compositions of the results, and we acknowledge that these models are illustrative; they are not intended to represent a particular magmatic system, and different parameters and starting bulk compositions will, indeed, yield different results. By presenting these cases, our intent is, first, to highlight the rich data sets that can be generated by MCS. Second, by describing the results in some detail, we hope to provide a roadmap for how MCS results can be used to unravel the RASFC evolution of a particular magmatic system. Table 3 lists MCS variables and typical ranges used in modeling of crustal systems. It also provides examples of petrological and geochemical data that can be used to both inform choice of input and to evaluate how MCS output can be utilized to determine 'best-fit' results. Finally, via these specific models, we elucidate characteristics of magma systems that may—or may not—allow identification of a specific process like crustal assimilation or magma recharge/mixing. A related longer-term goal is to use MCS, in a vastly expanded way, to develop a systematic framework for identifying and distinguishing magma processes such as recharge, crustal assimilation, and crystallization.

For each simulation, the fixed composite system pressure is 0.1 GPa, which corresponds to the shallow crust at circa 3 km depth. The percolation threshold (FmZero) is 0.1 (mass fraction), which means that before anatectic melt can be transferred from wallrock to M melt, 10 wt.% melt must be present in wallrock; any mass above this threshold is transferred and equilibrated with M melt. For all simulations, the mass of wallrock involved is twice (200 mass units, m.u.) that of the initial magma (100 m.u.), yielding a wallrock/initial resident magma mass ratio of two. This choice of mass ratio implies that the heat available from the cooling and crystallization of M magma is allowed to thermally interact with country rock mass twice that of the original magma. Because the enthalpy generated by the crystallization

of ferromagnesian phases (olivine, clinopyroxene, spinel) in mafic magma is higher by about a factor of two than the fusion enthalpy of the salic phases in the wallrock and because the specific isobaric heat capacity increases with increasing temperature, a mass ratio of two is justified. However, it is important to note that in MCS, the ratio of wallrock to magma is an initial parameter of the calculation. The MCS is not a heat transport model. All simulations discussed here utilized rhyolite-MELTS v1.2.0. Tables 1 and 2 list compositions and other initial conditions for the five simulations.

The parental magma for the five simulations is depleted mantle-derived continental tholeiite from the ~180 Ma Karoo Large Igneous Province (sample P27-AVL, Luttinen & Furnes, 2000) (Table 1). Initial H_2O was set at ~2 wt.%, and the Fe^{2+} to Fe^{3+} ratio was initially calculated at FMQ (at liquidus temperature of 1129°C and pressure of 0.1 GPa); each simulation was then run under fO_2-buffer absent conditions. This means that the system is closed with respect to the addition or subtraction of oxygen, and thus, during the run, the fugacity of oxygen will rise or fall according to the dictates of Gibbs energy minimization of the composite system. Each simulation has a user-chosen magma temperature decrement of 5°C, which means that the state of the system (magma and wallrock melt, minerals, fluid phase) is determined and archived at 5°C temperature decrements for the FC case (Table 2). Within these 5-degree decrements, the M subsystem can be envisaged to evolve by equilibrium crystallization after which the formed minerals are fractionated to the cumulate pile before the next step. *MCS-PhaseEQ* internally adjusts the M melt and cumulate

Table 3. Typical Input Ranges of MCS Parameters, Constraints Provided by Plutonic and Volcanic Data, and Guidelines for Evaluating Model Results

MCS Parameter	Typical Range Employed in MCS for Crustal Magmatic Systems	Constraints Provided by Data from Plutonic and Volcanic Systems	Best-fit decision making: How Do I Evaluate the Model Parameter?
Pressure of crustal magma systems	<0.1 to ~1.0 GPa	Pressure-dependent phase assemblage, independent geobarometry	Different pressure runs may yield different major and trace element trends, cumulate assemblages, cumulate mineral compositions, sequence ('arrow of time') of cumulate mineral compositions
Oxygen fugacity of system	Unconstrained, IW, COH, QFM, NNO HM	Mineral equilibria For many systems without such constraints QFM or NNO buffer is appropriate; otherwise setting at QFM to determine ferrous/ferric in M parent melt and then running unconstrained is also appropriate	Different buffers may show different major and trace element trends; typically, FeO, Fe_2O_3, TiO_2 are most distinctive; different cumulate mineral assemblages may result from different fO_2 as well
FmZero (residual melt fraction held in wallrock)	0.04 to > 0.12	Melt inclusions may provide composition of partial melt Melt wets silicate and oxide grain boundaries to form interconnected network at low melt fractions; values at larger end of range for more silicic wallrock	Different FmZero will lead to different anatectic melt compositions, may yield different major and trace element trends, cumulate assemblages, cumulate mineral compositions Melt inclusions may represent anatectic melt, comparison between model output and these data may help constrain FmZero
Parent magma composition	Basalt to rhyolite	Most primitive of exposed suite of related rocks, estimate of parent magma based on melt inclusions, reconstruction of parental from mineral data	Comparison of most primitive sample with initial composition of MCS run

Wallrock composition	Peridotite to granite	Outcrops, drill cores, xenoliths, met inclusions, seismic data	Different wallrock compositions may yield different major/trace element/isotope trends, cumulate assemblages, cumulate mineral compositions, sequence ('arrow of time') of cumulate mineral compositions, in *situ* isotopic record
Initial wallrock temperature	0 to ~750°C	Pressure estimates coupled with estimates of geothermal gradient, evidence of thermal priming	Different wallrock temperatures may yield different major/trace element/isotope trends, cumulate assemblages, cumulate mineral compositions, sequence ('arrow of time') of cumulate mineral compositions/isotopes Will also change temperature of magma at which assimilation begins, this record may be detected in compositional and isotopic data in cumulate crystals, and *via* changes in isotopes in samples where absolute or relative ages are documented
Ratio of initial wallrock mass to initial magma mass	0 to ~3	Upper limit from enthalpy balance; lower limit (0) is for uncontaminated magma evolution For natural systems, the value depends on many transport and thermophysical properties as well as the state of stress in wallrock (both 'tectonic' stress and thermal stress); each natural system requires unique characterization	Different ratio may yield different major/trace element/isotope trends, cumulate assemblages, cumulate mineral compositions, sequence ('arrow of time') of cumulate mineral compositions/isotopes Will also change temperature of magma at which assimilation begins, this record may be detected in compositional and isotopic data in cumulate crystals, and *via* changes in isotopes in samples where absolute or relative ages are documented
Recharge magma composition	Basalt to rhyolite	Reconstructions based on compositional zoning of crystals in solidified products, composition of enclaves, end-member composition of distinct members of mingled rocks, composition of melt inclusions	Different compositions may yield different major/trace element/isotope trends, cumulate assemblages, cumulate mineral compositions, sequence ('arrow of time') of cumulate mineral compositions/isotopes
Temperature of magma when recharge/stoping event occurs ('trigger temperature')	Liquidus temperature to near solidus temperature	Geothermometry applied to zoned crystals, to melt inclusions, and to mingled rocks, eruption temperature	Different compositions may yield different major/trace element/isotope trends, cumulate assemblages, cumulate mineral compositions, sequence ('arrow of time') of cumulate mineral compositions/isotopes

			First evidence of recharge also dependent on 'trigger' temperature, record may be detected in *in situ* compositional and isotopic data in cumulate crystals, may also be detected through changes in isotopes in samples where absolute or relative ages are documented
Temperature and crystallinity ("state') of recharge magma at recharge event	Liquidus temperature to below solidus temperature, 100% melt to solid	Character of enclaves (i.e., crystal versus glass/groundmass), crystal populations in solidified products that might inform state of recharge magma	Different 'state' may yield different major/trace element/isotope trends, cumulate assemblages, cumulate mineral compositions, sequence ('arrow of time') of cumulate mineral compositions/isotopes 'State' also impacts M melt temperature change when recharge occurs; this may be documented *via* geothermometry of cumulate crystals
Ratio of recharge mass to initial magma mass	<0.1 to > 2	Compositional contrasts documented in rock suites that have relative or absolute age information (e.g., dacitic eruption followed by basaltic eruption), composition of enclaves, melt inclusions	Different ratio may yield different major/trace element/isotope trends, cumulate assemblages, cumulate mineral compositions, sequence ('arrow of time') of cumulate mineral compositions/isotopes
Temperature and crystallinity ('state') of stoped wallrock at stoping event	Near to below solidus temperature	Xenoliths or xenocrysts of crustal origin, melt inclusions	Different 'state' may yield different major/trace element/isotope trends, cumulate assemblages, cumulate mineral compositions, sequence ('arrow of time') of cumulate mineral compositions/isotopes 'State' also impacts M melt temperature change when stoping occurs; this may be documented *via* geothermometry of cumulate crystals
Ratio of stoped block(s) mass to initial magma mass	<1	Compositional and isotopic contrasts documented in rock suites that have relative or absolute age information	Different ratio may yield different major/trace element/isotope trends, cumulate assemblages, cumulate mineral compositions, sequence ('arrow of time') of cumulate mineral compositions/isotopes

temperature to values other than those defined by the user-defined decrement in response to the homogenization of recharge magma(s), stoped block(s), or anatectic melt with M melt.

For the cases involving recharge (i.e., R_2FC, R_2AFC), the recharge magma compositions (including initial H_2O wt.% and fO_2) are identical to parent (resident) magma. Wallrock bulk composition is average upper continental crust from Rudnick & Gao (2003), with initial fO_2 calculated at FMQ (at 740°C and 0.1 GPa), initial H_2O of ~2 wt.%, and initial CO_2 of ~1 wt.% (Table 1).

The models are discussed and compared in detail below. Online Resource 1 provides input for the cases (similar to Table 1 but in Excel format), and Online Resources 2-5 present detailed comparison data for mass and temperature outcomes, mineral assemblage, fluid saturation, and selected melt compositional parameters for resident magma, wallrock, and recharge magmas for each case. Figure 2 shows the model outcomes in illustrations that are annotated snapshots from the MCS Visualizer tool and Figures 3–8 illustrate selected mass, thermal, and compositional data for melt and minerals for resident magma and wallrock.

All model input and output is presented in Online Resource 6, and we recommend viewing the output files (concentrating on the *RunSummary* tab) simultaneously when reading the following sections. The structure of the output files is uniform across all cases and, hence, time invested in learning the structure of the output makes the digestion of data relatively easy after an investment of effort. By way of introduction, the different tabs of the output that store the relevant information are specifically named in the discussion of the FC case. In addition, the MES input files are included in Online Resource 7; this means that all the cases discussed here can be replicated. It should be noted that there can be small differences at the part per

thousand level when MCS is run in different computing environments. These differences are well below levels that have an impact on interpretation of results in cases where we have studied this phenomenon. Finally, case-specific animations that help to follow the c the bulk system and which were built with the MCS Visualizer are given in Online Resource 8.

1. Case 1: Fractional Crystallization (FC)

The output of the FC case is stored in "MCS-FC_output_PhaseEQ.xlsx" file in Online Resource 6. The parent basalt specified above has a liquidus temperature of ~1129°C at 0.1 GPa and the FC simulation ends at a user-chosen temperature of ~900°C. Via fractional crystallization, the melt composition evolves from tholeiitic basalt to dacite, with the dacitic melt forming through ~76 wt.% fractional crystallization (Figs. 2a and 3, see *ChartTAS* tab in the output). Magma melt becomes H_2O-saturated at ~1029°C. At the end-temperature (~900°C), the H_2O-fluid phase constitutes ~1 wt.% of the magma system, with melt composing the remaining ~23 wt.% (Fig. 3) as noted by examination of columns I through L on row 52 of the *RunSummary* tab in the output. Major oxide trends behave as anticipated for a basaltic system undergoing fractional crystallization (Fig. 4).

Olivine is the first liquidus phase (see column Z of the *RunSummary* tab), and its composition is Fo_{82} (line 269, *SolidFormulas* tab, color code darker blue). It is followed closely by clinopyroxene (first appearance at ~1119°C) and plagioclase (first appearance at ~1084°C, An_{84}). Additional phases include spinel (first appearance at ~1069°C) and rhombohedral oxide (first appearance at ~984°C). By the end of crystallization, the cumulate is dominated by clinopyroxene and plagioclase, each of which composes ~40 wt.% of the bulk cumulate mass; olivine constitutes ~15 wt.%, spinel ~6 wt.% and rhombohedral oxide < 1 wt.% (Fig. 5). This information is graphically portrayed on the output tabs *ChartMassFrac*,

ChartPPD, and *ChartPMD*. The compositional range of minerals is large (see output *SolidFormulas* tab and Online Resource 3), as anticipated for a parental basaltic melt that evolves to dacitic after significant fractional crystallization.

The initial wallrock temperature for this simulation is 100°C. Enthalpy transferred from magma due to cooling and crystallization yields a final wallrock temperature of ~329°C (Fig. 2a), too low for any partial melting to occur. Thus, although the wallrock heats up, it remains below its solidus temperature, and no mass transfer occurs.

2. Case 2: Recharge-Fractional Crystallization (R_2FC)

The output of the R_2FC case is stored in "MCS-R2FC_output_PhaseEQ.xlsx" file in Online Resource 6. Two recharge events simulate intrusion of mantle-derived magma into resident magma melt as it evolves by fractional crystallization in an upper crustal (0.1 GPa) magma storage system. The first recharge event involves a recharge magma/initial magma mass ratio of 0.75 (that is, for an initial parent melt mass of 100 m.u., 75 m.u. of recharge magma is added (Table 2). This recharge magma at ~1130°C (100 wt.% melt) intrudes into and fully hybridizes with resident melt at ~1049°C (Tables 1 and 2, Online Resource 2). Note that the temperature at which recharge actually occurs differs slightly from that reported in the input (Table 2, 1050°C) because the recharge event occurs in the step after the target temperature is reached. Prior to the first recharge event, the resident magma had been crystallizing a mineral assemblage of olivine (Fo_{70}) + clinopyroxene ($Mg_{\#77}$) + plagioclase (An_{81}) + spinel. Immediately following the recharge event, the new, equilibrated state of hybridized M melt yields a new temperature of 1093°C due to addition of enthalpy from recharge magma, and crystallization of clinopyroxene, plagioclase, and spinel is suppressed. Thus, in response to mixing, resident magma (melt + cumulates) temperature increases by

almost 50°C and the hybridized magma crystallizes only olivine that is more magnesian (Fo_{78}) than olivine crystallizing just prior to the recharge event. With 5°C of additional post-recharge cooling, clinopyroxene ($Mg_{\#82}$) returns to the M crystallizing assemblage, and with an additional ~25–30°C of cooling, plagioclase (An_{82}) and spinel also return to the crystallizing assemblage. For most major oxides, the first recharge event has only a subtle effect on resident melt composition: the most pronounced changes are an increase in MgO from ~4.4 to 6.2 wt.%, and a decrease in SiO_2 from 52.6 to 50.9 wt.% (Fig. 4).

The second recharge event is compositionally identical to and has the same mass constraints as the first (75 m.u.), but for this recharge event, the temperature of the recharge magma is ~1080°C; thus the magma is 21 wt.% crystalline (mode of the assemblage is ~12 wt.% is olivine (Fo_{76}), ~82 wt.% is clinopyroxene ($Mg_{\#81}$), and ~6 wt.% is plagioclase (An_{83})) at the time recharge is triggered (Online Resource 5). This second "event" yields a new M temperature of ~1040°C, an increase of ~40°C. Plagioclase and spinel crystallization is suppressed for only ~5°·C. The compositions of the minerals change in response to recharge: olivine ($Fo_{55} \rightarrow Fo_{68}$) + clinopyroxene ($Mg_{\#70} \rightarrow Mg_{\#77}$) + plagioclase ($An_{71} \rightarrow An_{77}$). At 985°C, orthopyroxene joins the mineral assemblage, followed by rhombohedral oxide at ~980°C; orthopyroxene crystallization ceases at 955°C. Importantly, some of the major oxide changes pre- and post-recharge are more profound compared to the first recharge event, because the contrast between resident melt and recharge magma is greater. For example, from pre- to post-recharge, SiO_2 decreases from ~58 to 54.5 wt.% (as opposed to a decrease of <2 wt.% SiO_2 in M following Recharge event 1; see also Fig. 4).

The final temperature of the R_2FC simulation is ~900°C, and the final melt composition is dacitic. The final R_2FC melt major oxide compositions are similar to those of the FC case;

that is, the record of the increases in MgO and decreases in SiO_2 is not preserved in the final melt composition (Fig. 4) although a record is preserved in the compositional record of the cumulate phases. The proportion of crystals, melt, and fluid phase at the final simulation temperature is similar between R_2FC and FC (~77 wt.% crystals, 22 wt.% melt, 1 wt.% fluid for R_2FC versus ~76 wt.% crystals, 23 wt.% melt, 1 wt.% fluid for FC, respectively; Fig. 3). The proportions of phases in the final cumulate are similar, with the obvious exception of orthopyroxene, which makes up ~2 wt.% of the final cumulate in R_2FC (Fig. 5). The general range of mineral compositions is also similar (Online Resource 3).

What is distinctly different between FC and R_2FC is the overall mass of the system, which is ~2.5 times greater in R_2FC because the recharge events add 150 (2 x 75) m.u. into the system. Thus, the total mass of the R_2FC system is 250 m.u., compared to 100 m.u. in the FC case. The masses of melt, cumulates, and fluid are also proportionally larger, as anticipated (Fig. 3). Finally, the larger magma system mass significantly affects the wallrock temperature, with a final wallrock temperature of ~656°C, compared to ~329°C for FC alone (Fig. 2). The hotter wallrock is due to the added enthalpy of recharge magma intruding into resident melt. This suggests that recharge systems are more prone to induce partial melting in their host rocks due to this 'enthalpy-pumping' effect (all other conditions remaining constant).

3. Case 3: Assimilation of Wallrock Anatectic Melts-Fractional Crystallization (AFC)

The output of the AFC case is stored in "MCS-AFC_output_PhaseEQ.xlsx" file in Online Resource 6. This case reflects assimilation of upper continental crust by a depleted continental tholeiite evolving in an upper crustal (0.1 GPa) magma storage system. All other parameters being identical, the initial conditions of the AFC simulation contrast with those of the FC case with regard to the initial temperature of wallrock; it is 700°C compared to 100°C. The elevated

wallrock temperature is intended to maximize the assimilation signature and simulates assimilation in crust that has been thermally primed by previous episodes of magmatism (e.g., Moore *et al.,* 2018).

As resident melt cools from its liquidus, it first evolves like in the FC case. For a wallrock/initial magma mass ratio of two, anatectic (wallrock) partial melt begins to contaminate magma melt at a M melt temperature of ~1069°C (Fig. 3a). At this point, the wallrock is ~747°C and its percolation threshold (10 wt.%) for anatectic melt has been exceeded. Anatectic melt above this limit is transferred into, and thoroughly hybridized and equilibrated with M melt. Note that because incoming anatectic melt is at a lower temperature and different specific enthalpy than M melt, the assimilation of wallrock partial melts drives M melt to a slightly lower temperature. This is a consequence of the isenthalpic AFC process. That is, the energy for partial melting of wallrock is derived by the cooling and crystallization of the M subsystem. The new, lower magma temperature following assimilation can catalyze crystallization of the contaminated melt. These crystals, like all crystals in *MCS-PhaseEQ*, become part of the cumulate reservoir, where they remain in thermal contact with M melt.

At the onset of assimilation, the assemblage that crystallizes continues to be olivine + clinopyroxene + plagioclase + spinel, albeit in slightly smaller proportions than before AFC onset. Contaminated melt becomes fluid saturated at ~985°C, which is ~44°C lower than the FC case; this is most likely due to the design feature in MCS that does not (currently) permit fluid phase transfer with anatectic melt, although H_2O does enter into M magma because anatectic melt is H_2O-saturated. This effect is mediated by pressure. At the low pressure of the simulation, the water-content of anatectic melt is low since the solubility of water in anatectic melt is small. At higher pressure, more H_2O component would be delivered to M

magma by partial melt assimilation. At magma temperature ~1000°C, olivine becomes unstable, and is replaced by orthopyroxene. At ~952°C, rhombohedral oxide joins the stable mineral assemblage and clinopyroxene crystallization effectively ceases (Fig. 5).

By the terminus of the run (M-WR equilibration temperature of ~852°C), contaminated M melt has evolved to a dacitic composition; at that temperature, the final wt.% SiO_2 produced by the FC and AFC runs are within 1 wt.% (69 versus 70 wt. %, Fig. 4) of each other. Once assimilation begins, at the same SiO_2 compared to FC, AFC Al_2O_3 and K_2O have distinctly higher concentrations, whereas Na_2O, H_2O, and FeO are lower. CaO, MgO, Fe_2O_3, and TiO_2 are similar, and P_2O_5 behavior is more complicated: it is initially a bit higher and then distinctly lower at the same SiO_2 (Fig. 4).

The effect of assimilation on crystallization is marked; the proportion of crystals in the cumulate reservoir of the AFC magma system (~43 wt.%) is much smaller than that associated with FC (76 wt.%); the proportion of fluid phase in AFC is an order of magnitude smaller (0.1 versus 1 wt.%) (Fig. 3). The final AFC cumulate is different than the FC one; there is slightly less olivine and clinopyroxene, very similar percentage of plagioclase, and in AFC, orthopyroxene makes up ~12 wt.% of the final cumulate (Fig. 5). In addition, the total ranges in olivine and plagioclase compositions are different (Online Resource 3). The last olivine to crystallize in AFC is Fo_{62} (compared to Fo_{23} in FC) and the final plagioclase to crystallize is slightly more anorthitic (An_{54}) compared to FC (An_{47}). Thus, addition of anatectic melt changes not only the crystallizing assemblage (e.g., orthopyroxene precipitates, and olivine and clinopyroxene disappear as cumulus phases) but also changes the balance of melt versus cumulate (Fig. 3). AFC also delays the onset of fluid saturation by tens of degrees, and the

total proportion of the magma system that is an exsolved fluid phase is much smaller (Fig. 2c).

The mineral abundances of wallrock at its solidus are plagioclase >> quartz > alkali feldspar > orthopyroxene; spinel + rhombohedral oxide + biotite + apatite are accessory phases (Online Resource 4). Note also that wallrock is fluid saturated. Wallrock reaches its percolation threshold temperature at ~747°C; in the first instance of partial melting above the percolation threshold, apatite reacts and ceases to be a part of the wallrock residual mineral assemblage; the same is true of biotite. The restite assemblage of plagioclase + quartz + alkali feldspar + orthopyroxene, with accessory spinel + rhombohedral oxide, persists until wallrock temperature ~782°C, at which point, alkali feldspar is totally consumed (Fig. 6a). The remaining minerals persist in wallrock restite to the equilibration temperature.

For each step of anatectic melt transfer into M melt (except the first one), the size of anatectic melt increment is ~2-3 wt.% of the initial mass of the wallrock system (i.e., mass transfer involves ~4 to 6 m.u. of the initial 200 m.u. of wallrock). This mass rate of melt transfer changes when alkali feldspar completely dissolves. After this (wallrock T ~782°C, Fig. 6a), wallrock melt productivity decreases, and the size of the increments transferred goes down to <1 wt.% of the initial wallrock mass (<2 mass units) (Fig. 7, magma T ~920°C where slope changes slightly). Anatectic melt that is transferred and homogenized with resident magma melt is mostly rhyolitic, varying in SiO2 between ~70 (at onset of assimilation) and 76 wt.% (at the equilibration temperature). The cumulative percent anatectic melt added to the magma system can be viewed in two different ways. The total proportion of the wallrock system that was assimilated into resident magma is ~35 wt.% (~71 m.u. of the initial 200 m.u., Fig. 7). When assessed as a part of the resident magma, this assimilated mass represents about

41 wt.% of the final resident magma (melt + crystals + fluid phase body mass: ~71 m.u. of the final 171 m.u. system). By the time thermal equilibrium is attained, the wallrock has melted ~42 wt.%; this value is different than the total amount of wallrock assimilated because 10 wt.% anatectic melt remains within the wallrock system. See Online Resource 2 for details of these mass relations.

In the current available version of MCS, fluid phase present in WR is not permitted to transfer from WR to M. There may be circumstances that favor fluid phase bulk transfer with partial melt as it percolates into M magma. For example, fluid bubbles of low viscosity may be swept into M melt by the same Darcian percolative flow that transports partial melt. The likelihood of such transport depends on many factors including the bulk H2O content of wallrock as well as the stability of possible hydrous phases such as amphibole or biotite. Work to provide the user with the ability to transfer fluid phase, when it exists in wallrock is ongoing and will be presented in an updated version of MCS. To assess the effects of possible fluid transfer on the results presented here, 4 comparisons were run in which the M melt compositions at two temperatures (1061°C and 861°C) were adjusted by arbitrarily adding 20 wt.% and 40 wt.% of the mixed (H_2O+CO_2) fluid present in wallrock at the relevant temperatures (i.e., the temperature of WR in the AFC run at the M temperatures of 1061 and 861°C) of 747°C and 845·°C, respectively. These new, "fluid-enhanced" magmas were examined in rhyolite-MELTS v 1.2.0 at 1055°C and 855°C using the equilibrium crystallization function. (i.e., 5 °C below the temperature of fluid enhancement). The phase assemblages between the MCS results and the rhyolite-MELTS results are virtually identical, as are the M melt compositions. The only significant difference is the mass/proportion of fluid phase in the melt. The likelihood that M magma fluid saturates is obviously higher when fluid

phase is allowed to migrate across the wallrock-magma subsystem boundary. See Online Resource 9 for the outcomes of this comparison.

4. Case 4: Assimilation of Stoped Wallrock Blocks-Fractional Crystallization (S_2FC)

The output of the S_2FC case is stored in "MCS-S2FC_output_PhaseEQ.xlsx" file in Online Resource 6. Stoping in MCS is considered as a process whereby crustal contamination (synonymous with crustal assimilation) occurs via reaction of a block (or a set of multiple small blocks with a combined mass equal to the respective S event) of wallrock incorporated wholesale into magma melt. The pre-stoping temperature of the stoped block dictates its thermodynamic state; that is, the block can be stoped with different proportions of crystals, melt, and fluid phase. The S_2FC case presented here involves two stoping events, with all other parameters being identical to those of the FC case.

In MCS, stoped blocks are incorporated into M melt using the recharge function since the thermodynamics of stoping are identical to those of magma recharge and mixing. The initial (bulk) composition of the stoped blocks, however, is the same as initial wallrock in the AFC case (Table 1). Stoped block temperatures and masses were chosen, where possible, to provide relevant comparison with the AFC case. For stoping event 1, the mass of the stoped block was chosen to reflect the cumulative mass of anatectic melt assimilated by M by ~1015°C (~17 m.u.; the ratio of stoped block to initial magma mass is 0.17); the temperature of the stoped block was chosen to reflect the wallrock temperature at that point as well (~760°C). At 760°C, the (mushy) block is composed of ~78 wt.% crystals, 20 wt.% melt and 2 wt.% fluid phase, and its mineral assemblage is plagioclase > quartz > orthopyroxene > alkali feldspar, with spinel and rhombohedral oxide as accessory phases. The co-existing melt is rhyolitic and fluid-saturated. We note that in contrast to the current version of MCS in which fluid phase is

not able to transfer into M melt during partial melt assimilation, stoping allows the fluid phase to be incorporated into M melt. Prior to the first stoping event, resident magma temperature was ~1014°C, and M melt was crystallizing olivine + clinopyroxene + plagioclase + spinel. Following complete homogenization of the stoped block (including its fluid phase), the resident magma temperature decreased to 967°C, and orthopyroxene becomes stable in the cumulate assemblage over the range 967°C to 947°C. Rhombohedral oxide is the final phase to join the crystallizing assemblage at a magma temperature of 942°C. Upon stoping, resident magma melt SiO2 increases from ~56 to ~62 wt.% (Fig. 4).

The second stoped block reflects the conditions of the wallrock in the AFC run at M temperature ~908°C; at this temperature, the wallrock is ~795°C and cumulative anatectic melt assimilated is ~55 m.u. (ratio to initial magma mass is ~0.55). Stoped block 2 therefore has a temperature of ~795°C and its mass is 38 m.u. (55 – 17 that was assimilated in the first stoping event). Stoped block 2 is hotter than stoped block 1, and therefore it has proportionally more melt: crystal, melt, fluid phase proportions are 60, 38, and ~2 wt.%, respectively. Its mineral composition is plagioclase >> orthopyroxene > quartz, with accessory spinel and rhombohedral oxide. Like stoped block 1, the co-existing melt is rhyolitic and fluid saturated. For stoping event 2, the magma temperature before stoping is ~907°C and after stoping is 862°C. Prior to the second stoping event, resident magma was crystallizing olivine + clinopyroxene + plagioclase + spinel + rhombohedral oxide. Following assimilation of the second stoped block, olivine and clinopyroxene cease to crystallize, and orthopyroxene becomes a part of the cumulate assemblage. Upon the second stoping event, SiO_2 increases from ~67 to ~73 wt.% (Fig. 4).

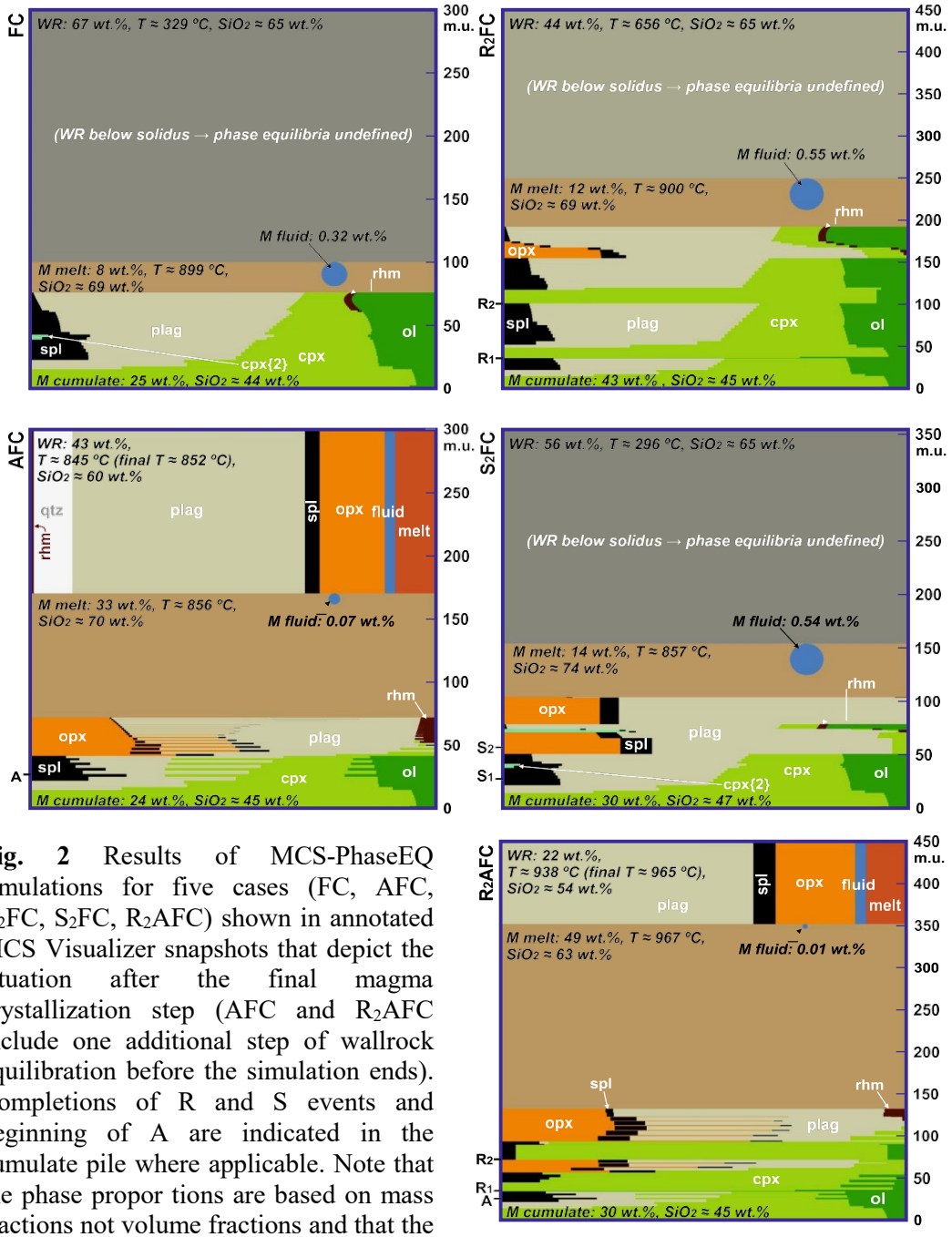

Fig. 2 Results of MCS-PhaseEQ simulations for five cases (FC, AFC, R_2FC, S_2FC, R_2AFC) shown in annotated MCS Visualizer snapshots that depict the situation after the final magma crystallization step (AFC and R_2AFC include one additional step of wallrock equilibration before the simulation ends). Completions of R and S events and beginning of A are indicated in the cumulate pile where applicable. Note that the phase propor tions are based on mass fractions not volume fractions and that the wt.% of the subsystems are relative to the whole magma-wallrock system; M melt, M fluid, and M cumulate comprise the total magma chamber mass. See Online Resource 8bfor full animations. Mineral abbreviations: ol = olivine, opx = orthopyroxene, cpx = clinopyroxene (FC and S_2FC include two separately output cpx solid-solution phases, see the respective outputs in Online Resource 6), plag = plagioclase, qtz = quartz, spl = spinel, rhm = rhombohedral oxide.

This simulation ends at ~856°C, which is a similar end temperature to that of the AFC case. Compared to assimilation of anatectic melt ('classical' AFC), stoping favors crystallization, as the resultant proportion of crystals in the magma system is higher in S_2FC (68 wt.%) than AFC (43 wt.%; Fig. 3d). The percent fluid phase is also higher in S_2FC (Fig. 3e). The final cumulate shares some characteristics with those of the AFC case: similar percentages of olivine, spinel, and orthopyroxene, slightly less clinopyroxene and less rhombohedral oxide, and slightly more plagioclase (Fig. 5). The range of olivine composition is more similar to the FC case. Interestingly, plagioclase in S_2FC is the most albitic of all the simulations (Online Resource 3). The final melt at ~856°C is rhyolitic. Oxide concentrations are more similar to the FC case than the AFC case (Fig. 4). For example, the distinct enrichment in Al_2O_3 seen in the AFC case is absent in the stoping case. K2O is enriched compared to FC, but less so than AFC.

The final temperature of wallrock is 296°C. This is the lowest final wallrock temperature of the five simulations. Adding cooler stoped bocks impacts the amount of enthalpy available for wallrock heating. In addition, upon stoping, in the new equilibrium M melt, quartz and alkali feldspar (where present in the stoped block) are not stable. Hence, there is an enthalpy cost to resorbing/reacting these phases, which decreases enthalpy available for transfer into the wallrock.

5. Case 5: Recharge-Assimilation of Wallrock Anatectic Melts- Fractional Crystallization (R_2AFC)

The output of the R2AFC case is stored in "MCS-R_2AFC_output_PhaseEQ.xlsx" file in Online Resource 6. The two recharge events from the R_2FC case were imposed on the AFC

case; recall that the wallrock initial temperature is high (700°C) and reflects an assumption that previous magma intrusion raised the wallrock temperature compared to an ambient geotherm. For the two recharge events, like R_2FC, the recharge magma/initial magma mass ratio is 0.75, and the temperatures of the recharge magmas at the instance of recharge are 1130°C and 1080°C for recharge events 1 and 2, respectively. Also, like R_2FC, recharge magma 1 is 100 wt.% melt, and recharge magma 2 is 21 wt.% crystalline. Assimilation begins at magma temperature of ~1069°C as in the AFC run (Fig. 3a), and by recharge event 1, M has assimilated ~8 wt.% anatectic melt (where percent is calculated based on the initial mass of resident magma - i.e., cumulative addition of 8 m.u. of anatectic melt). Immediately preceding recharge event 1, the magma temperature is ~1041°C, with a crystallizing mineral assemblage of olivine + clinopyroxene + plagioclase + spinel. In response to recharge event 1, the resident magma temperature increases to ~1087°C, and plagioclase and spinel stop crystallizing. SiO_2 decreases from ~54 to 52 wt.% and MgO increases from 3.9 to 5.8 wt.% (Fig. 4).

After the first recharge event, AFC continues; at ~1050°C, spinel rejoins the crystallizing assemblage, and at magma temperature ~1020°C, orthopyroxene starts to crystallize and at ~1014°C, plagioclase rejoins the crystallizing assemblage. Recharge event 2 is triggered when the resident magma is 998°C; the addition of enthalpy via recharge heats the resident magma to ~1026°C. Olivine begins to crystallize again for a small temperature interval, and plagioclase and orthopyroxene briefly stop crystallizing. After ~10°C of cooling, the mineral assemblage returns to its pre-recharge assemblage of clinopyroxene + plagioclase + spinel + orthopyroxene. At 991°C, clinopyroxene ceases to crystallize, and magma melt reaches fluid saturation (with a mixed H2O + CO2 fluid), but the proportion of fluid phase in the magma

system is quite small (~0.001 m.u.; Fig. 3e). At 979°C, rhombohedral oxide joins the assemblage. A modest change in melt composition is noted; upon recharge, SiO_2 again decreases, this time from ~60 to 57.5 wt.% and MgO increases from 2.3 to 3.2 wt.% (Fig. 4).

The equilibration temperature for R_2AFC is ~965°C. The final magma melt composition is distinctly lower in SiO_2 compared to the other four simulations and plots at the low SiO_2 end of the dacitic field. R_2AFC manifests a similar enrichment in Al_2O_3 and K_2O compared to AFC; likewise, the depletions in FeO, H_2O and Na_2O are similar to AFC (Fig. 4). P_2O_5 is the least enriched among all cases. Like AFC, R_2AFC suppresses crystallization. Regardless of their high absolute mass of 133 m.u., crystals make up only ~38 wt.% of the magma body in the R_2AFC run, compared to ~76 wt.% in FC, and R_2AFC expresses the smallest degree of fluid saturation (Fig. 3). The range of olivine and plagioclase compositions is most similar to AFC, with the most Fe-rich olivine being Fo_{66} and the most Na-rich plagioclase being An_{70} (Online Resource 3).

For each step of anatectic melt transfer into magma melt, the size of anatectic melt increment is ~2 to 5 wt.% of the initial wallrock system (i.e., 4 to 10 m.u.) and generally increases as wallrock heats up. This changes after alkali feldspar completely reacts and ceases to be part of the wallrock solid assemblage. After this (wallrock temperature of ~788°C, magma temperature ~1015°C, Fig. 7), wallrock melt productivity decreases and the size of the increments transferred decreases to 1-2 wt.% of the initial wallrock mass (3-4 m.u.). Melt productivity increases again at wallrock temperature of ~845°C. Like the wallrock melt in AFC, the anatectic melt that is transferred and homogenized with resident magma melt is mostly rhyolitic (~70 to 76 SiO_2).

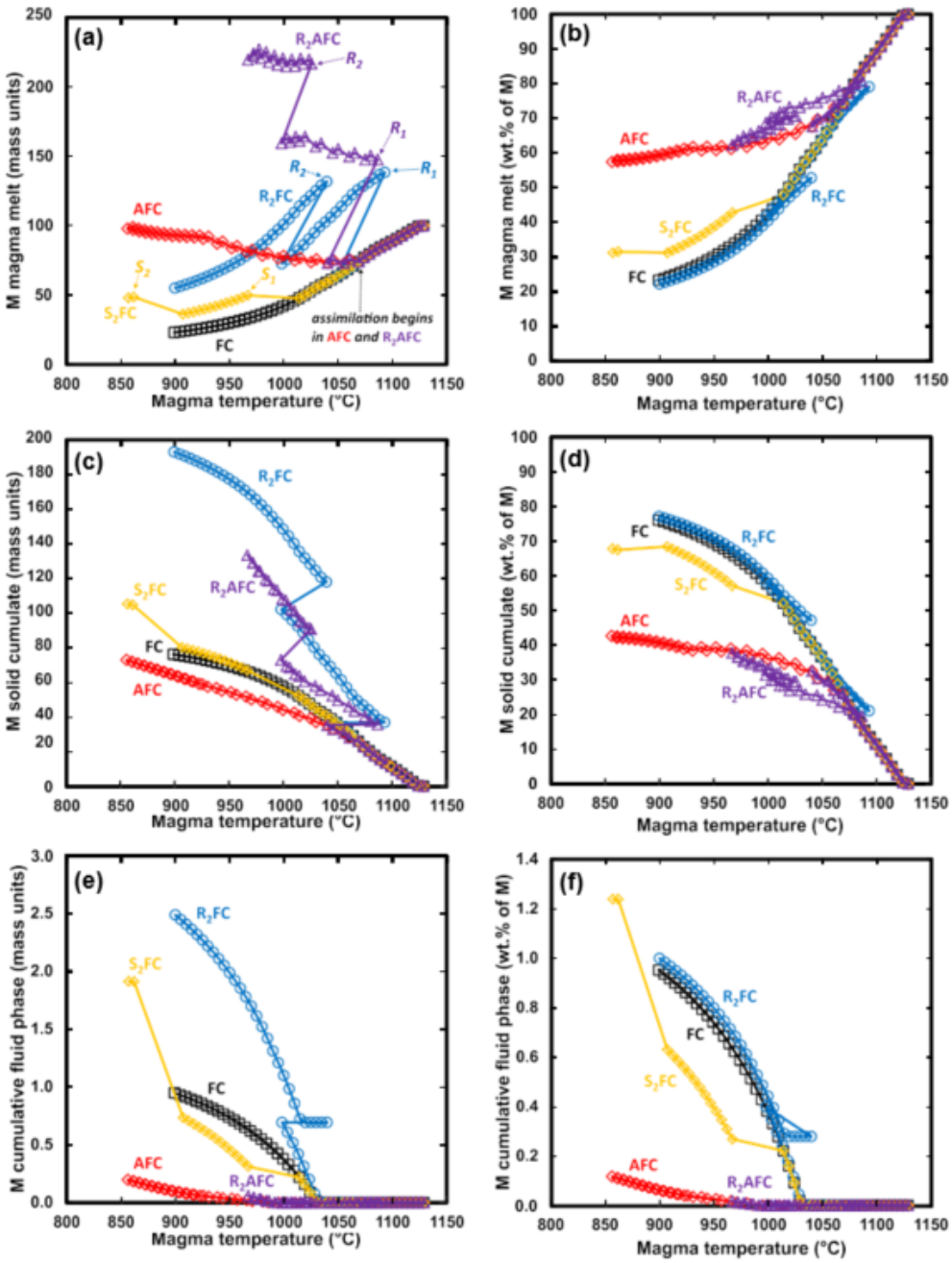

Fig. 3 Results of MCS-PhaseEQ simulations for five cases (FC, AFC, R_2FC, S_2FC, R_2AFC) shown in magma temperature (°C) versus (a) absolute and (b) relative M magma liquid (melt) mass, (c) absolute and (d) relative total cumulative mass of crystals removed to the cumulate reservoir, and (e) absolute and (f) relative total cumulative mass of fluid phase. Each simulation runs from parent magma liquidus temperature to the end of the simulation. For cases involving assimilation, the simulation ends when magma and wallrock are at or close to thermal equilibrium. For cases that do not involve assimilation, the simulation ends at a user-defined "hard stop" temperature. Completions of R and S events and beginning of A are indicated for the relevant runs in a. See text, tables and Online Resources for additional details.

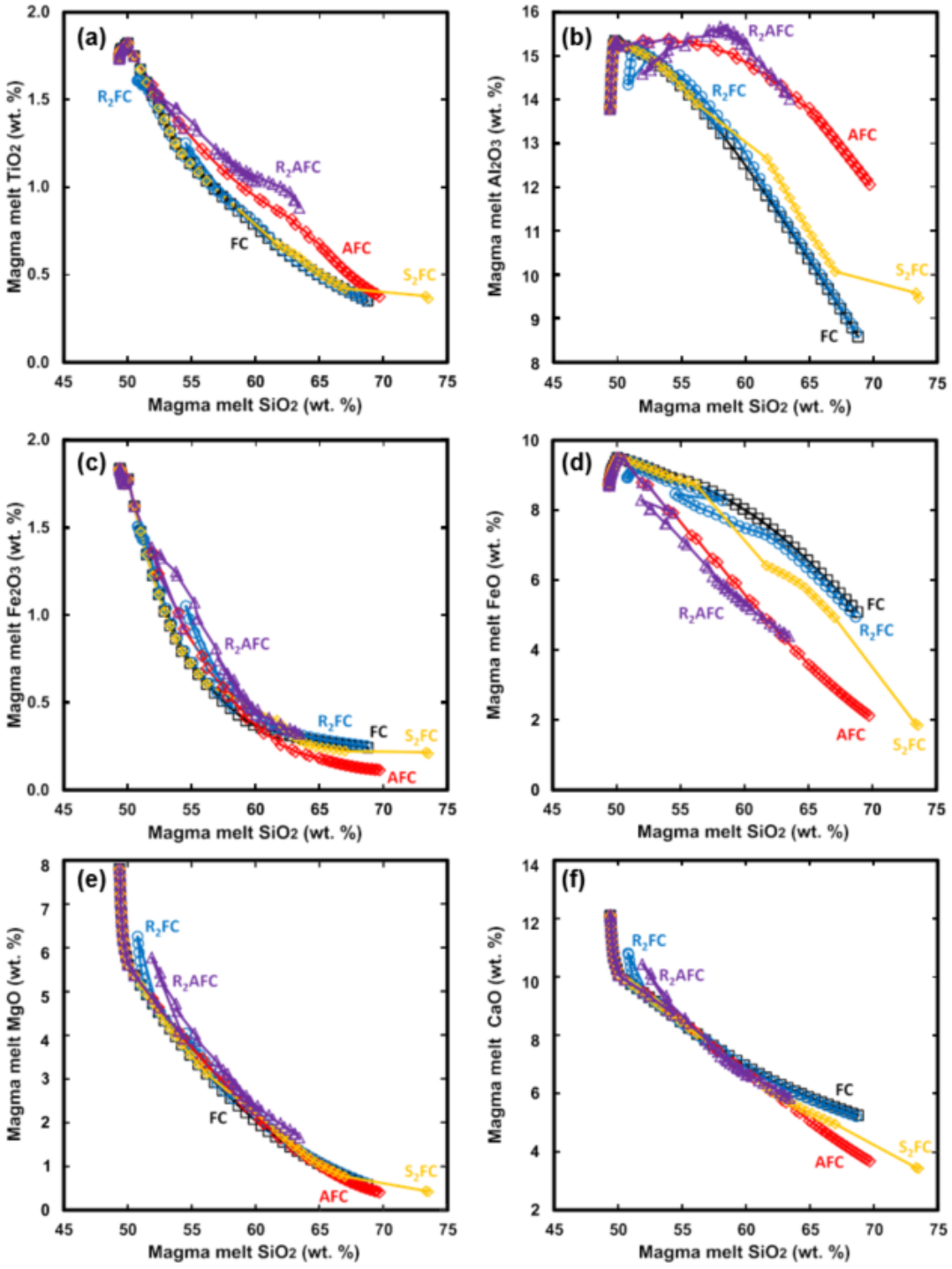

Fig. 4 Results of MCS simulations for five cases (FC, AFC, R_2FC, S_2FC, R_2AFC) shown in magma melt SiO_2 (wt.%) versus (a) TiO_2, (b) Al_2O_3, (c) Fe_2O_3, (d) FeO, (e) MgO, (f) CaO, (g) Na_2O, (h) K_2O, (i) P_2O_5, and (j) H_2O (wt.%).

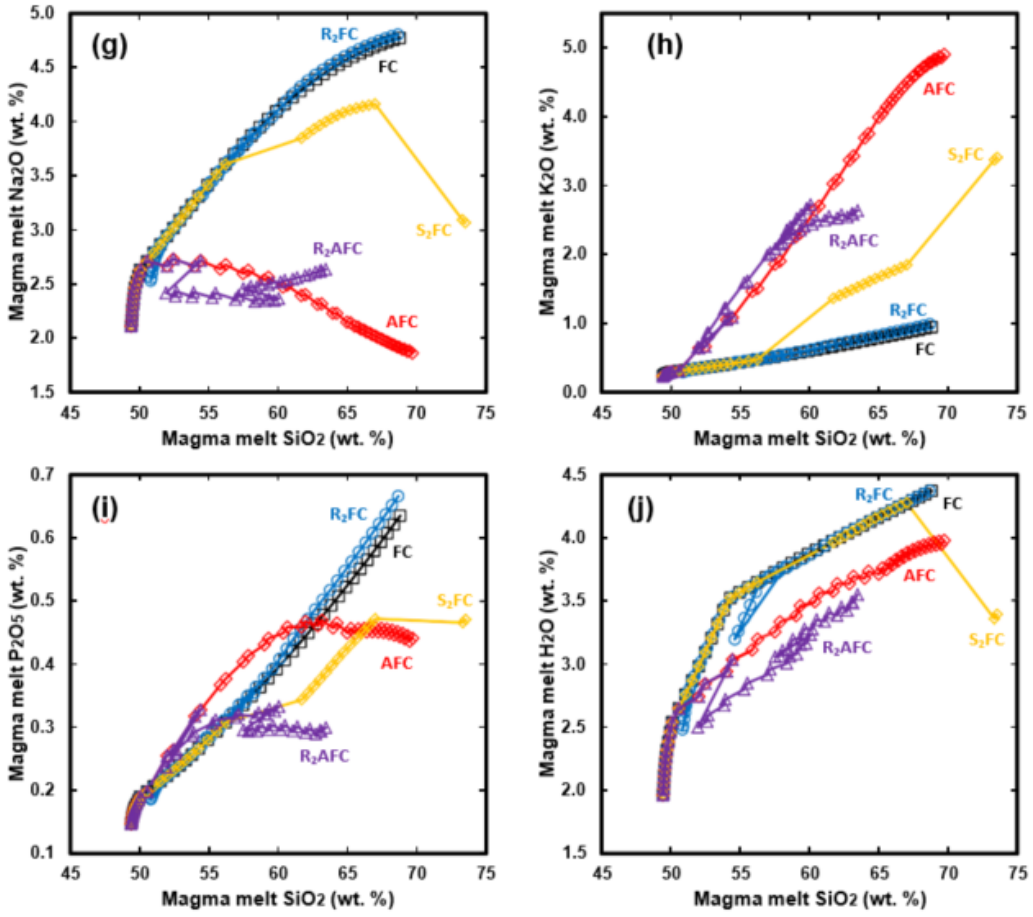

Fig. 4, cont'd. Results of MCS simulations for five cases (FC, AFC, R_2FC, S_2FC, R_2AFC) shown in magma melt SiO_2 (wt.%) versus (a) TiO_2, (b) Al_2O_3, (c) Fe_2O_3, (d) FeO, (e) MgO, (f) CaO, (g) Na_2O, (h) K_2O, (i) P_2O_5, and (j) H_2O (wt.%).

At the equilibration temperature of ~965°C, ~51 wt.% of the wallrock system has been assimilated into the resident magma (102 m.u. out of the original 200; Fig. 7a). Thus, substantially more anatectic melt was assimilated due to recharge, consistent with more enthalpy being available from magma cooling and crystallization to heat wallrock compared to AFC. However, when assessed as a percentage of the resident magma system, this assimilated mass represents only ~29 wt.% of the final magma body (melt +crystals + fluid phase) - in contrast to 41 wt.% of the final magma body in the AFC case (Fig. 7b); thus, although the mass assimilated is larger, the addition of recharge magma "dilutes" the crustal

signature. Like the R_2FC case (compared to FC), the size of the magma body system (melt + cumulate + fluid phase, 352 m.u.) is substantially greater than AFC (Fig. 3).

D. Discussion

It is instructive to compare outcomes of the cases described above (FC, R_2FC, AFC, S_2FC, R_2AFC) to illustrate how fractional crystallization, recharge, and contamination (by assimilation of wallrock partial melts or by assimilation of stoped blocks) affect the evolution of the composite shallow crustal magma system. We have purposely kept the compositions of M, WR, and R magmas constant in order to focus upon process and sequence rather than subsystem compositional variations. These five cases reflect a very small fraction of possible RASFC scenarios, but they underscore some of the challenges petrologists face in trying to identify crustal processes that dictate magma compositions.

1. Comparison of Thermal and Mass Characteristics

The final modeled wallrock temperature is related to the overall size of the magma body, the mass of cumulates formed, and the mass and thermodynamic state of the recharge magma/anatectic melt/stoped blocks added to the magma system. AFC and R_2AFC provide a contrast that illustrates the impact of magma recharge; the final wallrock temperature of R_2AFC (965°C) is higher than that of AFC (852°C), reflecting the addition of recharge magma with its attendant enthalpy (Fig. 6). All other parameters of these simulations are the same, including the initial wallrock temperature of 700°C. The added enthalpy from hotter recharge magma into resident magma yields a larger increase in wallrock temperature during resident magma cooling and crystallization. Not only is there more resident magma to cool (i.e., more sensible heat), but the mass of crystals formed in R_2AFC is also greater, adding more latent

heat of crystallization. The higher final wallrock temperature also means that wallrock melts to a greater extent for R_2AFC than AFC (56 wt.% versus 42 wt.%, respectively). More anatectic melt is transferred into the magma body per decrement of magma cooling (Fig. 7a), and thus, the cumulative amount of wallrock partial melt transferred is larger in R_2AFC. However, while the total mass of anatectic melt added to resident melt is larger in R_2AFC than AFC (~102 versus 71 m.u.; Fig. 7a), the percentage of the magma system mass that comes from anatectic melt is smaller (29 wt.% in R_2AFC versus 41 wt.% in AFC; Fig. 7b) due to the added recharge magma mass that makes the R_2AFC total magma system mass larger (~352 versus 171 m.u. for R_2AFC versus AFC, respectively, Online Resource 2). These collective differences, although perfectly clear in hindsight, are neither trivial nor easily predicted. They also bring into focus the difficulty of defining "rates" or amounts of assimilation. Furthermore, the enhancement of assimilation in systems with significant recharge might not be obvious geochemically due to the effects of recharge in diluting the geochemical signature of assimilated partial melt. Even in this simple comparison, one notes the complex feedbacks that can take place. The magnitude of these non-linear compositional effects varies depending on most of the sensible parameters of a given simulation. Although it is difficult to make broad brush statements, appreciation of these complex feedbacks clearly emerges once the MCS RAFC models are computed.

The final wallrock temperatures for FC, R_2FC and S_2FC are 329°C, 656°C, and 296°C (Fig. 2), respectively. The lowest temperature of the stoping case is due to addition of cold blocks of wallrock. In addition, minerals in the blocks such as quartz and alkali feldspar are not stable after the blocks equilibrate with M melt. The energetic cost of resorbing these is debited to the magma, and thus magma has less enthalpy available to transfer to wallrock. The

higher final WR temperature of R_2FC of 656°C (compared to FC and S_2FC) is a function of added enthalpy due to recharge and underscores the energy impact and thermal priming potential that recharge can have: with two recharge events of modest recharge to initial magma mass ratio (0.75), the wallrock temperature increases from its initial (100°C) to a temperature that reflects a relatively high geothermal gradient akin to the assimilation cases presented here. While different parameters will yield different outcomes, these examples highlight the potential for thermal priming via recharge.

The total mass of the magma system (which does not include the residual wallrock) is an obvious outcome of MCS, and one that is simple to contrast. FC, a "closed-system" process, yields the smallest magma body size, where the magma body includes resident magma melt + cumulates + fluid phase. The AFC and S_2FC cases are ~1.5 to 1.7x bigger than the FC magma body, R_2FC is ~2.5x bigger, and R_2AFC is the biggest at ~3.5x (Online Resource 2; these comparisons relate masses upon completion of the simulations). These differences are obviously related to addition of recharge magma, anatectic melt and/or stoped crustal blocks and have implications for the sizes of potential eruptions, the growth of the crust (i.e., mass of magma added to the crust), its state of stress, and local geotherms.

Another difference, not necessarily obvious, is the percent melt versus crystals among these different magma systems. AFC and R_2AFC suppress crystallization, compared to the other cases. In the AFC and R_2AFC cases, the cumulate reservoir composes about 38-43 wt.% of the resident magma system, whereas it is ~76 wt.% of the magma body mass in the FC and R_2FC cases; S_2FC yields approximately 67 wt.% crystals (Fig. 3d). Suppression of crystallization is caused by addition of anatectic melt, which changes the temperature-composition relationships such that the mass of crystals that form per decrement of cooling of

M melt is lower when assimilation is ongoing (e.g., the slope of the magma temperature versus percent cumulative crystals is lower for AFC and for the assimilation-influenced parts of the R_2AFC compared to FC and R_2FC, Fig. 3d). Thus, in the two cases that invoke assimilation, the magma system is dominated by melt: 57 wt.% for AFC and 62 wt.% for R_2FC (Fig. 3b). The higher equilibration temperature for R_2AFC plays a role in the high proportion of melt, but even if the slope of the R_2AFC magma temperature versus percent cumulative crystals trend (Fig. 3d) is extrapolated to a higher final magma temperature, the percent crystals is still lower than the R_2FC and FC cases. Note that although the proportion of crystals in R_2AFC is smaller than in FC and S_2FC (Fig. 3d), the total mass of crystals is larger (Fig. 3c), as expected from the larger total system mass. This outcome leads to the prediction that basaltic systems recharged with magmas similar to the initial parent magma will build large cumulate piles whereas basaltic systems that experience contamination by average upper crust may be melt dominated systems.

Explicit tracking of instantaneous and cumulative masses of minerals crystallized and anatectic melt assimilated (versions of the DePaolo (1981) "r", which was defined in this paper as mass assimilation rate/mass fractional crystallization rate) provides a platform by which to examine the ratio of mass of anatectic melt assimilated to the mass of cumulates formed during AFC. Here, instantaneous refers to the ratio of the mass of anatectic melt assimilated divided by the mass of crystals formed in a single (circa 5 °C) AFC magma temperature decrement (i.e., crystallization followed by assimilation); in the case when recharge occurs (R_2AFC), the crystal mass includes crystals formed upon recharge added to those formed in a fractional crystallization "event." Cumulative refers to the total mass of anatectic melt divided by the total mass of crystals from the first step in the simulation to the

present temperature step. For AFC, instantaneous and cumulative "r" values vary from 0.71 to 2.6 and 0.13 to 0.99, and for R_2AFC from 0.16 to 2.0 and 0.13 to 0.83, respectively (values reflect start of assimilation to end of the simulation, Fig. 8). For the first part of the AFC instantaneous and cumulative trends (from M melt temperate of ~1055°C to 930°C), the productivity of melt in wallrock systematically increases as magma temperature goes down. The marked change (decrease) in instantaneous "r" between ~930°C and 922°C reflects decreased anatectic melt productivity because alkali feldspar is no longer part of the wallrock assemblage; this change is reflected in the change in slope of the cumulative plot as well (Fig. 8). The subsequent increase in instantaneous "r" is due to a decrease in the mass of crystals produced with each AFC "event."

For the R_2AFC case, instantaneous and cumulate "r" are the same as AFC until the first recharge event. Upon recharge (event 1, R_2AFC, Fig. 8a), instantaneous "r" increases systematically (offset to a higher temperature due to the effects of recharge) because the mass of anatectic melt transferred from wallrock after the recharge events is higher than before; this leads to an increase in instantaneous "r". The decrease in R_2AFC instantaneous "r" at temperatures between ~1020°C and 998°C (before recharge event 2) occurs because alkali feldspar in the wallrock is fully reacted, and anatectic melt productivity decreases as a result. A consequence of the second recharge event (that brings the magma temperature up to ~1026°C), is a short-lived pulse of crystallization that yields a decrease in both instantaneous and cumulative "r" (Fig. 8). Following this, the somewhat complex trend seen in the instantaneous "r" is the result of changes in crystallization as the magma system responds to being heated by recharge as well as the changing restitic mineral composition of wallrock and the associated consequences on wallrock melt production.

Three outcomes of the analysis above are that (1) crystallization and assimilation "rates" are difficult if not impossible to predict in the absence of thermodynamic treatment, and thus, (2) quantitative thermodynamic treatment of RAFC processes is absolutely essential to characterize these rates. Furthermore, (3) these rates are therefore neither predictable nor constant, and models that use constant "r" values as defined, for example, by DePaolo (1981) do not reflect the phase equilibria or energetic consequences of these processes. Given the availability of computational tools that provide thermodynamic estimations of magma systems, we suggest that tools that lack phase equilibria treatment of igneous systems may, at best, provide only rough estimates of natural processes and therefore should be used with considerable caution. In addition, one should be wary of conventional arguments and inferences often applied when analyzing petrological and geochemical data. Many of these notions are based on closed system behavior and/or bulk assimilation without inclusion of phase equilibria.

2. Geochemical and Petrological Indicators of Open-System Processes

The major oxide signatures of open-system magmatic processes manifest in ways that may not be obvious or intuitive. Among the best indicators of open-system processes are radiogenic and stable isotopes, assuming that there is isotopic contrast between resident magma, crust, and recharge magma. Why then toil to identify or quantify fingerprints of RASFC using major element data? The first reason is practical; typically, many more samples are analyzed for major elements than for isotopes and some trace elements. Second, careful reconstruction of major element characteristics as well as the crystallizing mineral assemblage is required for accurate calculation of trace element and isotopic signatures of an open-system magma via the use of mineral/melt and mineral/fluid distribution coefficients. Thus, to document trace

element and isotopic open system signatures, one must know the open-system history of melt, minerals, and fluid. The third reason is that a higher number of constraints (major oxides, trace elements, isotopes) leads to better models, and better models can lead to more refined interpretations. For example, determining whether a magma storage system is more likely located in the shallow versus deep crust has implications for volcanic eruption monitoring and hazard mitigation. All such models should naturally always be assessed in relation to MCS-independent evidence such as geophysical constraints. Fourth, as has been shown in numerous studies, in some cases isotopic contrast between magma and wallrock, for example, is lacking (e.g., Stern & Johnson, 2010), and thus pursuit of open-system major element and phase equilibria models is an absolute necessity.

Below, we highlight major element and phase equilibria comparisons that illustrate the complexity of identifying open-system processes and that emphasize the value of thermodynamic modeling.

a. Identifying the Fingerprint of Magma Mixing from Melt and Mineral Data

Classic linear trajectories often ascribed to binary mixing are not present in many of the R_2FC major element plots (e.g., SiO_2 versus MgO, Na_2O, TiO_2; Fig. 4). This is because homogenization is followed by crystal removal through fractional crystallization. The inverse is also true; there are segments of some of the FC oxide arrays that are approximately linear (e.g., K_2O, P_2O_5, H_2O, Al_2O_3 at SiO_2 > ~55 wt.%), and thus may resemble mixing trends. Thus, the assumption that mixing can be diagnosed by linear trends is misleading.

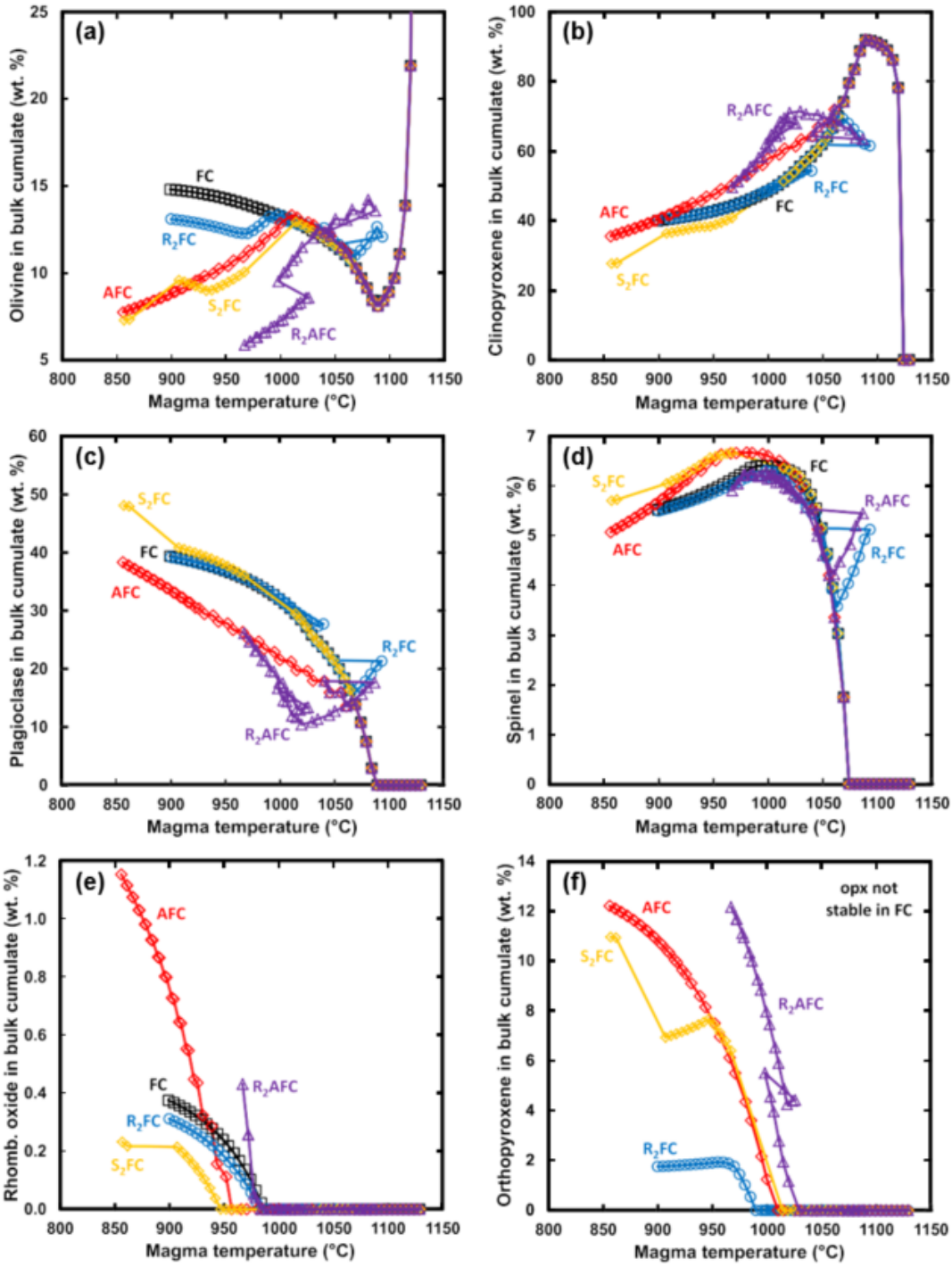

Fig. 5 Magma temperature (°C) versus wt.% of minerals in the bulk cumulate in the five MCS simulations. (a) olivine, (b) clinopyroxene (cpx), (c) plagioclase, (d) spinel, (e) rhombohedral oxide, and (f) orthopyroxene (opx).

The similarity of many oxide trends for FC and R_2FC (Fig. 4) underscores the difficulty of diagnosing process using such data. But some oxides can show distinctive behavior with recharge. In the simulations highlighted here, MgO is the most telling. Its concentration changes beyond analytical uncertainty when recharge with a more primitive magma occurs, but the difference between FC and R_2FC is subtle and might be difficult to detect in a suite of samples that lack stratigraphic control.

As recognized in numerous studies, crystal cargo (e.g., Davidson *et al.* 2007; Streck 2008, and references therein; Edwards *et al*. 2019, Ubide *et al.* 2019; Ubide & Kramer 2018; Streck *et al.* 2008; Ginibre *et al*. 2007; Davidson *et al.* 1997) can provide a rich inventory of mixing histories. Are MCS results applicable to such data? The answer is yes, with careful consideration of the design features of MCS. The current version of MCS immediately fractionates all crystals, and thus zoned crystals are technically not produced and no resorption of cumulates is permitted. What is produced is a sequential record of crystallization. The crystals that are fractionated into a separate cumulate reservoir during progressive RFC "events" can be reimagined as growing, zoned crystals that remain in the M melt and interact thermally but not chemically with host magma; the mass and energy balance for such zoned crystals is the same as it is for crystals fractionated to the cumulate reservoir. By using the sequential record and carefully applying it to crystal cargo data (subject to the limitation in the current version of MCS that crystals do not chemically interact with M melt), one can utilize MCS results to better understand possible crystal behavior that results from RASFC.

Envisioning crystals as growing in this way, the R_2FC modeling results indicate that in some cases, the record of recharge may be selective. In R_2FC, the complete record of mixing is not preserved in plagioclase, which is not stable upon mixing, but returns to the stable

assemblage within ~25°C of cooling after the first recharge event and ~5°C of cooling after the second. Its compositional change is small after the first event (An_{81} to An_{82}) but larger and detectable after the second (An_{71} to An_{77}). In stark contrast to plagioclase behavior, olivine crystallizes both before and after mixing, thus recording a complete phase equilibria record of the effects of mixing. The mineral changes composition abruptly from Fo_{70} to Fo_{78} after the first recharge/mixing event, and from Fo_{55} to Fo_{68} after the second event. These changes are easily detected by electron microprobe analysis, provided the zoning is preserved.

Crystals produced during mixing may also preserve a record of temperature changes. For R_2FC, the temperature of the magma increases 40–50 degrees after each mixing event. That record may be preserved in mineral geothermometry. In R_2FC, olivine and clinopyroxene would be the best indicators of the temperature change, as they preserve the most complete record of mixing. In contrast, plagioclase would not likely record heating associated with the first recharge event for the reasons discussed in the previous paragraph. The takeaway lesson from this single example is that in order to fully document temperature excursions associated with recharge that are recorded in minerals, one needs a complete picture of the phase equilibria changes that occur in response to the mixing event. Even with such data, documenting temperature changes may be challenging given the equilibrium requirements and uncertainties of many geothermometers (e.g., Putirka 2017).

The presence or absence of distinctive recharge signatures is a function of the magma mixing scenario. In the cases highlighted here, the same parent magma is mixed into its evolving counterpart. Different scenarios will lead to different mixing fingerprints. For example, the mass of the recharge event compared to the resident magma/melt mass will influence the extent to which pre- and post-recharge magmas change composition, and a

substantial compositional contrast between resident melt and recharge magma may yield recharge signatures that are more obvious than those presented here. Myriad forward modeling case studies can be done in MCS to examine the temperature, composition, and mass landscape of mixing and crystallization processes.

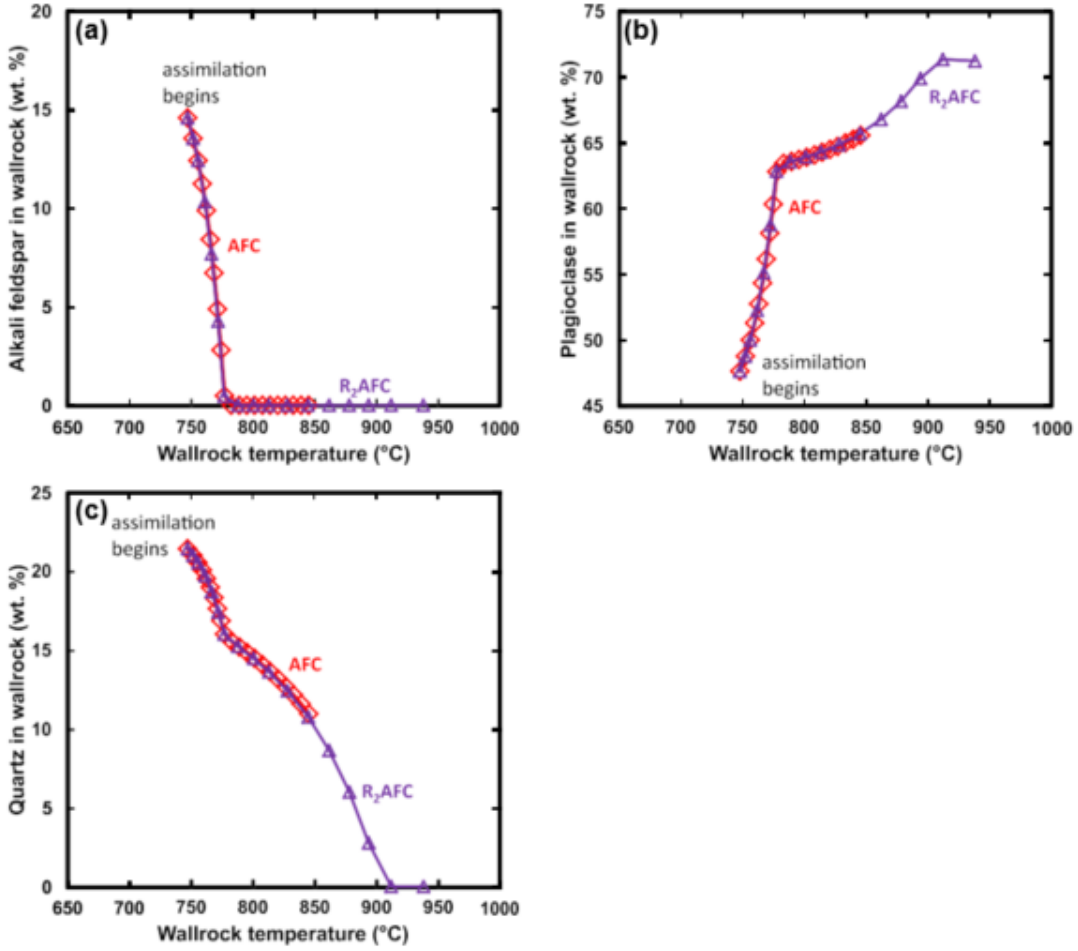

Fig. 6 Wallrock temperature (°C) versus wt.% of (a) alkali feldspar, (b) plagioclase, and (c) quartz in wallrock solids (restite after partial melt is transferred to magma) for two MCS cases involving assimilation of wallrock anatectic melt (AFC, R_2AFC). Wallrock initial temperature is 700°C, and assimilation starts at wallrock temperature of 747 °C when the percolation threshold has been exceeded. Wallrock heats up to the end of the simulation, where magma and wallrock temperature are at or close to thermal equilibrium.

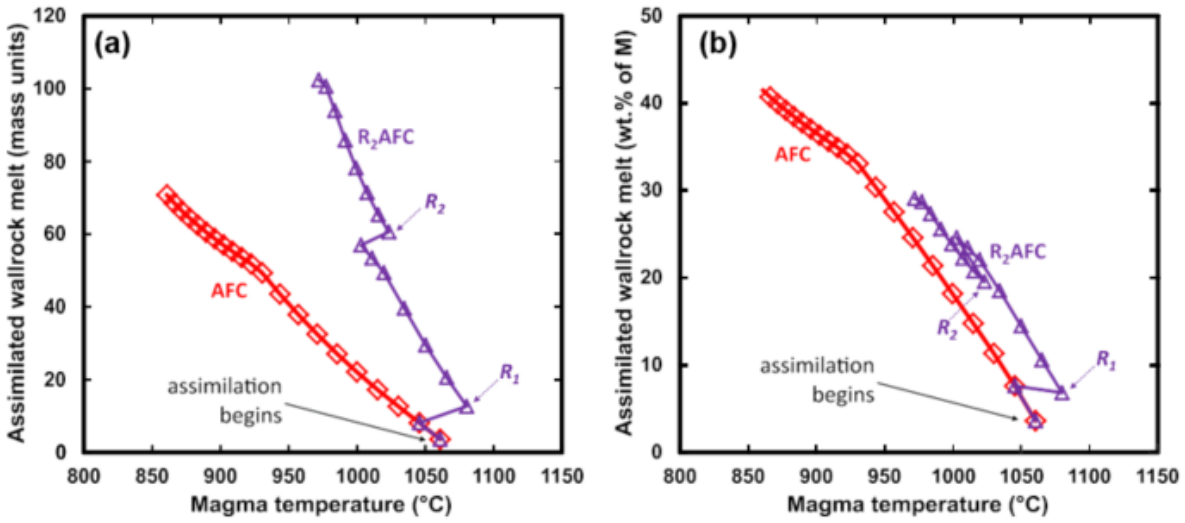

Fig. 7 Magma temperature (°C) versus (a) absolute and (b) relative amount of cumulative anatectic melt assimilated into M melt once assimilation begins. Completions of the R events for the R_2AFC case are indicated.

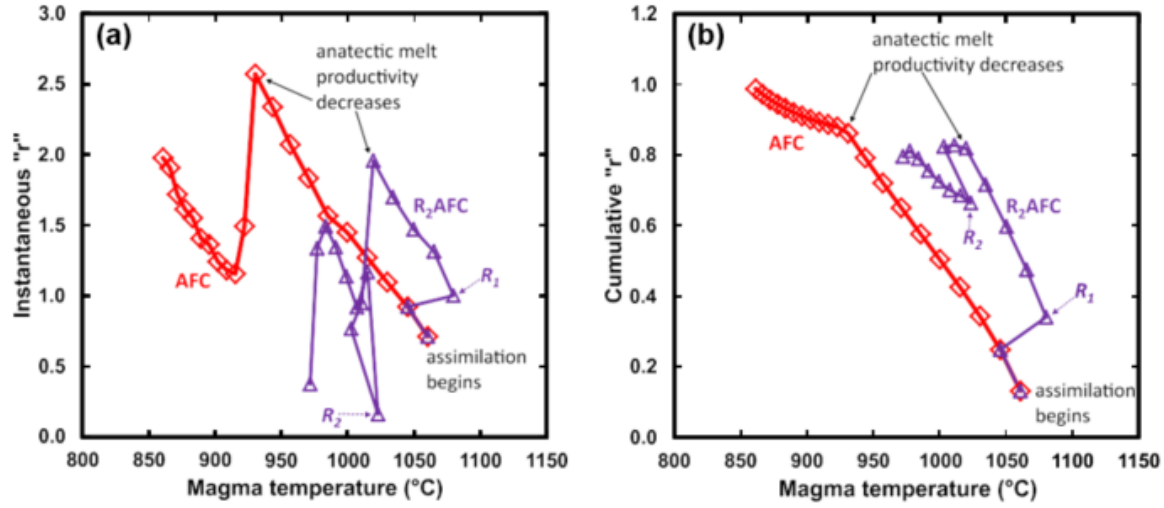

Fig. 8 Magma temperature (°C) versus (a) instantaneous "r", and (b) cumulative "r" shown for two MCS cases with assimilation of wallrock anatectic melt (AFC, R_2AFC). The definition of "r" is based on DePaolo (1981) and is the mass of anatectic melt assimilated/mass of crystals formed. Instantaneous refers to those masses for each individual temperature step where assimilation ± recharge occurs, and cumulative refers to the total mass of anatectic melt assimilated/total mass of cumulates produced from the start of the simulation to the magma temperature shown. The value of "r" is zero before assimilation begins, and for simplicity, this part of the AFC or R_2AFC is not shown. Instantaneous and cumulative "r" after completion of recharge events 1 and 2 labeled, as are the values at which anatectic melt productivity decreases due to complete reaction of alkali feldspar. See text for discussion.

b. Identifying the Fingerprint of Crustal Assimilation from Melt and Mineral Data

Similar to the FC versus R_2FC comparison, some major oxides do not show evidence of crustal assimilation. For example, AFC and R_2AFC are generally similar to FC and R_2FC in SiO_2 versus MgO (with the exception of the notable change immediately after the recharge events for R_2AFC and R_2FC) and CaO (Fig. 4). This is an interesting result given the anatectic melt and recharge magma have very different concentrations of these oxides, and yet, the SiO_2 versus CaO and MgO trends are indistinguishable for these 4 cases at >55 wt.% SiO_2.

In contrast, three major elements that show quite distinct differences are K_2O, Na_2O, and Al_2O_3 (Fig. 4). Once assimilation begins, Al_2O_3 is more concentrated in AFC and R_2AFC than in their non-assimilation equivalents (at the same SiO_2). Because these cases contrast with respect to not just the bulk composition of the added anatectic melt, but also in the mass and identity of cumulus phases, there could be a number of explanations for these differences. The total final percentage of cumulus plagioclase in FC and AFC is similar (~39 wt.%) whereas for R_2AFC, it is smaller (~26 wt.%) (Fig. 5c). Thus, for FC and AFC, about the same final proportional amount of plagioclase was removed as a fractionating phase, but that final tally obscures differences as the systems evolve. Reference to Fig. 5c shows that plagioclase makes up a smaller proportion of the cumulate assemblage in AFC, compared to FC, for most of the simulation. The reason the final proportions are similar is because the end temperature of AFC (~856°C) is lower than that for FC (~899°C), which provides a slightly longer crystallization temperature interval for plagioclase in the AFC case. For most of the AFC simulation, for each cooling step, less plagioclase forms, and thus the resident melt is not debited in Al_2O_3 as extensively as in the FC case (Fig. 4b). In the case of R_2AFC, Al_2O_3 is slightly higher at the same wt.% SiO_2 than in the AFC case and reflects the lower cumulate plagioclase proportion,

compared to AFC (Fig. 5c). Thus, less Al_2O_3 is removed from resident melt. R_2AFC and AFC have distinctly lower Na_2O at the same SiO_2 (once assimilation begins), whereas K_2O is distinctly higher than FC and R_2FC (Fig. 4g, h). The bulk composition of wallrock and the way it melts are responsible for these differences. Alkali feldspar melts disproportionately into anatectic melt, enriching the melt in K2O. Plagioclase (~$An_{37–35}$), on the other hand, disproportionately increases in abundance in wallrock restite, and thus, anatectic melt addition dilutes Na2O in resident magma melt. All these changes are recorded in the respective output files in the Online Resource 6.

Resident melt H_2O is less concentrated in AFC and R_2AFC compared to FC and R_2FC (Fig. 4j) due to an assumption imposed on the current version of MCS. As discussed in the section entitled Case 3: Assimilation-Fractional Crystallization (AFC), while wallrock is fluid-saturated upon initiation of melting, the fluid phase is not incorporated into magma melt although H_2O dissolved in anatectic melt is. Once assimilation begins, dilution due to anatectic melt addition is evident, and lower rates of crystallization (i.e., mass of crystals fractionated per decrement of cooling in resident magma) of anhydrous minerals in the AFC case lessens the amount of H_2O enrichment. R_2AFC parallels the AFC trend until the first recharge event, which dilutes H_2O. The second causes additional dilution. The combination of recharge and lower rates of crystallization yields the lowest magma melt H_2O contents of all the cases by the termination of the simulation. The remaining oxides also show differences, but these are less pronounced and are due to differences in anatectic melt versus magma melt compositions and the associated phase equilibria differences between the FC and AFC cases.

Based on the analysis above, for the AFC and R_2AFC cases presented here in which a depleted basalt is being contaminated by anatectic melt from average upper continental crust,

the only major element and phase equilibria indicators that are likely to be diagnostic are the resident melt K_2O, which is enriched by ~5x by the end of the AFC versus FC simulation; (Fig. 4h). An expectation that crustal assimilation would lead to more profound and obvious changes in other oxides might yield a misinterpretation of these data that attributes the geochemical signals to mantle heterogeneity. Likewise, depletion of Na_2O might be easily misinterpreted as representative of mantle heterogeneity and/or alteration. While the AFC/R_2AFC Al_2O_3 versus SiO_2 trends are distinct from those of FC, Al_2O_3 may be difficult to interpret as its concentration is partly a function of the amount of plagioclase crystallization, which may vary according to crystallization conditions. While we recognize that these results are case specific, they underscore the importance of open-system models that evaluate phase equilibria.

Mineral fingerprints of assimilation are potentially preserved in the cumulate assemblage. The most obvious is the presence of orthopyroxene, which is not stable in FC and is in much smaller proportion in R_2FC (~1 wt.%) compared to >10 wt.% for AFC and R_2AFC (Fig. 5f). Orthopyroxene is stabilized by SiO_2 added by anatectic melt; on the other hand, fractionation of orthopyroxene enriches M melt in SiO_2 less than crystallization of olivine so the effect of adding SiO_2 into the system by assimilation is counteracted (Fig. 4). Other wt.% differences for the cumulate assemblages are evident. For example, olivine and clinopyroxene do not crystallize for the full AFC simulation whereas they do in FC.

Similar to predictions about the effects of magma recharge and mixing, the case studies involving assimilation bring into focus the difficulty of postulating a priori the patterns expected on element and oxide variation diagrams and in mineral compositions and identities. Major element and mineralogical responses to these processes may not be easily predicted or

distinguished. The overarching conclusion of the recharge and assimilation case studies is that using closed system reasoning may produce misleading and spurious conclusions because the effects of open-system processes are non-linear and, in many cases, non-intuitive.

c. Distinguishing the Mode of Crustal Contamination: Crustal Assimilation versus Stoping

Here, we compare and contrast AFC and S_2FC to illustrate a possible range of effects from different mechanisms of crustal contamination. As anticipated, evidence of bulk assimilation of stoped blocks compared to assimilation of anatectic melt is preserved in some oxide trends, but not in others.

In the S_2FC scenario, SiO_2 versus MgO and CaO are quite similar to AFC, and TiO_2, Fe_2O_3, and P_2O_5 show only subtle differences (Fig. 4). In contrast, Al_2O_3, FeO, K_2O, Na_2O, and H_2O are markedly different for AFC versus S_2FC. For the first stoping event, Al_2O_3 versus SiO_2 has a slope that is rather similar to FC and R_2FC trends, and thus is much lower in concentration (at the same SiO_2) compared to AFC. While the Al_2O_3 content of the stoped block is slightly higher than M melt, addition of the stoped block (with its Al_2O_3) is apparently offset by a "pulse" of plagioclase crystallization (described in the next paragraph) that removes Al_2O_3. While intuition may dictate that adding an Al-rich stoped block would lead to increased Al_2O_3 in M melt, this will not always be the case and this example again illustrates how simplistic reasoning can be misleading (e.g., polyphase mixing is not identical to melt-melt mixing). Likewise, Al_2O_3 remains at lower concentrations compared to AFC during and after the second stoping event for the same reason. Spinel also experiences a pulse of crystallization with both stoping events, and likely contributes to the lower Al_2O_3 in the S_2FC case. S_2FC Na_2O is higher than AFC (Fig. 4g); by the first stoping event, Na_2O in the stoped

block is much higher than in the equivalent anatectic melt (i.e., at approximately the same wallrock temperature), and thus Na_2O in the S_2FC case is higher than in the AFC case. K_2O is the opposite (Fig. 4h). S_2FC K_2O is not as enriched as in the AFC case because the stoped block K_2O concentration is lower than that of anatectic melts. These differences are both a direct result of the difference in style of contamination. Through assimilation by stoping, bulk wallrock contaminates M melt, whereas the process of partial melting during AFC enriches K_2O content and depletes Na_2O in anatectic melt. H_2O is more enriched at a given SiO_2 in S_2FC than in AFC because, in the current version of MCS, all of the fluid phase is transferred into resident melt via stoping, as opposed to remaining in wallrock restite in the AFC case.

Assimilation by stoping also has an effect on the cumulate assemblage. Upon homogenization of the first stoped block, all of the quartz and alkali feldspar react away. As noted above, a "burst" (i.e., large mass) of plagioclase crystallizes (Fig. 5c; 7.5x more than had been crystallizing in prior magma temperature decrements) in response to assimilation of the stoped block. Spinel also experiences a crystallization burst (Fig. 5d; increase by 7x), but the total mass is much smaller than plagioclase. Similar to stoping event 1, during homogenization of stoped block 2, quartz completely reacts, and, plagioclase and spinel crystallization bursts occur, and these are proportionally much larger than after stoping event 1 (Fig. 5; e.g., for plagioclase, ~30x more than had been crystallizing in prior magma temperature decrements). While plagioclase continuously crystallizes in both AFC and S_2FC, the mass, thermal and compositional records are quite different. In AFC, each set of fractional crystallization-assimilation "events" yields about the same mass of plagioclase, and its composition varies smoothly from An83 when assimilation begins to An54 at the simulation's termination. The temperature record is also smoothly varying with decreases of ~15°C per

fractional crystallization-assimilation "event". For stoping events 1 and 2, there is a dramatic increase in the mass rate of plagioclase crystallization and an abrupt change in plagioclase Na content (from An_{75} to An_{65} for event 1, and from An_{51} to An_{38} for event 2), and the melt temperature decreases are ~47°C and 45°C, respectively. Both of these changes would be detectable by modern analytical methods and geothermometers. By the end of the simulation, plagioclase in S_2FC is distinctly more albitic than that in AFC (An_{37} versus An_{54}), consistent with the addition of Na_2O from stoped blocks compared to the "dilution" effect seen in AFC due to partial melting of wallrock. The difference in plagioclase composition highlights the difference in bulk addition of a stoped block versus addition of partial melt from wallrock. Partial melting favors reaction of alkali feldspar over plagioclase, and thus the resulting anatectic melts substantially enriches resident melt in K and depletes it in Na. These elemental differences influence the M melt phase equilibria response.

4. Quantifying Mantle versus Crustal Contributions to Magma Systems

A key goal in petrology and geochemistry — to distinguish and quantify how mantle versus crustal contributions to a magma system change in space and time — informs models of crustal growth and evolution, models of mantle evolution, and mass and thermal fluxes between these reservoirs. The literature abounds with studies of magmatic systems in which geochemical and petrologic signatures are quantitatively or qualitatively attributed to mantle versus crust (e.g., Hildreth & Moorbath 1988; Asmerom *et al*. 1991; Arndt *et al.* 1993; Wooden *et al.* 1993; Baker *et al.* 2000). Modeling results presented here illustrate the complexity associated with this enterprise and some potential pitfalls. The FC case assumes that mantle-derived magma intrudes the crust and undergoes fractional crystallization without involvement of any crust. Thus, the entire compositional signal derives from the mantle

mediated by low-pressure crystal fractionation. Magmas that have undergone only fractional crystallization without interaction with crust and/or without magma mixing are probably uncommon given the realities of moving low-viscosity materials through large sections of crust of contrasting composition as well as the episodic nature of magma intrusion. The case of FC only is therefore admittedly a simplification but serves as a point of comparison. Discussion of how the mass of mantle versus crust is portrayed, as discussed in the section Comparison of Thermal and Mass Characteristics underscores the challenges with quantifying crust versus mantle.

Based on many thousands of MCS models we have collectively run over the past several years, we suggest a top-down approach to distinguishing crust versus mantle contributions. That is, we recommend characterizing and quantifying possible open system crustal processes first. Once plausible and potential RASFC scenarios are fully explored (i.e., running many MCS models), remaining discrepancies between model results and data from a natural system might then be postulated to be caused by mantle heterogeneity of the M subsystem magma.

E. Magma Chamber Simulator: Ongoing Developments

The MCS has undergone continuous development and improvement since its first incarnation and we continue to expand its functionality. Here we review four major extensions presently under development.

A critical enhancement of MCS is to free it from its dependence on Excel, which is a temperamental platform on which to build and sustain development. A high priority for MCS is to port the code to a new platform with an accessible web user interface. The second enhancement addresses the limitation that cumulate crystals cannot react with M melt. It is well established in the rock record that crystal (cumulate)-melt interaction occurs. As one

example, the concept of crystal resorption has been part of the petrological literature for a long time (e.g., Fries 1939; Wiebe 1968; Couch *et al.* 2001; Ginibre e*t al.* 2007; Erdmann *et al*. 2012); orthopyroxene rims on olivine-cored crystals is perhaps the type example (e.g., Ambler and Ashley 1977). MCS will be modified to allow some fraction of earlier formed cumulates to react with M melt. A third MCS future development, as noted, is to allow transfer of some proportion of the fluid phase in wallrock to transfer into M melt. Finally, planning is underway to implement a Monte Carlo version of the MCS. To run a single R_2AFC simulation like the one illustrated here, circa 80 parameters should be specified in the MES input file (including all the oxides for magma, wallrock, and recharge magmas). In attempting to model a natural system, one recognizes that there are inherent uncertainties in these parameters. Therefore, the MCS algorithm will be extended by adoption of a Monte Carlo approach by allowing each input parameter to be specified as a possible range of values (e.g., SiO_2 of the wallrock lies between 67 and 69 wt.% etc.). Once ranges for all input parameters have been defined, the algorithm will select randomly or by Bayesian methods a particular set of initial conditions. In this manner, thousands or even tens of thousands of MCS models can be run, each with a unique set of input parameters and associated output. Once archived in a searchable database, the user can then ask questions such as: Of the thousands of simulations run, which ones compare best to the data from the particular natural system under study? Using this Monte Carlo approach, solutions can be filtered to find the best fit to observables using some objective criterion such as the residuals of the squared differences between the model and the observations.

F. Conclusions

Analysis of attributes of igneous systems suggests that open system behavior is dominated by crystal fractionation, magma mixing, and the interaction of magmas with their host environments via partial melting and stoping of wallrock. An important task for the petrologist/geochemist is to unravel the most important RASFC processes by quantification and temporal ordering. Establishing a magmatic 'arrow of time' is intrinsically a complex task due to the vast range of temporal and spatial scales involved—from microns to kilometers and from hours to several million years. Deciphering such records demands a variety of approaches.

As precision and spatial resolution of analyses of magmatic products have improved, so has the petrologist's ability to quantify the magmatic processes that generate compositional diversity. Forty years of progress have seen improvements in modeling, from those that focused exclusively on mass balance, to mass and enthalpy balance, to those that are underpinned by a thermodynamic database. The Magma Chamber Simulator is a mass- and energy-balanced, thermodynamic tool that addresses open-system magmatic processes that govern the evolution of a multicomponent-multiphase composite system of wallrock, resident magma, and recharge/stoping reservoirs. MCS-PhaseEQ models the major element and phase equilibria consequences of RASFC, and MCS-Traces, the subject of a companion paper, models trace elements and isotopes. MCS-PhaseEQ relies on rhyolite- and pMELTS as its thermodynamic engine and Visual Basic as its executive brain. MCS provides significant insight into crustal magma processes and the origin of compositional diversity via modeling how variations in specific input (e.g., pressure, parental magma composition, wallrock initial temperature, number and mass of recharge events) contribute to magma diversity and

eruptability. Systematic modeling of this sort affords the development of a framework for systematizing potentially distinctive characteristics of RASFC processes. MCS forward modeling also abounds with potential for describing the evolution of particular volcanic and plutonic rock suites, thus providing a quantitative framework for interpreting the remarkable and abundant compositional and isotopic data sets that are now routinely generated for igneous rocks. The five case studies we discuss (FC, R_2FC, AFC, S_2FC, and R_2AFC) illustrate the rich data set that MCS produces and elucidate both the challenges of identifying open system processes from major element and phase equilibria data and the utility of using open system thermodynamic models such as MCS to document open magma systems.

G. Acknowledgements

We are indebted to numerous MCS users and workshop attendees who have contributed to improving MCS. We also thank CWU students Jennifer McLeod, Alec Melone, Rachel Sanchez, and Rebekah Krohn for their work on improving MCS. We also send a hearty thank you to Dr. Mark Ghiorso, whose cooperation in developing MCS, was critical. We thank an anonymous reviewer and Paul Asimow for insightful reviews and Othmar Muntener for his expert editorial handling. This work was funded by NSF grants to WA Bohrson and FJ Spera and by the Academy of Finland grants 295129 and 306962 to JS Heinonen and E Suikkanen.

H. Electronic Supplementary Materials

This chapter was originally published in Contributions to Mineralogy and Petrology under a Creative Commons Open-Access CC-BY-4.0 license as Bohrson *et al.* (2020). An electronic supplement is available at https://link.springer.com/article/10.1007/s00410-020-01722-z.

I. References

Albarède, F. (1995) Introduction to Geochemical Modeling. Cambridge: Cambridge University Press.

Ambler EP, Ashley PM (1977) Vermicular orthopyroxene-magnetite symplectites from the Wateranga layered mafic intrusion, Queensland, Australia. Lithos 10:163-172. https://doi.org/https://doi.org/10.1016/0024-4937(77)90044-5

Arndt NT, Czamanske GK, Wooden JL, Fedorenko VA (1993) Mantle and crustal contributions to continental flood volcanism. Tectonophysics 223:39-52. https://doi.org/10.1016/0040-1951(93)90156-e

Asimow PD, Ghiorso MS (1998) Algorithmic Modifications Extending MELTS to Calculate Subsolidus Phase Relations. American Mineralogist 83, 1127-1131

Asmerom Y, Patchett PJ, Damon PE (1991) Crust-mantle interaction in continental arcs: inferences from the Mesozoic arc in the southwestern United States. Contrib Mineral Petrol 107:124-134. https://doi.org/10.1007/BF00311190

Baker JA, Macpherson CG, Menzies MA, Thirlwall MF, AL-Kadasi M, Mattey DP (2000) Resolving Crustal and Mantle Contributions to Continental Flood Volcanism, Yemen; Constraints from Mineral Oxygen Isotope Data. Journal of Petrology 41:1805-1820. https://doi.org/10.1093/petrology/41.12.1805

Becerril L, Galindo I, Gudmundsson A, Morales JM (2013) Depth of origin of magma in eruptions. Sci Rep 3:2762. https://doi.org/10.1038/srep02762

Bohrson WA, Spera FJ, Ghiorso MS, Brown GA, Creamer JB, Mayfield A (2014) Thermodynamic Model for Energy-Constrained Open-System Evolution of Crustal Magma Bodies Undergoing Simultaneous Recharge, Assimilation and Crystallization: the Magma Chamber Simulator. J Petrol 55:1685-1717. https://doi.org/10.1093/petrology/egu036

Borisova AY, Bohrson WA, Grégoire M (2017) Origin of primitive ocean island basalts by crustal gabbro assimilation and multiple recharge of plume-derived melts. Geochem Geophys Geosyst 18:2701-2716. https://doi.org/10.1002/2017GC006986

Bowen NL (1928) The evolution of igneous rocks. Dover Publications, New York, United States p 334

Coogan LA, Saunders AD, Wilson RN (2014) Aluminum-in-olivine thermometry of primitive basalts: Evidence of an anomalously hot mantle source for large igneous provinces. Chem Geol 368:1-10. https://doi.org/10.1016/j.chemgeo.2014.01.004

Costa F, Dohmen R, Chakraborty S (2008) Time Scales of Magmatic Processes from Modeling the Zoning Patterns of Crystals. In: Putirka KD, Tepley FJ,III (eds)

Minerals, Inclusions and Volcanic Processes, vol 69. Mineralogical Society of America, pp 545-594. https://doi.org/10.2138/rmg.2008.69.14

Couch S, Sparks RSJ, Carroll MR (2001) Mineral disequilibrium in lavas explained by convective self-mixing in open magma chambers. Nature 411:1037-1039. https://doi.org/10.1038/35082540

Cox KG, Hawkesworth CJ (1984) Relative contribution of crust and mantle to flood basalt magmatism, Mahabaleshwar area, Deccan Traps. Philosophical Transactions of the Royal Society of London Series A, Mathematical and Physical Sciences 310:627-641. https://doi.org/10.1098/rsta.1984.0011

Davidson JP, Morgan DJ, Charlier BLA, Harlou R, Hora JM (2007) Microsampling and Isotopic Analysis of Igneous Rocks: Implications for the Study of Magmatic Systems. Annual Rev Earth Planet Sci 35:273-311

Davidson, J.P. and Tepley, F.J. (1997), Recharge in volcanic systems: evidence from isotope profiles of phenocrysts, Science, 80 (275), 826-829, 10.1126/science.275.5301.826.

DePaolo DJ (1981) Trace element and isotopic effects of combined wallrock assimilation and fractional crystallization. Earth Planet Sci Lett 53:189-202. https://doi.org/10.1016/0012-821x(81)90153-9

Edwards, M.A., Jackson, M.G., Kylander-Clark, A.R.C., Harvey, J., Hagen-Peter, G.A., Seward, G.G.E., Till, C.B., Adams, J.V., Cottle, J.M., Hacker, B.R., and Spera, F.J. (2019), Extreme enriched and heterogenous $^{87}Sr/^{86}Sr$ ratios recorded in magmatic plagioclase from the Samoan hotspot, Earth and Planetary Sci. Lett., 511, 190-201, 10.1016/j.epsl.2019.01.040.

Erdmann S, Scaillet B, Kellett DA (2012) Textures of Peritectic Crystals as Guides to Reactive Minerals in Magmatic Systems: New Insights from Melting Experiments. J Petrol 53:2231-2258. https://doi.org/10.1093/petrology/egs048

Ghiorso MS, Gualda GAR (2015) An H2O–CO2 mixed fluid saturation model compatible with rhyolite-MELTS. Contrib Mineral Petrol 169:53. https://doi.org/10.1007/s00410-015-1141-8

Ghiorso MS, Hirschmann MM, Reiners PW, Kress III VC (2002) The pMELTS: A revision of MELTS for improved calculation of phase relations and major element partitioning related to partial melting of the mantle to 3 GPa. Geochem Geophys Geosyst 3:1-35. https://doi.org/10.1029/2001GC000217

Ghiorso MS, Sack RO (1995) Chemical mass transfer in magmatic processes IV. A revised and internally consistent thermodynamic model for the interpolation and extrapolation of liquid-solid equilibria in magmatic systems at elevated temperatures and pressures. Contrib Mineral Petrol 119:197-212. https://doi.org/10.1007/bf00307281

Ginibre C, Wörner G, Kronz A (2007) Crystal Zoning as an Archive for Magma Evolution. Elements 3:261-266. https://doi.org/10.2113/gselements.3.4.261

Grove TL, Kinzler RJ, Bryan WB (1992) Fractionation of Mid-Ocean Ridge Basalt (MORB). In: Morgan JP, Blackman DK, Sinton JM (eds) Mantle Flow and Melt Generation at Mid-Ocean Ridges, Geophysical Monograph Series. Geophysical Monograph Series, vol. 71, American Geophysical Union, pp 281-310. https://doi.org/doi:10.1029/GM071p0281

Gualda GAR, Ghiorso MS, Lemons RV, Carley TL (2012) Rhyolite-MELTS: a Modified Calibration of MELTS Optimized for Silica-rich, Fluid-bearing Magmatic Systems. J Petrol 53:875-890. https://doi.org/10.1093/petrology/egr080

Heinonen JS, Luttinen AV, Spera FJ, Bohrson WA (in press) Deep open storage and shallow closed transport system for a continental flood basalt sequence revealed with Magma Chamber Simulator. Contrib Mineral Petrol.

Heinonen JS, Bohrson WA, Spera FJ, Brown GA, Scruggs M, Adams J (submitted) Diagnosing Open-System Magmatic Processes Using the Magma Chamber Simulator (MCS): Part II – Trace elements and Isotopes. Contrib Mineral Petrol.

Hildreth W, Moorbath S (1988) Crustal contributions to arc magmatism in the Andes of Central Chile. Contrib Mineral Petrol 98:455-489. https://doi.org/10.1007/BF00372365

Lesher CE, Spera FJ (2015) Thermodynamic and Transport Properties of Silicate Melts and Magma. In: Sigurdsson H (ed) The Encyclopedia of Volcanoes (Second Edition). Academic Press, Amsterdam, pp 113-141. https://doi.org/10.1016/b978-0-12-385938-9.00005-5

Luttinen AV, Furnes H (2000) Flood basalts of Vestfjella: Jurassic magmatism across an Archaean-Proterozoic lithospheric boundary in Dronning Maud Land, Antarctica. J Petrol 41:1271-1305. https://doi.org/10.1093/petrology/41.8.1271

Mangiacapra A, Moretti R, Rutherford M, Civetta L, Orsi G, Papale P (2008) The deep magmatic system of the Campi Flegrei caldera (Italy). Geophys Res Lett 35: https://doi.org/10.1029/2008GL035550

Moore NE, Grunder AL, Bohrson WA (2018) The three-stage petrochemical evolution of the Steens Basalt (southeast Oregon, USA) compared to large igneous provinces and layered mafic intrusions. Geosphere 14:2505-2532. https://doi.org/10.1130/GES01665.1

Neave DA, Putirka KD (2017) A new clinopyroxene-liquid barometer, and implications for magma storage pressures under Icelandic rift zones. Am Min 102:777-794. https://doi.org/10.2138/am-2017-5968

Oldenburg CM, Spera FJ, Yuen DA, Sewell G (1989) Dynamic mixing in magma bodies: Theory, simulations, and implications. J Geophys Res 94:9215-9236. https://doi.org/10.1029/JB094iB07p09215

Putirka K (2017) Geothermometry and Geobarometry. In: White WM (ed) Encyclopedia of Geochemistry: A Comprehensive Reference Source on the Chemistry of the Earth. Springer International Publishing, Cham, pp 1-19. https://doi.org/10.1007/978-3-319-39193-9_322-1

Putirka KD (2008) Excess temperatures at ocean islands: Implications for mantle layering and convection. Geology (Boulder) 36:283-286. https://doi.org/10.1130/G24615A.1

Powell R, Holland TJB (1988) An internally consistent dataset with uncertainties and correlations: 3. Applications to geobarometry, worked examples and a computer program. Journal of Metamorphic Petrology, https://doi.org/10.1111/j.1525-1314.1988.tb00415.x.

Powell R, Holland TJB (1994) Optimal geothermometry and geobarometry: American Mineralogist 79:120-133.

Powell R, Holland, TJB Worley B (1998) Calculating phase diagrams involving solid solution via non-linear equations, with examples from THERMOCALC. Journal of Metamorphic Petrology, https://doi.org/10.1111/j.1525-1314.1998.00157.x.

Rudnick RL, Gao S (2003) The Composition of the Continental Crust. In: Rudnick RL (ed) The Crust, Treatise on Geochemistry, vol 3. Elsevier-Pergamon, Oxford, pp 1-64. https://doi.org/10.1016/b0-08-043751-6/03016-4

Scruggs, MA, Putirka KD (2018) Eruption triggering by partial crystallization of mafic enclaves at Chaos Crags, Lassen Volcanic Center, California. Am Min 103:1575-1590.

Spera FJ, Bohrson WA (2001) Energy-constrained open-system magmatic processes I: General model and energy-constrained assimilation and fractional crystallization (EC-AFC) formulation. J Petrol 42:999-1018. https://doi.org/10.1093/petrology/42.5.999

Spera FJ, Schmidt JS, Bohrson WA, Brown GA (2016) Dynamics and thermodynamics of magma mixing: Insights from a simple exploratory model. Am Min 101:627-643. https://doi.org/10.2138/am-2016-5305

Streck MJ (2008) Mineral textures and zoning as evidence for open system processes. Reviews in Mineralogy and Geochemistry 69:595-622. https://doi.org/10.2138/rmg.2008.69.15

Stern R, Johnson PR (2010) Continental lithosphere of the Arabian Plate: A geologic, petrologic, and geophysical synthesis. Earth-Sciences review 10.1016/j.earscirev.2010.01.002.

Takach MK (2018) Quantifying Crustal Assimilation in Historical to Recent (1329-2005) Lavas at Mt. Etna, Italy: Insights from Thermodynamic Modeling. All Master's Theses. 1006. https://digitalcommons.cwu.edu/etd/1006

Taylor HP, Jr (1980), The effects of assimilation of country rocks by magmas of $^{18}O/^{16}O$ and $^{87}Sr/^{86}Sr$ in igneous rocks, Earth and Planetary Science Letters, https://doi.org/10.1016/0012-821X(80)90040-0

Tepley FJ III, Davidson JP, Tilling RI, Arth JG (2000) Magma Mixing, Recharge and Eruption Histories Recorded in Plagioclase Phenocrysts from El Chichón Volcano, Mexico. J Petrol 41:1397-1411. https://doi.org/10.1093/petrology/41.9.1397

Tepley FJ III, de Silva, S, Salas G (2013) Magma Dynamics and Petrological Evolution Leading to the VEI 5 2000 BP Eruption of El Misti Volcano, Southern Peru, J Petrol, v. 54, n. 10, p. 2033-2065, doi:10.1093/petrology/egt040.

Tikoff B, Teyssier C (1992) Crustal-scale, en echelon "P-shear" tensional bridges: A possible solution to the batholithic room problem. Geology 20:927-930. https://doi.org/10.1130/0091-7613(1992)020<0927:CSEEPS>2.3.CO;2

Ubide T, Kamber BS (2018) Volcanic crystals as time capsules of eruption history. Nat Commun 9:326. https://doi.org/10.1038/s41467-017-02274-w.

Ubide, T., Mollo, S., Zhao, J., Nazzari, M., and Scarlato, P. (2019), Sector-zoned clinopyroxene as a recorder of magma history, eruption triggers, and ascent rates, Geochimica et Cosmochimica Acta, 251, 265-283, 10.1016/j.gca.2019.02.021.

Villiger S, Müntener O, Ulmer P (2007) Crystallization pressures of mid-ocean ridge basalts derived from major element variations of glasses from equilibrium and fractional crystallization experiments. J Geophys Res 112: https://doi.org/10.1029/2006JB004342.

Wade JA, Plank T, Hauri EH, Kelley KA, Roggensack K, Zimmer M (2008) Prediction of magmatic water contents via measurement of H2O in clinopyroxene phenocrysts. Geology 36:799-802. https://doi.org/10.1130/G24964A.1.

Walker JA, Williams SN, Kalamarides RI, Feigenson MD (1993) Shallow open-system evolution of basaltic magma beneath a subduction zone volcano: The Masaya Caldera Complex, Nicaragua. J Volcanol Geotherm Res 56:379-400. https://doi.org/https://doi.org/10.1016/0377-0273(93)90004-B.

Wark DA, Hildreth W, Spear FS, Cherniak DJ, Watson EB (2007) Pre-eruption recharge of the Bishop magma system. Geology 35:235-238. https://doi.org/10.1130/G23316A.1.

Weber G, Castro JM (2017) Phase petrology reveals shallow magma storage prior to large explosive silicic eruptions at Hekla volcano, Iceland. Earth Planet Sci Lett 466:168-180. https://doi.org/10.1016/j.epsl.2017.03.015.

Wiebe RA (1968) Plagioclase stratigraphy; a record of magmatic conditions and events in a granite stock. Am J Sci 266:690-703. https://doi.org/10.2475/ajs.266.8.690.

Wooden JL, Czamanske GK, Fedorenko VA, Arndt NT, Chauvel C, Bouse RM, King BW, Knight RJ, Siems DF (1993) Isotopic and trace-element constraints on mantle and crustal contributions to Siberian continental flood basalts, Noril'sk area, Siberia. Geochim Cosmochim Acta 57:3677-3704.

Yoder HS, JR., Tilley CE (1962) Origin of Basalt Magmas: An Experimental Study of Natural and Synthetic Rock Systems. J Petrol 3:342-532. https://doi.org/10.1093/petrology/3.3.342.

II. Diagnosing Open-System Magmatic Processes Using the Magma Chamber Simulator (MCS): Part II – Trace Elements and Isotopes

A. Introduction

Phase equilibria in magmatic systems at given P-T-conditions are controlled by the major element composition and thermodynamic properties of the magma. Major (± minor) elements are usually reported as oxides in geochemical datasets and are primary stoichiometric constituents of mineral phases that are stable in the magma. Modeling of phase equilibria and major element evolution of an igneous system requires knowledge of the thermodynamic properties of the liquid + solid + fluid phases present in the system. These include the standard state properties of all end-member components in all phases as well as the activity-composition relations of all phases.

The Magma Chamber Simulator (MCS; Bohrson et al., 2014) is a computational tool that uses the family of MELTS engines (Ghiorso and Sack, 1995; Ghiorso et al., 2002; Gualda et al., 2012; Ghiorso and Gualda, 2015) to numerically quantify these parameters in an isobaric open-system resident magma body subsystem (M: melt ± solids ± fluid) that evolves by fractional crystallization (FC) and can simultaneously experience magma recharge/mixing (R) and assimilation of either anatectic melts (A) and/or stoped blocks (S) of wallrock (WR). The utilization and application of MCS-PhaseEQ and its bearing on the evolution of phase equilibria and major elements has been described in a companion paper (Bohrson et al., 2020).

Trace elements are found in dilute quantities (usually ≤ 0.1 wt.%) and are not primary stoichiometric constituents of common phases in magmatic systems. They generally do not influence phase equilibria, but their relative concentrations and isotopic compositions can nevertheless record important information about the sources and evolution of magmatic

systems. The activities of trace elements vary in direct relation to their concentrations, and their behavior is controlled primarily by their relative compatibility among melt, solids (i.e., minerals) and fluid. This behavior is defined by a partition coefficient (K), which in igneous petrology is a ratio of the concentration of an element in a mineral versus the concentration of the element in the melt (K_{sm}) or fluid (K_{sf}) in equilibrium with the mineral. Because information on the composition and relative amounts of stable phases in a magmatic system is required to constrain bulk partition coefficients (D_{sm} and D_{sf}), detailed modeling of trace elements is not possible without a record of phase equilibria of the system.

In this study, we describe the MCS-Traces tool that uses primary MCS-PhaseEQ output as input and adds equations for modeling up to 48 trace elements in a R_nAS_nFC system. The program input consists of MCS-PhaseEQ output, initial trace element concentrations for the M parental melt, Rn+Sn ($n_{tot} \leq 30$), and WR, and phase-specific K_{sm} ($\pm K_{s/H2O} \pm K_{s/CO2}$ for possible fluid phases) values for M and WR. An option to take account the T-dependence of K values is available. In addition to trace elements, MCS-Traces computes radiogenic isotope ($^{87}Sr/^{86}Sr$, $^{143}Nd/^{144}Nd$, $^{176}Hf/^{177}Hf$, $^{206}Pb/^{204}Pb$, $^{207}Pb/^{204}Pb$, $^{208}Pb/^{204}Pb$, and $^{187}Os/^{188}Os$ as defaults) and stable O isotope ($^{\delta 18}O$) compositional evolution of the open-system resident melt based on user-input isotope ratios for the parental resident melt, WR, and each R magma. A description of the tool is provided along with results and comparisons of case studies that correspond to the ones introduced in the companion paper. An example of MCS-Traces applied to a natural magmatic system (continental flood basalts) is given in Heinonen et al. (2019).

B. Design and operational details of MCS-Traces

1. How does *MCS-Traces* work?

MCS-Traces utilizes the primary output ("*RunSummary*") of the *MCS-PhaseEQ* modeling tool. This output is read as the manual for what is going on in the R_nAS_nFC system (in terms of phase equilibria and mass balance) and *MCS-Traces* executes the trace element and isotope calculations based on it and user-input initial concentrations, isotope ratios, and K values. Primary output of fluid composition is used by the *MCS-Traces* tool to calculate K_{sf} values and temperature information is required for runs with T-dependent K values. Because of these utilizations, *MCS-Traces* cannot be used without output from a successfully executed *MCS-PhaseEQ* model. The MCS-derived trace element solution has the advantage of being self-consistent and more complete in the sense that a proper reckoning is made between trace elements and isotopes and major element phase compositions, modal abundances, pressure, and temperature.

The tool itself is composed of two main parts: 1) the user interface built in Visual Basic environment, and 2) the trace element and isotope engine that is a separate Excel worksheet, in which all the computations are performed. The current versions are available for both Mac and PC; the reader is referred to the website for the most up-to-date information on the different versions. In short, the user interface feeds input into the engine and, after the calculations have been performed, collects the output in an easily accessible and digestible form that is then amalgamated as a set of additional worksheets with the original *MCS-PhaseEQ* output. Consequently, the entire petrological-geochemical solution to a complex RASFC scenario is given in one workbook with multiple tabs. More detailed descriptions are given in the following sections and on the MCS website (https://mcs.geol.ucsb.edu/).

2. Trace Element and Isotope Equations

The basic framework of modeling trace elements and isotopes in *MCS-Traces* is described in Bohrson et al. (2014); we will complement and update that description here. For M, each temperature step is considered to be an equilibrium crystallization step. At the end of the step and before the model proceeds, however, the newly formed solid and fluid phases are fractionated from M in separate cumulate reservoirs. The model thus never represents a pure equilibrium or fractional crystallization case and thus better mimics natural systems – the larger the user-defined temperature step is, the larger is the role for equilibrium crystallization. Wallrock is always in internal equilibrium. The trace element equations for equilibrium crystallization in a melt ± solid ± fluid system developed by Spera et al. (2007) form the backbone of the trace element engine:

$$\frac{C_m}{C^0} = \left[f_m(1 - D_{sm}) + D_{sm}\left(1 - f_f\right) + \frac{f_f D_{sm}}{D_{sf}}\right]^{-1} \quad (1)$$

$$\frac{C_s}{C^0} = D_{sm}/D_{sf}\left[f_m(1 - D_{sm}) + D_{sm}\left(1 - f_f\right) + \frac{f_f D_{sm}}{D_{sf}}\right]^{-1} \quad (2)$$

$$\frac{c_f}{c^0} = D_{sm}/D_{sf}\left[f_m(1 - D_{sm}) + D_{sm}\left(1 - f_f\right) + \frac{f_f D_{sm}}{D_{sf}}\right]^{-1} \quad (3)$$

In equations 1–3, C_m, C_s, and C_f stand for trace element concentration in the melt, solid, and fluid, respectively, whereas C^0 is the initial trace element concentration in the system in internal equilibrium. Because of the structure of the model code, C^0 in equations 1–3 represents the composition of M melt initially or at the end of the previous fractionation step. In equations 1–3 for WR, which is always in internal equilibrium, C^0 represents the bulk composition of WR initially or after the previous anatectic melt removal event. D_{sm} and D_{sf} are solid/melt and solid/fluid bulk partition coefficients for a given element, and f_m and f_f

mass fractions of melt and fluid, respectively. D values for M (D_{sm}^{M} and D_{sf}^{M}) and WR (D_{sm}^{WR} and D_{sf}^{WR}) are calculated on the basis input element-specific K values and the mass fractions of stable equilibrium phases (x) for each step, as shown below:

$$D = \sum_i^n x_i K_i \quad (4)$$

Respective K_{sf} values have to be input only if a separate fluid phase consisting of either H_2O or CO_2 or both (possible in *MCS-PhaseEQ* runs using rhyolite-MELTS 1.1.0 or 1.2.0) saturates in M and/or WR When the fluid phase contains both components, the effective K_{sf} is computed according to:

$$K_{sf} = \frac{w_{H2O}}{K_{s/H2O}} + \frac{1-w_{H2O}}{K_{s/CO2}} \quad (5)$$

in which w_{H2O} is the mass fraction of H_2O in the fluid phase and $K_{s/H2O}$ and $K_{s/CO2}$ are the solid-H_2O and solid-CO_2 partition coefficients, respectively.

Note that although phase proportions are calculated in *MCS-PhaseEQ* for recharge magma and stoped WR blocks, they are homogenized before mixing with M, and thus, the partitioning of elements into solid, melt and fluid is not relevant to their mass balance. Therefore, constraints on $K_{sm} \pm K_{sf}$ are only needed for M and, in the case of AFC, for WR. Note that any possible negative solid and fluid masses produced by *MCS-PhaseEQ* (these are related to how MELTS algorithm performs the calculations; see MCS website) have been approximated as zero for the trace element calculations. This ensures that these very small negative masses of mineral phases do not cause negative trace element concentrations for those elements which have high K_{sm} or K_{sf} values. The effect of this approximation on the trace element model results has been determined to be negligible (<0.1% difference in regards to total masses, i.e., less than the analytical error of any major and trace element geochemical data).

Also, T-dependence of K_{sm} and K_{sf} can be invoked in *MCS-Traces*. The engine calculates the K at a given temperature [°C] logarithmically based on A and B values, which, in turn are calculated based on two user-input K values at two different temperatures [°C]:

$$K(T) = e^{\left(\frac{A+BT}{T}\right)} \tag{6}$$

$$A = \frac{T_1 T_2 \ln\left(\frac{K_2}{K_1}\right)}{T_1 - T_2} \tag{7}$$

$$B = \ln K_2 - \frac{A}{T_2} = \ln K_2 - \frac{T_1 \ln\left(\frac{K_2}{K_1}\right)}{T_1 - T_2} \tag{8}$$

The temperature-dependence of K is identical in form to that of any reaction with the isobaric heat capacity change of the reaction set to zero. Note that for many elements and solid phases, the effects of composition (of melt and the solid phases themselves) and temperature (and other physical and chemical factors) on K values are difficult to distinguish from each other (e.g., Blundy and Wood, 2003). These effects, however, are also effectively intertwined in magmatic systems, and, for example, T-dependency can thus be used to approximate the compositional dependency with some caution (e.g., Blundy and Wood, 1991).

When a mass of WR anatectic melt above the user-input percolation threshold value (FmZero) or R or S is added to M melt, simple mixing equations are utilized to calculate the resulting hybridized composition of M melt:

$$C_M = f_M C_M^{prev.\ step} + (1 - f_M) C_{WR\ melt/R/S} \tag{9}$$

In the case of assimilation of WR partial melt, the assimilated mass of the trace element is then removed from the WR reservoir.

In the case of isotopes, isotopic equilibrium within the subsystems (M, WR, R) is assumed and high-T isotope fractionation during melting and crystallization is not taken into account. Minor high-T fractionation of relatively light O isotopes during melting and crystallization is a well-known process, but the geochemical effect of this fractionation is generally quite small (usually <1 ‰ in a magmatic series) compared to that of adding isotopically distinct components into resident melt (see, e.g., Eiler, 2001). Therefore, and because additional input of such fractionation factors would be needed for each stable phase, high-T fractionation of O isotopes is not considered in *MCS-Traces*. Simple mixing between the subsystems is assumed in the case of all isotope compositions (ε):

$$\varepsilon_M = f_M \left(\frac{C_M^{prev.\ step}}{C_M}\right) \varepsilon_M^{prev.\ step} + (1 - f_M) \left(\frac{C_{WR\ melt/R/S}}{C_M}\right) \varepsilon_{WR\ melt/R/S} \qquad (10)$$

For O isotopes, O mass fractions are calculated for the M melt, R, and WR melt (or S) on the basis of MCS major element output at each step.

3. General overview of using *MCS-Traces*

For detailed instructions on the operation and input and output of both MCS tools, the reader is referred to the MCS website (http://mcs.geol.ucsb.edu); a generalized overview of the *MCS-Traces* is presented here.

MCS-Traces should be run with the same platform that was used to run *MCS-PhaseEQ*. *MCS-Traces* should never be updated or configured separately from *MCS-PhaseEQ* and, in the case of possible updates, we always recommend downloading the most up-to-date versions of both programs from the website. An internal compatibility check performed by the software will prevent use of outdated or otherwise incompatible *MCS-PhaseEQ* output in the *MCS-*

Traces tool. If one has used *MCS-PhaseEQ* to produce output required for *MCS-Traces*, the installation of the whole MCS package has been successful.

The general layout of *MCS-Traces* interface is presented in Fig. 1. The command buttons are set so that the default work flow proceeds primarily downwards and secondarily from left to right. Input consists of initial concentrations and phase-specific K_{sm} values (+ $K_{s/H2O}$ and/or $K_{s/CO2}$ if fluid is present in the simulation) for up to 48 trace elements and initial isotopic compositions for up to eight isotopic systems (Sr, Nd, Hf, 3xPb, Os, and O). Input is given separately for the different subsystems (M, WR, and R). Note that Ti, Cr, Ni, Mn, and Co are forced disabled as trace elements if these were modeled as respective oxides in *MCS-PhaseEQ*. The concentration input is not bound to a unit so the user can input the concentrations in ppm, ppb, or any other unit as long as the unit is uniform across the different subsystems.

Input can be saved and previous input loaded in the form of PAR files. Some recommended sources for K_{sm} values for igneous systems are Rollinson (1993), the Geochemical Earth Reference Model (GERM) Partition Coefficient Database (https://earthref.org/KDD/), and EarthChem traceDs (http://earthchem.org/traceds), which is in preparation, but already includes up-to-date compilations of K_{sm} values for some common igneous phases. A compilation of K_{sf} values is available in Spera et al. (2007), and the reader is also directed to the original publications that support this compilation. PAR files which store input for all the *MCS-Traces* simulations of this study are included in Online Resource 1. Although the associated partition coefficient input data can be loaded in *MCS-Traces* to be utilized for any simulation, we recommend users to search for partition coefficients that are the most suitable for the geological environment to be modeled.

Once the computation is complete, the *MCS-Traces* output can be accessed by opening the original *MCS-PhaseEQ* output file (see Online Resource 2). Two to three new tabs in the *MCS-PhaseEQ* output worksheet have been produced. Information regarding the trace element and isotope budget in the magma chamber and wallrock (if present in the simulation) are compiled in the "Traces_X_Magma" and "Traces_X_Wallrock" tabs, respectively. Both are appended with echoed input and relevant data from the primary *MCS-PhaseEQ* output. Finally, tab "Traces_X_OUTPUT" tabulates the full output from the *MCS-Traces* computation. Note that *MCS-Traces* can be run multiple times against the same *MCS-PhaseEQ* output file, the double/triplet tab sets are then distinguished by numbers (X = 1, 2, 3…) as they are introduced.

C. Comparison of closed (fractional crystallization) and open-system magma evolution illustrated by MCS

We present and compare trace element (Ni, Sr, Zr, Ba, La, Nd, and Yb) and isotopic ($^{87}Sr/^{86}Sr$, $^{144}Nd/^{143}Nd$, and $\delta^{18}O$) results of the same five MCS simulations introduced in the companion paper (Bohrson et al., in revision). These models are: 1) fractional crystallization (FC), 2) fractional crystallization + recharge (n = 2) (R_2FC), 3) fractional crystallization + assimilation of wallrock anatectic melts (AFC), 4) fractional crystallization + assimilation by stoping (n = 2) (S_2FC), and 5) fractional crystallization + recharge (n = 2) + assimilation of wallrock anatectic melts (R_2AFC) (Table 1). The input and results of *MCS-PhaseEQ* modeling are only briefly outlined here to place the trace element and isotope results in context. The outcomes of the simulations are illustrated as block models built with the help of MCS Visualizer (see MCS website) in Fig. 2. The reader should refer to the companion paper for details of initial conditions and thermal, mass, phase equilibria, and major element output.

Note that the presented models have been built dominantly for the purpose of displaying the features of MCS, and are not directly applicable to a particular natural case. They broadly represent a setting of anorogenic magmatism, where magmas from a hot asthenospheric source intrude shallow levels of cratonic continental crust. We encourage MCS users to carefully select the parameters for the specific system to be simulated (see Bohrson et al., 2014).

The five example simulations use a depleted mantle-derived tholeiite from the ~180 Ma Karoo large igneous province (sample P27-AVL; Luttinen and Furnes, 2000) as the initial melt and recharge magma major and trace element composition with ~2 wt.% of H_2O added (Table 2). Initial redox conditions were set at quartz-fayalite-magnetite (QFM) buffer, but the run itself was closed for oxygen, i.e., oxygen fugacity was determined by the relevant internal chemical equilibria of the system. The Sr and Nd isotope compositions were set to those of mean MORB (Gale et al., 2013), and O isotope composition was adopted based on representative analyses of MORB glasses (Eiler et al., 2000).

The major element, trace element, and isotope compositions of the wallrock and the stoped blocks represent the granodioritic average upper continental crust of Rudnick and Gao (2003) with ~2 wt.% of H_2O and 1 wt.% of CO_2 added and initial Fe oxidation state set at QFM (Table 2). The Sr and Nd isotope composition has been constrained on the basis of global river waters (Goldstein and Jacobsen, 1988) and the O isotope composition is within the range of felsic crustal rock types (Eiler, 2001). The mass of WR was twice that of the initial M, and the percolation threshold (FmZero) of the WR was set to a melt mass fraction of 0.1. In the models involving assimilation of wallrock anatectic melts (AFC and R_2AFC), the initial temperature of the wallrock was set at 700 °C (close to its solidus) to simulate preheating by

hypothetical earlier magma pulses and maximize the assimilation potential for comparison with the other cases.

The degree of contamination of the resident magma can be presented in two sensible ways in the models: 1) relative to the mass of the parental melt or 2) relative to the mass of the resident magma chamber (the whole M subsystem). The former may be relevant for cases without recharge, but here we use the latter approach that takes account recharge pulses and is in line with the companion paper. Note that the models that do not involve assimilation of WR anatectic melts (FC, R_2FC, and S_2FC) still included WR in the modeling for the purpose of studying its thermal evolution due to heat released by the cooling and crystallizing magma. Therefore, initial composition and K_{sm}^{WR} values were part of the input in *MCS-Traces* modeling also in these three cases. Because the temperature of the wallrock does not reach its solidus, and hence no anatectic melt forms or is assimilated by the resident melt, the input values do not affect the outcome of these models, and can thus be ignored.

Models were run at 0.1 GPa with an M temperature decrement of 5 °C. The relatively low pressure was set in order to accommodate separation of fluid. K_{sm} values used in the models have been compiled from Mahood and Hildreth (1983), Bacon and Druitt (1988), Rollinson (1993), Bea et al. (1994), Ewart and Griffin (1994), recent version of PELE software (see Boudreau, 1999), and Kessel et al. (2005). and are listed in Table 3. We selected consistent sets of K_{sm} values widely used and appropriate for the modeled compositions. Because MCS is thermodynamically controlled modeling tool, we utilized T-dependent K_{sm} values for all phases that are stable in a wide range of temperatures and for which applicable element-specific data has been published (Table 3). Two additional trace element simulations were run for the AFC case to illustrate the effects of using hypothetical maximum and minimum values

for $K_{ol/m}$(Ni), $K_{cpx/m}$(Ni), and $K_{plag/m}$(Sr) (compiled from the Tables 4.1–4.3 of Rollinson, 1993). K_{sf} values (for H_2O and CO_2) are 1000 for all general runs to minimize incompatible element concentrations in the fluid phase. We also ran a FC trace element simulation that utilized more realistic D_{sf}^{M} values (Kessel et al., 2005), and illustrates the partitioning of mobile elements (D_{sf}^{M} for Sr, Ba, La, and Nd < 1) into a separate fluid phase in the resident magma. The total number of *MCS-Traces* runs illustrated and discussed below is thus 8 (Table 1).

The results of the simulations are discussed below and illustrated in Figs. 2–7. Online Resources 1–3 include complete input and output for both MCS tools in case-specific files. We recommend viewing the outputs (Online Resource 2) simultaneously when reading the following sections. For more detailed discussion on the phase equilibria and major element evolution in the *MCS-PhaseEQ* models, the reader is referred to the companion paper (Bohrson et al., 2020); concise summaries of those results are presented herein.

Table 1: *MCS-Traces* models discussed in this study

***MCS-PhaseEQ* model**	***MCS-Traces* model**
FC	default element-specific D_{sf}^{M} values
R_2FC	default
AFC	default maximum $K_{ol\text{-}m}$(Ni), $K_{cpx\text{-}m}$(Ni), and $K_{pl\text{-}m}$(Sr) minimum $K_{ol\text{-}m}$(Ni), $K_{cpx\text{-}m}$(Ni), and $K_{pl\text{-}m}$(Sr)
S_2FC	default
R_2AFC	default

Table 2: Parental melt (PM) and wallrock (WR) compositions used in the models

	PM[a]	WR[b]
SiO_2 (wt.%)	49.38	64.53
TiO_2	1.73	0.62
Al_2O_3	13.79	14.92
Fe_2O_3	1.83	1.30
FeO	8.73	3.71
MnO	0.18	0.10
MgO	7.82	2.40
CaO	12.09	3.48
Na_2O	2.12	3.17
K_2O	0.23	2.71
P_2O_5	0.25	0.15
H_2O	1.96	1.94
CO_2	0.00	0.97
Ni (ppm)	154	47
Sr	226	320
Zr	70	193
Ba	86	628
La	4.97	31
Nd	10.53	27
Yb	1.73	1.96
$^{87}Sr/^{86}Sr$	0.702819	0.716000
$^{143}Nd/^{144}Nd$	0.513074	0.511780
$\delta^{18}O$ (‰)	+5.5	+12

Major elements discussed and modeled in Bohrson *et al.* (2020). Sources for the trace element and isotope values are given in the text.

[a]PM refers to the recharge magma composition in the R_2FC and R_2AFC simulations

[b]WR refers to the "recharge magma" (stoped WR block) composition in the S_2FC simulation.

Table 3: Element- and phase-specific K_{sm} values used in the MCS simulations

	ol	opx	cpx	pl	ksf	qtz	spl	rhm	bt	ap
K_{sm} Constant values[#]										
Ni	**10[a]**				0.25[e]	0	**10[a]**	**17[a]**	**15.1[c]**	0.4[a]
Sr	0.0004[a]				0.77[e]	0			0.25[c]	**2[d]**
Zr	0.001[a]				0.0435[c]	0				
Ba	0.0003[a]				**3.77[e]**	0		0.09[a]		
La	0.0003[a]				**1.01[e]**	0				
Nd	0.0002[a]				0.51[e]	0				
Yb	0.0052[a]				0.64[e]	0				
K_{sm} values for high-T basaltic magma compositions (T_1=1130˚C)[*]										
Ni		**3.5[a]**	**2[a]**	0.04[a]						
Sr		0.0012[a]	0.1283[a]	3.2487[a]			0.0006[a]	0.7[a]		
Zr		0.032[a]	0.26[a]	0.04[a]			0.015[a]	0.33[a]		
Ba		0.0005[a]	0.0007[a]	0.459[a]			0.0005[a]			
La		0.0008[a]	0.0536[a]	0.124[a]			0.0006[a]	0.0023[a]		
Nd		0.0056[a]	0.1873[a]	0.068[a]			0.0006[a]	0.0012[a]		
Yb		0.22[a]	0.43[a]	0.0097[a]			0.0045[a]	0.057[a]		
K_{sm} values for low-T rhyolitic magma compositions (T_2=740˚C)[*]										
Ni		**6.9[c]**	**6.2[c]**	0.9[c]						
Sr		0.124[c]	**1.65[c]**	**6.815[c]**			0.2935[c]	0.552[c]		
Zr		0.0805[c]	0.685[c]	0.14[c]			0.137[c]	0.935[c]		
Ba		0.0735[c]	0.692[c]	0.375[c]			0.1[d]			
La		0.4[d]	0.052[d]	0.3[d]			0.66[d]	**1.31[f]**		
Nd		0.6[d]	**1.4[d]**	0.19[d]			0.93[d]	0.96[f]		
Yb		0.91[d]	**3[d]**	0.1[d]			0.44[d]	0.55[f]		
K_{sm} Constant values for special cases[†]										
Ni	**58[b]**		**14[b]**							
Sr	**5.9[b]**		**1.5[b]**							
Zr				**15.633[b]**						
Ba				**1.6[b]**						

Mineral abbreviations: *ol* olivine, *opx* orthopyroxene, *cpx* clinopyroxene, *pl* plagioclase, *ksf* alkali feldspar, *qtz* quartz, *spl* spinel, *rhm* rhombohedral oxide, *bt* biotite, *ap* apatite. *Ksm* values > 1 shown in bold.

Sources for the *Ksm* values: [a]Jean Bedard's *Ksm* values for basaltic magmas from PELE software (version 7.03 (2010); see Boudreau, 1999), [b]Tables 4.1, 4.2, 4.3 of Rollinson (1993; original sources: Philpotts & Schnetzler, 1970; Gill 1981; Nash & Crecraft 1985), [c]Ewart & Griffin (1994; average of minimum and maximum values for low-Si rhyolite; if not available, for leucitite, dacite, or peralkaline rhyolite), [d]Bacon & Druitt (1988); [e]Bea et al. (1994); [f]Mahood & Hildreth (1983).

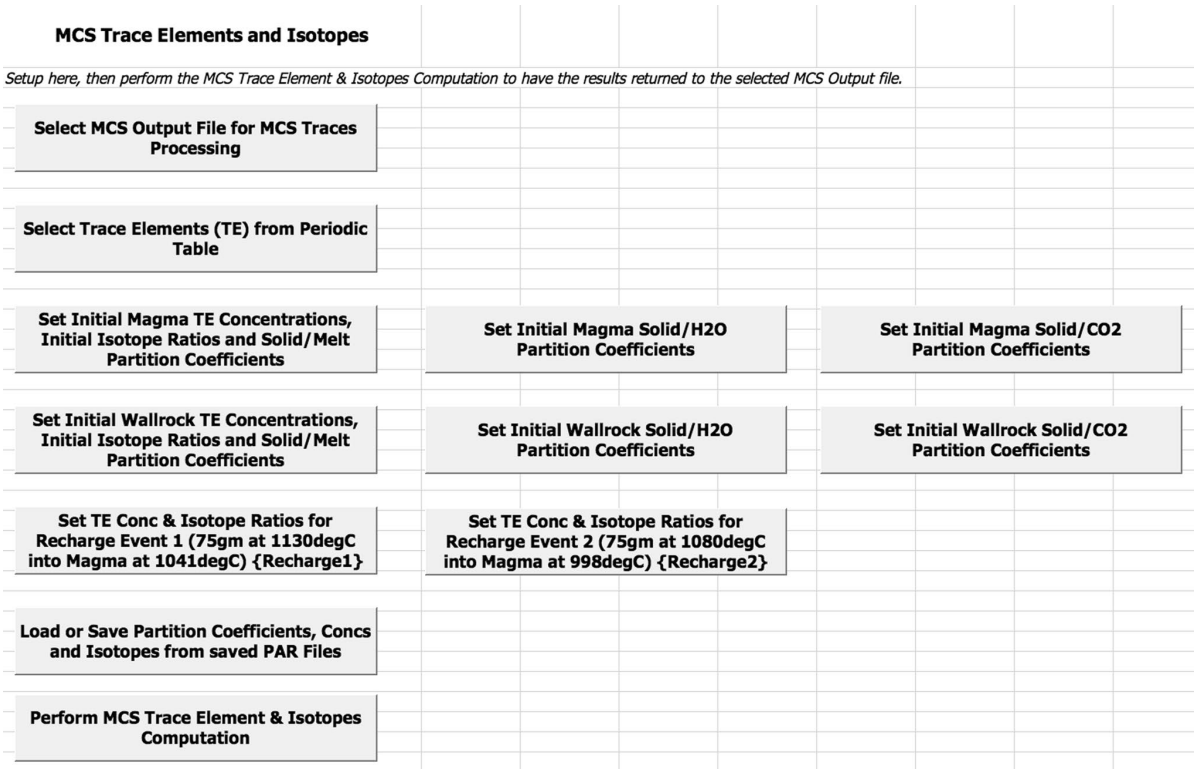

Fig. 1 The user interface of the *MCS-Traces* tool. The number of buttons on rows 3-5 vary according to the uploaded *MCS-PhaseEQ* output. In this run, which is the R_2AFC case of this study, both M and WR contain a fluid phase composed of a mixture of H_2O and CO_2, and two R events took place.

1. Case 1: Fractional Crystallization (FC)

In the primary MCS FC simulation, the melt composition evolves from basaltic (SiO_2 ≈ 49 wt.% at liquidus temperature of ~1129 °C) to dacitic (SiO_2 ≈ 69 wt.% at ~899 °C) by ~76 wt.% of crystallization of the magma chamber (Fig. 2a). Because of the high H_2O content in the initial magma, a separate H_2O fluid phase forms after ~46 wt.% crystallization and accumulates up to ~1 wt.% of the magma chamber in total by the end of the run. The fractionated phases and their approximate relative proportions in the bulk solid cumulate are in order of appearance: olivine (15 wt.%), clinopyroxene (40 wt.%), plagioclase (39 wt.%), spinel (6 wt.%), and rhombohedral oxide (0.4 wt.%).

In terms of trace elements, Ni is compatible in the incremental solids throughout the default FC run (Fig. 3a), because all of the associated solid phases except plagioclase have K^M_{sm}(Ni) values of ≥ 1 (Table 3; D^M_{sm}(Ni) = 2–10). Strontium is incompatible in the solids and enriched in the resident melt until the fractionation of plagioclase begins when Sr contents in the melt have reached about 260 ppm (Fig. 3b). After this, D^M_{sm}(Sr) varies between 1.3–3.2 until the end of the simulation. All other elements are incompatible in the crystallizing phases and behave incompatibly throughout the run (Fig. 3c–f). Fractional crystallization has a negligible effect on rare earth element (REE) ratios, and isotope compositions obviously remain unchanged (Fig. 4).

The effect of adjusted D^M_{sf} values is negligible for elements with $D^M_{sf} > 0.5$ in the alternative FC trace element simulations (Fig. 5a, b). However, the effect becomes more important for more soluble elements, such as Sr and Ba with $D^M_{sf} < 0.1$, even when the total mass of fractionated fluid in the FC run does not exceed 1 wt.% of the magma chamber mass (Fig. 5c, d). The Sr and Ba contents at the end of the adjusted D^M_{sf} run are about 70 % and 30 % lower, respectively, than at the end of the default run. Compared to Ba, the effect on Sr is proportionally larger because Sr has a higher D^M_{sm} after the onset of plagioclase fractionation for most of the run, whereas D^M_{sm}(Ba) stays below 0.4 throughout.

2. Case 2: Recharge-Fractional Crystallization (R_2FC)

The R_2FC model simulates replenishment of the magma chamber with two batches of mantle–derived magma that are equivalent to the parental melt composition (Table 2). The two R events of 75 mass units (m.u.) are introduced at ~1049 °C (resident melt SiO_2 ≈ 52 wt.%) and at ~998 °C (resident melt SiO_2 ≈ 58 wt.%). Because of the large R events, the total

magma chamber mass at the conclusion of the simulation is 250 m.u. The second R magma is below liquidus temperature (at 1080 °C; $T_{liq} \approx 1129$ °C) and thus contains ~21 wt.% of crystal cargo (but no fluid); this does not affect the trace element run, however, as bulk R magmas (i.e., all crystals + melt ± fluid) are always fully hybridized with the resident melt in MCS.

The R_2FC model terminates after ~77 wt.% of crystallization of the magma chamber with ~22 wt.% (~55 m.u.) of dacitic ($SiO_2 \approx 69$ wt.% at 900 °C) melt left and ~1 wt.% of fluid separated (Fig. 2b). The composition of the bulk solid cumulate is ~13 wt.% olivine, ~40 wt.% clinopyroxene, ~39 wt.% plagioclase, ~5 wt.% spinel, ~2 wt.% orthopyroxene, and <1 wt.% rhombohedral oxide (listed in the order of appearance), which is very similar to that of FC with the exception of orthopyroxene being stable in the R_2FC simulation.

At almost any given SiO_2 content, the concentrations and ratios of the modeled trace elements in the R_2FC run are very similar to those produced by the FC runs (Figs. 3, 4a). The only notable differences are in regard to Ni and Sr that show mostly compatible behavior (Fig. 3a, b). The resident melt is enriched in Ni due to the added primitive R pulses (that have higher Ni contents than the resident melt at the instance of R), especially the second R event (R2) that triggers considerable precipitation of clinopyroxene (~15 m.u.), which has consistently lower K_{sm}^{M}(Ni) than olivine (Table 3) that is the sole crystallizing phase one step after R1. In the case of Sr, R1 lowers the Sr content of the resident melt slightly, whereas R2 increases it; this is because the recharge events take place when resident melt Sr concentrations are higher (~234 ppm before R1) and lower (160 ppm before R2) than in the recharge magma (226 ppm; Table 2). In terms of fully incompatible elements (Fig. 3c–f), the recharge events do not cause notable deviation from the rather linear geochemical trends. The implications of these observations will be discussed later.

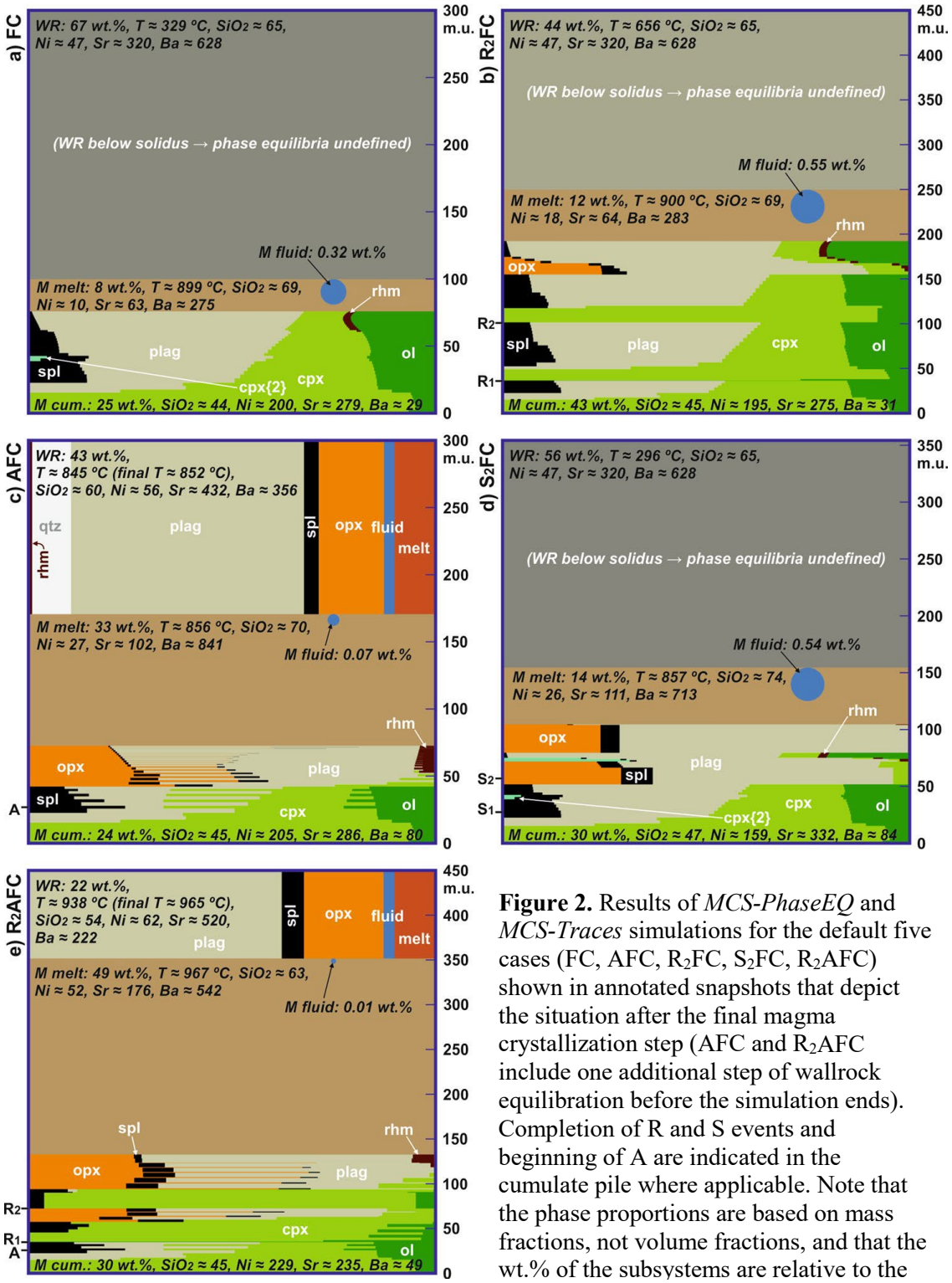

Figure 2. Results of *MCS-PhaseEQ* and *MCS-Traces* simulations for the default five cases (FC, AFC, R_2FC, S_2FC, R_2AFC) shown in annotated snapshots that depict the situation after the final magma crystallization step (AFC and R_2AFC include one additional step of wallrock equilibration before the simulation ends). Completion of R and S events and beginning of A are indicated in the cumulate pile where applicable. Note that the phase proportions are based on mass fractions, not volume fractions, and that the wt.% of the subsystems are relative to the whole magma-wallrock system; M melt, M fluid, and M cumulate (M cumul.) comprise the total magma chamber mass. For the subsystems, SiO_2 is given in wt.% and trace elements in ppm. See Bohrson *et al.* (2020) for more information.

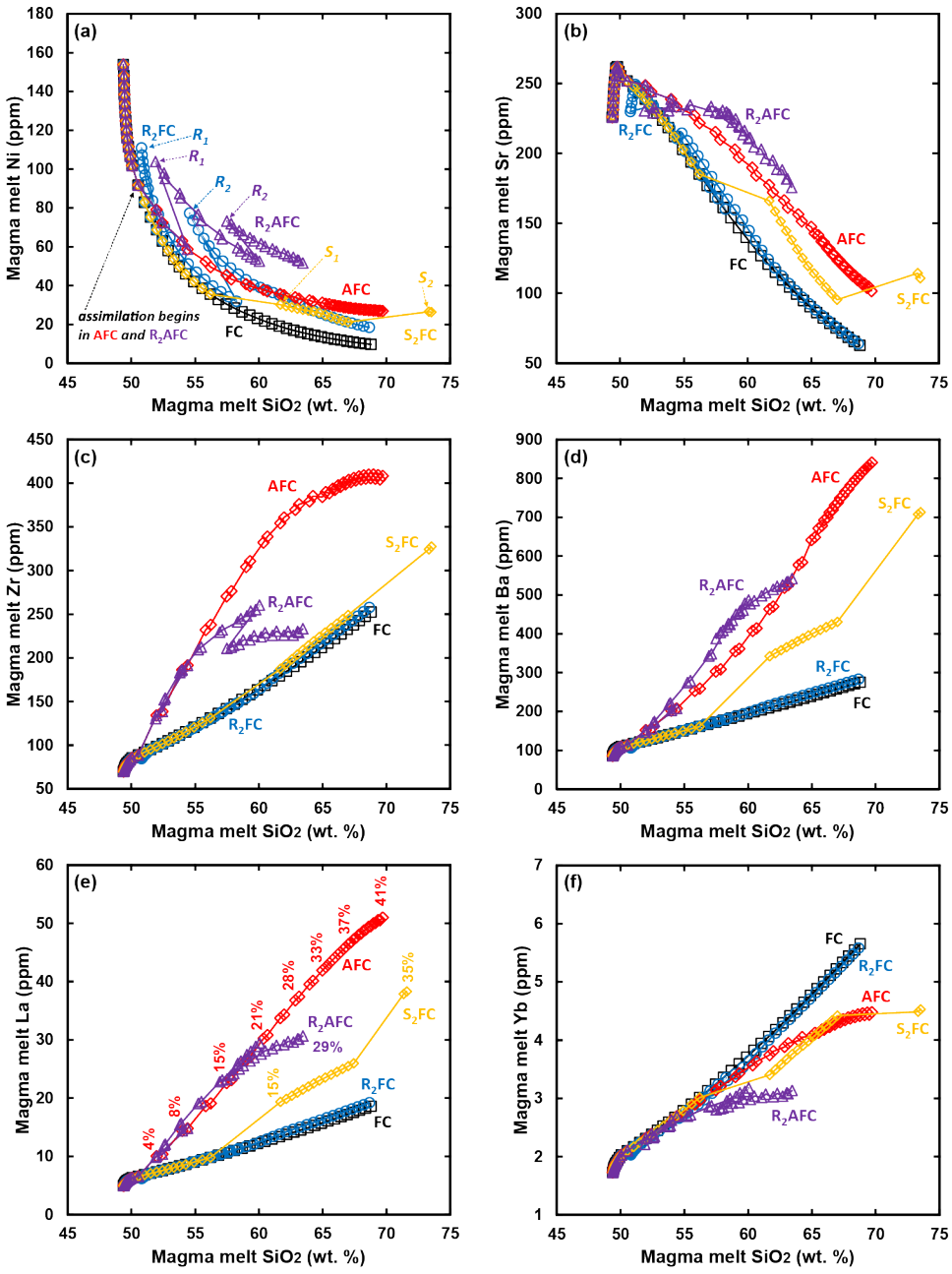

Figure 3. SiO_2 vs. Ni (**a**), Sr (**b**), Zr (**c**), Ba (**d**), La (**e**), and Yb (**f**) (ppm) diagrams for the resident melt in the example case studies (FC, R_2FC, AFC, S_2FC, and R_2AFC). In (**a**), beginning of assimilation and R and S events are indicated. Percentages shown in SiO_2 vs. La for the cases involving assimilation (**e**) reflect the mass of assimilated material relative to the mass of the M subsystem. All of these are applicable for all diagrams and a given SiO_2 but are only shown in (**a**, **e**) to preserve clarity.

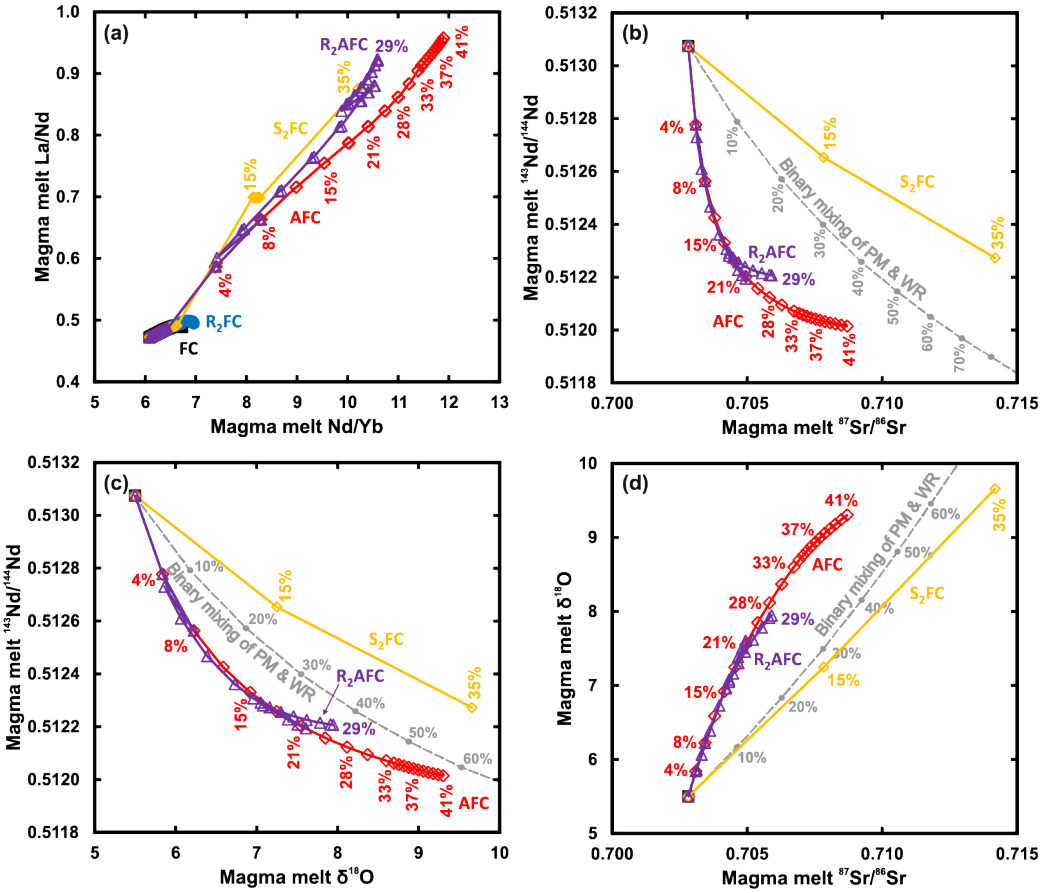

Figure 4. Nd/Yb vs. La/Nd diagram (**a**) and Sr, Nd, and O isotope diagrams (**b-d**) for the resident melt in the example case studies (FC, R_2FC, AFC, S_2FC, and R_2AFC). Note that FC and R_2FC are not shown in the isotopic diagrams because these models do not result in isotopic changes in the resident melt. Percentages given for the model curves involving assimilation reflect the mass of assimilated material relative to the total mass of the M subsystem (magma chamber). Simple binary mixing models are also shown in the isotopic diagrams; percentages indicate the relative amount of WR in the mixture and are broadly comparable to the percentages in the MCS run (there is no fractional crystallization in binary mixing, however).

3. Case 3: Assimilation of wallrock anatectic melts-fractional crystallization (AFC)

The AFC model is the first one involving assimilation of wallrock that has a considerably higher initial temperature (700 °C) than in the FC and R_2FC (and S_2FC) cases (100 °C). The assimilation of WR partial melts begins when the temperature of the resident melt has dropped to ~1069 °C (~51 wt. SiO_2; ~26 wt.% crystallization at that point). The heat released from the crystallizing M before this has heated the relatively large mass of wallrock (200 m.u.) from

its initial temperature above the temperature (~740 °C) at which its percolation threshold (10 wt.% of melting) is exceeded.

The AFC model terminates after ~43 wt.% of crystallization at a total magma chamber mass of ~171 m.u. (~71 m.u. of WR melt added which is ~41 wt.% of the magma chamber) with ~57 wt.% of dacitic (nearly rhyolitic; $SiO_2 \approx 70$ wt.% at 856 °C) melt left and <1 wt.% of fluid separated (Fig. 2c). The degree of partial melting of the WR is ~42 wt.%. The notably large degree of WR partial melting and the amount of assimilation are related to the high initial T of the WR and because the simulation proceeds until thermal equilibrium between M and WR has been reached; it takes a lot of crystallization and release of latent heat and thus assimilation of the large WR mass to reach this thermal equilibrium state at ~840 °C. The comparatively small amount of total fractionated solid cumulate consists of approximately 8 wt.% olivine, 35 wt.% clinopyroxene, 38 wt.% plagioclase, 5 wt.% spinel, 12 wt.% orthopyroxene, and ~1 wt.% rhombohedral oxide (listed in the order of appearance). Note that addition of felsic WR melts increases the stability of orthopyroxene at the expense of olivine relative to the FC run. The residual WR during the run consists of varying amounts of orthopyroxene, plagioclase, alkali feldspar, quartz, spinel, rhombohedral oxide, and apatite. The WR phases that contribute most to the partial melting are alkali feldspar (disappears completely from the WR at ~782 °C) and quartz.

The default AFC run shows drastic differences relative to that of the default FC run. Rather surprisingly, the compatible element Ni is higher in the resident melt in the AFC model than in the FC model after assimilation begins (Fig. 3a). This is because the crystallization of olivine with high K_{sm}^{M}(Ni) is subdued in the AFC simulation and because the WR anatectic melt batches have higher Ni (~30 ppm) than the evolved resident melt in the FC model (< 30

ppm below 1000 °C). Strontium is also enriched in the AFC resident melt (Fig. 3b) at any given SiO_2 content after assimilation begins even when D_{sm}^{WR}(Sr) remains relatively high (mostly above 1, up to 4; Fig. 6d) . This enrichment in resident melt is primarily caused by subdued plagioclase crystallization in AFC relative to FC (~16 wt.% vs. ~28 wt.% of the magma chamber). In addition, the WR anatectic melt batches introduced into the resident melt become increasingly Sr-rich (from ~108 to ~139 ppm) as the simulation proceeds.

Incompatible trace elements (D_{sm} < 1 in both M and WR) that are enriched in the WR (i.e., Zr, Ba, La) are considerably enriched in the AFC resident melt compared with the FC resident melt after the onset of assimilation in the former (Fig. 3c–e). The contrary is true for Yb that is found in relatively lower quantities in the WR (Fig. 3f). Assimilation has drastic effects on REE ratios and isotope compositions of the resident melt (Fig. 4). Note that compatibility of Sr in the WR (Fig. 6d) results in delayed increase in $^{87}Sr/^{86}Sr$ at a given $^{143}Nd/^{144}Nd$ in comparison to a simple binary mixing model (Fig. 4b). Similarly, the incompatibility of Nd and its enrichment in the WR anatectic melt decreases $^{143}Nd/^{144}Nd$ more efficiently than $\delta^{18}O$ is increased in the resident melt relative to a binary mixing model (Fig. 4c). The opposite is true when comparing $^{87}Sr/^{86}Sr$ and $\delta^{18}O$, the latter being showing stronger increase in the resident melt (Fig. 43d).

The effects of using constant "maximum" or "minimum" $K_{ol/m}$(Ni), $K_{cpx/m}$(Ni), and $K_{plag/m}$(Sr) values compiled in Rollinson (1993) are compared to those of the default AFC model in Fig. 6. Varying these values in the model input causes drastic differences to the outcomes of the otherwise uniform simulations. For example, the final Sr concentration in the resident melt of the "maximum K_{sm}" simulation is ~9 ppm, considerably lower than in the default run (~102 ppm) or in the "minimum K_{sm}" run (~314 ppm).

The jigsaw pattern for D_{sm}^{M}(Sr) (Fig. 6d) reflects the working principles of the primary MCS tool: low points in the jigsaw pattern are the result of crystallization in relation to assimilation of the WR melt that causes decreased plagioclase stability and thus low D_{sm}^{M}(Sr), whereas each high point in the diagram represents a normal 5 °C FC step with increased plagioclase stability and thus high D_{sm}^{M}(Sr). The reason for the continuous depletion of Sr in the resident melt in the default AFC run (Fig. 6b) – in spite of D_{sm}^{M}(Sr) being less than 1 at some temperatures (between ~1060–1010 °C; Fig. 6d) – is due to the dilution effect of adding relatively Sr-poor WR anatectic melt into the resident melt (Fig. 7). The inflection points in the AFC-T D_{sm}^{WR}(Sr) trends at around WR temperature of 780 °C (Fig. 6d) are caused by the disappearance of alkali feldspar and increased consumption of plagioclase both of which possess relatively high K_{sm}(Sr) in the residual wallrock (plagioclase higher than alkali feldspar; Table 3). Again, all these are examples of complex relationships between the different processes and variables included in MCS, and are natural consequences of open system behavior that are counterintuitive to reasoning that either implicitly or explicitly assumes closed system behavior.

Finally, Fig. 7 illustrates the compositional evolution of not only the resident melt, but also the bulk cumulate, WR melt, and WR residual (solid + melt + fluid) in the default AFC run. Nickel concentration in the bulk cumulate is highest in the beginning when olivine ± clinopyroxene with high K_{sm}^{M}(Ni) are the sole fractionating phases. Strontium content in the bulk cumulate begins to notably increase after the addition of plagioclase in the fractionating assemblage. Because Ni and Sr are compatible in WR solids, the WR partial melt shows little change in its composition, whereas the WR residual gets progressively enriched in these elements. Note that all the data presented in Fig. 7 can be collected from *MCS-Traces* output

with minimal effort. Correlating specific trends in trace element evolution is simple, as major element and phase abundances for each step of the scenario are output alongside the trace element concentrations.

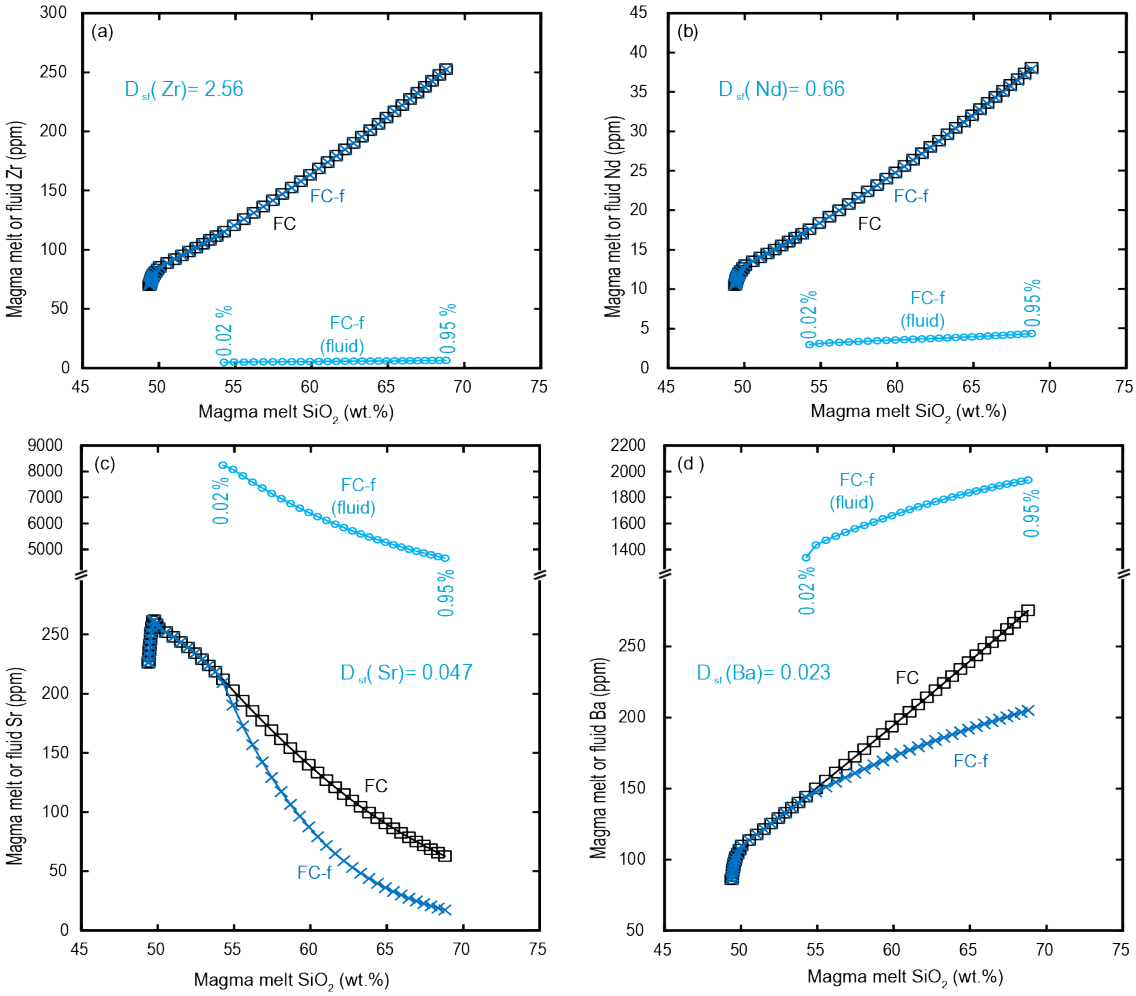

Figure 5. Comparison of resident melt concentrations of the FC trace element simulations with elements considered incompatible in the fluid (i.e. D_{sf}^{M}=1000; FC, same as in Fig. 3) and with element-specific D^{M} employed (FC-f) (Tables 1,3). Cumulative fluid composition is also shown; in (**a**) and (**b**) the fluid compositions are shown in the same diagram with the resident melt compositions and in (**c**, **d**) the highly enriched fluid compositions are shown in a separate scale. The mass of the separated fluid relative to the mass of the magma chamber (or initial melt) is indicate with percentages at the beginning of fluid separation and at the end of the run; the respective percentages in relation to the remaining M melt mass are 0.03% and 4.11%.

4. Case 4: Assimilation of stoped wallrock blocks-fractional crystallization (S_2FC)

The S_2FC model simulates complete assimilation of two stoped wallrock blocks – or two sets of multiple small blocks each with a combined mass equal to the respective S event – by the resident melt. The stoped blocks are of WR composition, and are introduced into the magma using the recharge function at resident M temperatures of ~1014 °C and ~907 °C. The masses of the blocks are 17 and 38 m.u.. These masses roughly correspond to the total mass of assimilated WR partial melts in the AFC model at the given magma temperatures to enable comparison. The temperatures of the blocks at homogenization are 760 °C (composed of ~78 wt.% solid, ~20 wt.% melt, and ~2 wt.% of fluid) and 795 °C (composed of ~60 wt.% solid, ~38 wt.% melt, and ~2 wt.% of fluid), respectively. These temperatures are above WR liquidus in order to enable MELTS engine to calculate their phase state at the time of stoping. Note that the total mass of the stoped blocks cannot represent the total mass of WR partial melts assimilated in the AFC scenario (~71 m.u.), because wholesale melting of the rather cold stoped blocks requires relatively lot of heat. Since the WR blocks are completely melted and homogenized in M, the decrease in temperature and mass of crystallization in M after each stoping event is considerable (~47°C and ~15 m.u. and ~45 °C and ~25 m.u., respectively).

The S_2FC model terminates after ~68 wt.% of crystallization at a total magma chamber mass of 155 m.u. (55 m.u. of stoped WR assimilated which is ~35 wt.% of the magma system) with ~31 wt.% of rhyolitic ($SiO_2 \approx 72$ wt.% at 840 °C) melt left and ~1 wt.% of fluid separated (Fig. 2d). The bulk solid cumulate consists of approximately 7 wt.% olivine, 28 wt.% clinopyroxene, 48 wt.% plagioclase, 6 wt.% spinel, 11 wt.% orthopyroxene, and <1 wt.% rhombohedral oxide (listed in the order of appearance). Although WR blocks are composed

of solids, melt, and fluid at hybridization, their phase identity is irrelevant for the outcome of the *MCS-Traces* modeling as the R function in MCS produces a new, completely homogenized and equilibrated state. Similar to the AFC case, the addition of Si-rich WR increases orthopyroxene stability at the expense of olivine relative to the FC run.

Relative to the R_2FC and FC runs at a given SiO_2 content, S_2FC resident melt shows varying degrees of enrichment of Sr, Ba, and La (elements notably enriched in the WR), and depletion of Yb (element notably depleted in the WR; Fig. 3). The complete homogenization of a stoped WR block in the resident melt results in a significant compositional change for most elements immediately after each stoping event (Figs. 3 and 4). Interestingly, the SiO_2 vs. Zr trend of the S_2FC run does not considerably differ from those of R_2FC or FC (Fig. 3c), because Zr and SiO_2 are equally enriched in the stoped WR blocks relative to the resident melt. The rather small differences in the respective SiO_2 vs. Ni trends (Fig. 3a) are caused by the compatibility of Ni in the crystallizing minerals lowering the Ni concentrations in the resident melt close to that of the WR blocks (47 ppm; Table 2)

Relative to the AFC run, S_2FC shows some differences that are related to the contamination process. In resident melt that has experienced wholesale assimilation of stoped blocks, Sr, which is compatible during WR melting, gets relatively enriched in the resident melt following assimilation by stoping (Fig. 3a, b), whereas elements that are enriched in the WR and behave incompatibly (e.g., Zr, Ba, and La; Fig. 3c, d, e) get less enriched; the comparisons are again made at a given SiO_2 content after the beginning of assimilation. On the other hand, incompatible element Yb is depleted in the S_2FC resident melt relative to the AFC run right after the stoping events because of the low concentration of Yb in the bulk WR (1.96 ppm; Table 2) compared to that of resident melt before the stoping events (3.0 and 4.4

ppm, respectively). The differences between AFC and S_2FC arise because contamination by stoping represents incorporation of the bulk WR, rather than the assimilation of anatectic melt, in which compatible elements are relatively depleted and incompatible elements enriched in relation to bulk WR. The degree of enrichment in the assimilated WR anatectic melt batches is dictated by the thermodynamically derived degree of melting and the user-input percolation threshold (FmZero) and K_{sm}^{WR} and K_{sf}^{WR} values.

For isotopes, $^{87}Sr/^{86}Sr$ and $\delta^{18}O$ are higher at a given $^{143}Nd/^{144}Nd$ in the S_2FC resident melt than in the AFC run or in a binary mixing scenario (Fig. 4b, c). In the case of $^{87}Sr/^{86}Sr$, this is both because Sr is progressively depleted from the resident melt by fractional crystallization of plagioclase, and because assimilation of bulk stoped WR adds more Sr to the resident melt (per unit addition of added mass) than relatively Sr-poor anatectic melt does. Strontium released from the assimilated WR blocks thus changes the Sr isotopic composition of the melt more effectively than in the case of binary mixing or AFC. The explanation for the higher $\delta^{18}O$ at a given $^{143}Nd/^{144}Nd$ relative to the binary mixing scenario is less intuitive, but stems from the fact that Nd is enriched in the resident melt at the time of the stoping events relative to the parental melt used in the binary mixing model. Therefore, $^{143}Nd/^{144}Nd$ of the S_2FC resident melt is not as easily affected by assimilation of stoped WR. The higher $\delta^{18}O$ of S_2FC resident melt relative to that of the AFC model at similar degrees of contamination (e.g., around 35 wt.%, Fig. 4c, d) can be associated with relatively higher resident melt mass in the AFC simulation; $\delta^{18}O$ is more efficiently buffered by resident melt composition in a larger melt pool.

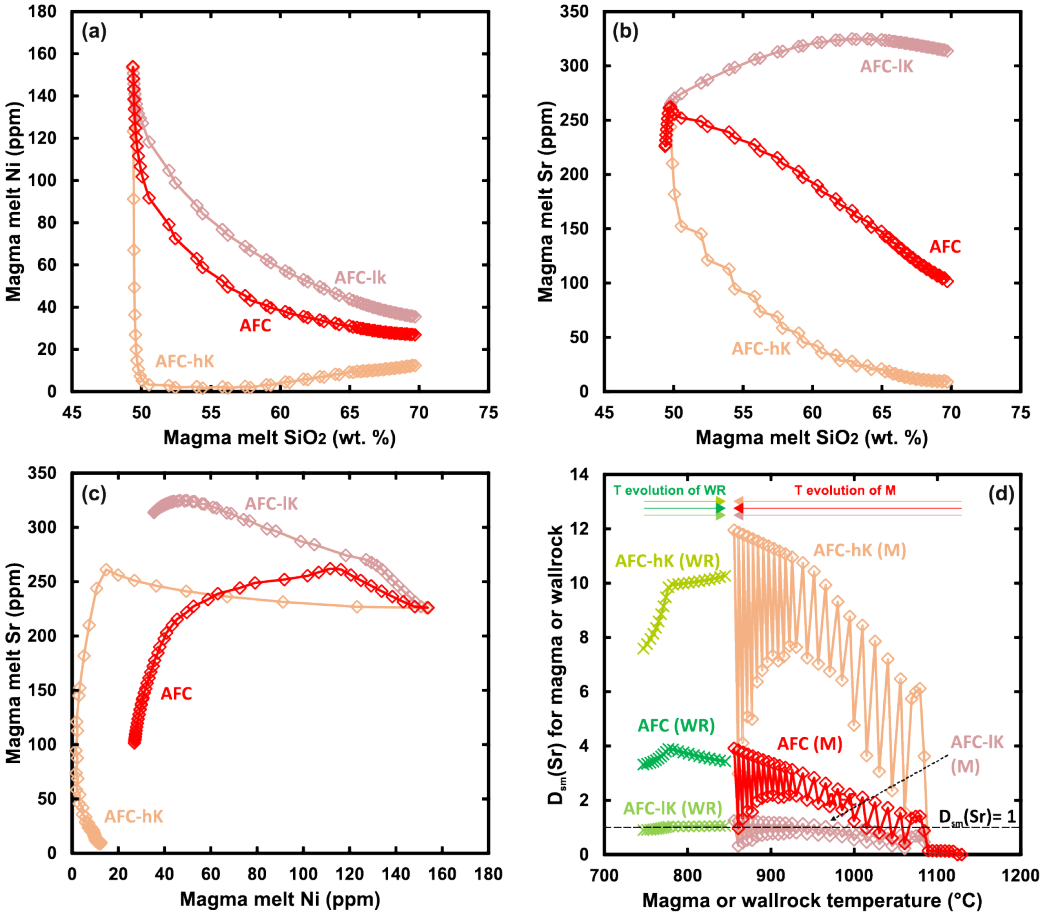

Figure 6. Comparison of the resident melt Ni and Sr concentrations (**a-c**) and D_{sm}(Sr) (**d**; for both M and WR) of the AFC trace element simulations using default (same as in Fig. 3), constant maximum (AFC-hK), or constant minimum (AFC-lK) $K_{ol\text{-}m}$(Ni), $K_{cpx\text{-}m}$(Ni), and $K_{pl\text{-}m}$(Sr) values. In (**d**), D_{sm}(Sr) of 1 is highlighted with a dashed line, and the thermal evolution of the resident melt and WR are indicated. The oscillating pattern for $D_{sm}{}^{M}$(Sr) in the AFC runs reflects the working principles of the primary MCS tool after assimilation begins: low points in the pattern are first steps after assimilation of WR anatectic melt, whereas each high point in the diagram represents a normal 5˚C decrement step. See text for more details.

5. Case 5: Recharge-assimilation of wallrock anatectic melts-fractional crystallization (R_2AFC)

In the exemplary R_2AFC model that combines magma replenishment with assimilation of WR partial melts, the R events are set as in the R_2FC model and WR parameters are set as in the AFC model.

Assimilation begins in the R_2AFC simulation as in the AFC model when the temperature of the resident melt has dropped to ~1069 °C (~51 wt. SiO_2; ~26 wt.% crystallization of the magma chamber at that point). This precedes recharge events at M temperatures of ~1041 °C (~54 wt. SiO_2) and 998 °C (~60 wt. SiO_2). The R_2AFC model terminates after ~38 wt.% of crystallization at a total magma chamber mass of ~352 m.u. with ~60 wt.% of dacitic ($SiO_2 \approx$ 63 wt.% at 967 °C) melt left and less than 0.02 wt.% of fluid separated (Fig. 2e). The large magma chamber mass includes ~102 m.u. (~29 wt.%) of added WR anatectic melt and 150 m.u. (~43 wt.%) of added R magma. The fractionated bulk solid cumulate consists of approximately 6 wt.% olivine, 50 wt.% clinopyroxene, 26 wt.% plagioclase, 6 wt.% spinel, 12 wt.% orthopyroxene, and <1 wt.% rhombohedral oxide (listed in the order of appearance). The residual WR mineral composition and behavior is similar to the AFC model, although additional heat provided by the R magmas has melted the WR to a greater degree and has exhausted it of quartz by the end of the simulation.

When assimilation is simulated together with recharge events, the resident melt begins to show complex trace element trends (Fig. 3). These effects are the result of mass exchange between the resident melt and either "depleted" primitive R magmas or "enriched" WR partial melt batches and the resulting changes in phase equilibria and D values that can be reviewed in detail in the related model output. The effects of R events for contamination-sensitive trace element and radiogenic isotope ratios are less drastic, however, although the respective trends of the R_2AFC run closely parallel to those of the AFC run (Fig. 4). What is very different in these models, however, are the masses of the components (see Fig. 2). The final resident melt composition of the R_2AFC run is the result of assimilation of ~102 m.u. of WR anatectic melt by 250 m.u. of initial and R magmas. The resulting compositions correspond to those of the

AFC run after ~30–35 m.u. of WR anatectic melts has been assimilated by 100 m.u. of initial melt. Note that in the end of the R_2AFC run, the amount of assimilation relative the resident magma chamber mass is nevertheless similar (~30 wt.%) to that of the AFC run at a given isotopic composition (Fig. 4).

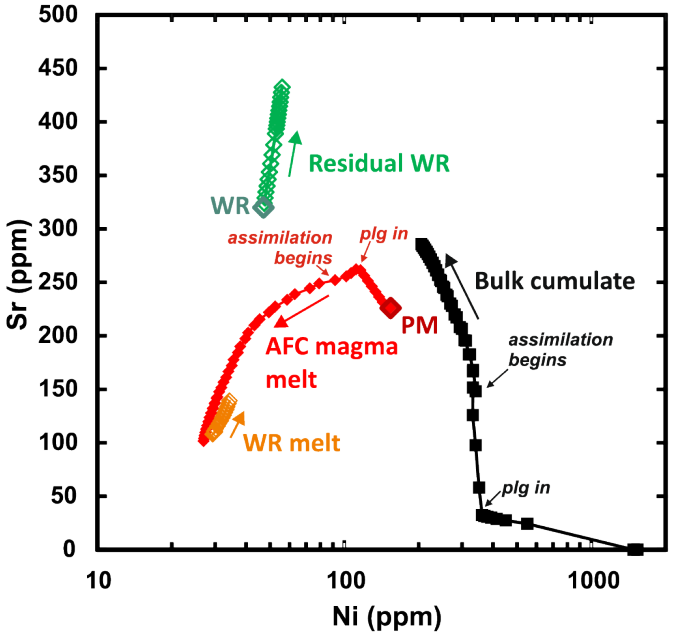

Figure 7. Ni (ppm) vs. Sr (ppm) in the resident melt, bulk cumulate, WR melt, and WR bulk residue (solid+melt+fluids) of the default AFC model. Initial parental melt (PM) and WR compositions are labeled. Arrows indicate the direction of evolution in the MCS simulation. The causes for the major inflection points are marked for the resident melt and bulk cumulate composition.

D. Discussion

1. Selecting partition coefficients

For any reasonable trace element and radiogenic isotope model of a magmatic system, selection of feasible partition coefficients is crucial. Given the number of studies on partitioning of elements in different phases in different magma compositions and at different P-T-conditions, it is easy to get overwhelmed in the quest for such information.

For our example models presented here, we used a set of partition coefficients compiled from other modeling software or from individual publications of systems similar to the

resident melt and WR partial melt compositions in the MCS models. In addition, we applied T-dependence whenever it was feasible and enough relevant data was available (Table 3).

The example of using hypothetical "maximum" or "minimum" K_{sm} reported in the compilation of Rollinson (1993) demonstrates the issue of selecting partition coefficients (Fig. 6). Partition coefficients are often considered constant in the still widely used AFC model of DePaolo (1981) and in the EC-AFC class of models (Spera and Bohrson, 2001, 2002, 2004; Bohrson and Spera, 2007) that only model trace elements and do not consider phase equilibria. In the MCS models presented here, the resident melt evolves from basaltic to dacitic/rhyolitic and crystallizes and melts a wide range of silicate, oxide, and phosphate phases, which propel considerable difficulties for selecting constant K_{sm} values for the whole run. Therefore, we strongly recommend running *MCS-Traces* models with T-dependent K input, especially for cases that span large compositional and temperature ranges. If such data are not available, running with different sets of constant partition coefficients (e.g., using relevant minimum and maximum reported K_{sm} values for each phase) could be a viable option. A multifaceted approach will provide a framework for the relative importance of reported K_{sm} variance and strengthen the presented models. The benefit of relying on highly compatible or incompatible elements is that possible magnitude-scale variations reported for K_{sm} values (e.g., from 100 to 10 or from 0.01 to 0.001) will have a minute effect on the resulting geochemical trends. Whatever is the selected approach, it is important to clearly state which K_{sm} values were used, what was the reason they were selected, and what the referred sources are.

Finally, additional complexity in element partitioning in MCS models is caused by the appearance of a fluid phase, either in the resident magma or in the wallrock (Fig. 5). Unfortunately, K_{sf} values are highly underrepresented relative to K_{sm} values in experimental

petrology and petrologic literature in general. This still is an important aspect of the modeling, because if an element is highly fluid-compatible, even small amounts of fluid separation may have drastic effects on its concentrations in the resident melt (e.g., Cs, Rb, Th; for Sr and Ba, see Fig. 5). Geochemical models based upon the assumption that trace elements are insoluble can lead to inaccurate source composition estimates if, in fact, appreciable amounts of trace elements are removed from the system by volatiles. Furthermore, assimilation of the fluid phase from the wallrock is not presently handled by MCS (see Bohrson et al., in revision), so highly fluid-compatible elements may be primarily concentrated in the residual wallrock and not assimilated with the wallrock partial melts in AFC scenarios. Therefore, we recommend using caution in selecting K_{sf} values for the resident magma and especially for the wallrock in modeling fluid-saturated systems.

2. Trace elements and isotopes as indicators of open-system processes

Trace elements and isotopes have traditionally been regarded as useful indicators of open-system processes in igneous systems. This is because major element and mineral compositional evolution is controlled by phase equilibria, and effects of recharge and assimilation processes on these may be minute or difficult to identify at least from bulk compositions (as illustrated in the companion paper). In the sections below, we review and, on the basis of *MCS-Traces* modeling, re-evaluate the usefulness of trace elements and isotopes as such indicators.

a. Identifying fingerprints of magma recharge

Identifying recharge (and complete homogenization) of magma pulses having the same composition with the parental melt based on major element evidence is challenging (Bohrson

et al., in revision), and the same is true for incompatible trace elements: Zr, Ba, La, and Yb trends for both the FC and R_2FC scenarios are practically uniform (Fig. 3c–f). Some variation is evident in the case of Ni, which behaves mostly compatibly throughout the run, as well as Sr, which is incompatible before the onset of plagioclase fractionation (Fig. 3a, b). In both cases, slight offsets from the FC trend can be seen following recharge. Such offsets may nevertheless be difficult to distinguish from natural sample variation due to other factors (such as sample inhomogeneity) and analytical uncertainty.

We conclude that magma recharge processes are very difficult to identify in differentiating magmatic systems on the basis of major or trace element trends alone if the recharge melts are of uniform composition. Instead, one or more of the following three premises should preferably be fulfilled: 1) the recharge magma has a distinct composition relative to earlier initial or parental melts of the system (e.g., Pietruszka and Garcia, 1999); 2) stratigraphic or other temporal sample control enables detection of "reverse" geochemical and/or mineral compositional trends (e.g., increase in MgO or Ni contents) that are best explained by addition of more primitive magma into the system (e.g., Cox, 1988; Blight et al., 2010; Yuan et al., 2017); and/or 3) there is a representative crystal cargo available in order to study crystalline microtextures and textural relationships, and major and trace element compositional variations. In the case of zoned crystals, this can be regarded as an intracrystalline stratigraphic control, and its importance in indicating magma recharge has been recognized in different magmatic environments, especially those related to subduction settings (e.g., Ginibre and Wörner, 2007; Streck, 2008; Ginibre and Davidson, 2014; Bouvet de Maisonneuve et al., 2016). However, evidence from *MCS-PhaseEQ* modeling suggests that recharge is not necessarily recorded similarly in all phases (e.g., in those that show varying stability in a

replenishing system; Bohrson et al., in revision). In addition, post-crystallization re-equilibration of crystals by diffusion may readily erase some elemental zoning in certain minerals (see, e.g., Costa et al., 2008). Note that for studying the effects of recharge on individual phase compositions, mineral major and trace element compositions are also recorded in MCS output.

b. Identifying fingerprints of crustal assimilation

Crustal assimilation was also surprisingly difficult to recognize based only on major element oxides from MCS model output in standard AFC and SFC scenarios (Bohrson et al., in revision), even though the amount of assimilation in the presented models is very large. Notable differences in the modeled AFC scenario relative to FC or R_2FC scenarios were only identified in terms of K_2O (5x enrichment relative to FC or R_2FC model due to melting of alkali feldspar in the wallrock) with subtler differences also present in Al_2O_3, CaO, and Na_2O. These differences were even less obvious if the degree of contamination was lower or happened by wholesale incorporation of stoped blocks (S_2FC case).

In contrast, AFC, S_2FC, and R_2AFC cases are readily distinguished from FC and R_2FC cases in terms of incompatible elements and isotopic compositions (Figs. 3 and 4). These will be reviewed in case-specific sections below.

i. Assimilation of wallrock anatectic melts

Assimilation of wallrock anatectic melts (AFC in MCS jargon) will dominate in settings where wallrock xenoliths are not efficiently introduced into the resident melt, but assimilation takes place within a contact zone of the wallrock and the resident melt. Such conditions largely prevail in middle to lower crustal magma chambers, where the wallrock is not highly

fractured, behaves in ductile manner, and boundary temperatures are high (see Bohrson et al., 2014).

MCS modeling shows that partial melting of the wallrock considerably enriches the wallrock partial melt and thus the contaminated resident melt in incompatible elements that are found in high quantities in the wallrock (e.g., Zr, Ba, and La) already during early stages of assimilation (Fig. 3c–e). In fact, the first batches of WR partial melts are most important in enriching the resident melt, since they are loaded with such elements – the melting WR, and thus WR partial melts, will get progressively depleted in incompatible elements after each assimilation step, which then dilutes this effect. The presented MCS models suggest that the relative amounts of assimilation in natural systems on the basis of incompatible trace element concentrations or their isotopes, without some kind of control on the thermodynamics, phase equilibria, and style of assimilation, may often be significantly overestimated (see Heinonen et al., 2016). The contrary is true if elements are incompatible but present in low quantities within the wallrock (e.g., Yb; Fig. 3f). Ytterbium is initially slightly enriched in the contaminated resident melt, because it effectively enters the assimilated wallrock partial melt (D_{sm}^{WR}(Yb) is 0.1–0.3 throughout the run). Because of the initially low concentration in the wallrock (1.96 ppm relative to 1.73 ppm in PM; Table 2), however, the wallrock partial melts become depleted in Yb quite rapidly relative to, for example, SiO_2, Zr, Ba, or La.

Compatible element Ni shows unexpected behavior (Fig. 3a): its concentrations in M melt in the AFC case are relatively higher than in the FC case, although assimilation of relatively Ni-poor WR (Table 2) would be expected to dilute its concentrations in the contaminated melt. As stated previously, this surprising effect is because assimilation suppresses the crystallization of olivine with high K_{sm}(Ni) in the AFC case relative to the FC case, and

because Ni is not as compatible in WR (D_{sm}^{WR}(Ni) ≈ 1.7–1.9) as it is in the magma chamber (D_{sm}^{M}(Ni) ≈ 2–10). The different degrees of enrichment/depletion shown by variably compatible elements in AFC resident melt underline the importance of defining phase equilibria and evaluating the role of assimilation in natural systems based on several and not just one or two different elements.

The isotopic effects of assimilation of wallrock partial melts are clear and most drastic for elements that show incompatible behavior in the wallrock and are relatively depleted in the resident melt (Fig. 6). If the partially melting wallrock contains residual plagioclase in significant proportions such that D_{sm}^{WR}(Sr) > 1, $^{144}Nd/^{143}Nd$ is expected to show more drastic changes than $^{87}Sr/^{86}Sr$. Oxygen isotopes have been considered as useful indicators of crustal contributions to mantle-derived magmatic systems, because O concentrations in magmas and wallrock are usually very similar whereas their O isotopic compositions are different. Therefore, binary mixing or traditional AFC curves (with O isotopes often considered together with radiogenic isotopes) have been used to estimate the relative amounts of mantle and crust end-members and importance of assimilation vs. source heterogeneity in such systems (e.g., Taylor, 1980; James, 1981; Martinez et al., 1996; Baker et al., 2000; France et al., 2016). The results of MCS modeling illustrated in Fig. 4 indicate that the differences in the compatibility of the trace elements (both in the magma and in wallrock), O budget of the crystallizing resident melt vs. assimilant, and style of assimilation have considerable effects on such isotopic comparisons in different contamination scenarios. It is evident from Fig. 4 that relative contributions from crustal sources may be considerably overestimated using binary mixing models based on O isotopes.

If magma recharge is concurrent with anatectic wallrock assimilation, the latter process controls enrichment in incompatible elements. We emphasize, however, that this observation is highly dependent on the composition of the recharge magma and the wallrock, and the mass balances among the three subsystems. Finally, in addition to being able to follow the geochemical evolution of the resident melt, MCS records the geochemical evolution of the residual wallrock (Fig. 7). In cases where such information is available (e.g., contact zones of intrusions, inclusions of anatectic melt), MCS can be used in accordance with other information on the magmatic system to confirm or refine scenarios involving wallrock partial melting.

ii. Wholesale assimilation of stoped blocks

Wholesale assimilation of stoped blocks (SFC in MCS jargon) will dominate in settings where wallrock xenoliths are efficiently introduced into the resident melt. Such conditions may prevail in upper crustal magma chambers or feeding channels, where the wallrock is highly fractured and behaves in brittle manner, and boundary temperatures are low (see Bohrson et al., 2014). The smaller the stoped blocks are, the higher the chance of rapid thermalization and partial or wholesale melting and, eventual equilibration with resident melt because small blocks heat up internally faster than larger ones (Carslaw and Jaeger, 1959). Note that a single S event in MCS can be considered as stoping of multiple small xenoliths, the combined mass of which equals the total mass of the S event.

When wallrock is completely homogenized and equilibrated with the resident melt (i.e. bulk assimilation), partition coefficients for the wallrock phases do not play a role: i.e., the effect of assimilation on trace element contents of the resident melt is fully dictated by their concentration in the wallrock and the mass of the assimilated wallrock block. Therefore, in

assimilation by stoping, any element that is relatively enriched in the assimilated wallrock block will also be enriched in the resident melt. Such effects may subsequently be diluted by fractional crystallization, however.

The isotopic model results very clearly illustrate the differences between assimilation by stoping (i.e., bulk incorporation of wallrock) and assimilation of anatectic melts (Fig. 4). Whereas Nd is incompatible and Sr compatible in wallrock in the case of wallrock partial melting (AFC; see previous section for details), in S_2FC, the isotopic composition of the resident melt is only controlled by bulk assimilation of the wallrock blocks into the resident melt. Depending on the compatibility of the associated elements and the process of contamination, the curves in isotope diagrams can be convex upwards or downwards (cf. Sr and Nd isotopes relative to $\delta^{18}O$ in AFC and S_2FC in Fig. 4b, c), making the distinction between wallrock contamination vs. source heterogeneity rather difficult (cf. Taylor, 1980; James, 1981).

If AFC and S_2FC are thought of as end-members of assimilation process, anything in between could take place in natural systems, where there is always a middle ground between wholesale melting of stoped blocks and partial melting of the wallrock. In most cases, MCS modeling would benefit from considering both options. Note that it is also possible to model SFC and AFC together in a single run to simulate such a system.

E. Model assumptions and limitations and future development of the MCS-Traces

MCS is a versatile, mass- and energy-balanced thermodynamic tool that can model complex scenarios that involve R_nAS_nFC. One of its shortcomings is that it is "only" an equilibrium thermodynamic model; it therefore does not account for time-dependent kinetic, diffusion, or transport phenomena, or other processes that may result in chemical

disequilibrium – a well know feature of most igneous systems. Many of these limitations have been discussed in the companion paper (Bohrson et al., in revision) and the reader is referred to it for more information, but we will further concentrate on those that are particularly relevant to modeling trace elements and their respective isotope systems.

A potentially important limitation in terms of trace element modeling is related to the MELTS engines. Current versions do not incorporate some minor phases such as zircon or monazite. Such phases are not usually important in terms of major element evolution of igneous systems, but they serve as important hosts for many otherwise incompatible trace elements (e.g., in the case of zircon and monazite, Zr and Th + REE, respectively). For example, Zr is modeled here as a generally incompatible trace element in the wallrock, but in an average crustal granitoid, zircon is almost always present, and it will thus influence the behavior of Zr during wallrock partial melting. If zircon remains in the wallrock residue, wallrock partial melts will be relatively depleted in Zr, which will in turn affect the Zr evolution of the evolving resident melt. We recommend that the possibility of minor phases retaining some trace elements in the wallrock residue should be evaluated in MCS scenarios. In addition, MELTS engines provide limited thermodynamic data for water-bearing phases (e.g., biotite and amphiboles; see Gualda et al., 2012; Bohrson et al., in revision) which are often not stabilized by the engines in systems where they are expected. This could have a negative impact on comparisons of *MCS-Traces* models to fluid-rich natural systems. If fluid-bearing phases are common in the studied natural system, trace elements incompatible to them should be preferred in the modeling until more robust thermodynamic data is available for the MELTS engines.

A designed future extension of *MCS-Traces* is to allow for isotopic disequilibrium during the partial melting of wallrock as demonstrated by Iles et al., (2018). In its current form, wallrock has an isotopic ratio that is the same as all phases in the wallrock. In the case of radiogenic isotopes, for example, this implies that differential ingrowth has not occurred in any of the minerals, and hence the isotopic ratio in anatectic melt does not change during assimilation. However, pre-magmatic in-growth of daughter isotopes in wallrock phases, dictated by phase-specific parent daughter ratios and time leads to variations in the respective isotopic ratios among mineral phases. In addition, although radiogenic ingrowth does not concern O isotopes, O isotopic heterogeneity between mineral phases in the same rock is also a common feature. It is easy to envision, for example, an Archean granitic wallrock where coexisting minerals (e.g., biotite, alkali feldspar, and plagioclase with distinct Rb/Sr) have distinct $^{87}Sr/^{86}Sr$. As wallrock undergoes partial melting, partial melt will have $^{87}Sr/^{86}Sr$ that is a function of the contribution each crystalline phase makes to the melt. Hence the isotopic composition of wallrock melt will change during the partial melt assimilation process. The potential effects of isotope fractionation between an isotopically heterogeneous wallrock and its partial melt batches can currently be approximated by, e.g., running two models using representative minimum and maximum radiogenic isotope ratios for the wallrock. Extension of MCS to include disequilibrium isotopes would allow a more quantitative and high-fidelity approach to this issue.

Similar to *MCS-PhaseEQ*, there is an urge to translate *MCS-Traces* to a programming language that would combine the two and be platform-independent. While the advantages to the two stage calculation presented here are many, merging the two tools would enable the Monte Carlo approach to trace element and isotope calculations, as has been proposed for the

major element and phase equilibria calculations (see Bohrson et al., in revision). This modeling environment would allow users to produce a large number of models relatively rapidly, and with less human bias in choosing parameters. Future improvements will also likely include statistical tools for enhanced handling of the model results. The users are encouraged to check the MCS website for software updates.

Finally, one of the most important things to realize as a petrologist and a potential user of MCS is the scale and the relative importance of the involved processes. If some crystals in the studied natural system are zoned, full of solid inclusions, or exhibit any disequilibrium textures, this does not instantly mean that MCS could not be used to constrain the general magmatic evolution of the system. Although current versions of MCS assume thermodynamic equilibration of a magma during open-system processes, the processes which produce such disequilibrium textures, such as recharge and magma mixing, are those which MCS was designed to model, and thus can reasonably approximate. In addition, with the ability to record major and trace element concentrations of melt, fluid, and each mineral in every step, MCS can provide important constraints on the thermal histories and geochemical conditions during the generation of crystal zoning; of course, interpretations of model results must be placed in context and compared with those derived from other data sources. In other words, when attempting to understand a natural system, one can search for the best MCS model by perturbing initial conditions and parameters iteratively, while remaining within the realm of reasonability. Such a 'best' model will, in all likelihood remain imperfect, perhaps in significant ways. Such imperfection should not be seen as a failure. Instead, by struggling with *the root cause* of the imperfections, valuable clues to the systems petrological and geochemical evolution may be elucidated. That is, the nature of the transport, kinetic and

dynamic phenomena, precisely those ignored in thermodynamic models, may rise to the top to be addressed by 'beyond thermodynamic' analysis. This confrontation with reality and attempt to model complex systems is the ultimate goal of petrology. We close the MCS companion papers citing the final few words in N.L. Bowens 1928 opus on the *Evolution of the Igneous Rocks* (Bowen, 1928*):* "No implication is intended that our knowledge is all that could be desired. That can never be."

F. Summary

The Magma Chamber Simulator *MCS-Traces* computer program calculates the simultaneous evolution of 48 trace elements, seven radiogenic isotope systems (Sr, Nd, Hf, 3xPb, and Os), and O isotopes for a magma (melt + crystals ± fluid phase) in an igneous system influenced by magma recharge, assimilation (either of wallrock partial melts or stoped blocks), and fractional crystallization (R_nAS_nFC). In addition, the trace element evolution of the cumulate pile and residual wallrock is output. *MCS-Traces* requires output from the *MCS-PhaseEQ* computational tool, which is described in a companion paper (Bohrson et al., in revision), to perform the calculations. Our analysis of example case studies of depleted mantle magma crystallizing ± experiencing recharge pulses ± assimilating average granodioritic crust at 0.1 GPa reveals key characteristics of the different processes. For the case studies presented here, the effects of magma recharge are difficult to recognize from trace element or radiogenic isotope data alone; a temporal (e.g., stratigraphic or intracrystalline) reference frame is required and we also note that recharge may be more evident when there is greater contrast between resident melt and intruding magma(s). In contrast, assimilation (especially in the case of assimilation of wallrock anatectic melts) may have drastic effects on incompatible trace element and isotopic compositions of the resident melt. The magnitude of these effects

depends predominantly on phase equilibria, element partitioning, style of contamination (by wallrock partial melts vs. stoped blocks) and the geochemical differences between the resident melt and the wallrock. In many cases, the effects of assimilation on trace elements and isotopes are counterintuitive and varied and considerable caution should be practiced in ruling out potential assimilation scenarios. The case studies presented here highlight the challenges that petrologists and geochemists face when diagnosing open-system processes. Discrepancies between observations and the 'best' open system model(s) have the potential to reveal details of the role of kinetic and transport phenomena (non-equilibrium) in petrogenesis. There are plethora of ways to use MCS to solve petrogenetic questions related to magmatism in wide range of igneous environments.

G. Electronic Supplementary Materials

This chapter was originally published in Contributions to Mineralogy and Petrology under a Creative Commons Open-Access CC-BY-4.0 license as Heinonen *et al.* (2020). An electronic supplement is available at https://link.springer.com/article/10.1007/s00410-020-01718-9.

H. References

Bacon CR, Druitt TH (1988) Compositional evolution of the zoned calcalkaline magma chamber of Mount Mazama, Crater Lake, Oregon. Contrib Mineral Petrol 98:224–256. https://doi.org/10.1007/BF00402114

Baker JA, Macpherson CG, Menzies MA, Thirlwall MF, AL-Kadasi M, Mattey DP (2000) Resolving crustal and mantle contributions to continental flood volcanism, Yemen; constraints from mineral oxygen isotope data. J Petrol 41:1805–1820. https://doi.org/10.1093/petrology/41.12.1805

Bea F, Pereira MD, Stroh A (1994) Mineral/leucosome trace-element partitioning in a peraluminous migmatite (a laser ablation-ICP-MS study). Chem Geol 117:291–312. https://doi.org/10.1016/0009-2541(94)90133-3

Blight JHS, Petterson MG, Crowley QG, Cunningham D (2010) The Oyut Ulaan Volcanic Group: stratigraphy, magmatic evolution and timing of Carboniferous arc development in SE Mongolia. J Geol Soc London 167:491–509. https://doi.org/10.1144/0016-76492009-094

Blundy J, Wood B (2003) Partitioning of trace elements between crystals and melts. Earth Planet Sci Lett 210:383–397. https://doi.org/10.1016/S0012-821X(03)00129-8

Blundy JD, Wood BJ (1991) Crystal-chemical controls on the partitioning of Sr and Ba between plagioclase feldspar, silicate melts, and hydrothermal solutions. Geochim Cosmochim Acta 55:193–209. https://doi.org/10.1016/0016-7037(91)90411-W

Bohrson WA, Spera FJ (2007) Energy-Constrained Recharge, Assimilation, and Fractional Crystallization (EC-RAXFC): A Visual Basic computer code for calculating trace element and isotope variations of open-system magmatic systems. Geochem Geophys Geosyst 8:Q11003. https://doi.org/10.1029/2007GC001781

Bohrson WA, Spera FJ, Ghiorso MS, Brown GA, Creamer JB, Mayfield A (2014) Thermodynamic model for energy-constrained open-system evolution of crustal magma bodies undergoing simultaneous recharge, assimilation and crystallization: the Magma Chamber Simulator. J Petrol 55:1685–1717. https://doi.org/10.1093/petrology/egu036

Bohrson WA, Spera FJ, Heinonen JS, Brown GA, Scruggs MA, Adams J, Takach M, Zeff G, Suikkanen E (in revision). Diagnosing open-system magmatic processes using the Magma Chamber Simulator (MCS): Part I - major elements and phase equilibria. Contrib Mineral Petrol.

Boudreau AE (1999) PELE – a version of the MELTS software program for the PC platform. Comput Geosci 25:201–203. https://doi.org/10.1016/s0098-3004(98)00117-4

Bouvet de Maisonneuve C, Costa F, Huber C, Vonlanthen P, Bachmann O, Dungan MA (2016) How do olivines record magmatic events? Insights from major and trace element zoning. Contrib Mineral Petrol 171:56. https://doi.org/10.1007/s00410-016-1264-6

Bowen NL (1928) The evolution of igneous rocks. Dover Publications, New York, United States, 334 p.

Carslaw HS, Jaeger JC (1959) Conduction of heat in solids. Oxford University Press, Oxford, United Kingdom, 510 p.

Costa F, Dohmen R, Chakraborty S (2008) Time scales of magmatic processes from modeling the zoning patterns of crystals. In: Putirka KD, Tepley FJ,III (eds) Minerals, inclusions and volcanic processes. Rev Mineral Geochem 69:545–594. https://doi.org/10.2138/rmg.2008.69.14

Cox KG (1988) Numerical modelling of a randomized RTF magma chamber: a comparison with continental flood basalt sequences. J Petrol 29:681–697. https://doi.org/10.1093/petrology/29.3.681

DePaolo DJ (1981) Trace element and isotopic effects of combined wallrock assimilation and fractional crystallization. Earth Planet Sci Lett 53:189–202. https://doi.org/10.1016/0012-821x(81)90153-9

Eiler JM (2001) Oxygen isotope variations of basaltic lavas and upper mantle rocks. In: Valley JW, Cole DR (eds) Stable isotope geochemistry. Rev Mineral Geochem 43:319–364. https://doi.org/10.2138/gsrmg.43.1.319

Eiler JM, Schiano P, Kitchen N, Stolper EM (2000) Oxygen-isotope evidence for recycled crust in the sources of mid-ocean-ridge basalts. Nature 403:530–534. https://doi.org/10.1038/35000553

Ewart A, Griffin WL (1994) Application of proton-microprobe data to trace-element partitioning in volcanic rocks. Chem Geol 117:251–284. https://doi.org/10.1016/0009-2541(94)90131-7

France L, Demacon M, Gurenko AA, Briot D (2016) Oxygen isotopes reveal crustal contamination and a large, still partially molten magma chamber in Chaîne des Puys (French Massif Central). Lithos 260:328–338. https://doi.org/10.1016/j.lithos.2016.05.013

Gale A, Dalton CA, Langmuir CH, Su Y, Schilling J (2013) The mean composition of ocean ridge basalts. Geochem Geophys Geosyst 14:3. https://doi.org/10.1029/2012GC004334

Ghiorso MS, Gualda GAR (2015) An H_2O–CO_2 mixed fluid saturation model compatible with rhyolite-MELTS. Contrib Mineral Petrol 169:53. https://doi.org/10.1007/s00410-015-1141-8

Ghiorso MS, Hirschmann MM, Reiners PW, Kress III VC (2002) The pMELTS: A revision of MELTS for improved calculation of phase relations and major element partitioning related to partial melting of the mantle to 3 GPa. Geochem Geophys Geosyst 3:5. https://doi.org/10.1029/2001GC000217

Ghiorso MS, Sack RO (1995) Chemical mass transfer in magmatic processes IV. A revised and internally consistent thermodynamic model for the interpolation and extrapolation of liquid-solid equilibria in magmatic systems at elevated temperatures and pressures. Contrib Mineral Petrol 119:197–212. https://doi.org/10.1007/bf00307281

Gill JB (1981) Orogenic andesites and plate tectonics. Springer Berlin, Heidelberg, Germany, 315 p. https://doi.org/10.1007/978-3-642-68012-0

Ginibre C, Davidson JP (2014) Sr isotope zoning in plagioclase from Parinacota Volcano (Northern Chile): quantifying magma mixing and crustal contamination. J Petrol 55:1203–1238. https://doi.org/10.1093/petrology/egu023

Ginibre C, Wörner G (2007) Variable parent magmas and recharge regimes of the Parinacota magma system (N. Chile) revealed by Fe, Mg and Sr zoning in plagioclase. Lithos 98:118–140. https://doi.org/10.1016/j.lithos.2007.03.004

Goldstein SJ, Jacobsen SB (1988) Nd and Sr isotopic systematics of river water suspended material: implications for crustal evolution. Earth Planet Sci Lett 87:249–265. https://doi.org/10.1016/0012-821X(88)90013-1

Gualda GAR, Ghiorso MS, Lemons RV, Carley TL (2012) Rhyolite-MELTS: a modified calibration of MELTS optimized for silica-rich, fluid-bearing magmatic systems. J Petrol 53:875–890. https://doi.org/10.1093/petrology/egr080

Heinonen JS, Luttinen AV, Bohrson WA (2016) Enriched continental flood basalts from depleted mantle melts: modeling the lithospheric contamination of Karoo lavas from Antarctica. Contrib Mineral Petrol 171:9. https://doi.org/10.1007/s00410-015-1214-8

Heinonen JS, Luttinen AV, Spera FJ, Bohrson WA (2019) Deep open storage and shallow closed transport system for a continental flood basalt sequence revealed with Magma Chamber Simulator. Contrib Mineral Petrol 174:87. https://doi.org/10.1007/s00410-019-1624-0

Iles KA, Hergt JM, Woodhead JD (2018) Modelling Isotopic Responses to Disequilibrium Melting in Granitic Systems. J Petrol 59:87–113. https://doi.org/10.1093/petrology/egy019

James DE (1981) The combined use of oxygen and radiogenic isotopes as indicators of crustal contamination. Annu Rev Earth Planet Sci 9:311–344. https://doi.org/10.1146/annurev.ea.09.050181.001523

Kessel R, Schmidt MW, Ulmer P, Pettke T (2005) Trace element signature of subduction-zone fluids, melts and supercritical liquids at 120–180 km depth. Nature 437:724–727. https://doi.org/10.1038/nature03971

Luttinen AV, Furnes H (2000) Flood basalts of Vestfjella: Jurassic magmatism across an Archaean-Proterozoic lithospheric boundary in Dronning Maud Land, Antarctica. J Petrol 41:1271–1305. https://doi.org/10.1093/petrology/41.8.1271

Mahood G, Hildreth W (1983) Large partition coefficients for trace elements in high-silica rhyolites. Geochim Cosmochim Acta 47:11–30. https://doi.org/10.1016/0016-7037(83)90087-X

Martinez IA, Harris C, Le Roex AP, Milner SC (1996) Oxygen isotope evidence for extensive crustal contamination in the Okenyenya igneous complex, Namibia. Geochim Cosmochim Acta 60:4497–4508. https://doi.org/10.1016/S0016-7037(96)00239-6

Nash WP, Crecraft HR (1985) Partition coefficients for trace elements in silicic magmas. Geochim Cosmochim Acta 49:2309–2322. https://doi.org/ 10.1016/0016-7037(85)90231-5

Philpotts JA, Schnetzler CC (1970) Phenocryst-matrix partition coefficients for K, Rb, Sr and Ba, with applications to anorthosite and basalt genesis. Geochim Cosmochim Acta 34:307–322. https://doi.org/10.1016/0016-7037(70)90108-0

Pietruszka AJ, Garcia MO (1999) A rapid fluctuation in the mantle source and melting history of Kilauea Volcano inferred from the geochemistry of its historical summit lavas (1790–1982). J Petrol 40:1321–1342. https://doi.org/10.1093/petroj/40.8.1321

Rollinson HR (1993) Using geochemical data: Evaluation, presentation, interpretation. Taylor & Francis, London, United Kingdom, 384 p. https://doi.org/10.4324/9781315845548

Rudnick RL, Gao S (2003) Composition of the continental crust. In: Rudnick RL (ed) The crust. Treatise on Geochemistry, vol 3. Elsevier-Pergamon, Oxford, United Kingdom, pp 1–64. https://doi.org/10.1016/b0-08-043751-6/03016-4

Spera FJ, Bohrson WA (2004) Open-system magma chamber evolution: an Energy-Constrained geochemical model incorporating the effects of concurrent Eruption, Recharge, variable Assimilation and Fractional Crystallization (EC-E'RAχFC). J Petrol 45:2459–2480. https://doi.org/10.1093/petrology/egh072

Spera FJ, Bohrson WA (2002) Energy-constrained open-system magmatic processes 3. Energy-Constrained Recharge, Assimilation, and Fractional Crystallization (EC-RAFC). Geochem Geophys Geosyst 3:12. https://doi.org/10.1029/2002GC000315

Spera FJ, Bohrson WA (2001) Energy-constrained open-system magmatic processes I: General model and Energy-Constrained Assimilation and Fractional Crystallization (EC-AFC) formulation. J Petrol 42:999–1018. https://doi.org/10.1093/petrology/42.5.999

Spera FJ, Bohrson WA, Till CB, Ghiorso MS (2007) Partitioning of trace elements among coexisting crystals, melt, and supercritical fluid during isobaric crystallization and melting. Am Mineral 92:1881–1898. https://doi.org/10.2138/am.2007.2326

Streck MJ (2008) Mineral textures and zoning as evidence for open system processes. In: Putirka KD, Tepley FJ,III (eds) Minerals, inclusions and volcanic processes. Rev Mineral Geochem 69:595–622. https://doi.org/10.2138/rmg.2008.69.15

Taylor HP (1980) The effects of assimilation of country rocks by magmas on $^{18}O/^{16}O$ and $^{87}Sr/^{86}Sr$ systematics in igneous rocks. Earth Planet Sci Lett 47:243–254. https://doi.org/10.1016/0012-821X(80)90040-0

Yuan Q, Namur O, Fischer LA, Roberts RJ, Lü X, Charlier B (2017) Pulses of plagioclase-laden magmas and stratigraphic evolution in the Upper Zone of the Bushveld Complex, South Africa. J Petrol 58:1619–1643. https://doi.org/10.1093/petrology/egx067

III. A geodetically-constrained petrogenetic model for evolved lavas from the January 1997 fissure eruption of Kilauea Volcano

A. Introduction

Nearly-continuous eruptive activity at the summit of Kilauea Volcano and along its East Rift Zone (ERZ) have fascinated both the public and scientists around the world for over three decades. Fortuitously, rapid technological advances of the late 20th and early 21st century—throughout the duration of the 1983-2018 Pu'U 'O'o eruption—provided detailed records of the eruption, making Kilauea one of the best monitored and most intensely studied volcanoes on Earth. This was exemplified from March through April 2018 during the last gasp of the Pu'U 'O'o eruption, as USGS volcanologists were able to accurately forecast the onset of eruptive activity in the Leilani Estates subdivision in time to avoid loss of life (Neal *et al*. 2019).

The Pu'U 'O'o eruption initiated along the ERZ on 3 Jan 1983, when a dike from Kilauea's summit reservoir intruded into a section of the Upper ERZ and encountered a small body of differentiated, rift-stored magma likely remaining from Kilauea's 1977 eruption (Garcia *et al*. 1992, 2000). What followed was a series of eruptions that would last, almost continuously, over 35 years (Neal *et al.* 2019). Decade-long periods of passive effusion were routinely punctuated by discrete mixing events, where magmas intruded into the ERZ during the Pu'U 'O'o eruption encountered arrested dike remnants from previous eruptions in the area (Thornber *et al.* 2003a; Greene *et al.* 2013; Wright & Klein 2014), often resulting in the relocation of eruptive vents and/or major reorganization of the underlying system (Orr 2014). Here we explore using these individual mixing events as a petrologic tool to monitor changes

in—and components of—Kilauea's magma storage and transport system, focusing on a series of fissure eruptions at the end of January 1997—colloquially known as Episode 54.

B. Geologic Setting

Stretching ~6,000 km over the northern Pacific Ocean, the Hawaiian-Emperor seamount chain preserves an 82-million-year record of Hawaiian mantle plume activity (Clague & Brent, 1987; O'Conner *et al*., 2013). The northern terminus of the chain, represented by the oldest seamount Meiji, is in the process of being subducted beneath the Aleutian arc (Clague & Brent, 1987; Neall & Trewick, 2008; O'Conner *et al*., 2013). A slightly southward migration of the Hawaiian hotspot beginning at ~76 Ma, followed by a major shift in the direction of Pacific plate movement to WNW at ~47 Ma, is recorded by the pronounced bend of the Hawaii-Emperor seamount chain (Neall & Trewick, 2008; O'Conner *et al*., 2013). Magmatism continues at the mantle plume's current location, as recorded by the Hawaiian Islands and their accompanying seamounts (Neall & Trewick, 2008; O'Conner *et al*., 2013). The youngest active volcano—Loihi seamount—lies at the southern terminus of the Hawaiian archipelago, and represents the current position of the Hawaiian mantle plume (Clague & Brent, 1987). A thorough recollection of Hawaiian geologic history is provided in Walker (1990) and the comprehensive bibliography by Wright & Takahashi (1998).

1. A Brief Chronology of the 1983-2018 Pu'U 'O'o eruption

The Pu'U 'O'o eruption initiated along the ERZ (Fig. 1a) on 3 Jan 1983, when a dike from Kilauea's summit reservoir intruded into a section of the Upper ERZ and encountered a small remnant of differentiated magma likely remaining from Kilauea's 1977 eruption (Garcia *et al.* 1992, 2000). Approximately 24 hours after the intrusion was detected, a series of fissures

opened down-rift of Napau Crater (Garcia *et al*. 1992), eventually establishing a vent at Pu'U 'O'o that became the primary locus of eruptive activity for the following 35 years (Neal *et al*. 2019).

From June 1983 until July 1986, volcanic activity was dominated by intermittent episodes of fire fountaining and concurrent construction of the 255 m Pu'U 'O'o cone (Heliker *et al.* 2003; Girard *et al.* 2017). In July 1986 the Kupaianaha vent formed ~3 km down-rift of Pu'U 'O'o and erupted effusively for the next five-and-a-half years (Mangan *et al.* 1995; Garcia *et al*. 1996). In 1991, eruptive activity began migrating back up-rift, causing low-fountaining fissures; activity had completely relocated to the flanks of Pu'U 'O'o as of February 1992 (Mangan *et al*. 1995; Heliker *et al*. 2003). Contemporaneous lava pond activity and steady-state effusive eruptions from a number of flank vents were punctuated by brief intrusive events until the evening of 29 January 1997 HST (0600 30 January 1997 UTC), when the lava pond inside of the Pu'U 'O'o crater suddenly drained and the crater collapsed (Heliker & Mattox 2003; Thornber *et al*. 2003a). Drain back from Pu'U 'O'o contributed a significant volume of magma to the intrusion, which fed the 22-hour period of fissure eruptions that is the focus of this study—now referred to as Episode 54—in the already-weakened section of the rift zone bound by Napau Crater and Pu'u 'O'o (Harris *et al*., 1997; Thornber *et al*. 2003a).

Twenty-four days after the January 1997 eruption, activity resumed as lava returned to the Pu'U 'O'o cone (Thornber *et al.* 2003a), and after three months of sporadic flank eruptions, steady-state effusive activity developed and continued for over a decade (Thornber 2001; Heliker & Mattox 2003; Thornber *et al.* 2003a; Greene *et al.* 2013). By July 1997, a lava tube on the south side of Pu'U 'O'o had established a route to the ocean and steadily disgorged lava until 12 September 1999, when an intrusion up-rift of Pu'U 'O'o disrupted magma supply

(Cervelli *et al.* 2002; Orr *et al.* 2015). Lava returned to Pu'U 'O'o and effusive activity resumed in the already-established tube system 11 days later; occasional breakouts atop this tube system produced a number of rootless shields that completely overtook the tube system by December 2001 (Orr *et al.* 2015). Disrupted by only a minor pause in eruptive activity during February 2000 (Orr *et al*. 2015), the rootless shields grew until March 2004, when much of the magma supply was redirected from the lava tube system to a weakened area on the south flank of Pu'U' 'O'o (Orr *et al.* 2015). Eruptive activity from the new south flank vent established a new series of flows and lava tubes that reached the ocean in early May 2005 and continued until March 2007 (Poland & Orr 2014; Orr *et al*. 2015).

From 2003 to 2007, magma supply rates to Kilauea almost doubled (Poland *et al*., 2012), requiring an increase in spatial accommodation within both the ERZ and the Southwest Rift Zone (SWRZ; Wright & Klein 2014). Heightened magma supply rates culminated on 17 June 2007, when an up-rift intrusion disrupted the magma supply to Pu'U 'O'o, triggering collapse of its crater floor and ending a decade of nearly continuous effusive activity (Poland *et al*. 2008; Orr 2014). Two days later, a fissure briefly erupted (<1 day) near Kane Nui O Hamo crater, ~6 km up-rift of Pu'U 'O'o (Wright & Klein 2014; Orr 2014). After a 10-day repose period, the Pu'U 'O'o crater began refilling and eruptive activity resumed (Greene *et al*. 2013; Orr 2014; Wright & Klein 2014). On 21 July 2007, a number of intrusive events triggered a second collapse of Pu'U 'O'o's crater floor, opening a series of fissures ~3 km down-rift near Kupaianaha (Montgomery-Brown *et al.* 2010; Orr *et al*. 2015); eruptive activity eventually focused at an individual vent (later named the Episode 58 vent) and continued to direct lava towards the ocean until March of 2011 (Orr *et al*. 2015).

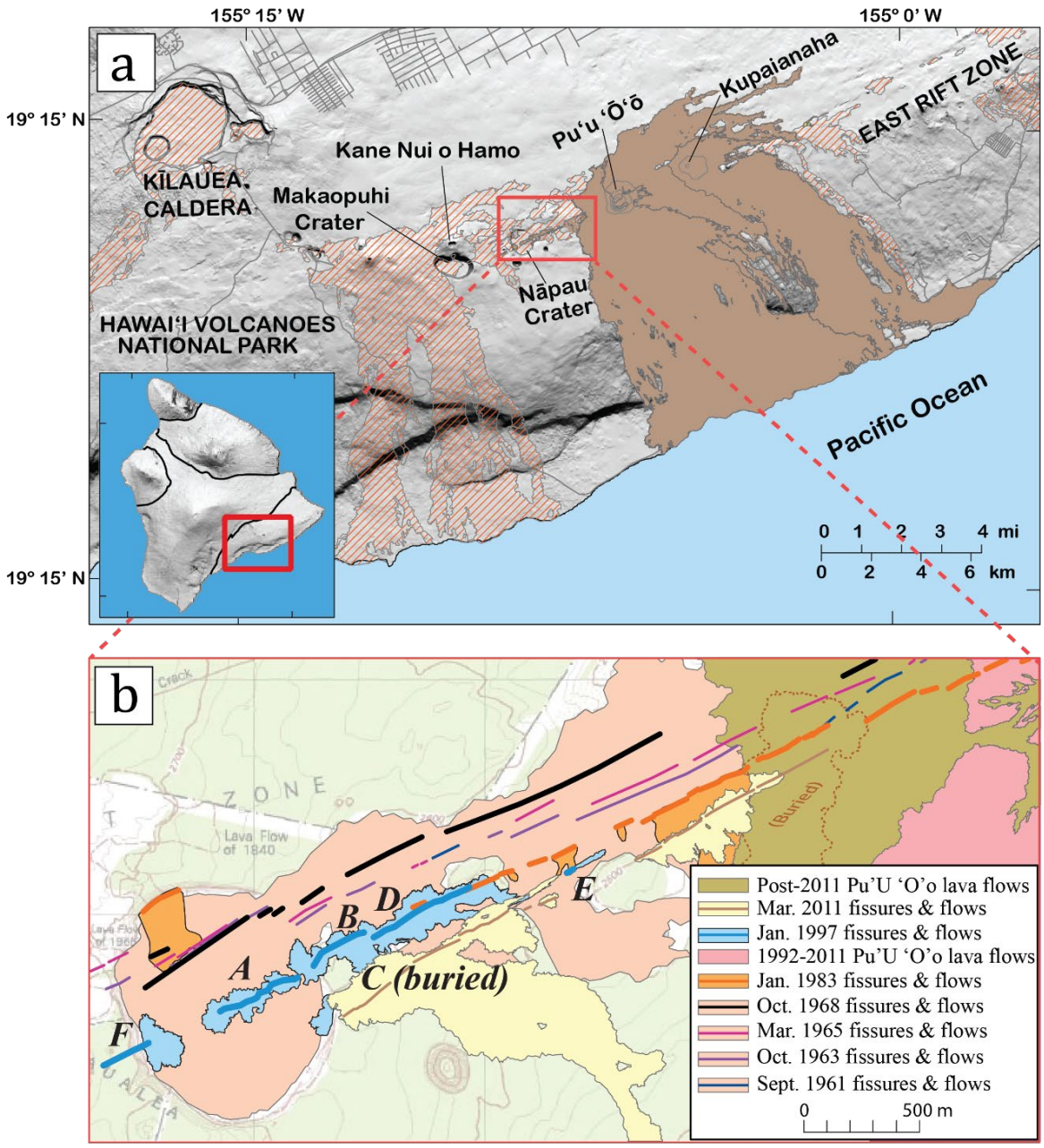

Figure 1. Map of Kilauea volcano on the island of Hawai'i (a; after Orr 2014), and map of fissures within Napau Crater (b; modified from Thornber et al. 2015). Brown lavas in panel (a) are lavas of the Pu'U 'O'o eruption erupted between 1983-2011; those displayed in a red hatched pattern are pre-1983 lavas.

An explosive eruption at Kilauea's summit on 19 March 2008 heralded an era of concurrent active volcanism at both Kilauea's summit and along the ERZ (Girard *et al.* 2017). A new vent formed in the eastern wall of Halema'uma'u crater at the summit of Kilauea,

filling it with a lava lake that persisted until 2018 (Girard *et al*. 2017; Neal *et al*. 2019). For nearly a decade, eruptive activity occurred concurrently at Kilauea's summit and Pu'U' 'O'o (Patrick *et al*. 2019).

On 5 March 2011, an intrusion into the edifice beneath Napau Crater triggered a series of events nearly identical to those of Episode 54 (Orr *et al*. 2015). This intrusion caused subsidence at both Pu'U 'O'o and the summit caldera, drawing magma from these sources to contribute to the volume of the new intrusion, resulting in a short (five day) eruptive episode from a ~1 km-long fissure system at the same weakened area within the ERZ where Episode 54 erupted (Fig. 1; Orr *et al*. 2015). Mirroring the 1997 eruptive sequence, a 16.5-day pause in eruptive activity occurred as the Pu'U 'O'o reservoir refilled, followed by intermittent eruptions and re-equilibration of the magmatic system by December 2011 (Orr *et al.* 2015). Steady-state effusive activity established and fed a series of lava tubes that drained to the ocean (Orr *et al*. 2015). On 19 January 2013, a new vent opened at Pu'U 'O'o that would siphon off the lava tubes' magma supply until ocean entry abated in November 2013; this new vent redirected lava to the northeast towards populated areas of the Big Island (Orr *et al*. 2015; Poland *et al.* 2016), encroaching on residential areas in the Puna District of Hawai'i from late June 2014 through late May 2015 and resulted in the destruction of one home in the region (Poland *et al*. 2016; Global Volcanism Program, 2016). New vent formation on the flanks of Pu'U 'O'o in May 2016 interrupted within-crater activity and produced a rapidly-moving lava flow to the northeast of Pu'U 'O'o's cone, and another to the southeast that reached the ocean on 26 July 2016 (Global Volcanism Program, 2016). The northeasterly-directed lava flow had become inactive by 8 June 2016, but the remaining active lava flow would continue to erupt effusively for the remainder of the Pu'U 'O'o eruption (Global Volcanism Program, 2016). In

March 2018, the geodetic record suggests the onset of magma accumulation beneath Pu'U 'O'o, increasing magmatic overpressure (Neal *et al*. 2019; Geshi *et al.* 2020) within the middle- to upper-ERZ so much that both the Pu'U 'O'o and the Halema'uma'u lava lakes overflowed (Neal *et al*. 2019). The ~35-year-long Pu'U 'O'o eruption ended with the sudden collapse of its crater floor on 30 April 2018, when the increase in magmatic overpressure triggered an intrusive event, partially draining the summit and entirely draining the Pu'U 'O'o magma reservoirs and allowing that magma to continue down-rift to the lower ERZ, where it erupted in the populated Leilani Estates subdivision—without loss of life (Neal *et al*. 2019). Approximately 20 km down-rift of Pu'U 'O'o, lava began erupting from a new series of fissures in the Leilani Estates subdivision on 3 May 2018 (Neal *et al.* 2019; Patrick *et al*. 2020); by the end of the month, twenty-four fissures had opened and eruptive activity was primarily centered at Fissure 8 (Gansecki *et al.* 2019; Patrick *et al*. 2020). A lava lake that had persisted in the Kilauea Summit caldera since 2008 began to withdraw on 2 May 2018 as magma migrated down the rift zone (Anderson *et al.* 2019; Patrick *et al.* 2020). Slippage occurred along Kilauea's decollement on 4 May 2018, producing a Mw 6.9 earthquake and causing further retreat of the lava lake from the summit caldera, which had drained into the void within a week (Anderson *et al.* 2019). Collapse of the Kilauea summit began on 16 May 2018, but continued sporadically through early August, ending a decade of concurrent activity at the summit caldera and along the ERZ (Anderson *et al*. 2019; Patrick *et al*. 2020).

Groundwater recharge of the edifice following the disappearance of the Halema'uma'u lava lake formed a small crater lake that appeared on 26 July 2019 (Ingebritsen *et al.* 2021), growing to a maximum depth of ~50 m on 20 December 2020, when a new eruption at the Kilauea Summit evaporated the water lake and replaced it with a lava lake in a matter of days

(USGS). The last active surface lava at Halema'uma'u was observed on 25 May 2021, and as of the writing of this manuscript, no new eruptive activity has occurred (USGS).

2. A Detailed Look at the Events Surrounding Episode 54

Prior to the events culminating in the Episode 54 eruption, Kilauea Volcano had been erupting effusively from the Pu'U 'O'o cone/ocean entry for four years (Wright & Klein 2014). At 0445 UTC on 30 January 1997 (18:45 Honolulu Time, 29 January 1997), a series of volcanic tremors were accompanied by slippage of the south flank decollement and extension across the East Rift Zone in the vicinity of Napau Crater (Owen *et al.* 2000; Segall *et al.* 2001). Within an hour, "a loud whooshing roar" (Harris *et al.* 1997) accompanied ground deflation measured at both Makaopuhi Crater and the Kilauea summit—consistent with the removal of magma from those sources—and the disappearance of lava from Pu'U 'O'o (Harris *et al.* 1997; Owen *et al.* 2000). Geodetic measurements indicate that rift failure initiated a fracture that rapidly grew, filling with magma from storage reservoirs both up- and down-rift (Owen *et al.* 2000; Segall *et al.* 2001; Desmarias & Segall 2007). This passive intrusion intersected the ground surface at ~1240 UTC (~2:40 a.m. HST, 30 January 1997), initiating Episode 54, a 22-hour-long fissure eruption up-rift of Pu'U 'O'o, at Napau Crater (Fig. 1b), which ended at 1033 UTC (12:33 a.m. HST, 31 January 1997 (Harris *et al.* 1997). After a 24-day hiatus in activity, a small lava pond appeared within Pu'U 'O'o, signaling that Kilauea's plumbing system was returning to its previous steady state and also marking the start of Episode 55 (Harris *et al.*, 1997; Owen *et al.* 2000; Thornber *et al.* 2003a). The lava lake refilled for a period of 32 days, and sporadic outbreaks of lava from the flanks of Pu'U 'O'o began on 28 March 1997 (Thornber *et al.* 2003a). Eruptive activity continued, reaching steady-state effusive activity in August 1997 (Thornber *et al.* 2003a). These physical events

are geochemically distinct, as lavas erupted during this time period became progressively more and more mafic, peaking at 9.25 wt.% MgO, before settling into steady-state eruptive activity for a decade (Fig. 2; Thornber *et al.* 2003a).

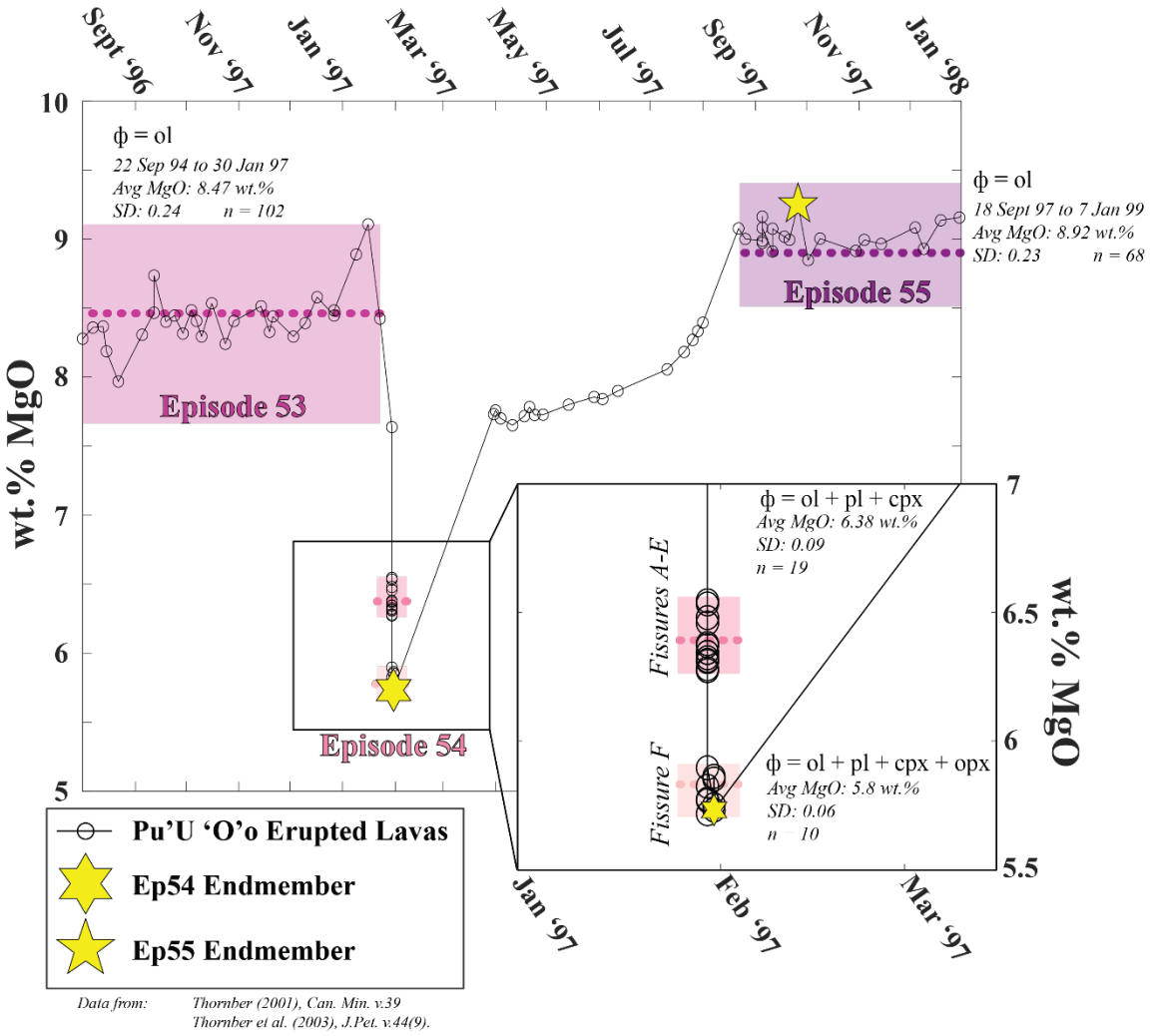

Figure 2. Chemical evolution of lavas erupted immediately preceding, during, and after the Episode 54 event. Compositional and mineralogical data from Thornber (2001) and Thornber *et al.* (2003a). Shaded areas note the maximum and minimum extent of chemical variations within different groups of lavas, with the dashed line representing the average composition for that group.

Erupted lavas of Episode 54 are unusual in that their composition became *much* less magnesian over the course of the eruptive sequence, with terminal lavas reaching >51.25 wt.% SiO_2 and <5.75 wt.% MgO (Fig. 2; Thornber *et al.* 2003a, 2003b). Prior to Ep 54, Ep 53 lavas

(22 September 1994 to 30 January 1997) were significantly more mafic, averaging ~8.47 wt.% MgO (Fig. 2); Pu'U 'O'o lavas returned to a high wt.% MgO early during Episode 55, reaching a maximum of 9.25 wt.% MgO just six months after lava returned to Pu'U 'O'o. Petrologic and geochemical evidence suggests that the low-wt.% MgO lavas erupted during Episode 54 were a result of mixing between magmas that normally occupied the Kilauean magma storage system and one (or more) previously-intruded, differentiated rift magma(s) (Garcia *et al.* 2000; Thornber *et al.* 2003a; Thornber *et al.* 2015). Considering the likely geometry of the inferred dike complex underlying Kilauea (Walker 1986; Cervelli *et al*. 2002; Wallace & Anderson 1998) and the location of dikes recently emplaced in and around Napau Crater (Fig. 1), it is not unreasonable to imagine that one dike could intrude into another.

C. The Magma Chamber Simulator

Phase-equilibria models constructed in this study were done using the Magma Chamber Simulator (MCS; Bohrson *et al.* 2014, 2020). MCS is a thermodynamic model for computing phase equilibria, trace element, and isotope systematics in open systems undergoing concurrent or serial fractional crystallization (FC), assimilation of partial melts (A), digestion of stoped blocks (S), and/or magma mixing via magma replenishment/recharge (R). The MCS code, including documentation, examples, and instructional videos are available at http://mcs.geol.ucsb.edu (open access). The phase equilibria engine incorporated within the MCS software is powered by Rhyolite-MELTS (Gualda et al., 2012; Ghiorso & Gualda, 2015). Symbols used in the text for MCS calculations are provided in Table 1.

This study uses MCS to determine the source identity and thermodynamic state of the mixing endmembers involved in Episode 54 eruptions. We propose that MCS can be used as a tool to aid in petrologic monitoring of ongoing eruptions by demonstrating its usefulness in

modeling past eruptions. Lavas erupted during Episode 54 were "variably choked with ~3 mm aggregates of pl, cpx and ol…." (Thornber 2001) and are "~20% to 50% crystalline… contain[ing] an assortment of rounded and angular phenocryst fragments that includes… pyroxene and plagioclase in addition to… olivine phenocrysts" (Thornber 2001), indicating the presence of a highly-crystalline mixing endmember in addition to the near-liquidus 'olivine-control' magmas that typically occupy the Kilauean magma storage and transport system (Thornber *et al.* 2003a; Orr 2014; Gansecki *et al*. 2019). Here we build mixing Recharge-Fractional Crystallization (RFC) models simulating 'olivine-control' Kilauean magmas mixing with a more evolved, partially-crystalline, ol+cpx+plag-bearing rift-stored magma, triggering the onset of Episode 54. Using MCS, the primary goal of this study is to identify the composition and thermodynamic state of the stored magma body responsible for the presence of evolved melts and glomeroxenocrystic clots within Episode 54 lavas. This is accomplished by comparing mineral assemblages and compositions *computed* using phase equilibria models to *observed* mineral compositions and assemblages from Episode 54 eruptive products (Thornber 2001; Thornber *et al.* 2003a). As our petrogenetic model provides likely compositions and proportions for each mixing endmember as inferred from previous geodetic (Owen *et al.* 2000; Segall 2001; Desmarias & Segall 2008) and geochemical (Jackson *et al.* 1975; Thornber *et al.* 2003a) studies, a secondary goal of this research is to determine if a self-consistent petrogenetic model of Episodes 53-55 is also consistent with geodetically-constrained volume displacements (Owen *et al.* 2000; Segall 2001; Desmarias & Segall 2008).

Table 1. Input Parameters for the Magma Chamber Simulator (Bohrson *et al.* 2014; Bohrson *et al.* 2020)

Input Parameters for Composite System	
Pressure:	P (bars)
fO_2 constraint	fO_2 buffer or initial Fe^{2+}/Fe^{3+}
Temperature decrement to subsystem M during approach towards T_{end}:	ΔT (°C)
Desired final temperature for end of MCS simulation:	T_{end} (°C)
M subsystem melt temperature for *j*th recharge event:	T_1^M, T_2^M, etc.
Ratio of mass of mafic recharge event to initial mass of rift-stored magma body:	M_j^{MME} / M_0^{Rmagma}

Magma body & Recharge magma subsystem inputs for MCS Simulations				
Subsystem	Initial bulk major oxide, trace element, and isotopic composition (for *i* components)	Temperature	Distribution Coefficient	Mass
Magma body (M)	X_0^M	initial T of subsystem T_0^M	D for each component & mineral phase	initial mass of subsystem (100% melt), M_0^M
Recharge, *j* events (R_j)	$X_{0,j}^R$	T_j^R	D for each component & mineral phase	mass of *j*th recharge increment, M_j^R

D. Volume Estimates of Episode 54 Mixing Endmembers

The events surrounding Episode 54 were captured in detail by a continuous Global Positioning System (GPS) network previously installed on Kilauea volcano (Owen *et al.* 2000; Segall *et al.* 2001). Seismic tremors occurred for ~8 hours preceding eruption onset, accompanied by drainback of Pu'U 'O'o's magma reservoir, deflation of the summit caldera, and seismic activity underneath Makaopuhi Crater—indicating the migration of magma from these three areas (Owen *et al.* 2000; Thornber *et al.* 2003a). Over the ~6-hour period prior to the first fissure opening, extension within the southeastern flank of Kilauea's edifice created a "void" space, allowing a passive intrusion to form in a weakened area of the ERZ beneath Napau Crater (Owen *et al.* 2000; Thornber *et al.* 2003a; Desmarais & Segall, 2007). By the conclusion of this eruptive episode, approximately 23 Mm^3 of magma had accumulated beneath Napau Crater, forming a roughly planar body that extended 5.15 km in length, 1.96 m in width, and ~2.24 km in depth (dipping so that the base of the intrusion is at ~2.4 km depth; see also Plate 2 in Owen *et al.* 2000).

Point-source "Mogi-style" models developed by Owen *et al*. (2000) and Segall *et al.* (2001) suggest the Episode 54 intrusion was sourced from four reservoirs: (1) 1.50 Mm^3 of magma from the Kilauea Summit reservoir; (2) 1.20 Mm^3 of magma from a reservoir underlying Makaopuhi Crater; (3) 12.7 Mm^3 of magma representing drain-back from the Pu'U 'O'o lava lake; and (4) a cooler, triply-saturated (ol+cpx+plag) magma of unknown mass that had previously intruded into the rift zone (rift-stored magma). This model was further refined by Desmarais & Segall (2007), who later provided revised estimates of intrusion along strike and down-dip lengths to 5.3 km and 2.7 km, respectively, with an additional 0.08 m of post-intrusion opening towards the base of the dike and transient deformation continuing for ~6

months following the Episode 54 eruption. These estimates coincide with the findings of Segall *et al.* (2001), who demonstrate that two-thirds of the final dike volume had been intruded at the time of eruption, and that further volume accumulation continued after the Episode 54 eruption, albeit at a lower rate. From these models, we calculate that the volume of the intrusion at the time of the Episode 54 eruption was 22.91 Mm^3, and that the total final volume of the intrusion was 29.19 Mm^3, in good agreement with transient deformation models (Segall *et al.* 2001; Desmarais & Segall, 2007). We calculated the volume of Owen *et al.*'s unknown fourth component – an already present, crystallized, and fractionated hypabyssal intrusion left over from a prior eruption (Thornber 2001; Thornber *et al.* 2003a) to be 7.51 Mm^3 by mass closure. The parameters obtained from the literature and the results of our volume calculations are presented in Table 2. For purposes of internal consistency, volumes quoted above are given to two decimal places; however, uncertainties are of the same order of magnitude as those estimated by Owen *et al.* (2000). For the petrogenetic modeling, however, relative volumes are more important than absolute values.

Table 2. Dike and volume estimates for the Episode 54 intrusive event

[1]Along-strike Dike Length (m):	5,150
[1]Vertical Dike Width (m):	2,240
[1]Horizontal Dike Opening (m):	1.96
[1]Eruptive Volume Episode 54 (Mm^3):	0.30
[1]Calculated Intrusion Volume at Time of Eruption (Mm^3):	**22.91**
[1,2]Contribution from Pu'U 'O'o (Mm^3):	12.70
[1,2]Contribution from Makaopuhi (Mm^3):	1.20
[1,2]Contribution from Kilauea Summit (Mm^3):	1.50
Calculated Volume of Gabbroic Rift-Stored Pod (Mm^3):	**7.51**
Calculated Post-Eruptive Transient Volume Accumulation (Mm^3):	6.58
[2]Final Calculated Intrusion Volume (Mm^3):	**29.49**

[1]Owen et al. (2000)
[2]Desmarais & Segall (2007)

Table 3. Major oxide compositions used in Episode 54 mixing models

	Kilauea Summit Component[1]	Makaopuhi Crater Component[2]	Pu'U 'O'o Drainback (Bulk Rock)[3]	Mixed Mafic Endmember (P = Bulk)[4]	Ep 55 Mafic Recharge Magma[6]
SiO_2:	50.61	50.06	51.01	50.90	50.39
TiO_2:	2.40	2.62	2.44	2.45	2.31
Al_2O_3:	13.19	13.19	13.43	13.39	13.05
FeO_{tot}:	11.5	11.28	11.40	11.40	11.51
MgO:	8.47	8.49	7.64	7.79	9.25
MnO:	0.17	0.17	0.17	0.17	0.17
CaO:	10.83	10.73	11.06	11.01	10.57
Na_2O:	2.15	2.28	2.16	2.17	2.10
K_2O:	0.42	0.53	0.43	0.44	0.39
P_2O_5:	0.26	0.27	0.25	0.25	0.25
H_2O:	0.30	0.20	0.30	0.29	0.70
CO_2:	0.02	0.01	0.02	0.02	0.02

[1]Episode 53 steady-state average composition, Table 1 in Thornber *et al*. (2003a). Wt.% H_2O & wt.% CO_2 imputed from values given in Mangan *et al.* (2014).
[2]Makaopuhi Crater Pumice M26, erupted 15 March 1965, Table 6 in Wright *et al.* (1968).
[3]Episode 53 KE53-1844, erupted 30 January 1997, in Thornber *et al*. (2003b). Wt.% H_2O & wt.% CO_2 imputed from values given in Mangan *et al.* (2014).
[4]Calculated MME from mixing Components 1-3.
[5]Episode 53 KE53-1846, erupted 29 January 1997, in Thornber *et al*. (2003b). Wt.% H_2O & wt.% CO_2 imputed from values given in Mangan *et al.* (2014).
[6]Episode 55 KE55-1924, erupted September 26, 1997, in Thornber *et al*. (2003b). Wt.% H_2O & wt.% CO_2 imputed from values given in Wallace & Anderson (1998) and Mangan *et al.* (2014).

E. Construction of the Mixed Mafic Endmember (MME) Magma

The geodetic data (Owen *et al.* 2000; Segall *et al.* 2001; Desmarias & Segall 2008) support a magma mixing model for the Episode 54 lavas wherein separate batches of mafic magma from the Kilauea Summit reservoir, a reservoir below Makaopuhi Crater, and drain-back from Pu'U 'O'o interacted with an arrested and partially crystallized intrusive body (rift stored magma). For our petrogenetic modeling, we used published geochemical data to estimate the major oxide composition of each source of mafic magma, then combined them to create a single "Mixed Mafic Endmember" (MME) composition (Table 3; Fig. 3) in proportions constrained by the geodetic relations. The MME was then mixed with a modeled composition of the rift stored magma in an attempt to recreate the composition of the Episode 54 lavas.

As magmas from Kilauea's summit reservoir are reasonably homogenized prior to their arrival and subsequent eruption at the East Rift Zone (Edmonds *et al.* 2015), the average steady-state composition of Episode 53 lavas erupted from Pu'U 'O'o (Thornber *et al.* 2003a) was used to represent the Kilauea summit component of the MME. A pumice (similar in composition to the Kilauea Summit component) from the 1968 Makaopuhi Crater eruption (Wright *et al.* 1968) was used for magmas derived from that area. Finally, the largest ingredient (~83%) in the MME comes from magmas present in the Pu'U 'O'o conduit & underlying reservoir (Harris *et al*. 1997; Owen *et al.* 2000; Thornber *et al.* 2003a) immediately preceding the onset of Episode 54, modeled using the last-erupted bulk lava sample from Episode 53 (KE53-1844; Thornber *et al.* 2003b). Using compositions presented in Table 3, coupled with proportions constrained by geodetic measurements (see Table 2), the MME composition was generated by linear mixing and renormalized to 100 wt.% (Table 3). Stability of the MME composition was verified by constructing a FC model using MCS. Unless

otherwise reported, FeO/FeO_{tot} was initially set at a value corresponding to fO_2 = QFM-1, and all phase equilibria models run at P = 0.5 kbar and 0.5 wt.% H_2O_i without restricting fO_2 along a buffer (Appendix A). Although there is some uncertainty in the exact composition and volumes of the mixing components, the composition of the MME is dominated by the large volume drain-back from Pu'U 'O'o'—suggested by geodetic measurements to provide the largest volume of melt (Owen *et al.* 2000)—*and* the composition of the three components of the MME are relatively similar (Wright *et al.* 1968; Thornber *et al.* 2003a, 2003b). As a result, although our MME is constrained by geodetic model results (Owen *et al.* 2000; Desmarais & Segall, 2008), the assumed composition is relatively insensitive to the exact endmember compositions and volumes.

F. Identification of the More Evolved, Rift-Stored Endmember

Prior to the Episode 54 eruption, Kilauea Volcano steadily effused near-liquidus, ol-bearing, high (~8.47 wt.%) MgO basaltic lavas for almost a decade (Thornber *et al.* 2003a, 2003b). Episode 54 lavas are markedly different from those lavas erupted either before or after 30-31 January 1997: the more evolved lavas (avg. MgO = 6.38 wt.%; Fig. 2) erupted from Fissures A-E contain complexly zoned phenocrysts and microphenocrysts of ol, cpx, and pl, occurring either as individual crystals or as glomerocrysts containing <80% interstitial glass; Fissure F lavas are petrographically similar to Fissure A-E lavas, but are even less magnesian (avg. MgO = 5.8 wt.%; Fig. 2) and bear opx, either as scarce, reversely-zoned opx crystals or as exsolution lamellae within augite (Thornber 2001; Thornber *et al.* 2003a). The complex mixing history preserved in Episode 54 eruptive products was extensively documented by Thornber *et al.* (2003a), who suggested that a partially-crystalline and evolved magma body bearing cpx, pl, and metastable opx was rapidly reheated by and mixed with higher-*T* less

viscous mafic magmas, then erupted over a limited range of temperatures. Although there is disagreement about the identity of the more evolved magmas required to produce Episode 54 bulk rock and mineral compositions (Garcia *et al.* 2000; Thornber *et al.* 2003a), there is unanimous consensus that mixing of more typical, mafic Kilauean magmas (olivine-control; our MME) with a crystalline, less magnesian, and multiply-saturated magma *must* have occurred.

Previous work by Thornber *et al.* (2003a) suggests that the evolved, rift-stored mixing component was derived from nearly 40% fractionation of a composition equivalent to an opx-bearing lava erupted from the Lower East Rift Zone in 1955. After reviewing available literature and examining fissure locations in and around Napau Crater (Fig. 1; Thornber *et al.* 2003a; Thornber *et al.* 2015), we identified four potential candidates for the arrested dike composition: N68-4 and N68-8, erupted in October 1968 (Jackson *et al.* 1975), and KE1-1 and KE1-49, erupted at the very beginning of the Pu'U 'O'o eruption (Thornber *et al.* 2003a, 2003b). To constrain potential compositions of the evolved dike at the time of mixing, we first used MELTS to model the evolution of dike liquids as they fractionally crystallize (ornamented dashed lines in Fig. 3, Appendix A). Lavas erupted from Fissures A-E and Fissure F are compositionally distinct (Figs. 2-4), suggesting that the mafic endmember mixed with two different compositions—one more evolved (Fissure F) than the other (Fissures A-E)—as represented by the dashed green mixing lines (l^{mix}) in Figure 3a. Geochemical differences between the two sample populations, coupled with the paucity of Fe-Ti oxides in Episode 54 lavas, place an upper fractionation limit on the evolution of the arrested dike composition at around 4.5 wt.% MgO, where the FC models reach ilmenite saturation. Thus, the evolved endmember must have had ≥4.5 wt.% MgO. Ol, pyx and pl compositions are best

reproduced by fractionation of a magma with an initial bulk composition equivalent to N68-4 (Fig. 3, see also Appendix A). This composition is more similar to lavas erupted from Kilauea Volcano during periods of steady-state activity than the other dikes examined, implying that N68-4 (Table 2) is likely more representative of the initial bulk composition of the dike at the time of its emplacement than other compositions considered (Table 2). Consequently, dike N68-4 was selected as the best reference LLD (liquid line of descent) for construction of the more evolved, rift-stored endmember.

To estimate compositions of each distinct, rift-stored endmember magma, we constructed two different mixing lines (l^{mix}) by calculating a regression line between the MME composition (green star) and the average composition of lavas from Fissures A-E (AE^{avg}), and another between the MME and the Fissure F average composition (F^{avg}; Fig. 3, Table 3). Each l^{mix} was then projected past its intersection with the LLD (represented by blue asterisks in Fig. 3), as produced by fractionation of the rift-stored magma body. When comparing wt.% MgO vs. wt.% Al_2O_3 for the data set, the geochemical variations depicted in Figure 3 (see also Supplemental Figure A1 for the full suite of bivariate diagrams) illustrate the orthogonal relationships between all LLDs and the two calculated l^{mix} regression lines. The intersection between each l^{mix} and the LLD in MgO-Al_2O_3 space was used to determine the wt.% MgO of the low-MgO mixing endmember magmas required to produce the lava compositions and mineral assemblages of both AE^{avg} and F^{avg} (i.e., how fractionated the rift-stored dike was at the time of mixing). The l^{mix} for AE^{avg} intersects N68-4's LLD at ~5.1 wt.% MgO, and the l^{mix} for F^{avg} intersects at ~3.5 wt.% MgO, as represented by the vertical blue lines in Figure 3. Ideally, each l^{mix} would intersect the LLD for every major element at the same wt.% MgO, but in reality, this is not the case; at no point along any LLD does there appear to be a single

composition that could be used as an evolved endmember to match either AE^{avg} or F^{avg}. This is likely due to the analytical uncertainties in the original analyses of the dike compositions, the geologic uncertainties in the models (e.g., f_{O2}, wt.% H_2O, P), and inherent uncertainties within the phase-equilibria models, which we have quantified in Appendix A.

Although the above method allows us to find the *exact* intersection between an LLD and each l^{mix}, the amount of model uncertainty (Appendix A) affords us the opportunity to 'adjust' the compositions to values that satisfy the requirements of linear mixing, which could then be used as the low-MgO endmembers. Untangling a mixing scenario to identify its endmembers and mixing proportions requires a first-order rule to be followed: because mixing is a linear process, the entire composition of the rock must be made up of identical proportions of the same endmembers (von Engelhardt 1989). We therefore took the approach of defining two best-fit endmember compositions—one falling on the l^{mix} for AE^{avg}, and the other falling on the l^{mix} for F^{avg}—by using the LLD as a reference point for least squares regression. At any given MgO, the l^{mix} predicts a concentration for each major oxide; wt.% MgO was adjusted to that value which minimized the sum of the residuals between predicted wt.% major oxide and the LLD produced by fractionation of N68-4. This was done twice—first by minimizing the squared residual of wt.% MgO, and second by minimizing the sum of squared residuals for all oxides. The singular data point along l^{mix} that satisfies both these requirements is considered to be the most likely low-MgO endmember responsible for forming the hybrid compositions—i.e., we picked a single MgO value that minimized the distance in composition space of the hypothetical endmember from the LLD for dike N68-4 (Figure 4; Table 4). To estimate the degree of fractionation and wt.% H_2O of the low-MgO endmember magma (Table 4), we used the mean and standard deviation of those numerical models constructed to estimate

the uncertainty in geologic parameters (Appendix A). By this method, we find that the stored magma body responsible for the evolved nature of Episode 54 lavas (Table 4) was derived from ~23% (Fissures A–E) to ~35% (Fissure F) fractionation of an intruded magma *very* similar in composition to sample N68-4 (Jackson *et al.* 1975)—a basalt collected from the October 1968 fissure eruption and associated intrusion at Napau Crater. The low H_2O contents of more mafic Kilauean lavas, coupled with the high vesicularity of Episode 54 lavas, suggests the presence of an exsolved fluid phase within the low-MgO endmember, consistent with significant fractionation. We emphasize that although the regressed endmember composition does not fall exactly on the LLD for dike N68-4, it is within (or close to within) estimated geologic and phase-equilibria uncertainties (Appendix A), and that the selected MgO—and therefore degree of fractionation—is constrained by the orthogonal relationship between the LLD and the l^{mix} required by the MME and the composition of the erupted lavas from Fissures A–E and Fissure F.

G. Volume Estimates of Episode 54 Mixing Endmembers

After determining the best-fit endmember compositions needed to reproduce AE^{avg} and F^{avg}, we conducted two series of numerical experiments to constrain the state of the arrested dike at the time of the Episode 54 mixing event. For each of the above-described low-MgO endmembers, equilibrium crystallization of each residual liquid composition was modeled over a range of T that correlates with crystal contents from 20-80% (φ=20-80) for that liquid composition. The mushy, low-MgO endmember was then mixed with the near-liquidus (φ<1) MME; mixing proportions required to reproduce AE^{avg} and F^{avg} (Table 3; Thornber *et al.* 2003a) were determined by linear combination, and are given in Table 4 along with other input parameters for each numerical experiment conducted. The resultant bulk hybridized

magma compositions (Fig. 4) are a good match for average Episode 54 lava compositions (Thornber *et al.* 2003a); MCS results, supplemental figures, and individual MCS output files may be found in Appendix B.

Mineral compositions in equilibrium with the hybrid lavas produced in the RFC models can be compared with observed compositions from erupted Episode 54 lavas to estimate the crystallinity of the low-MgO magma at the time of the mixing event. Thornber (2001) and Thornber *et al.* (2003a) report that Episode 54 lavas are highly vesiculated and relatively aphyric, containing <5 vol.% phenocrysts of ol, pl, and cpx, in addition to cpx+pl glomerocrysts. Thornber *et al.* (2003a) also report that groundmass crystallinity of Episode 54 lavas varies considerably, with glass making up anywhere between ~1 and ~80 vol.% of the matrix. Additionally, Fissure F lavas contain both rare opx and high-Mg# opx lamellae within cpx phenocrysts, requiring that the low-MgO endmember in this case was two-pyx saturated.

Compositions of ol, cpx, and pl present in lavas erupted from Fissures A-E are best reproduced by those MCS models where the dike is φ=20-50% crystalline at t_{mix} (φ = 20-50; Fig. 5). Although not present in Fissure A-E lavas, MCS predicts opx stability in the A-E low-MgO endmember when it is ≥50% crystalline (Appendix B). Whereas MCS-produced hybrid lavas easily replicate the species and compositions of minerals present in Fissures A-E lavas, pyroxenes produced in the MCS models have consistently lower Mg# than those measured in Fissure F lavas (Fig. 5). Still, calculated MCS pl compositions for Fissure F hybrid lavas match extremely well with measured pl compositions recovered from Fissure F if the low-MgO endmember is φ=30-60% crystalline at t_{mix}, and opx is stable in the MCS-produced low-MgO endmember when it is φ=40-60% crystalline (Fig. 5). MCS-produced hybrid

compositions are saturated in ol, cpx (both low-Ca and high-Ca), and pl when the low-MgO endmember is φ≈40-50% crystalline at t_{mix} (Appendix B).

Table 4. Major oxide compositions of magma and recharge compositions and selected input parameters for Episode 54 mixing models

	Mixed Mafic Endmember (MME)[1]	Dike X[2] to match MME & A-E lavas	Dike X[3] to match MME & F lavas
SiO_2:	50.76	50.64	51.03
TiO_2:	2.45	3.39	4.11
Al_2O_3:	13.35	14.14	13.84
FeO_{tot}:	11.37	11.86	12.37
MgO:	7.76	5.28	4.43
MnO:	0.17	0.17	0.17
CaO:	10.98	9.99	8.80
Na_2O:	2.16	2.75	3.08
K_2O:	0.43	0.72	0.90
P_2O_5:	0.25	0.40	0.51
H_2O:	0.29	0.65	0.76
CO_2:	0.02	0.02	0.02
% fractionated from initial X:	0.03	23.25 ± 3.25	34.93 ± 5.15
f_{mix} low-MgO:	--	0.57 ± 0.01	0.60 ± 0.00
P (kbar):	--	500	100
M^{MME} / $M^{rift\text{-}stored}$:	--	0.75	0.67
T^M (°C):	1181	--	--
ΔT (°C):	5	--	--
20% Xlln T^R (°C):	--	1096	1084
30% Xlln T^R (°C):	--	1087	1076
40% Xlln T^R (°C):	--	1075	1067
50% Xlln T^R (°C):	--	1057	1053
60% Xlln T^R (°C):	--	1031	1036
70% Xlln T^R (°C):	--	994	1012
80% Xlln T^R (°C):	--	948	970
T_{stop} (°C):	900	900	900

[1]Calculated MME from Table 2 renormalized to 100 wt.% in rhyolite-MELTS v1.1.0, with initial Fe^{2+}:Fe^{3+} set at QFM-1 values.
[2]Best-fit felsic endmember to reproduce Fiss A-E lavas, renormalized to 100 wt.% in rhyolite-MELTS v1.1.0, with initial Fe^{2+}:Fe^{3+} set at QFM values.
[3]Best-fit felsic endmember to reproduce Fiss F lavas, renormalized to 100 wt.% in rhyolite-MELTS v1.1.0, with initial Fe^{2+}:Fe^{3+} set at QFM values.

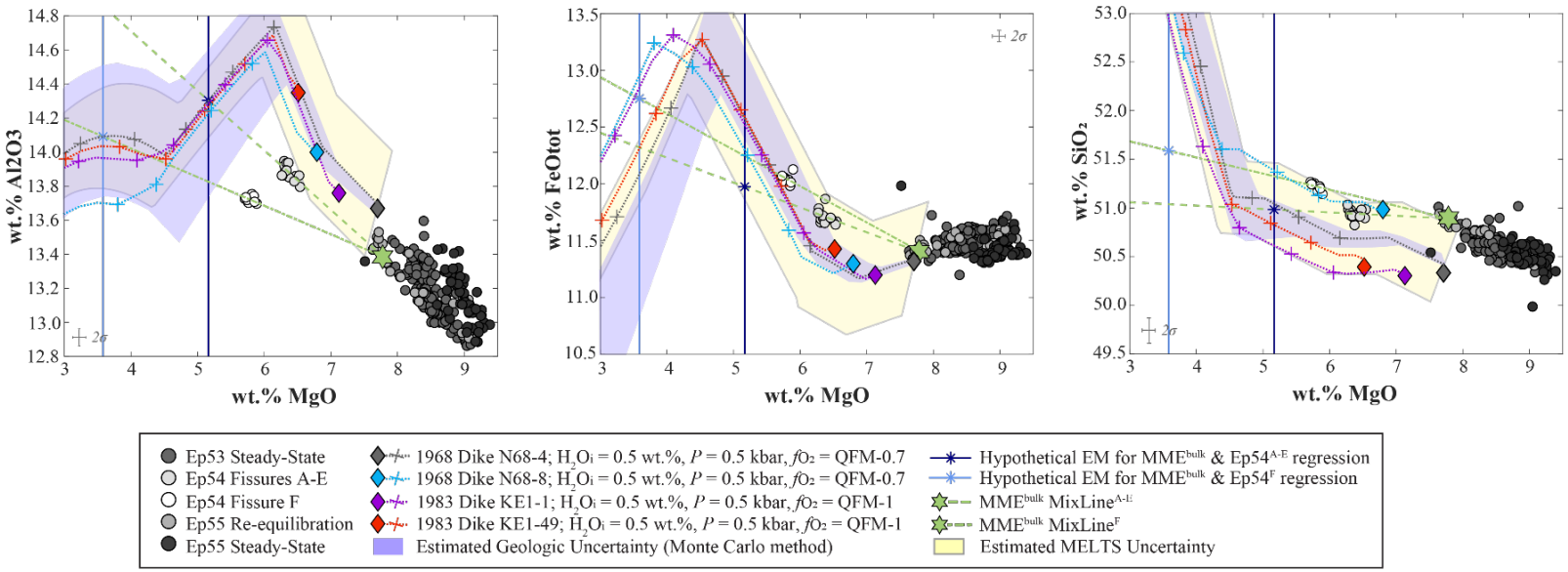

Figure 3. Variations in melt compositions produced by fractional crystallization (FC; Bohrson *et al.* 2014, 2020) models of four candidate low-MgO endmember (arrested dike) compositions. Of the four dikes tested, mineral compositions and modal abundances (a) from Episode 54 lavas are best reproduced by FC of Dike N68-4. Mixing lines (l^{mix}) were constructed by linear regression of the mixed mafic endmember (MME) with measured lava compositions from Fissures A-E and Fissure F, respectively. The wt.% MgO for the low-MgO endmember is determined by the intersection between l^{mix} and the LLD on the Al_2O_3 vs. MgO plot, and wt.% MgO along each l^{mix} is denoted by the blue asterisks and associated blue vertical line.

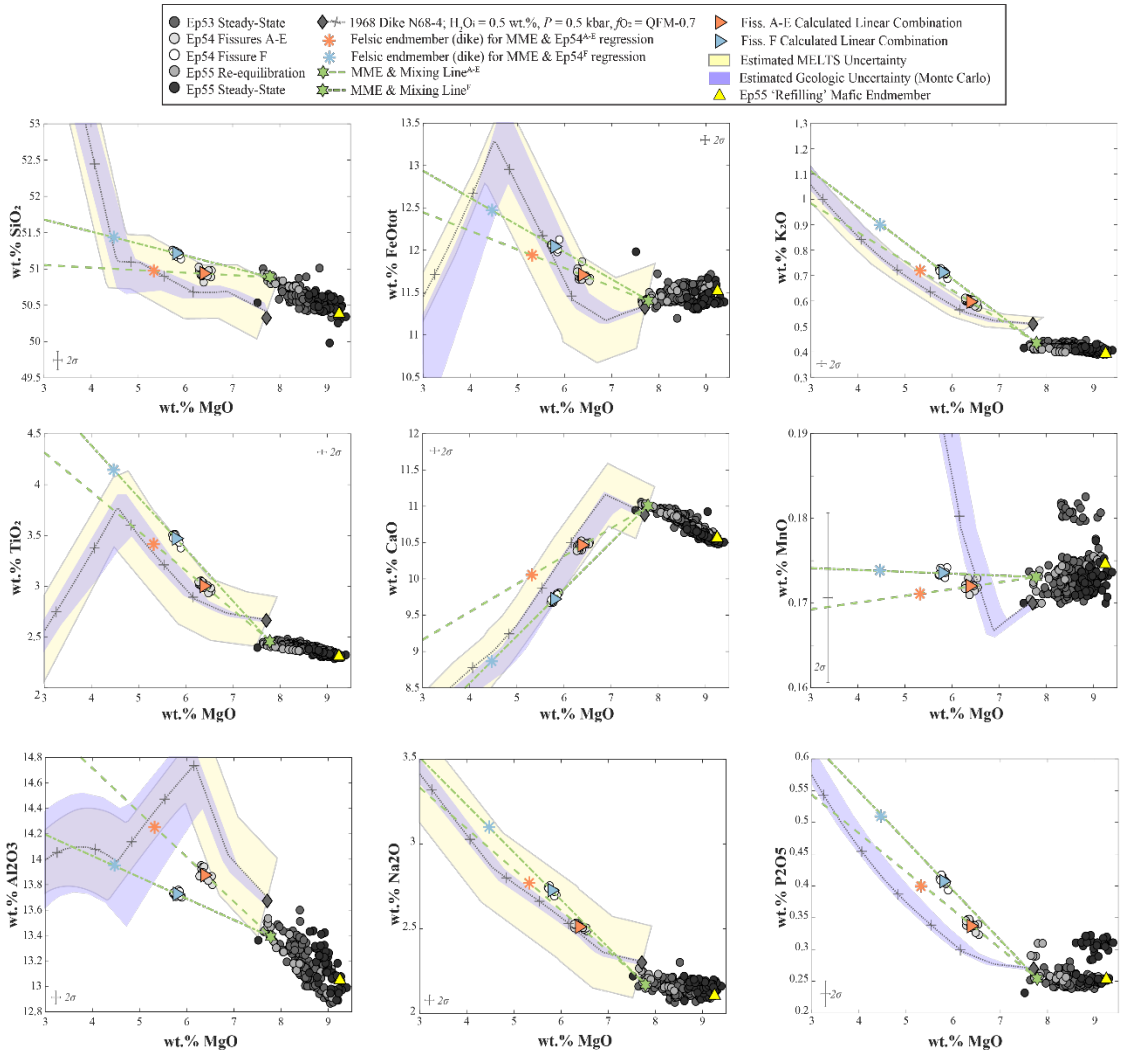

Figure 4. Constructed low-MgO endmember composition (SSR-minimized method) and Episode 54 mixing model results as calculated by linear combination. Note that although the low-MgO endmember compositions do not lie exactly along the liquid line of descent, they are within either analytical, geologic, or model uncertainty, with the exception of K_2O, P_2O_5 and MnO (see Appendix A for further explanation).

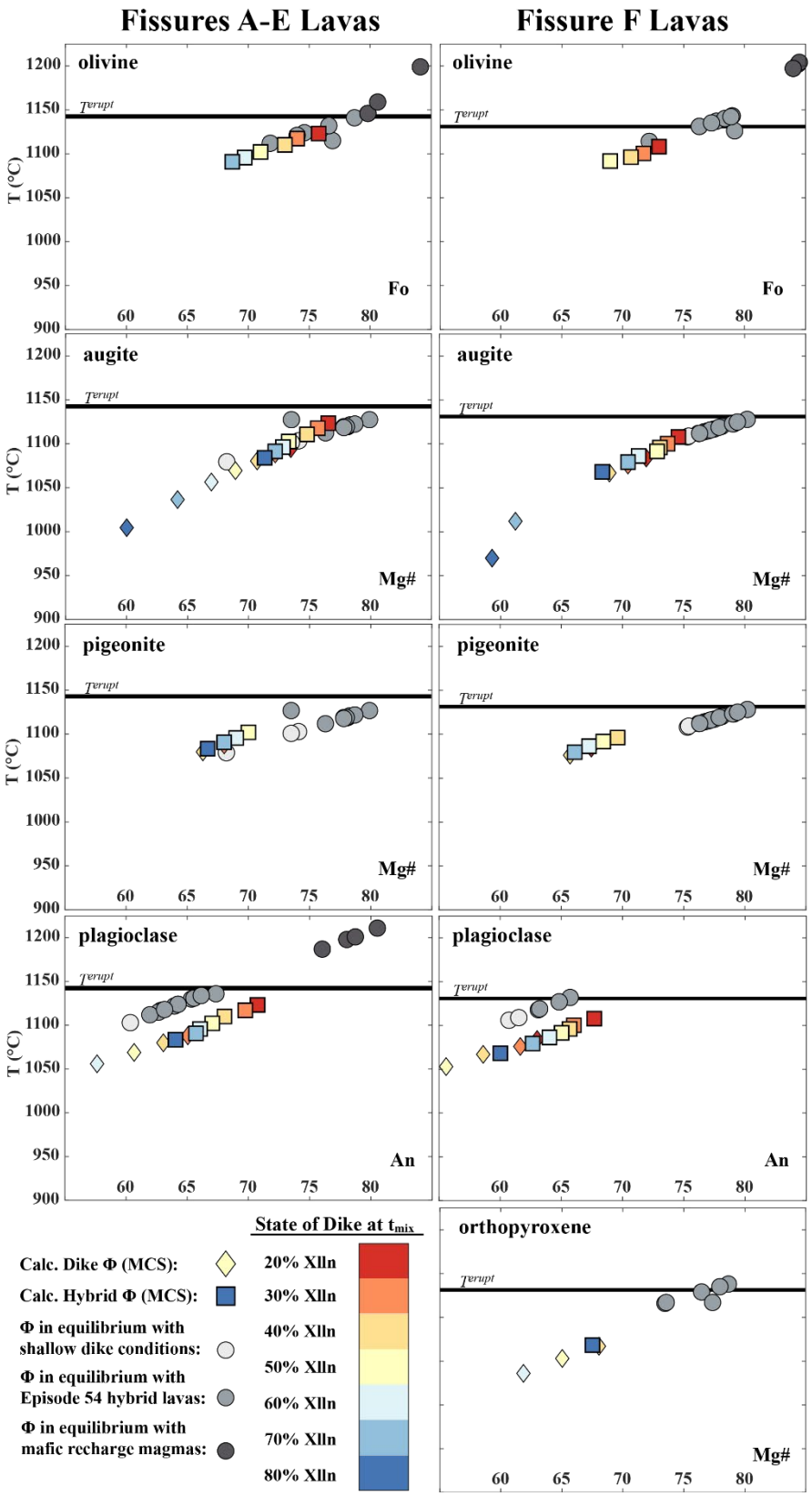

Figure 5. Mineral compositions and crystallization temperatures of phases recovered from Episode 54 lavas (Thornber *et al.* 2003a) compared against phases produced by Magma Chamber Simulator (MCS) mixing models. Symbol colors for MCS-produced phases represent the crystallinity (Φ) of the low-MgO (dike) magma at the time of recharge and hybridization. Minerals recovered from Episode 54 lavas are colored in greyscale according to their source, as proposed by Thornber et al. (2003a).

H. Discussion

Previous studies have addressed the issue of magma mixing in the petrogenesis of Episode 54 eruptive products (Garcia *et al.* 2000; Thornber 2001; Thornber *et al.* 2003a). Fortuitously, the conclusion of the 35-year-long Pu'U 'O'o eruption affords us the opportunity to look at the eruption holistically, in order to find previously unseen patterns that could elucidate further understanding of the Kilauean magmatic system. In addition to reexamining the mixing processes responsible for Episode 54 lava compositions, the current study adds a geodetic and phase-equilibria perspective to the petrogenetic picture. Indeed, the advantage of a phase-equilibria study lies in the ability to compare more than just bulk rock compositions—modal abundance of phases and their compositions can be evaluated in addition to petrologic processes. Here we review the petrologic constraints on the low-MgO endmember based on the modal mineralogy and phase compositions of Episode 54 lavas, and discuss how these results—combined with our MCS modeling—constrain the composition and pre-eruptive state of the rift-stored magma body.

1. Determining the Identity and State of the Shallow, Rift-Stored Magma Body

Decreasing enthalpies of formation dictate the mineral phases and compositions that will be thermodynamically stable as the low-MgO endmember becomes more crystalline (Table 6). Therefore, we can use mineral compositions produced in the MCS forward models to further constrain the pre-eruptive state of the low-MgO intrusion. Because a thermodynamic model (MCS; Bohrson *et al.*, 2020) was used to model disequilibrium processes (the rapid mixing of different magma batches), great care was taken in the interpretation of model results.

Table 5. Mineral assemblages and compositions produced by MCS forward models for Fissure A-E lavas and resultant enthalpies of fusion for each equilibrated mineral assemblage.

MCS Run	Rift-Stored Magma		Phases Present in Rift-Stored Magma	Fo (ol)	Mg (cpx1)	Mg (cpx2)	An (pl)	Mg (opx)	$\Delta f H^0_{dike}$ (kJ/mol)
	Xllnty	T (°C)							
20JulB	19.64	1094	cpx + pl + mt		72.81		66.00		-1214
20JulC	29.15	1088	2cpx + pl + mt + il + fl		71.68	67.84	65.66		-1218
20JulA	39.42	1080	2cpx + pl + mt + il + fl		70.18	65.70	64.00		-1223
20JulD	49.42	1069	opx + cpx + pl + mt + il + fl		68.97		61.62	67.20	-1228
20JulF	58.83	1056	opx + cpx + pl + mt + il + fl		66.38		59.60	64.02	-1232
20JulG	68.87	1036	opx + cpx + pl + mt + il + ap + fl		63.72		55.56	60.00	-1238
20JulH	78.99	1004	opx + cpx + pl + mt + il + ap + fl		60.18		51.52	55.79	-1245
MCS Run	**Hybrid Lavas**		**Phases Present in Hybrid Lavas**	**Fo (ol)**	**Mg (cpx1)**	**Mg (cpx2)**	**An (pl)**	**Mg (opx)**	**$\Delta f H^0_{hyb}$ (kJ/mol)**
	Xllnty	**T (°C)**							
20JulB	7.96	1123.13	ol + cpx + pl + fl	75.76	76.52		70.71		-2814
20JulC	12.31	1117.17	ol + cpx + pl + fl	74.00	75.65		69.70		-2819
20JulA	17.11	1110.17	ol + cpx + pl + fl	73.00	74.78		68.00		-2826
20JulD	22.15	1102.20	ol + 2cpx + pl + fl	71.00	73.28	70.00	67.00		-2832
20JulF	27.95	1095.79	ol + 2cpx + pl + mt + fl	69.70	72.81	69.01	66.00		-2838
20JulG	35.71	1090.85	ol + 2cpx + pl + mt + il + fl	68.69	72.17	68.02	65.66		-2846
20JulH	44.50	1083.52	2cpx + pl + mt + il + fl		71.30	66.67	64.00		-2856

a. State of Low-MgO Endmember as constrained by Fissure A-E forward models

The results of the MCS forward models combined with major element trends demonstrate that a bulk composition produced by ~23% fractionation of a basalt similar to one intruded into the Napau crater region in 1968 (N68-4; Jackson *et al.* 1975) generates a low-MgO endmember magma that reproduces the mineral assemblages and compositions present in lavas erupted from Fissures A-E when mixed with the constructed MME. Mixing proportions are: ~57% low-MgO endmember component and ~43% mafic endmember component (Fig. 4, Table 4), and suggest that this low-MgO endmember was ~50% crystalline immediately preceding the Episode 54 mixing event.

Fissure A-E lavas are triply-saturated, containing ol, cpx, and pl (Fig. 5, see also Thornber *et al.* 2003a). Ol is a stable hybrid phase in the MCS models when the low-MgO endmember is <70% crystalline, and is completely replaced by pigeonite when the crystallinity of the low-MgO endmember increases to 80%, whereas augite remains a stable phase in all MCS models. There are two populations of Fissure A-E ol: a) higher Fo phenocrysts and microphenocrysts in equilibrium with the different mafic magmas sourced for the Episode 54 intrusion (dark gray circles in Fig. 5), and b) lower Fo microphenocrysts and syn-eruptive skeletal crystals and epitaxial overgrowths crystallized from the hybrid lavas (Thornber *et al.* 2003a; lighter gray circles in Fig. 5). Similarly, higher An pl in equilibrium with lavas more mafic than those erupted during Episode 54 were found alongside those with lower An which crystallized from hybrid melts (Thornber *et al.* 2003a). At low-MgO endmember crystallinities up to 50%, our MCS model results reproduce ol and augite compositions in equilibrium with hybrid melts (Fig. 5). For those phase-equilibria models where the low-MgO endmember is ≥40% crystalline, MCS-produced pl compositions overlap those measured in Episode 54 lavas (Fig.

5), but calculated *T* estimates of crystallization are higher for measured crystals than are predicted in our forward models—a disparity which may be accounted for when uncertainty in the geothermometry estimates (Thornber *et al.* 2003b), the MCS forward models (Appendix A), and the intrinsic disequilibrium nature of a rapid mixing event are considered. An upper limit of 50% crystallinity is further supported by the absence of Fe-Ti oxides or opx in episode 54 lavas (Thornber *et al.* 2003a); Fe-Ti oxides are produced as stable MCS hybrid phases for those models where the low-MgO endmember is ≥60% crystalline, and opx is stable in the low-MgO endmember if it is ≥50% crystalline. The lack of these phases in erupted lavas could be due to sampling bias, and so the trace amounts of opx in the modeled low-MgO endmember at φ=50% are geologically plausible—but, it should be considered that disequilibrium textures and mineral compositions may not necessarily be reflected in the results of an equilibrium model.

Finally, we can use the compositions of phases that crystallize from the low-MgO endmember in the MCS models prior to mixing to further constrain the magmas' thermodynamic state immediately preceding the mixing event. Cpx xenocrysts found in Fissure A-E lavas (Thornber *et al.* 2003a) can be reproduced by equilibrium crystallization of the low-MgO endmember over a range of ~1094-1056˚C (Fig. 5), correlating with φ = 20-50%. Further, measured hybrid pl from Fissure A-E lavas lie roughly along a mixing trend between a recovered An_{61} xenocryst and a measured An_{81} pl sourced from mafic recharge magmas (Fig. 5). Equilibrium crystallization of the low-MgO endmember at T=1069˚C (φ=50) reproduces An_{61} pl and, although estimates of crystallization *T* are higher than our MCS model results, pl compositions in all our Fissure A-E models mimic this same mixing

trend (Fig. 5). These additional constraints reinforce our finding that, prior to 29 January, 1997, the rift-stored magma body was roughly 40-50% crystalline.

b. State of Low-MgO Endmember as constrained by Fissure F forward models

Results of the MCS forward models demonstrate that a bulk composition produced by ~35% fractionation of the same initial basaltic intrusion (N68-4; Jackson *et al.* 1975) used to generate the Fissure A-E low-MgO endmember can also generate a low-MgO endmember magma that reasonably reproduces the mineral assemblages and compositions present in Fissure F lavas when mixed with the constructed mafic endmember. In this case, the hybrid magma is ~60% low-MgO endmember component and ~40% mafic endmember component. Mineral compositions produced in the MCS forward models further constrain the state of the evolved intrusion that mixed to form Fissure F lavas, and suggest that this low-MgO endmember was ~40% crystalline immediately preceding the Episode 54 mixing event.

Like the lavas that preceded them, Fissure F lavas are triply-saturated, bearing equilibrium ol, cpx, and pl. Ol is a stable hybrid phase in the MCS models when the low-MgO endmember is ≤50% crystalline at the time of mixing, pigeonite is present in hybrid lavas for those MCS models where the low-MgO endmember is 40-70% crystalline, and opx can only be produced in MCS as a hybrid phase when the low-MgO endmember is >70% crystalline (Fig. 5, Table 5). Ol with >Fo_{80} are sourced from mafic recharge magmas (Thornber *et al.* 2003b), and so we do not expect them to be equilibrium phases in our hybrid lavas. The least fayalitic ol measured in Fissure F lavas can be recreated in our lower-crystallinity (φ=20-30) MCS models, but the higher-Fo hybrid ol population present in Fissure F lavas was not reproducible in our forward models (Fig. 5). Correspondingly, both opx and cpx compositions produced in the Fissure F mixing models have lower Mg# than measured pyroxenes from hybrid Episode

54 lavas (Thornber *et al.* 2003a), and we address these compositional disparities later on in this section. Considering the same caveats as we did for our Fissure A-E model results, geothermometry estimates of crystallization *T* (Thornber *et al.* 2003b) for pl present in Fissure F lavas are higher than those produced in our MCS models (Fig. 5), and MCS-produced pl compositions overlap with measured Fissure F pl compositions when the low-MgO endmember in our MCS models is 30-70% crystalline. Although Fe-Ti oxides are not present in Episode 54 lavas, they appear as hybrid phases in our MCS models, increasing from <2 vol.% when the low-MgO endmember is 40% crystalline to ~16 vol.% at the maximum modeled crystallinity (φ=80). As myriad factors contribute to the saturation of a phase in rhyolite-MELTS, minor amounts (<2 vol.%) of oxides present in our model results are considered within the allowable geologic uncertainties.

As with Fissure A-E lavas, we place additional constraints upon the thermodynamic state of the rift-stored magma body tapped to produce Fissure F lavas by comparing the compositions of phases in equilibrium with the Fissure F low-MgO endmember to their measured compositions. Equilibrium crystallization of the low-MgO endmember produces a mineral assemblage of augite + pigeonite + pl at T≥1076˚C (corresponding with φ≤30); at T=1067-1036˚C (φ=40-60), pigeonite is replaced by opx, but returns at T≤1012˚C (φ≥70). Opx lamellae are present within some Fissure F cpx crystals, and a lone opx xenocryst was reported in Fissure F lavas by Thornber *et al.* (2003a). Although none of the forward models produce either opx or pigeonite with high Mg# comparable to those present in measured lavas, the forward models *do* produce opx as an equilibrium hybrid phase when the low-MgO endmember is ~80% crystalline (Fig. 5). More likely, however, are the results of the forward models where opx is a stable phase in the low-MgO endmember—this occurs during

equilibrium crystallization of this endmember over a range of T=1067-1036˚C, corresponding to φ=40-60% (Fig. 5). Pl compositions overlap when the low-MgO endmember is 30-70% crystalline (T=1076-1012˚C), and crystallization temperatures for our MCS-produced pl are again systematically lower than those calculated *T* estimates for Fissure F pl (Fig. 5). Our best estimate of the state of the low-MgO endmember required to reproduce F^{avg} at the time of mixing is therefore φ ≈ 40, where opx is a stable phase in the low-MgO endmember at the time of mixing, and the observed common mineral assemblage of ol + cpx + pl is stable in modeled hybrid lavas.

Table 6. Calculated bulk mamga densities for hypothetical felsic endmember compositions at individual state points (P = 0.1 kbar).

Felsic mixing endmember for Fissures A-E (~23% fractionated from initial intrusion)			
Dike Crystallinity (%)	**φ assemblage**	**Dike T (°C)**	**ρ bulk magma (g/cm^3)**
19.64	ol + cpx + pl + mt + fl	1094	2.44
29.15	2cpx + pl + mt + il + fl	1088	2.37
39.42	2cpx + pl + mt + il + fl	1080	2.23
49.42	opx + cpx + pl + mt + il + fl	1069	2.09
58.83	opx + cpx + pl + mt + il + fl	1056	1.96
68.87	opx + cpx + pl + mt + il + fl	1036	1.84
78.99	opx + cpx + pl + mt + il + whit + fl	1004	1.71
Felsic mixing endmember for Fissure F (~35% fractionated from initial intrusion)			
Dike Crystallinity (%)	**φ assemblage**	**Dike T (°C)**	**ρ bulk magma (g/cm^3)**
19.74	2cpx + pl + mt + il + fl	1084	2.22
30.02	2cpx + pl + mt + il + fl	1076	2.06
38.39	opx + cpx + pl + mt + il + fl	1067	1.94
49.37	opx + cpx + pl + mt + il + fl	1053	1.79
59.11	opx + cpx + pl + mt + il + fl	1036	1.67
69.82	2cpx + pl + mt + il + fl	1012	1.56
79.99	2cpx + pl + mt + il + fl	970	1.48

The Mg# of ferromagnesian phases produced in our MCS models is systematically lower than those measured in Fissure F lavas. Extensive exploratory modeling (Appendix A) was done to select the best intensive parameters for our initial phase-equilibria models (P=0.5 kbar and f_{O2}=QFM-0.7). As our MCS runs are a bifurcated process, modeling of magma mixing was able to be done at lower pressures (P=0.1 kbar) under more oxidized conditions (f_{O2}=QFM) to represent crystallization of a dike at shallow depth. Although running our mixing models at lower *P* increases pyroxene Mg# (Putirka 2008; see also Appendix A), *P*=0.1 kbar is the lowest-possible *P* for which our models would return a geologically-reasonable result. Adjustment of f_{O2} to more oxidized conditions would also increase pyroxene Mg# (Appendix A), but f_{O2}=QFM is near the upper limit of oxidation for Kilauean lavas (Carmichael 1991). Given the model and geologic limitations, we put more weight on reproducing the Fissure F mineral assemblage than attempting to match mineral compositions exactly. Thornber *et al.* (2003a) report that Fissure F lavas are triply-saturated (ol+cpx+pl), but also report the presence of rare, xenocrystic opx. Equilibrium crystallization of our Fissure F low-MgO endmember over *T*=1067-1036˚C (φ=40-60) stabilizes opx—analogous to the xenocrystic opx recovered from Fissure F lavas. Further, mixing of that low-MgO endmember when φ=40-50 produces a hybrid mineral assemblage of ol+cpx+pl. These additional constraints reinforce our finding that, prior to 29 January, 1997, the rift-stored magma body was between 40% and 50% crystalline.

The differences in the low-MgO endmember for the Fissure A–E and Fissure F lavas may reflect the geometry of the eruption and differences in magma density. Fissure F is ~2.25 km up-rift of Fissure E, and at a higher elevation (~53 m elevation difference; see Fig. 1 & Supp. Figure 2). Calculated bulk rock densities (Table 6) of the hypothetical low-MgO endmember

compositions show that, at P=0.1 kbar, the Fissure F low-MgO endmember magma (~35% fractionated from the original dike composition) is more buoyant than the less-evolved Fissure A-E low-MgO endmember (~23% fractionated), regardless of magma crystallinity. This is consistent with the Fissures A–E and Fissure F low-MgO endmembers being derived from a compositionally-stratified, differentiating arrested dike. Fissure eruptions from feeder dikes have been shown to propagate laterally as an eruption progresses (Geshi *et al.* 2020); lateral propagation of mafic recharge magmas interacting with an already emplaced, compositionally zoned and partially crystalline dike to form the final intrusive volume (Figure 6) may explain why the final fissure of the eruptive sequence opened up-rift, and why its lavas were more evolved than the lavas erupted down-rift from Fissures A-E.

2. Linking Petrology with Geodesy—an ideal hypothesis for Episode 54

A key goal of this study was to determine if a relationship can be established between pre- and syn-eruptive geodetic measurements, and the geochemistry of lavas associated with the observed deformation. The timing, volume, location, and degree/direction of ground deformation for Kilauea Volcano's Episode 54 eruption is well-documented (Harris *et al.* 1997; Owen *et al.* 2000; Desmarias & Segall 2007). The unique eruption narrative of Episode 54, when paired with seismic and geodetic constraints and a detailed geochemical and petrological time-series of samples, affords a useful opportunity to link the eruption chronology and geochemical compositions to magma volumes.

a. Reconciling Geodetically-Determined Intrusion Volumes with Petrologic Signatures

MCS models suggest that lavas erupted from Fissures A-E formed as a ~43:57 mixture between a near-liquidus mafic magma derived from multiple sources within the Kilauean

edifice (MME, Table 4), and a variably fractionated and compositionally stratified arrested dike that erupted from fissure openings in Napau Crater. The MCS models also suggest that the mafic magma interacted and mixed with a more evolved part of the same arrested dike to produce Fissure F lavas, but with a slightly greater mixing proportion of the low-MgO endmember. Although at first glance the low-MgO endmember composition proposed by Thornber *et al.* (2003)—a magma produced by "37% fractionation of… pl and cpx, with minor ol… [from] the 1968 parent"—appears capable of reproducing the major element compositions of Episode 54 hybrid lavas, the results of our mixing models demonstrate that Thornber's proposed endmember could *not* be the low-MgO endmember needed to generate both AE^{avg} and F^{avg}. Instead, as pointed out by Garcia *et al.* (2000) and as illustrated by major element compositions of erupted Episode 53-55 lavas and from the results of our magma mixing models (Figs. 3b-4), *two* low-MgO endmember compositions are required to reproduce the major element compositions of Episode 54 lavas. AE^{avg} (Table 3; Thornber *et al.* 2003a) is a mixture of 57% low-MgO magma ($f_{low\text{-}MgO}$ = 0.57 ±0.01)—derived by ~23% fractionation (Table 4) of an initial composition similar to N68-4 (Table 3; Jackson *et al.* 1975)—and 43% mafic magmas (MME, Table 4) derived from multiple sources within the Kilauean edifice (m^{mafic}:$m^{low\text{-}MgO} \approx 0.75$; Table 3). F^{avg} can be matched by a mixture of 60% low-MgO magma ($f_{low\text{-}MgO}$ = 0.60 ±0.005)—derived by ~35% fractionation (m^{mafic}:$m^{low\text{-}MgO} \approx$ 0.67; Table 4) of an initial composition similar to N68-4 (Table 3; Jackson *et al.* 1975)—and 43% mafic magmas (MME, Table 4).

In addition to contradicting the previously suggested mixing fraction of m^{mafic}:$m^{low\text{-}MgO} \approx$ 2 (Thornber *et al.* 2003a), our model results are also inconsistent with our volume closure calculations based on geodetic data. The 6.58 Mm^3 low-MgO, rift-stored magma body—

estimated by reconciling the physical dike parameters with geodetic volume estimates for mafic recharge magmas (Table 2)—suggests that the volumes involved in the Episode 54 mixing event were $m^{mafic}:m^{low\text{-}MgO} \approx 2$. This apparent contradiction does not invalidate the results of this study; rather, it provides insight into how localized mixing events are documented in the rock record and highlights how magma mixing is more often than not a heterogeneous process. The results of our bulk rock mixing calculations suggest that the two endmember magmas mixed in differing proportions—$m^{mafic}:m^{low\text{-}MgO} \approx 0.75$ to produce Fissures A-E lavas, and $m^{mafic}:m^{low\text{-}MgO} \approx 0.67$ to produce Fissure F lavas, and geochemical trends also make the different parageneses between lavas erupted from Fissures A-E and Fissure F quite apparent (Figs. 3-4)—hinting at the physically decoupled nature of mixing for this event. Indeed, for magma batches to mix and homogenize to completion within a 22-hour time period (Harris *et al.* 1997) would be unexpected, and so mixing in the above proportions as suggested by our forward models (Table 4) likely occurred, even though the entire volume of intruded magma was not involved.

Our phase-equilibria models are able to replicate the observed mineral assemblages, compositions, and bulk rock compositions of hybrid lavas erupted during Episode 54 of Kilauea Volcano's Pu'U 'O'o eruption within uncertainty, lending credence to our hypothesis that the volumes of stored rift magmas can be constrained by geodetically-assisted petrologic modeling at finer resolutions than either geodetic or petrologic models alone. However, the mixing proportions determined from volume closure calculations ($m^{mafic}:m^{low\text{-}MgO} \approx 2$ over the macroscopic scale associated with ground deformation of kilometers) disagree with the mixing proportions of the best phase-equilibria models for Episode 54 ($m^{mafic}:m^{low\text{-}MgO} \approx 0.75$ for Fissures A-E, and $m^{mafic}:m^{low\text{-}MgO} \approx 0.67$ for Fissure F) that are applicable over smaller

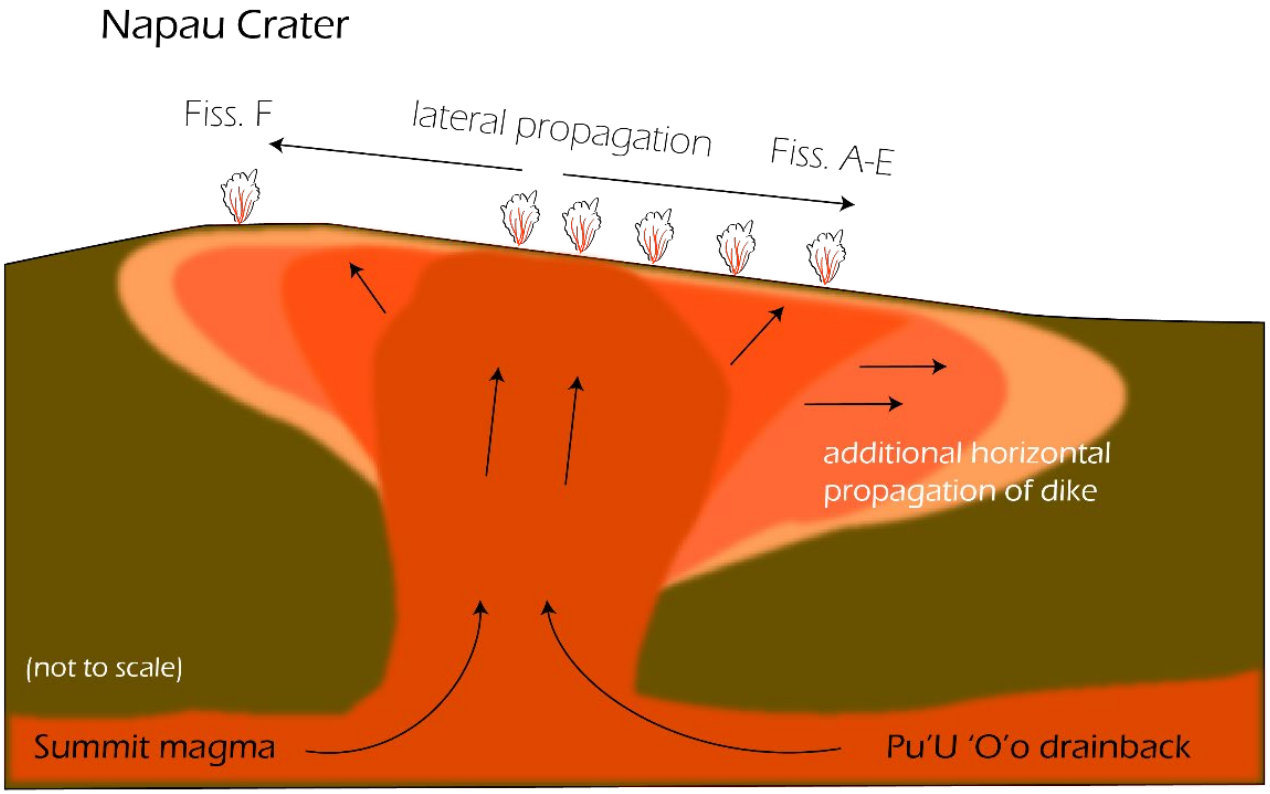

Figure 6. Cartoon schematic displaying lateral dike propagation in the presence of topographic relief (modified from Geshi *et al.* 2020). In the case of Episode 54, Fissures A-E "unzipped" downhill, but the eruption concluded uphill with the opening of Fissure F in the western wall of Napau Crater (see also Fig. 1 & Supp. Fig. 2). In our petrogenetic model, a compositionally stratified dike exists so that the lavas erupted from Fissures A-E are produced by mixing the mixed mafic endmember (MME) magma with a portion of the arrested dike that fractionated ~23% from the initial intrusion composition (similar to the bulk rock composition of N68-4, Jackson *et al.* 1975), and those portions of the dike involved in this mixing event were ~40-50% crystalline at the time of mixing, as constrained by the mineral compositions and assemblages produced in the MCS models, and compared against observed mineral assemblages in erupted lavas. Constructed low-MgO endmember magmas for the Fissure F mixing models are more buoyant (Table 6) than the Fissures A-E low-MgO endmember, and Fissure F opened up-rift at a slightly greater elevation than the previous fissures of this eruptive episode. The low-MgO mixing component necessary to replicate the average bulk composition of Fissure F lavas is derived by mixing of the mixed mafic endmember (MME) magma with a portion of the dike that is ~35% fractionated from the initial intrusion composition (similar to the bulk rock composition of N68-4, Jackson *et al.* 1975); these upper portions of the dike were ~40-50% crystalline at the time of mixing, as constrained by the mineral assemblages in the MCS models versus the observed mineral assemblages in erupted lavas.

spatial scales and with magma compositional heterogeneity developed within rift-stored magmas over decades. The low vol. % of phenocrysts and glomerocrysts reported by Thornber (2001) and Thornber *et al.* (2003a), when compared with the large volumes of magmas required by geodetic models, mixing proportions for the best phase-equilibria models, and low volumes of erupted magmas, suggest that the entire volume of the 1968 intrusion was likely not tapped during the Episode 54 eruption.

I. Conclusions and Implications

The conclusion of Kilauea Volcano's Pu'U 'O'o eruption in April 2018 presents an opportunity for holistic, retrospective studies. After initial eruption onset, activity was characterized by periods of steady-state effusion, interrupted sporadically by intrusions into a weakened area of the ERZ, which sometimes resulted in brief fissure eruptions, producing low-MgO lavas choked with glomerocrystic crystal clots derived from more evolved, rift-stored magma bodies (Orr et al. 2015; Thornber et al. 2015). With each new intrusion, the underground storage and transport system of Kilauea changed (Thornber 2001; Thornber et al. 2003a; Orr 2014; Orr et al. 2015; Gansecki et al. 2019). The results of this study demonstrate that whole rock and mineral chemistries, coupled with thermodynamically-constrained geochemical modeling, can provide new insight into mixing processes, the identity and physical state of rift stored bodies during mixing events, and the relative mixing proportions of mafic and rift-stored magmas that combine to erupt hybrid (*sensu lato*) lavas.

Lavas erupted from Episode 54 fissures are basaltic and relatively aphyric, containing <5% phenocrysts and glomerocrystic clots of cpx + pl (Thornber et al. 2003a), but having much lower MgO contents than lavas erupted before 30 January 1997 (Fig. 2). In agreement with previous research (Garcia et al. 2000; Thornber et al. 2003a), a previously emplaced,

evolved intrusion below Napau Crater mixed with mafic magmas from Kilauea Summit and Makaopuhi Crater, and mafic drainback from the Pu'U 'O'o reservoir, to form the low-MgO basalts erupted during Episode 54. Our findings differ from those of Thornber et al. (2003a) in that we find that magmas from a single, compositionally stratified magma body that was intruded into Napau Crater in 1968 (N68-4; Jackson et al. 1975) can mix with mafic Kilauea magmas to reproduce average Episode 54 bulk lava, mineralogy and mineral compositions. The portion of the intrusion-derived magma needed to produce lavas erupted from Fissures A-E was ~23% fractionated from the initial bulk composition, and 40-50% crystalline at the time of mixing. A stratigraphically-higher (and more evolved) region of the remnant 1968 intrusion, located underneath the western edge of Napau Crater, was produced by ~35% fractionation of the initial intrusion, and was 40-50% crystalline at the time Fissure F erupted. The mafic component mixed with the two, now compositionally distinct but petrogenetically-related, low-MgO endmembers in proportions of $m^{mafic}:m^{low\text{-}MgO} \approx 0.75$ and $m^{mafic}:m^{low\text{-}MgO} \approx 0.67$ to produce Fissures A-E and Fissure F lavas, respectively. We also find that the proportions of the individual magma sources, as constrained by geodetic measurements, can be used as a guide to construct mixing endmembers, but directly linking geodetic volume estimates to magma chemistry is complicated by complex mixing processes that occur rapidly prior to eruption, and a direct link between the total volume of a magma body and its geochemistry remains elusive when incomplete mixing occurs over short timescales.

This novel application of the Magma Chamber Simulator could be widely employed at other volcanic systems where the conditions of a partially-crystalline magma are in question, and eruptive products contain crystals derived from that partially-crystalline magma. Such conditions are nearly ubiquitous in arc lavas (Cooper 2019; de Maisonneuve et al. 2020), but

have only recently begun to be explored at tectonic settings that traditionally erupt more primitive compositions (Rooyakkers et al. 2021). Our results demonstrate that, like many arc volcanoes, sub-edificial intrusions at intraplate shield volcanoes may crystallize and evolve, only to be remobilized later by mafic recharge magmas. This scenario has played out at both Kilauea Volcano (Garcia et al. 1989, 2000; Thornber et al. 2003; Orr et al. 2015; Gansecki et al. 2019) and Krafla Volcano in Iceland (Rooyakkers et al. 2021)—tectonic settings not known for silicic, mushy magmas or typically explosive volcanism. This may imply that, although likely not as cold as mushes in arc volcanic systems, a version of "cold storage" does indeed exist in typically high-*T*, mafic systems. By using phase equilibria models to identify evolved remnant intrusions that are remobilized by later eruptive episodes, we stand to gain a better understanding of the spatial and chemical evolution of magmatic systems, even when geodetic techniques may not be of sufficient resolution to capture them.

J. Acknowledgements

Many thanks to Carl Thornber and Michael Garcia for their discussions and communications regarding the nature of this particular eruptive episode.

K. Electronic Supplemental Materials

This manuscript has not yet been submitted for publication. The following Electronic Appendices and Supplemental Materials have been uploaded to ProQuest to accompany this dissertation chapter:

Appendix A. Estimation of geologic and intensive parameter uncertainty and justification for selecting geologic parameters for MCS models.

(1) AppdxA.FCModelUncertainties.pdf

(2) TableA1_MonteCarloInputResults.xlsx

(3) Table A2_rMELTSExpts.xlsx

(4) Table A3_rMELTSUncertaintyResids.xlsx

(5) FigA1.MonteCarlo_N684lines_H2Ovary.png

(6) FigA2.FCMins_H2Ovary.png

(7) FigA3.MonteCarlo_N684lines_Pvary.png

(8) FigA4.ECPhasebyT.png

(9) FigA5.MonteCarlo_N684lines_fO2vary.png

(10) FigA6.MonteCarlo_IntenParamHistograms.png

(11) FigA7.MCSUncert_FennerPlots.png

(12) Compressed folder "AppdxA_SupportingFiles.zip", containing output files for those MCS runs used in Monte Carlo Simulations, and itemized in Table A1. Folder Structure itemized in Appendix A text.

Appendix B. Complete results of MCS-PhaseEQ Mixing Models for Episode 54.

(1) File "LinearMixing_Ep54.xlsx", containing the results of our bulk rock mixing models as calculated by linear combination.

(2) File "MCSMixing_Ep54.xlsx", containing the summarized results and recalculated bulk rock compositions of MCS-PhaseEQ Mixing Models for Episode 54.

(3) Folder "Fissures AtoE", containing all MCS-PhaseEQ RFC forward models organized by degree of crystallinity of low-MgO endmember at t_{mix}.

(4) Folder "Fissure F", containing all MCS-PhaseEQ RFC forward models organized by degree of crystallinity of low-MgO endmember at t_{mix}.

File “EC_Low-MgOEM_DensityCalcs.xlsx”, containing our density calculations for the low-MgO endmember compositions prior to t_{mix}.

L. References

Anderson, K.R., Johanson, I.A., Patrick, M.R., Gu, M., Segall, P., Poland, M.P., Montgomery-Brown, E.M. & Miklius, A. (2019) Magma reservoir failure and the onset of caldera collapse at Kilauea Volcano in 2018. *Science*, **366**, 1214. doi: 10.1126/science.aaz1822.

Bohrson, W.A., Spera, F.J., Ghiorso, M.S., Brown, G.A., Creamer, J.B. & Mayfield, A. (2014) Thermodynamic model for energy-constrained open-system evolution of crustal magma bodies undergoing simultaneous recharge, assimilation, and crystallization: the Magma Chamber Simulator. *Journal of Petrology*, **55(9)**, 1685-1717.

Bohrson, W.A., Spera, F.J., Heinonen, J.S., Brown, G.A., Scruggs, M.A., Adams, J.V., Zeff, G. & Suikkanen, E. (2020) Diagnosing open-system magmatic processes using the Magma Chamber Simulator (MCS): part I – major elements and phase equilibria. *Contributions to Mineralogy and Petrology*, **175**, 104. doi: 10.1007/s00410-020-01722-z.

Carmichael, I.S.E. (1991) The redox states of basic and silicic magmas: a reflection of their source regions? *Contributions to Mineralogy and Petrology*, **106**, 129-141.

Clague, David A. & Dalrymple, G. Brent (1987) The Hawaiian-Emperor Volcanic Chain. Part I: Geologic Evolution. U.S. Geological Survey Professional Paper 1350, Vol. 1, 23-72.

Cervelli, P., Segall, P., Amelung, F., Garbeil, H., Meertens, C., Owen, S., Miklius, A., and Lisowski, M. (2002) the 12 September 1999 Upper East Rift Zone dike intrusion at Kilauea Volcano, Hawaii. *Journal of Geophysical Research*, **107(B7)**, 2150, doi: 10.1029/2001JB000602.

Cooper, K.M. (2019) Time scales and temperatures of crystal storage in magma reservoirs: implications for magma reservoir dynamics. *Philosophical Transactions of the Royal Society A*, **377**, 20180009. doi: 10.1098/rsta.2018.0009.

de Maisonneuve, C.B., Dungan, M.A., Bachmann, O. & Burgisser, A. (2020) Insights into shallow magma storage and crystallization at Volcán Llaima (Andean Southern Volcanic Zone, Chile). *Journal of Volcanology and Geothermal Research*, **211-212**, 76-91.

Desmarais, E.K. & Segall, P. (2007) Transient deformation following the 30 January 1997 dike intrusion at Kilauea Volcano, Hawaii. *Bulletin of Volcanology*, **69**, 353-363.

Edmonds, M., Sides, I. & Maclennan, J. (2015) Insights into mixing, fractionation, and degassing of primitive melts at Kilauea Volcano, Hawai'i. In: Heliker, C., Swanson, D.A., & Takahashi, T.J. (eds.) *The Pu'U 'O'o-Kupaianaha Eruption of Kilauea Volcano, Hawai'i: The First 20 Years*. U.S. Geological Survey Professional Paper 1676, 323-350.

Gansecki, C., Lee, R.L., Shea, T., Lundblad, S.P., Hon, K. & Parcheta, C. (2019) The tangled tale of Kilauea's 2018 eruption as told by geochemical modeling. *Science*, **366**, eaaz0147.

Garcia, M.O., Rhodes, J.M., Trusdell, F.A. & Pietruszka, A.J. (1996) Petrology of lavas from the Puu Oo eruption of Kilauea Volcano: III. The Kupaianaha episode (1986-1992). *Bulletin of Volcanology*, **58**, 359-379.

Garcia, M.O., Pietruszka, A.J., Rhodes, J.M. & Swanson, K. (2000) Magmatic processes during the prolonged Pu'u 'O'o eruption of Kilauea Volcano, Hawaii. *Journal of Petrology*, **41(7)**, 967-990.

Garcia, M.O., Rhodes, J.M., Wolfe, E.W., Ulrich, G.E. & Ho, R.A. (1992) Petrology of lavas from episodes 2-47 of the Puu Oo eruption of Kilauea Volcano, Hawaii: evaluation of magmatic processes. *Bulletin of Volcanology*, **55**, 1-16.

Geshi, N., Browning, J. & Kusumoto, S. (2020) Magmatic overpressures, volatile exsolution and potential explosivity inferred via dike aspect ratios. *Nature Scientific Reports*, **10(9406)**, doi: 10.1038.S41598-020-66226-z.

Ghiorso, M.S. & Gualda, G.A.R. (2015) An H_2O-CO_2 mixed fluid saturation model compatible with rhyolite-MELTS. *Contributions to Mineralogy & Petrology*, **169(53)**, doi: 10.1007/s00410-015-1141-8.

Girard, G., Reagan, M.K., Sims, K.W.W., Thornber, C.R., Waters, C.L. & Phillips, E.H. (2017) ^{238}U-^{230}Th-^{226}Ra-^{210}Pb-^{210}Po disequilibria constraints on magma generation, ascent, and degassing during the ongoing eruption of Kilauea. *Journal of Petrology*, **58(6)**, 1199-1226.

Global Volcanism Program, 2016. Report on Kilauea (United States). In: Crafford, A.E. & Venzke E. (eds) *Bulletin of the Global Volcanism Network*, **41(8)**. Smithsonian Institution, doi: 10.5479/si.GVP.BGVN201608-332010.

Greene, A.R., Garcia, M.O., Pietruszka, A.J., Weis, D., Marske, J.P., Vollinger, M.J., & Eiler, J. (2013) Temporal geochemical variations in lavas from Kilauea's Pu'U 'O'o eruption (1983-2010): Cyclic variations from melting of source heterogeneities. *Geochemistry, Geophysics, Geosystems*, **14(11)**, doi: 10.1002/ggge.20285.

Gualda, G.A.R., Ghiorso, M.S., Lemons, R.V. & Carley, T.L. (2012) Rhyolite-MELTS: a modified calibration of MELTS optimized for silica-rich, fluid-bearing magmatic systems. *Journal of Petrology*, **53(5)**, 875-890. doi: 10.1093/petrology/egr080.

Harris, A.J.L., Keszthelyi, L., Flynn, L.P., Mouginis-Mark, P.J., Thornber, C., Kauahikaua, J., Sherrod, D., Trusdell, F., Sawyer, M.W., & Flament, P. (1997) Chronology of the episode 54 eruption at Kilauea Volcano, Hawaii, from GOES-9 satellite data. *Geophysical Research Letters*, **24(24)**, 3281-3284.

Heliker, C. & Mattox, T.N. (2003) The first two decades of the Pu'u 'O'o-Kupaianaha Eruption: chronology and selected bibliography. In: Heliker, C., Swanson, D.A., & Takahashi, T.J. (eds.) *The Pu'U 'O'o-Kupaianaha Eruption of Kilauea Volcano, Hawai'i: The First 20 Years*. U.S. Geological Survey Professional Paper 1676, 1-28.

Heliker, C., Kauahikaua, J., Sherrod, D.R., Lisowski, M. & Cervelli, P.F. (2003) The rise and fall of Pu'U 'O'o Cone, 1983-2002. In: Heliker, C., Swanson, D.A., & Takahashi, T.J. (eds.) *The Pu'U 'O'o-Kupaianaha Eruption of Kilauea Volcano, Hawai'i: The First 20 Years*. U.S. Geological Survey Professional Paper 1676, 29-51.

Ingebritsen, S.E., Flinders, A.F., Kauahikaua, J.P. & Hsieh, P.A. (2021) Modeling groundwater inflow to the New Crater Lake at Kilauea Volcano, Hawai'i. *Groundwater*, **59(1)**, 7-15.

Jackson, D.B., Swanson, D.A., Koyanagi, R.Y. & Wright, T.L. (1975) *The August and October 1968 East Rift Eruptions of Kilauea Volcano, Hawaii*. U.S. Geological Survey Professional Paper 890, 1-33.

Langmuir, C.H., Vocke, R.D., Jr., Hanson, G.N. & Hart, S.R. (1978) A general mixing equation with applications to Icelandic basalts. *Earth and Planetary Science Letters*, **37**, 380-392.

Mangan, M.T., Heliker, C.C., Mattox, T.N., Kauahikaua, J.P. & Helz, R.T. (1995) Episode 49 of the Pu'U 'O'o-Kupaianaha eruption of Kilauea volcano – breakdown of a steady-state eruptive era. *Bulletin of Volcanology*, **57**, 127-135.

Montgomery-Brown, E.K., Sinnett, D.K., Poland, M., Segall, P., Orr, T., Zebker, H. & Miklius, A. (2010) Geodetic evidence for en echelon dike emplacement and concurrent slow slip during the June 2007 intrusion and eruption at Kilauea volcano, Hawaii. *Journal of Geophysical Research*, **115(B07405)**, doi: 10.1029/2009JB006658.

Neal, C.A., Brantley, S.R., Antolik, L., Babb, J.L., Burgess, M., Calles, K., Cappos, M., Chang, J.C., Conway, S., Desmither, L., Dotray, P., Elias, T., Fukunaga, P., Fuke, S., Johanson, I.A., Kamibayashi, K., Kauahikaua, J., Lee, R.L., Pekalib, S., Miklius, A., Million, W., Moniz, C.J., Nadeau, P.A., Okubo, P., Parcheta, C., Patrick, M.R., Shiro, B., Swanson, D.A., Tollett, W., Trusdell, F., Younger, E.F., Zoeller, M.H., Montgomery-Brown, E.K., Anderson, K.R., Poland, M.P., Ball, J.L., Bard, J., Coombs, M., Dietterich, H.R., Kern, C., Thelen, W.A., Cervelli, P.F., Orr, T., Houghton, B.F., Gansecki, C., Hazlett, R., Lundgren, P., Diefenbach, A.K., Lerner, A.H., Waite, G., Kelley, P., Clor, L., Werner, C., Mulliken, K., Fisher, G. & Damby, D. (2019) The 2018 rift eruption and summit collapse of Kilauea Volcano. *Science*, **363**, 367-374.

Neall, V.E. & Trewick, S.A. (2008) The age and origin of the Pacific islands: a geological overview. *Philosophical Transactions of the Royal Society B*, **363**, 3293-3308.

O'Connor, J.M., Steinberger, B., Regelous, M., Koppers, A.A.P., Wijbrans, J.R., Haase, K.M., Stoffers, P., Jokat, W. & Garbe-Schönberg, D. (2013) Constraints on past plate and mantle motion from new ages for the Hawaiian-Emperor Seamount Chain. *Geochemistry, Geophysics, Geosystems*, **14(10)**, doi: 10.1002/ggge.20267.

Orr, T.R. (2014) The June-July 2007 collapse and refilling of the Pu'u 'O'o Crater, Kilauea Volcano, Hawai'i: U.S. Geological Survey Scientific Investigations Report 2014-5124, 15 p.

Orr, T.R., Poland, M.P., Patrick, M.R., Thelen, W.A., Sutton, A.J., Elias, T., Thornber, C.R., Parcheta, C., & Wooten, K.M. (2015) Kilauea's 5-9 March 2011 Kamoamoa Fissure Eruption and its relations to 30+ years of activity from Pu'U 'O'o. In: Carey, R., Cayol, V., Poland, M. & Weis, D. (eds) *Hawaiian Volcanoes: From Source to Surface*. Hoboken, NJ: John Wiley & Sons, 393-420.

Owen, S., Segall, P., Lisowski, M., Miklius, A., Murray, M., Bevis, M., & Foster, J. (2000) January 30, 1997 eruptive event on Kilauea Volcano, Hawaii, as monitored by continuous GPS. *Geophysical Research Letters*, **27(17)**, 2757-2760.

Patrick, M., Orr, T., Anderson, K. & Swanson, D. (2019) Eruptions in sync: Improved constraints on Kilauea Volcano's hydraulic connection. *Earth and Planetary Science Letters*, **507**, 50-61.

Patrick, M. Johanson, I., Shea, T. & Waite, G. (2020) The historic events at Kilauea Volcano in 2018: summit collapse, rift zone eruption, and Mw 6.9 earthquake: preface to the special issue. *Bulletin of Volcanology*, **82**, 46. doi: 10.1007/s00445-020-01377-5.

Poland, M.P. & Orr, T.R. (2014) Identifying hazards associated with lava deltas. *Bulletin of Volcanology*, **76**, 880. doi: 10.1007/s00445-014-0880-0.

Poland, M., Orr, T.R., Kauahikaua, J.P., Brantley, S.R., Babb, J.L., Patrick, M.R., Neal, C.A., Anderson, K.R., Antolik, L., Burgess, M., Elias, T., Fuke, S., Fukunaga, P., Johanson, I.A., Kagimoto, M., Kamibayashi, K., Lee, L., Miklius, A., Million, W., Moniz, C., Okubo, P.G., Sutton, A.J., Takahashi, T.J., Thelen, W.A., Tollett, W. & Trusdell, F.A. (2016) The 2014-2015 Pahoa lava flow crisis at Kilauea Volcano, Hawai'i: Disaster avoided and lessons learned. *GSA Today*, **26(2)**, 4-10.

Poland, M.P., Miklius, A., Orr, T., Sutton, J., Thornber, C. & Wilson, D. (2008) New episodes of volcanism at Kilauea Volcano, Hawaii. *Eos*, **89(5)**, 37-38.

Poland, M.P., Miklius, A., Sutton, A.J. & Thornber, C.R. (2012) A mantle-driven surge in magma supply to Kilauea Volcano during 2003-2007. *Nature Geoscience*, **5**, 295-300.

Rooyakkers, S.M., Stix, J., Berlo, K., Petrelli, M. & Sigmundsson, F. (2021) Eruption risks from covert silicic magma bodies. *Geology*, **49**, doi: 10.1130/G48697.1.

Putirka, K. (2008) Thermometers and barometers for volcanic systems. *Reviews in Mineralogy and Geochemistry*, **69**, 61-120.

Segall, P., Cervelli, P., Owen, S., Lisowski, M., & Miklius, A. (2001) Constraints on dike propagation from continuous GPS measurements. *Journal of Geophysical Research*, **106(B9)**, 19301-19317.

Thornber, C.R. (2001) Olivine-liquid relations of lava erupted by Kilauea Volcano from 1994 to 1998: Implications for shallow magmatic processes associated with the ongoing East-Rift-Zone eruption. *The Canadian Mineralogist*, **39**, 239-266.

Thornber, C.R., Heliker, C., Sherrod, D.R., Kauahikaua, J.P., Miklius, A., Okubo, P.G., Trusdell, F.A., Budahn, J.R., Ridley, W.I. & Meeker, G.P. (2003a) Kilauea East Rift Zone magmatism: An Episode 54 perspective. *Journal of Petrology*, **44(9)**, 1525-1559.

Thornber, C.R., Hon, K., Heliker, C. & Sherrod, D.A. (2003b) A compilation of whole-rock and glass major-element geochemistry of Kilauea Volcano, Hawai'i, near-vent eruptive products: January 1983 through September 2001. U.S. Geological Survey Open-File Report 03-477, 8 p.

Thornber, C.R., Orr, T.R., Heliker, C. & Hoblitt, R.P. (2015) Petrologic testament to changes in shallow magma storage and transport during 30+ years of recharge and eruption at Kilauea Volcano, Hawai'i. In: Carey, R., Cayol, V., Poland, M. & Weis, D. (eds) *Hawaiian Volcanoes: From Source to Surface*. Hoboken, NJ: John Wiley & Sons, 147-188.

USGS (2021) Water depth plot for Kilauea Volcano summit water lake. https://www.usgs.gov/media/images/water-depth-plot-kilauea-volcano-summit-water-lake, accessed 28 June 2021.

Vollmer, R. (1976) Rb-Sr and U-Th-Pb systematics of alkaline rocks: the alkaline rocks from Italy. *Geochimica et Cosmochimica Acta*, **40**, 283-295.

von Engelhardt, W. (1989) Remarks on "ratio plots" and "mixing lines". *Geochimica et Cosmochimica Acta*, **53**, 2443-2444.

Walker, G.P.L. (1986) Koolau Dike Complex, Oahu: Intensity and origin of a sheeted-dike complex high in a Hawaiian volcanic edifice. Geology, **14**, 310-313.

Walker, G.P.L. (1990) Geology and volcanology of the Hawaiian Islands. *Pacific Science*, **44(4)**, 315-347.

Wallace, P.J. & Anderson, Jr., A.T. (1998) Effects of eruption and lava drainback on the H_2O contents of basaltic magmas at Kilauea Volcano. *Bulletin of Volcanology*, **59**, 327-344.

Wright, T.L., Kinoshita, W.T. & Peck, D.L. (1968) March 1965 eruption of Kilauea Volcano and the formation of Makaopuhi Lava Lake. *Journal of Geophysical Research*, 73(10), 3,181-3,205.

Wright, T.L. & Klein, F.W. (2014) Two hundred years of magma transport and storage at Kilauea Volcano, Hawai'i, 1790-2008. U.S. Geological Survey Professional Paper 1806, 240 p.

Wright, T.L. & Takahashi, T.J. (1998) Hawaii bibliographic database. *Bulletin of Volcanology*, **59**, 276-280.

IV. Two-stage petrogenesis of enclaves at Chaos Crags, Lassen Volcanic Center, California, as inferred from isotopes, trace elements, phase equilibria and magma transport modeling

A. Introduction

A century after the classic studies of N.L. Bowen (1915, 1928), it is now widely accepted that in addition to fractional crystallization, magma mixing and assimilation are quantitatively significant processes that influence the evolution of crustal magmatic systems (Eichelberger, 1975; Taylor, 1980; Spera & Bohrson, 2002). Open system behavior, where both material and heat are exchanged between magma and its surroundings during its ascent from source to surface, appears to be the rule rather than the exception (Eichelberger *et al*., 2006; Bohrson *et al*., 2014, 2020; Turner & Langmuir, 2015; Weinberg *et al*., 2021). Unfortunately, these effects can be geochemically subtle and the deconvolution of assimilation, magma mixing and fractional crystallization processes can be difficult (Bohrson *et al*., 2020; Heinonen *et al.,* 2020). In particular, the relative importance of recharge (R), assimilation of partial melts (A), the complete homogenization of a stoped block (S), and fractional crystallization (FC) are likely to be unique to each magmatic system because so many factors come into play. Sorting out the effects of individual magmatic processes remains challenging—as such, in order to develop more general models, it is prudent to focus first on specific systems.

In this study, we examine the petrogenesis of the ~1100 BP Chaos Crags enclave-bearing lava domes at Lassen Volcanic National Park, California. A well-documented process at Chaos Crags is the recharge and mixing of an initially high-temperature, nearly aphyric mafic magma into a cooler, partially crystalline (volume fraction of crystals, $\varphi \approx 0.3$), resident

rhyodacitic magma body (Heiken & Eichelberger, 1980; Tepley *et al*., 1999; Klemetti & Clynne, 2014; Quinn, 2014; Scruggs & Putirka, 2018). The substantial variations in composition present within Chaos Crags lavas and their associated enclaves afford a series of high-resolution "snapshots" of the physical results of magma mixing and mingling, manifesting as texturally, geochemically, and isotopically heterogeneous mafic enclaves (Heiken & Eichelberger, 1980; Bacon, 1986; Tepley *et al*., 1999; Scruggs & Putirka, 2018; Weinberg *et al.* 2021). This magma mixing process can be modeled by the Recharge of mafic magma (R) into a partially crystallized, resident rhyodacitic magma at shallow depths within the upper crust (5-10 km). This aspect of Chaos Crags' magmatic history is not controversial. Our additional and more novel contribution is the resolution of isotopic signatures suggestive of an earlier phase of assimilation (A) of Sierra Nevada basement by the mafic endmember (Feeley *et al*., 2008a; Walowski *et al*., 2019), before the well-documented shallow-level mixing of mafic and rhyodacitic magmas. The goal of this study is to quantify the relative roles of deep contamination and shallow magma mixing by integrating new isotopic, and petrochemical data with quantitative modeling of serial AFC+R.

As the isotopic and trace element variability of a population of mafic enclaves cannot be explained by mixing between our least radiogenic mafic enclave composition and our most radiogenic host rhyodacite composition, it is evident that the mafic endmember itself was not of uniform composition. Here we argue that the compositional variation in the enclave population is partly due to an earlier (pre-mixing) AFC event within the mid- to upper crust, rather than calling on ad hoc mantle or lower crustal heterogeneity. While we are unable to conclusively rule out source heterogeneity, our approach is to test the hypothesis that AFC—for which there is clear evidence in the form of crustal xenoliths erupted at nearby volcanoes

within the LVC (Borg & Clynne, 1998; Feeley *et al*., 2008a)—was a significant process in the petrogenesis of the mafic enclaves at Chaos Crags. Furthermore, the crustal pollution process was temporally and spatially uneven, affecting mafic recharge magmas more appreciably in the latter half of the eruptive sequence (i.e., extremely radiogenic enclaves are more likely to be found in lavas from domes D-F than from domes A-C; see also Tepley *et al.*, 1999 and Scruggs & Putirka, 2018). We argue that contamination occurred during basalt ascent through a crack network via assimilation of partial melts of Sierra Nevada granitoid wallrocks (sensu lato).

To study this initial phase of contamination, we examined trace element and isotopic compositional variations within mafic enclaves of Chaos Crags in the context of previously-reported petrographic and mineralogical variations (Tepley *et al.,* 1999; Scruggs & Putirka, 2018). In particular, whole rock major oxide and trace element compositions and $^{87}Sr/^{86}Sr$ and $^{143}Nd/^{144}Nd$ isotopic ratios of mafic enclaves and their rhyodacitic host lavas are used in concert with open system phase equilibria computations [Magma Chamber Simulator (MCS; Bohrson *et al*., 2014; Bohrson *et al*., 2020; Heinonen *et al*., 2020)], including trace element and isotopic modeling, to ascertain the relative importance of magma mixing, crystal fractionation and assimilation to the petrogenesis of Chaos Crags mafic enclaves.

B. Geologic Setting

The active Cascadia subduction zone and its overlying continental volcanic arc (the Cascade Range) result from oblique subduction of the remnant Juan de Fuca and Gorda plates beneath the North American plate in the northwestern United States (Clynne, 1990; Guffanti *et al*., 1990). Several active volcanic centers are located within the Cascade Range, the southernmost of which is the Lassen Volcanic Center (LVC), located in northern California

(Fig. 1; Clynne & Muffler, 2010). The LVC is underlain by a ~4 km sequence of Cenozoic Cascade volcanic rocks (Berge & Stauber, 1987), which lie unconformably over 38 ± 4 km of Mesozoic Klamath-Sierra Nevada basement (Berge & Stauber, 1987; Guffanti *et al*., 1990; Borg *et al.*, 1997; Cecil *et al.*, 2012; Tavarez, 2015). *P-T* estimates of crystallization (Klemetti & Clynne, 2014; Scruggs & Putirka, 2018) and experimental determination of storage conditions (Quinn, 2014) suggest that the Chaos Crags magma body is located at 5-10 km depth, within the Mesozoic Klamath-Sierra Nevada basement section (Berge & Stauber, 1987; Guffanti *et al*., 1990; Borg & Clynne, 1998; Cecil *et al.*, 2012; Walowski *et al.*, 2019). The presence of a thick section of Sierra Nevada granitic rocks in the mid- to upper crust is of special significance to enclave petrogenesis at Chaos Crags.

1. Eruptive History of the Lassen Volcanic Center

Volcanism in the southernmost Cascades has been nearly continuous for the last ~7 Ma, mostly dominated by regional basaltic volcanism (Clynne, 1990; Guffanti *et al*., 1990), but accentuated by a few long-lived volcanic centers (Clynne & Muffler, 2010). The reader is referred to Christiansen *et al*. (2002) and Clynne & Muffler (2010) for an excellent summary of the eruptive history of volcanic centers at Lassen and nearby regions.

LVC volcanism commenced at ~825 ka and continues to date, with the most recent eruption being the 1915 eruption of Lassen Peak (Clynne *et al*., 2012). Volcanic activity may be divided into three major sequences: Rockland caldera complex (~825 to 609 ka), Brokeoff Volcano (590 to 385 ka), and the Lassen Domefield (~300 to 0 ka; Clynne & Muffler, 2010). Construction of Brokeoff Volcano, an andesitic stratocone, occurred during the Rockland caldera and Brokeoff Volcano sequences (~825 to 385 ka); caldera collapse of Brokeoff Volcano occurred ~385 ka (Clynne, 1990; Clynne & Muffler, 2010). The Lassen Domefield

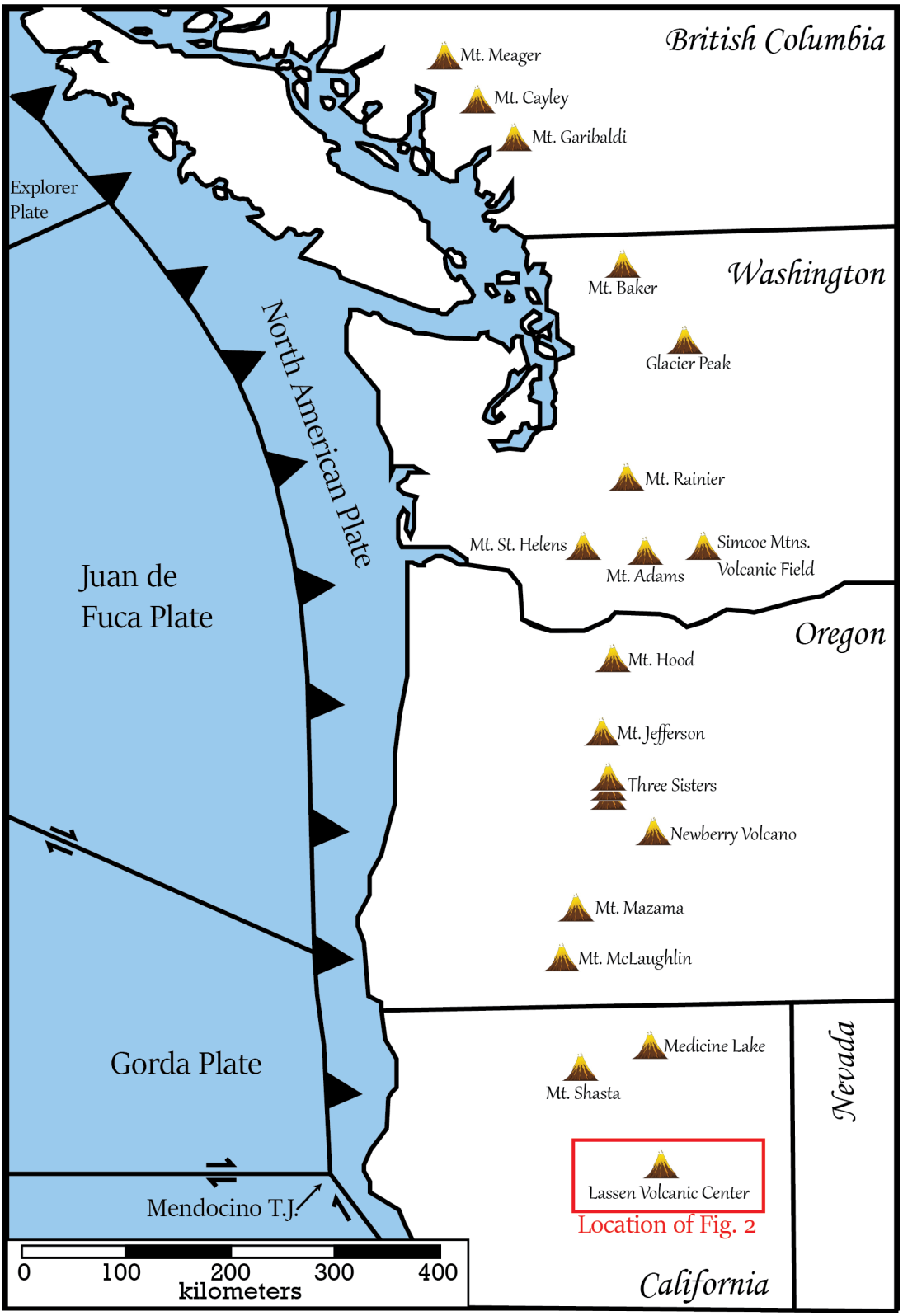

Figure 1. Map of the Cascadia Subduction Zone [after Schmidt *et al.* (2008)]. Red outline denotes location of Figure 2.

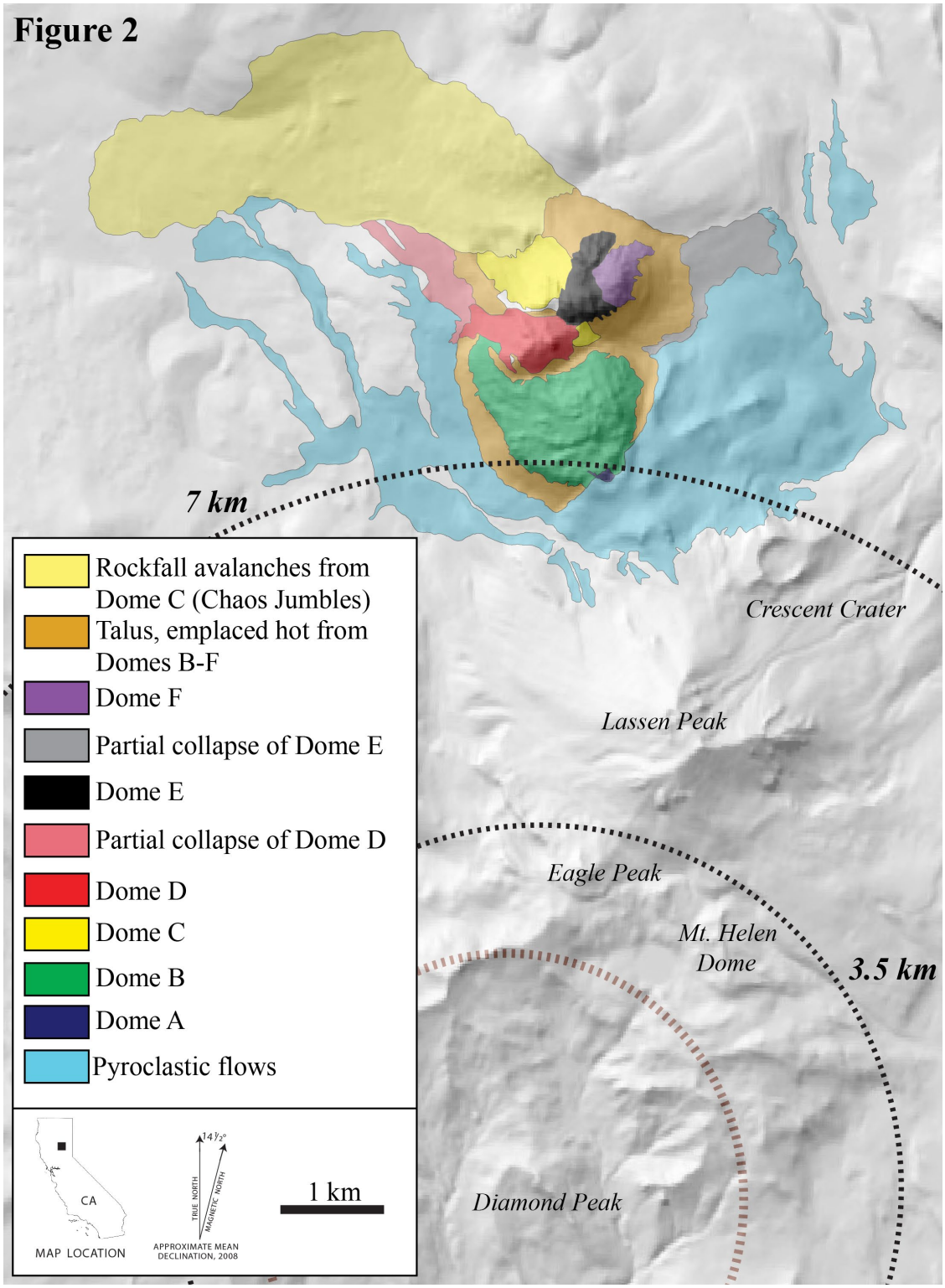

Figure 2. Simplified geologic map of Chaos Crags [after Feeley *et al.* (2003); modified from Scruggs & Putirka (2018)]. Dashed brown circle denotes the outline of the remnant ~80 km^3 Brokeoff Volcano; dashed black circles indicate distance from Diamond Peak, inferred to be at the center of the now-eroded volcanic core.

began construction in and on the northwestern edge of the remnant Brokeoff caldera at ~300 ka; eruptive activity of the Lassen Domefield may be divided into three sequences based upon age and silica content: Bumpass (~300 to 190 ka), Eagle Peak (~70 ka to present), and Twin Lake (~310 to 240 ka, and ~90 ka to present) sequences (Clynne & Muffler, 2010). Recent volcanic activity within the LVC has been attributed to sporadic, localized mafic magma-driven thermal 'rejuvenation' of the ~300 to 190 ka nascent Bumpass pluton (Clynne *et al.*, 2012; Klemetti & Clynne, 2014), and may belong to either the Twin Lakes sequence or the concurrently erupting Eagle Peak sequence (Clynne & Muffler, 2010; Klemetti & Clynne, 2014).

The youngest eruptions within the Eagle Peak sequence (Clynne & Muffler, 2010), Chaos Crags are a series of six lava domes (Domes A-F, in chronological order) that erupted sequentially beginning ~850 C.E. (1,103 ±13 years B.P.; Ryan et al., 2020); the subsequent collapse of Dome C at 1672 ±30 C.E. resulted in a rockfall avalanche deposit known as Chaos Jumbles (Fig. 2; Tepley *et al*., 1999; Ryan *et al*., 2020). Lavas of Chaos Crags are dacitic to rhyodacitic, and contain abundant basaltic to andesitic mafic enclaves that are characterized by the presence of disequilibrium textures and mineral assemblages (Heiken & Eichelberger, 1980; Tepley *et al*., 1999; Clynne & Muffler, 2010; Scruggs & Putirka, 2018); both rhyodacitic and dacitic host lava compositions are hereafter referred to as rhyodacitic for continuity with previous literature (Christiansen *et al*., 2002; Scruggs & Putirka, 2018).

C. Methods

In addition to presenting new geochemical data, we also present new analyses on host lavas and selected mafic enclaves presented in Scruggs & Putirka (2018). A suite of seven

host lavas and 21 mafic enclaves have been considered in detail for this study. Individual mafic enclaves were separated into their apparent cores/rims according to macroscopic textural differences, and each core and rim analyzed and reported as a unique sample. Where present, host lava was entirely removed from the exterior of each mafic enclave boundary, and visually distinct enclave fragments were removed from host lavas in an effort to preserve distinct enclave and host compositions insofar as possible (Scruggs & Putirka, 2018).

1. Major Oxide and Trace Element Compositions

Whole rock major oxide compositions were determined using the fused glass bead X-Ray Fluorescence (XRF) method, analyzed on a Phillips Analytical Wavelength Dispersive XRF Spectrometer at Pomona College (Johnson *et al*., 1999; Lackey *et al*., 2012). Whole rock trace element compositions were determined by laser ablation on XRF bead fragments using an Agilent 7700x quadrupole inductively coupled plasma mass spectrometer (Q-ICP-MS) housed at University of California, Santa Barbara, and data were processed using the Iolite data reduction software (Paton *et al*., 2011; Poletti *et al*., 2016).

2. $^{87}Sr/^{86}Sr$ and $^{143}Nd/^{144}Nd$ Isotopic Ratios

$^{87}Sr/^{86}Sr$ isotope ratios were determined using a VG Sector 54 Thermal Ionization Mass Spectrometer at the University of North Carolina – Chapel Hill. Methods for Sr sample preparation and analysis are given in Hedman *et al*. (2009), and further summarized in Jackson *et al.* (2016). Isotopic ratios of Sr were corrected for instrumental mass bias relative to a $^{86}Sr/^{88}Sr$ ratio of 0.1194 assuming exponential fractionation. Measured $^{87}Sr/^{86}Sr$ ratios were normalized by the offset between the average measured value of NBS-987 (0.710241 ±0.000012, 2SD [n=10]) and the preferred $^{87}Sr/^{86}Sr$ ratio of 0.710240 (Jackson *et al*., 2016).

Table 1. Input Parameters for the Magma Chamber Simulator (Bohrson et al. 2014)

Input Parameters for Composite System	
Pressure:	P (bars)
fO_2 constraint	fO_2 buffer or initial Fe^{2+}/Fe^{3+}
Ratio of initial WR mass to initial M mass:	M_0^{WR} / M_0^{M}
Critical melt fraction in WR:	f^{WR}_{crit}
Temperature decrement to subsystem M during approach towards thermal equilibrium of WR and M:	ΔT (°C)
Desired final temperature for end of MCS simulation:	T_{end} (°C)
M subsystem melt temperature for *j*th recharge event:	T_1^M, T_2^M, etc.
Ratio of mass of *j*th recharge event to initial mass of M:	M_j^R / M_0^M

Magma body, Wallrock, and Recharge magma subsystem inputs for MCS Simulations				
Subsystem	Initial bulk major oxide, trace element, and isotopic composition (for *i* components)	Temperature	Distribution Coefficient	Mass
Magma body (M)	X_0^M	initial T of subsystem T_0^M	D for each component & mineral phase	initial mass of subsystem (100% melt), M_0^M
Wallrock (WR)	X_0^{WR}	initial T of subsystem T_0^{WR}	D for each component & mineral phase	initial mass of subsystem, M_0^{WR}
Recharge, *j* events (R_j)	$X_{0,j}^R$	T_j^R	D for each component & mineral phase	mass of *j*th recharge increment, M_j^R

External precision of $^{87}Sr/^{86}Sr$ measurements is estimated to be 20 ppm (2σ); the total procedural Sr blank was <100 pg and no blank correction was performed.

$^{143}Nd/^{144}Nd$ isotope ratios were measured using a IsotopX Phoenix multi-collector Thermal Ionization Mass Spectrometer at the University of North Carolina – Chapel Hill. Methods for Nd sample preparation and analysis are given in Harvey & Baxter (2009), and further summarized in Jackson *et al*. (2016). Isotopic ratios of Nd were corrected for instrumental mass bias relative to a $^{146}Nd/^{144}Nd$ ratio of 0.7219 assuming exponential fractionation. Measured $^{143}Nd/^{144}Nd$ ratios were normalized by the offset between the average measured value of JNdi (0.512103 ±0.000009, 2SD [n=10]) and the preferred $^{143}Nd/^{144}Nd$ ratio of 0.512104 (Jackson *et al*., 2016). External precision of $^{143}Nd/^{144}Nd$ measurements is estimated to be better than 20 ppm (2σ); the total procedural Nd blank was <50 pg and no blank correction was performed.

3. Modeling of RASFC Processes

The Magma Chamber Simulator (MCS; Bohrson *et al*., 2014, 2020; Heinonen *et al*., 2020) is a thermodynamic model for computing phase equilibria, trace element, and isotope systematics in open systems undergoing concurrent or serial fractional crystallization, assimilation of partial melts, digestion of stoped blocks, and mixing (recharge) events. We used MCS to model serial contamination (AFC) and recharge (R) in this study. The MCS code, including documentation and examples are available (open access) at http://mcs.geol.ucsb.edu. The phase equilibria engine incorporated within the MCS software is powered by rhyolite-MELTS (Gualda *et al.*, 2012; Ghiorso & Gualda, 2015). Symbols used in the text to define MCS calculations are provided in Table 1; trace element partition

coefficients used in MCS calculations (and references) are presented in Appendix A. The MATLAB code used in our calculations is available at: https://github.com/VolcanoDoc/Chaos-Crags. The descriptions of and motivations behind our specific modeling techniques are described in the Discussion, and presented in detail in Appendices B and C.

D. Petrochemical and Isotopic Results

1. Mineralogy and Geochemistry of Host Lavas

Host lavas of Chaos Crags range from dacitic to rhyodacitic and contain abundant basaltic-andesitic to andesitic mafic enclaves of variable composition (Fig. 3). Results presented in this section focus on macroscopically-uncontaminated host rhyodacites (light gray circles and squares in Fig. 3); mafic enclaves are discussed in a later section. Comprehensive lithologic descriptions of the entire suite of Chaos Crags eruptive products are given in Christiansen *et al*. (2002); compositions and detailed descriptions of whole rock geochemistry of eruptive products and their disequilibrium mineral assemblages are given in Tepley *et al*. (1999), Underwood *et al.* (2012), and Scruggs & Putirka (2018). Here we focus on new analyses, but also draw on earlier results presented by Scruggs & Putirka (2018).

Chaos Crags host lavas are moderately porphyritic, ranging from ~30% to ~40% crystallinity (Underwood *et al*., 2012; Scruggs & Putirka, 2018). Phenocrysts in host lavas include plagioclase, biotite, amphibole, and quartz, with minor amounts of magnetite and ilmenite (Heiken & Eichelberger, 1980; Quinn, 2014). Host lavas also contain xenocrysts derived from mafic enclaves, including calcic plagioclase, clinopyroxene, orthopyroxene, and rare olivine (Tepley *et al.*, 1999; Scruggs & Putirka, 2018).

Major oxide and trace element compositions and isotopic values for host lavas analyzed

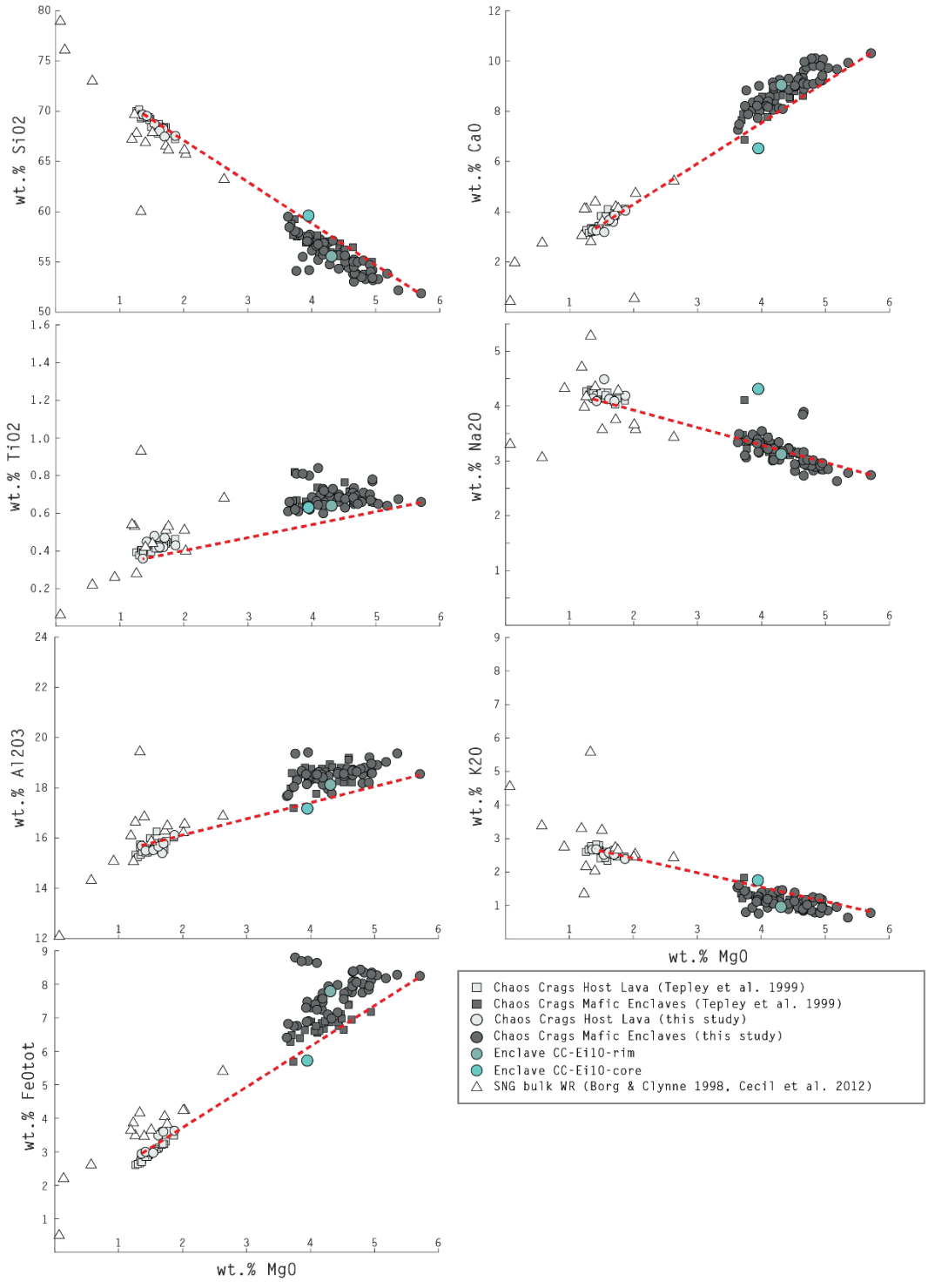

Figure 3. Major oxide compositions of Chaos Crags mafic eruptive products (circles and squares), and reported northern Sierra Nevada granitoid (*sensu lato*) wallrock compositions (triangles).

Table 2. Major Oxide, Trace Element, and Isotopic Compositions of Host Lavas

Sample	CC-A-H-1*	CC-B-H-2*	CC-B-I-11 adj. host*	CC-C-H-1*	CC-D-H-1	CC-E-H-1*	CC-F-H-2*
SiO_2	69.67	69.54	68.74	68.25	68.04	67.48	67.54
TiO_2	0.36	0.45	0.48	0.42	0.42	0.47	0.43
Al_2O_3	15.69	15.50	15.52	15.40	15.66	15.78	16.12
FeO_{tot}	2.94	3.00	2.97	3.60	3.49	3.60	3.63
MnO	0.07	0.06	0.07	0.07	0.07	0.07	0.07
MgO	1.36	1.42	1.54	1.68	1.62	1.70	1.87
CaO	3.27	3.25	3.19	3.60	3.68	3.87	4.04
Na_2O	4.14	4.09	4.49	4.11	4.13	4.09	4.19
K_2O	2.67	2.68	2.52	2.64	2.58	2.52	2.39
P_2O_5	0.12	0.00	0.11	0.10	0.11	0.10	0.11
Sum	100.29	99.99	99.63	99.87	99.80	99.68	100.39
LOI:	1.21	0.54	0.73	0.19	0.08	0.71	0.55
Qtz	25.22	24.94	22.77	22.73	22.55	21.94	21.26
Crndm	0.40	--	--	--	--	--	--
Or	15.78	15.84	14.89	15.60	15.25	14.89	14.12
Ab	35.03	34.61	37.99	34.78	34.95	34.61	35.45
An	15.24	16.02	14.75	15.77	16.57	17.26	18.12
Di (wo)	--	0.04	0.15	0.60	0.4	0.54	0.50
Di (en)	--	0.02	0.08	0.30	0.20	0.27	0.26
Di (fs)	--	0.02	0.07	0.29	0.20	0.26	0.23
Hy (en)	3.39	3.51	3.76	3.89	3.84	3.96	4.40
Hy (fs)	3.37	3.26	3.14	3.84	3.79	3.79	3.92
Mt	0.85	0.87	0.86	1.04	1.01	1.04	1.05
Il	0.68	0.85	0.91	0.80	0.80	0.89	0.82
Ap	0.35	--	0.25	0.23	0.25	0.23	0.25

*major oxide compositions for this sample from Scruggs and Putirka (2018)

in this study are given in Table 2. As noted by Scruggs & Putirka (2018), host lavas become progressively more modified by mafic recharge over the duration of the eruptive sequence. Chaos Crags host lavas exhibit the large ion lithophile (LILE) enrichment, Sr and Pb enrichments, and high-field strength element (HFSE) depletions relative to N-MORB (Gale *et al*., 2013) characteristic of subduction zone magmatism (Fig. 4a; Zheng, 2019). Host lavas display negative Eu and Ti anomalies, and a depletion of middle REE relative to LREE and HREE (Fig. 4b). $^{87}Sr/^{86}Sr$ and $^{143}Nd/^{144}Nd$ isotope systematics of Chaos Crags host lavas are negatively correlated and are respectively low (0.703977-0.704039) and high (0.512729-0.512793), relative to BSE (Table 2, Figure 5; Faure, 2001).

Table 2, cont'd. Major Oxide, Trace Element, and Isotopic Compositions of Host Lavas

Sample	CC-A-H-1*	CC-B-H-2*	CC-B-I-11 adj. host*	CC-C-H-1*	CC-D-H-1	CC-E-H-1*	CC-F-H-2*
Rb	82.7	75.8	78.1	80.5	74.9	80.4	71.8
Ba	776	775	779	780	749	757	733
Zr	131	130	132	133	130	122	122
Sr	335	323	335	329	341	353	361
Y	11.4	11.5	13.2	13.3	11.7	12.6	12.8
Ni	8.2	9.2	8.2	9.4	11.2	9.2	15.2
Sc	8.8	8.8	11.0	11.8	10.7	11.9	11.9
Cr	18.8	19.9	18.6	19.2	22.2	21.9	15.9
Cs	4.3	3.7	4.0	3.5	3.2	4.2	3.9
Hf	3.5	3.5	3.7	3.5	3.6	3.4	3.4
Th	10.0	10.0	10.0	10.3	9.6	9.2	9.5
U	4.0	3.6	3.6	3.8	3.5	3.7	3.3
La	20.5	20.5	21.2	20.9	19.4	19.9	19.9
Ce	39.7	38.8	39.7	40.9	37.3	38.2	37.6
Pb	10.4	9.2	8.9	6.7	8.6	10.3	5.6
Pr	4.0	4.1	4.3	4.2	3.9	4.0	3.9
Nd	14.3	13.6	15.0	14.9	13.1	14.4	13.8
Sm	2.2	2.4	2.6	2.6	2.4	2.5	2.4
Eu	0.7	0.7	0.7	0.6	0.8	0.6	0.6
Gd	2.0	2.0	2.4	2.5	2.0	2.4	2.2
Tb	0.3	0.3	0.4	0.4	0.3	0.3	0.3
Dy	1.8	1.7	2.1	2.2	1.8	2.0	2.1
Ho	0.4	0.4	0.4	0.5	0.4	0.4	0.4
Er	1.1	1.2	1.3	1.3	1.2	1.3	1.3
Tm	0.2	0.2	0.2	0.2	0.2	0.2	0.2
Yb	1.4	0.3	1.4	1.6	1.3	1.4	1.4
Lu	0.2	0.2	0.3	0.3	0.2	0.2	0.2
$^{87}Sr/^{86}Sr$	0.704039	0.704039	0.704035	0.703995	0.703991	0.704011	0.703977
$^{143}Nd/^{144}Nd$	--	0.512780	0.512779	0.512788	0.512787	0.512789	0.512793

2. Mineralogy and Geochemistry of Mafic Enclaves

Mafic enclaves enclosed within Chaos Crags host lavas have variable texture, composition, and modal mineralogy (Heiken & Eichelberger, 1980; Tepley *et al*., 1999; Scruggs & Putirka, 2018). Phenocrysts within mafic enclaves include calcic plagioclase, olivine, clinopyroxene, amphibole, and orthopyroxene, with minor amounts of magnetite and ilmenite (Heiken & Eichelberger, 1980; Tepley *et al.*, 1999; Christiansen *et al.*, 2002; Scruggs & Putirka, 2018). Xenocrysts derived from the host lavas are also present within mafic

enclaves, and include more sodic plagioclase, quartz, biotite, amphibole, and rare zircon (Tepley *et al*., 1999; Underwood *et al.*, 2012; Scruggs & Putirka, 2018). In >50% of the mafic enclaves, amphibole is a dominant ferromagnesian groundmass phase. However, closer inspection of enclave mineral reaction textures reveals both phenocrystic and groundmass pyroxene mantled by amphibole and Fe-Ti oxides (Fig. 6). These petrographic relationships suggest that parental mafic magmas were originally pyroxene-bearing, and that at least some amphibole formed via uralitization as a result of olivine + pyroxene-bearing recharge magmas mixing and mingling with hydrous resident host magmas (Arvin *et al*., 2004; Beard *et al.*, 2004; Cooper *et al.*, 2019).

Chaos Crags mafic enclaves exhibit significant geochemical variations over the entirety of the eruptive sequence (i.e., between individual lava domes; see Scruggs & Putirka, 2018), between mafic enclaves of an individual dome (spatial scale of tens of meters), and even within individual enclaves themselves (spatial scale of decimeters to millimeters). Enclaves range from basaltic-andesite to andesite; a few are relatively enriched in alkalis, although they remain subtrachytic (black circles and squares, Fig. 3). Most mafic enclaves analyzed in this study are quartz-normative tholeiitic basalt to andesite, however a small number (4%) are hypersthene-olivine normative (olivine tholeiite). Major oxide, trace element, and isotopic compositions for mafic enclaves analyzed in this study are given in Tables 3 and 4.

a. Trace and Rare-Earth Element Variations within Mafic Enclaves

Trace element compositions of Chaos Crags eruptive products exhibit geochemical signatures that are characteristic of subduction zone magmatism (Fig. 4; Zheng, 2019). However, unlike the small range of concentrations present within host lavas, mafic enclaves show a larger variation in the abundances of most trace elements (Fig. 4a; Table 4). Enclave

CC-E-I-10 (both core and rim samples) is especially interesting, as it displays a similar LREE enrichment and Ti depletion as the host lavas, but has *higher* REE concentrations than host lavas, yet an LILE signature more similar to mafic enclaves (Fig. 4).

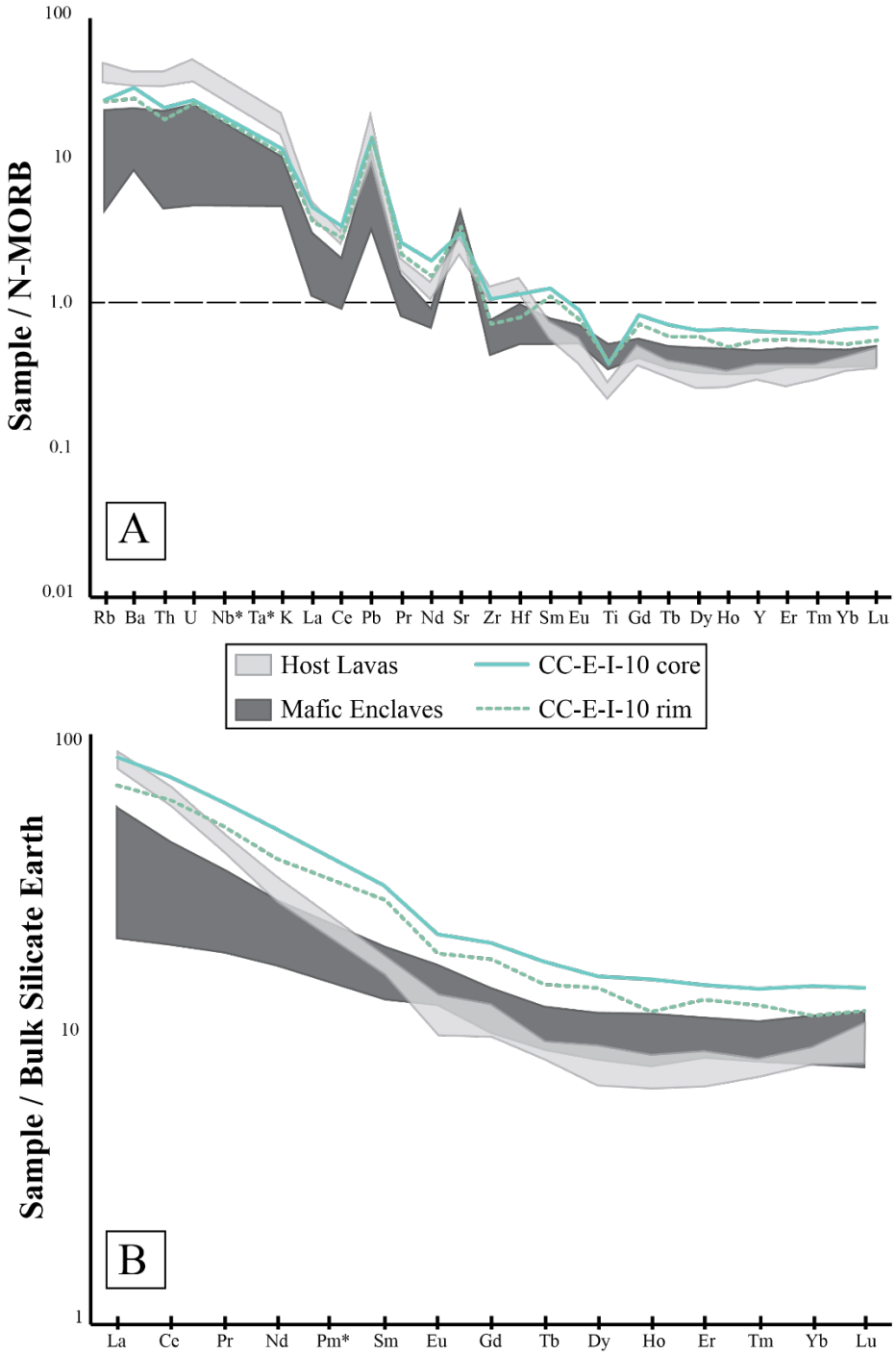

Figure 4. Trace element abundances of Chaos Crags eruptive products normalized to N-MORB (A; Gale *et al*., 2013). Rare earth element abundances of Chaos Crags eruptive products normalized to chondritic meteorite (B; McDonough & Sun 1995). Light gray denotes trace element and REE variation within host lavas; dark gray shows extent of trace element and REE variations within mafic enclaves. Note that enclave samples CC-E-I-10core and CC-E-I-10rim are extremely enriched in REEs relative to other Chaos Crags eruptive products.

b. Isotopic Variations within Mafic Enclaves

$^{87}Sr/^{86}Sr$ and $^{146}Nd/^{144}Nd$ isotope ratios were measured in nine of the 21 mafic enclaves studied. Selection of mafic enclaves for isotope analyses was based on macroscopic textural heterogeneities, as well as unusual major and trace element geochemistry (Tables 3 & 4). $^{87}Sr/^{86}Sr$ and $^{143}Nd/^{144}Nd$ isotope systematics of Chaos Crags mafic enclaves are negatively correlated (Fig. 4b) and are respectively low (0.703637-0.704085) and high (0.512818-0.512771), relative to bulk earth (Faure, 2001).

Significantly, $^{87}Sr/^{86}Sr$ ratios of enclave CC-E-I-10 (core and rim samples) are anomalously enriched relative to other enclaves; *the $^{87}Sr/^{86}Sr$ ratio of CC-E-I-10 core ($^{87}Sr/^{86}Sr$ = 0.704085) is greater than even that of Chaos Crags host lavas ($^{87}Sr/^{86}Sr$ = 0.703977-0.704039) (Figure 5)*. Both crustal xenoliths and Sierra Nevada granitoid basement rocks have more radiogenic Sr compared to the enclave-host mixing trends illustrated in Figures 5a and 5c—a feature explored in the discussion section. $^{143}Nd/^{144}Nd$ ratios of sample Enclave CC-E-I-10 (core and rim samples) are slightly lower than that of other enclaves. Measured $^{143}Nd/^{144}Nd$ of CC-E-I-10 core ($^{143}Nd/^{144}Nd$ = 0.512771) is lower than that of CC-E-I-10 rim ($^{143}Nd/^{144}Nd$ = 0.512780), well outside of analytical error; the lowest $^{143}Nd/^{144}Nd$ for any other enclave examined is $^{143}Nd/^{144}Nd$ = 0.512780 for CC-F-I-10 core (Table 4). Again, it should be noted that $^{143}Nd/^{144}Nd$ of the most evolved mafic enclaves analyzed in this study overlap those of host lavas ($^{143}Nd/^{144}Nd$ = 0.512793-0.512779), and that measured $^{143}Nd/^{144}Nd$ for CC-E-I-10 carries an isotopic signature that is more radiogenic than even that of Chaos Crags host lavas (Fig. 5).

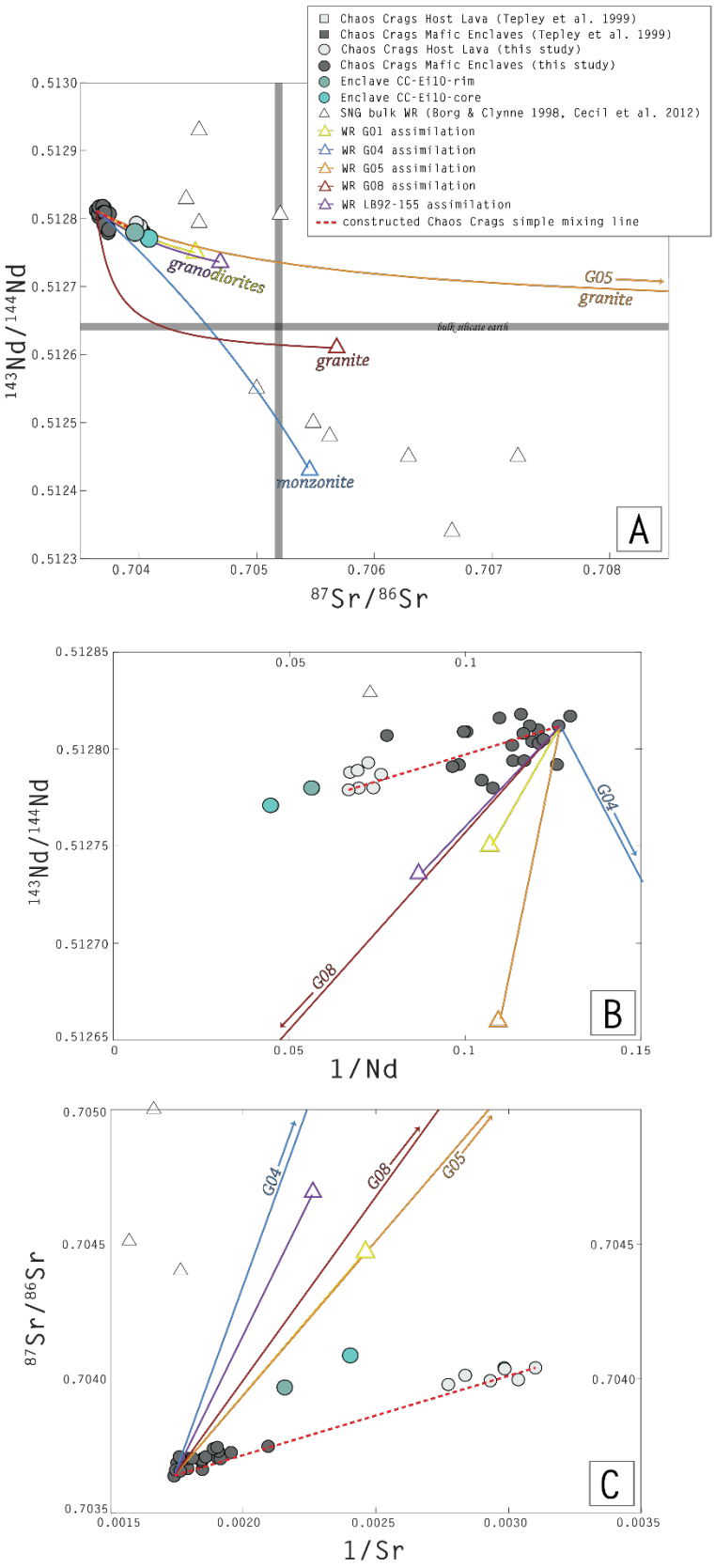

Figure 5. Sr-Nd isotope systematics of Chaos Crags mafic eruptive products (circles and squares), and reported northern Sierra Nevada granitoid (*sensu lato*) wallrock compositions (triangles). Two-endmember mixing between our least radiogenic mafic sample and Chaos Crags host lavas is represented by the red dashed line; notably, enclave CC-E-I-10 lies demonstrably off this mixing line. Wallrock compositions tested in this study are shown by the colored triangles, and the corresponding colored lines represented inferred compositional variations that would result from assimilation of that particular wallrock.

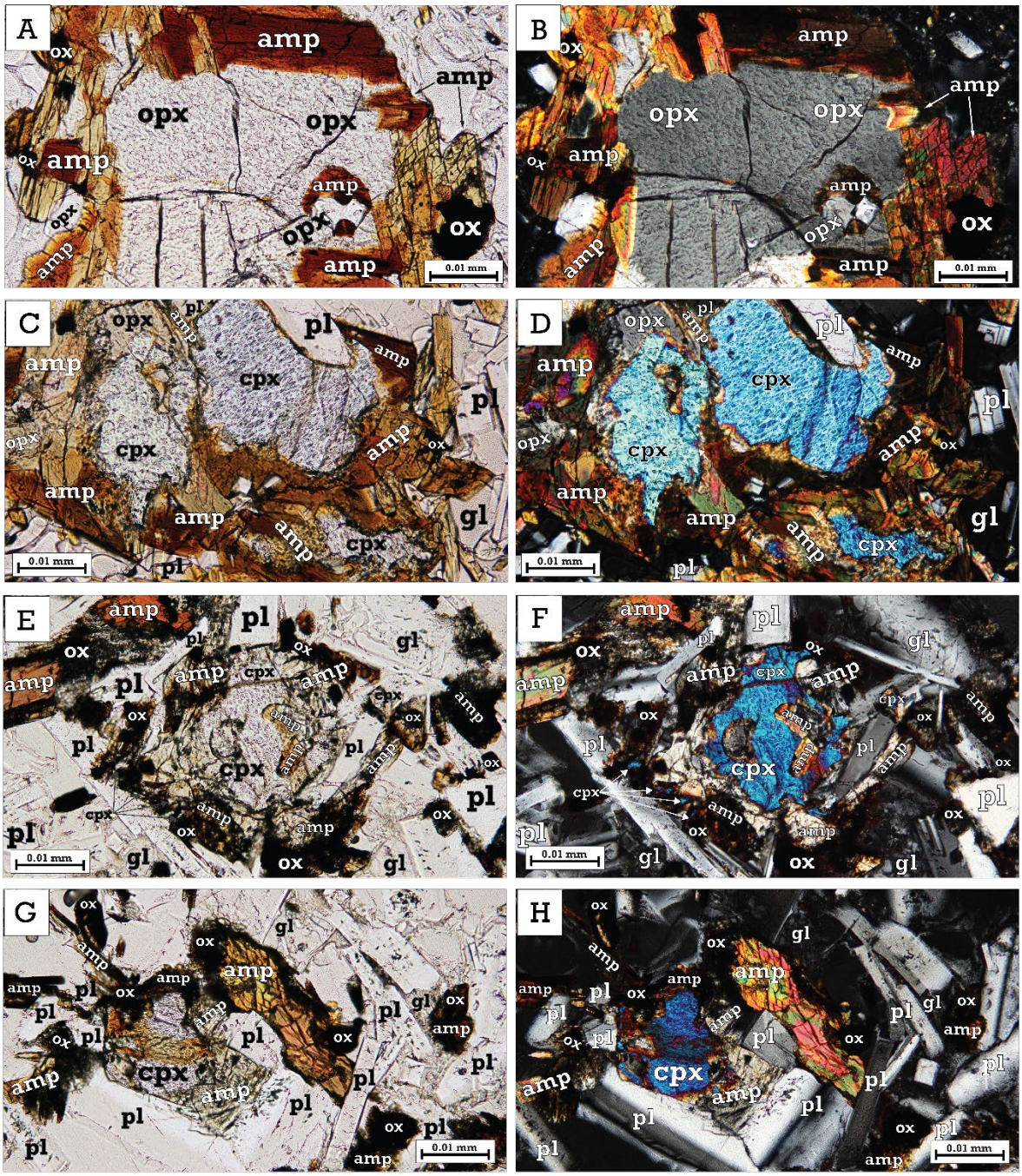

Figure 6. Hydrous crystallization of amphibole after primary pyroxene within Chaos Crags mafic enclaves. Although many enclaves have amphibole as a volumetrically significant groundmass phase, closer inspection of both phenocrystic and groundmass amphibole display relict pyroxene cores. Enclave-derived orthopyroxene in host rhyodacite near enclave-host boundary as seen in PPL (a) and XPL (b); the xenocryst is mantled by well-developed, euhedral amphibole, perhaps due to the high wt.% H_2O present in host lavas. A plagioclase + pyroxene glomerocryst in the rim of enclave CC-A-I-13 displays relict pyroxene cores, mantled by amphibole and Fe-Ti oxides in PPL (c) and XPL (d). Uralitic amphibole and Fe-Ti oxides after clinopyroxene are present as groundmass phases in enclave CC-C-I-11; PPL (e and g) and XPL (f and h).

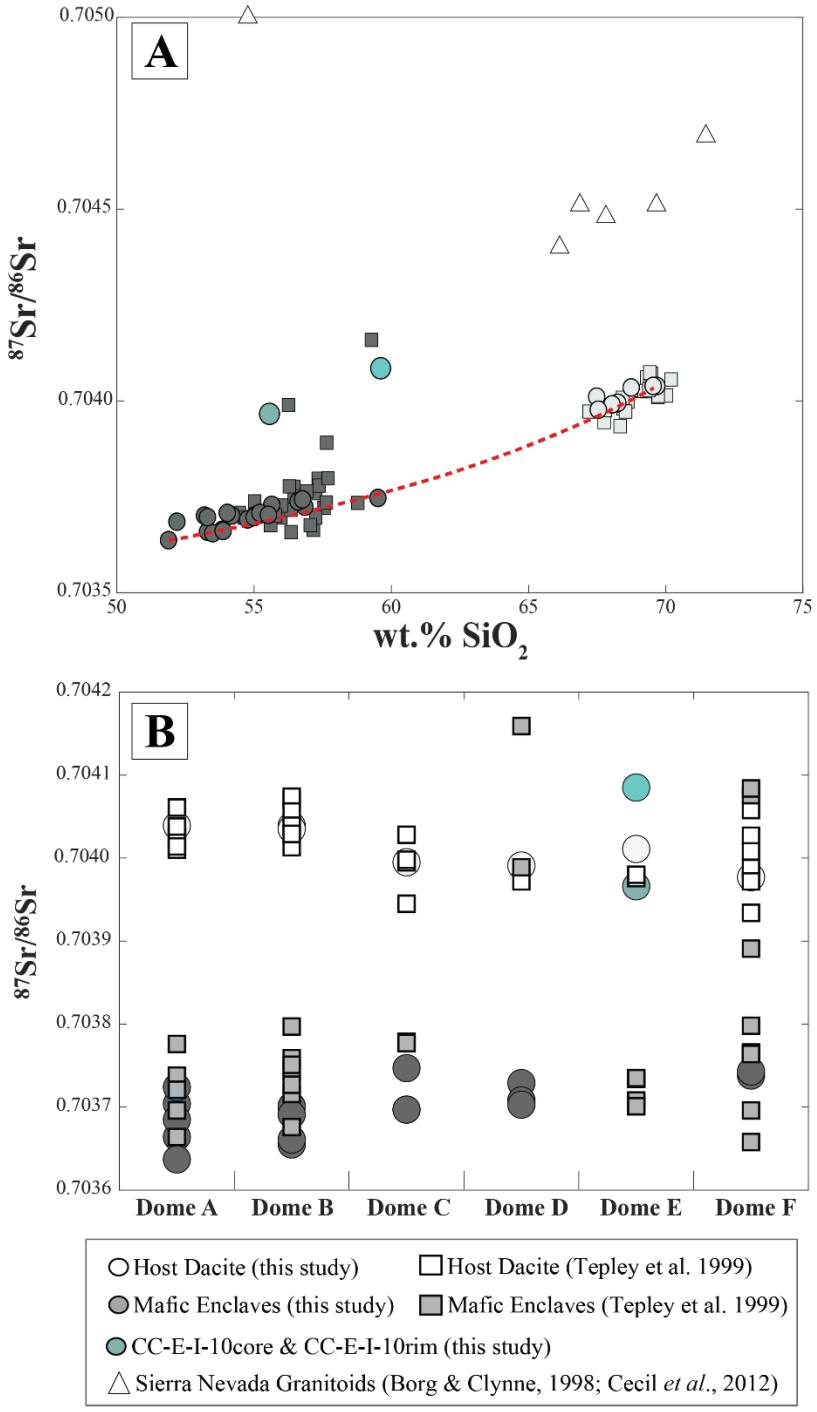

Figure 7. $^{87}Sr/^{86}Sr$ vs. wt.% SiO_2 (A), and arranged temporally by dome eruption (B; modified from Tepley *et al.*, 1999) for Chaos Crags mafic enclaves and host lavas reported in Tepley *et al.* (1999) and this study. Mafic enclaves with anomalously high $^{87}Sr/^{86}Sr$ (i.e., $^{87}Sr/^{86}Sr \geq 0.7039$) are present only in the later domes, and their positive correlation with SiO_2 (wt.%) is suggestive of an initially uniform mafic endmember composition (Bullen & Clynne, 1990). Analytical uncertainty is less than symbol size.

Table 3. Major Oxide and CIPW Normative Compositions for Mafic Enclaves.

Sample	CC-A-I-13 core*	CC-A-I-13 inner rim*	CC-A-I-13 outer rim*	CC-A-I-14 core	CC-A-I-14 rim	CC-A-I-16 inner core	CC-A-I-16 outer core	CC-A-I-16 rim	CC-UPF-I-1 core*	CC-UPF-I-1 rim*
SiO_2	53.84	55.25	56.85	53.04	54.33	53.83	54.44	55.67	51.88	52.19
TiO_2	0.64	0.65	0.60	0.73	0.70	0.71	0.69	0.69	0.66	0.68
Al_2O_3	19.03	18.73	18.26	18.69	18.63	18.53	18.76	18.57	18.55	19.37
FeO_{tot}	8.18	7.91	7.25	8.37	7.98	7.76	7.78	7.16	8.25	8.29
MnO	0.14	0.13	0.12	0.15	0.15	0.14	0.14	0.14	0.14	0.13
MgO	5.18	4.66	4.18	4.66	4.42	4.65	4.58	4.42	5.71	5.36
CaO	9.67	8.88	8.06	9.62	9.30	9.32	9.28	8.87	10.31	9.93
Na_2O	2.63	2.73	3.04	3.89	3.23	3.87	3.15	3.22	2.74	2.78
K_2O	0.96	1.16	1.35	0.84	0.90	1.05	0.96	1.05	0.78	0.64
P_2O_5	0.09	0.10	0.10	0.12	0.12	0.10	0.09	0.11	0.64	--
Sum	100.36	100.20	99.81	100.12	99.76	99.94	99.88	99.90	99.10	99.35
LOI:	0.71	0.80	0.07	5.67	1.40	2.52	2.27	0.96	0.43	1.94
Qtz	4.24	6.5	8.23	--	4.10	--	4.17	5.96	2.06	2.11
Or	5.67	6.86	7.98	4.97	5.30	6.20	5.69	6.21	4.08	3.78
Ab	22.25	23.10	25.72	32.95	27.34	32.52	26.68	27.27	24.62	23.52
An	37.28	35.43	32.19	31.05	33.68	30.21	34.20	33.09	37.29	38.48
Di (wo)	4.46	3.60	3.25	6.64	4.88	6.41	4.70	4.25	4.80	4.50
Di (en)	2.44	1.92	1.72	3.47	2.54	3.45	2.51	2.32	2.64	2.48
Di (fs)	1.86	1.57	1.43	2.98	2.20	2.75	2.04	1.78	1.98	1.85
Hy (en)	10.47	9.69	8.69	5.80	8.47	8.07	8.89	8.70	10.31	10.86
Hy (fs)	8.00	7.91	7.24	4.99	7.33	6.42	7.24	6.68	7.75	8.08
Ol (fo)	--	--	--	1.63	--	0.04	--	--	--	--
Ol (fa)	--	--	--	1.55	--	0.03	--	--	--	--
Mt	2.37	2.29	2.10	2.43	2.31	2.25	2.26	2.08	2.36	2.40
Il	1.22	1.23	1.14	1.39	1.33	1.35	1.30	1.30	1.31	1.28
Ap	--	--	--	0.27	0.27	0.24	0.21	0.26	0.19	--

*major oxide composition from Scruggs & Putirka (2018)

Table 3, cont'd. Major Oxide and CIPW Normative Compositions for Mafic Enclaves.

Sample	CC-B-I-11 core*	CC-B-I-11 rim	CC-B-I-17 core	CC-B-I-17 rim	CC-B-I-9 inner core*	CC-B-I-9 outer core*	CC-B-I-9 inner rim*	CC-B-I-9 mid rim*	CC-B-I-9 outer rim*	LHCC-B-6 core
SiO_2	54.18	55.02	53.81	53.75	53.30	53.49	53.87	53.19	54.76	54.52
TiO_2	0.77	0.68	0.69	0.68	0.70	0.66	0.66	0.66	0.69	0.67
Al_2O_3	18.66	18.47	18.64	18.54	18.80	18.75	18.67	18.58	18.47	18.51
FeO_{tot}	8.13	7.73	8.09	8.02	8.35	8.44	8.39	8.35	7.94	8.08
MnO	0.13	0.14	0.14	0.14	0.14	0.15	0.14	0.14	0.13	0.15
MgO	4.95	4.52	4.71	4.81	4.84	4.78	4.67	4.96	4.28	4.66
CaO	9.23	8.99	9.76	9.81	10.11	10.10	9.97	10.07	9.25	9.16
Na_2O	2.94	2.82	2.91	2.82	2.89	2.91	2.94	2.84	3.02	3.16
K_2O	1.18	1.39	1.17	1.12	0.79	0.85	0.94	0.97	1.13	0.88
P_2O_5	--	0.09	0.10	0.09	0.07	0.07	0.07	0.07	0.07	0.12
Sum	100.17	99.83	100.02	99.80	99.99	100.20	100.32	99.83	99.74	99.91
LOI:	1.43	1.39	1.61	1.92	1.61	1.76	1.40	1.45	0.76	1.54
Qtz	3.55	5.62	3.25	3.64	3.20	3.14	3.47	2.72	5.14	4.48
Or	6.97	8.20	6.92	6.63	4.67	5.02	5.56	5.73	6.68	5.20
Ab	24.88	23.83	24.65	23.89	24.45	24.62	24.88	24.03	25.55	26.74
An	34.23	33.66	34.32	34.61	35.99	35.59	34.97	35.08	33.50	33.72
Di (wo)	4.82	4.31	5.60	5.61	5.72	5.87	5.86	6.02	4.98	4.57
Di (en)	2.62	2.30	2.97	3.01	3.03	3.07	3.05	3.21	2.57	2.41
Di (fs)	2.03	1.88	2.45	2.41	2.51	2.63	2.65	2.62	2.28	2.02
Hy (en)	9.71	8.97	8.75	8.97	9.03	8.83	8.58	9.14	8.09	9.20
Hy (fs)	7.54	7.33	7.22	7.18	7.48	7.56	7.46	7.44	7.18	7.69
Ol (fo)	--	--	--	--	--	--	--	--	--	--
Ol (fa)	--	--	--	--	--	--	--	--	--	--
Mt	2.36	2.24	2.35	2.33	2.42	2.45	2.43	2.42	2.30	2.34
Il	1.46	1.28	1.32	1.30	1.33	1.25	1.25	1.25	1.31	1.27
Ap	0.01	0.22	0.24	0.21	0.17	0.16	0.16	0.16	0.16	0.28

*major oxide composition from Scruggs & Putirka (2018)

Table 3, cont'd. Major Oxide and CIPW Normative Compositions for Mafic Enclaves.

Sample	LHCC-B-6 rim	CC-C-I-1 core*	CC-C-I-1 rim*	CC-C-I-11 inner core*	CC-C-I-11 core*	CC-C-I-11 rim*	CC-C-I-13 core	CC-C-I-13 rim	CHCC-0921 core*	CHCC-0921 inner rim*
SiO_2	55.04	56.99	56.45	53.30	55.00	59.51	55.77	56.14	55.15	54.71
TiO_2	0.68	0.71	0.66	0.65	0.65	0.61	0.69	0.69	0.71	0.70
Al_2O_3	18.68	17.95	18.15	18.91	18.64	17.67	18.63	18.32	18.18	18.21
FeO_{tot}	7.94	7.10	7.73	8.27	8.06	6.41	7.53	7.31	7.75	7.84
MnO	0.14	0.12	0.14	0.14	0.14	0.11	0.13	0.13	0.13	0.13
MgO	4.65	4.27	4.19	5.04	4.72	3.63	4.13	4.00	4.81	4.91
CaO	9.10	8.13	8.91	9.72	9.07	7.26	8.57	8.32	9.09	9.21
Na_2O	3.01	3.34	3.15	2.85	3.02	3.34	3.22	3.54	3.01	2.95
K_2O	0.90	1.44	1.06	0.85	1.02	1.54	1.17	1.38	1.25	1.22
P_2O_5	0.10	0.09	0.08	0.09	0.09	0.10	0.12	0.12	0.08	0.08
Sum	100.26	100.14	100.52	99.82	100.41	100.18	99.97	99.97	100.16	99.96
LOI:	1.62	1.30	2.56	1.70	1.80	2.17	1.97	2.26	2.44	2.04
Qtz	5.71	6.90	7.21	3.28	5.08	11.50	6.23	5.11	4.88	4.47
Or	5.31	8.51	6.26	5.02	6.03	9.10	6.94	8.17	7.39	7.21
Ab	25.47	28.26	26.65	24.12	25.55	28.26	27.23	29.99	25.47	24.96
An	34.82	29.73	32.25	36.29	34.29	28.67	32.92	30.01	32.40	32.84
Di (wo)	4.04	4.18	4.78	4.75	4.23	2.80	3.67	4.36	5.09	5.16
Di (en)	2.15	2.26	2.47	2.56	2.24	1.48	1.91	2.27	2.78	2.82
Di (fs)	1.76	1.77	2.19	2.03	1.85	1.24	1.66	1.97	2.13	2.15
Hy (en)	9.44	8.37	7.97	10.00	9.51	7.56	8.37	7.70	9.20	9.41
Hy (fs)	7.73	6.54	7.06	7.94	7.84	6.32	7.26	6.68	7.04	7.16
Ol (fo)	--	--	--	--	--	--	--	--	--	--
Ol (fa)	--	--	--	--	--	--	--	--	--	--
Mt	2.30	2.06	2.24	2.40	2.34	1.86	2.18	2.12	2.25	2.27
Il	1.30	1.35	1.25	1.23	1.23	1.16	1.32	1.30	1.35	1.33
Ap	0.24	0.21	0.18	0.20	0.21	0.22	0.28	0.28	0.18	0.17

*major oxide composition from Scruggs & Putirka (2018)

Table 3, cont'd. Major Oxide and CIPW Normative Compositions for Mafic Enclaves.

Sample	CHCC-0921 outer rim*	CC-D-I-1 core*	CC-D-I-1 rim*	CC-D-I-2 core*	CC-D-I-2 rim*	CC-D-I-4 core*	CC-D-I-4 rim*	CC-D-I-5 core*	CC-D-I-5 rim*	CC-E-I-10 core*
SiO_2	57.13	54.02	55.64	57.73	57.94	54.19	54.11	55.21	55.52	59.61
TiO_2	0.73	0.67	0.63	0.62	0.61	0.80	0.81	0.84	0.81	0.63
Al_2O_3	17.77	19.21	18.56	18.36	18.31	19.41	19.36	18.37	18.67	17.17
FeO_{tot}	6.98	7.95	7.56	6.91	6.76	8.70	8.80	8.64	8.69	5.72
MnO	0.11	0.13	0.13	0.12	0.12	0.14	0.14	0.14	0.14	0.15
MgO	4.33	4.92	4.52	3.97	3.79	3.96	3.76	4.10	3.86	3.95
CaO	8.09	9.80	9.02	8.02	7.88	9.01	8.83	8.40	8.35	6.52
Na_2O	3.18	2.91	2.94	3.35	3.38	3.15	3.06	3.43	3.48	4.31
K_2O	1.46	0.78	1.13	1.26	1.33	0.76	0.80	0.94	0.94	1.75
P_2O_5	0.09	0.08	0.09	0.09	0.09	0.11	0.13	0.11	0.11	0.15
Sum	99.87	100.47	100.22	100.42	100.21	100.23	99.80	100.18	100.57	99.96
LOI:	2.97	2.46	2.10	2.42	2.61	4.16	3.34	1.50	1.61	2.49
Qtz	7.9	4.06	6.44	8.54	8.91	4.98	5.69	5.18	5.43	7.30
Or	8.63	4.61	6.68	7.45	7.86	4.49	4.73	5.56	5.56	10.34
Ab	26.91	24.62	24.88	28.35	28.60	26.65	25.89	29.02	29.45	36.47
An	29.90	37.05	34.11	31.34	30.86	36.58	36.73	31.95	32.55	22.33
Di (wo)	4.04	4.61	4.21	3.28	3.18	3.08	2.61	3.77	3.42	3.78
Di (en)	2.22	2.51	2.26	1.74	1.67	1.49	1.23	1.86	1.63	2.15
Di (fs)	1.67	1.94	1.81	1.44	1.42	1.55	1.36	1.84	1.74	1.46
Hy (en)	8.56	9.75	9.00	8.15	7.77	8.38	8.14	8.35	7.98	7.69
Hy (fs)	6.43	7.56	7.24	6.75	6.61	8.73	9.04	8.29	8.51	5.23
Ol (fo)	--	--	--	--	--	--	--	--	--	--
Ol (fa)	--	--	--	--	--	--	--	--	--	--
Mt	2.02	2.31	2.19	2.00	1.96	2.52	2.55	2.51	2.52	1.66
Il	1.39	1.27	1.20	1.18	1.16	1.52	1.54	1.60	1.54	1.20
Ap	0.20	0.19	0.20	0.21	0.22	0.26	0.29	0.24	0.24	0.34

*major oxide composition from Scruggs & Putirka (2018)

Table 3, cont'd. Major Oxide and CIPW Normative Compositions for Mafic Enclaves.

Sample	CC-E-I-10 rim*	CC-E-I-12 core*	CC-E-I-12 inner rim*	CC-E-I-12 outer rim*	CC-E-I-16 core*	CC-E-I-16 rim*	CHCC-0813 core	CHCC-0813 rim	CC-F-I-10 core*	CC-F-I-10 rim*
SiO_2	55.56	55.73	56.88	58.06	56.12	57.11	57.52	53.42	56.60	56.76
TiO_2	0.64	0.73	0.65	0.62	0.72	0.72	0.71	0.78	0.67	0.65
Al_2O_3	18.12	18.52	18.13	18.04	18.41	18.18	18.14	18.96	18.53	18.53
FeO_{tot}	7.79	7.55	7.47	6.75	7.57	7.48	6.88	8.30	7.41	7.25
MnO	0.13	0.13	0.13	0.12	0.13	0.13	0.12	0.14	0.12	0.12
MgO	4.31	4.18	4.19	3.74	4.19	3.95	3.94	4.95	4.08	4.10
CaO	9.04	9.15	8.90	8.21	8.99	8.44	7.73	9.42	8.21	8.17
Na_2O	3.12	3.01	3.02	3.10	3.22	3.17	3.39	2.96	3.23	3.22
K_2O	0.96	1.07	1.13	1.44	1.06	1.27	1.17	0.94	1.10	1.19
P_2O_5	0.07	0.08	0.08	0.07	0.08	0.09	0.10	0.09	0.11	0.11
Sum	99.74	100.12	100.56	100.15	100.49	100.53	99.70	99.96	100.04	100.07
LOI:	2.56	1.64	1.19	2.03	1.62	1.38	2.27	1.98	2.51	1.48
Qtz	6.43	6.89	8.24	9.89	6.45	8.19	8.99	3.09	7.79	7.83
Or	5.67	6.29	6.68	8.51	6.26	7.51	6.91	5.56	6.50	7.03
Ab	26.40	25.43	25.51	26.23	27.25	26.78	28.69	25.05	27.33	27.20
An	32.60	33.90	32.58	31.06	32.65	31.63	30.82	35.67	32.81	32.61
Di (wo)	4.93	4.58	4.63	3.85	4.77	4.03	2.88	4.38	3.02	3.00
Di (en)	2.56	2.40	2.42	2.01	2.50	2.07	1.54	2.36	1.57	1.58
Di (fs)	2.23	2.05	2.07	1.73	2.14	1.85	1.26	1.87	1.36	1.33
Hy (en)	8.17	8.00	8.01	7.30	7.94	7.77	8.28	9.97	8.58	8.63
Hy (fs)	7.11	6.83	6.85	6.27	6.79	6.95	6.77	7.92	7.43	7.27
Ol (fo)	--	--	--	--	--	--	--	--	--	--
Ol (fa)	--	--	--	--	--	--	--	--	--	--
Mt	2.26	2.19	2.17	1.96	2.20	2.17	2.00	2.41	2.15	2.10
Il	1.22	1.39	1.23	1.18	1.37	1.37	1.35	1.48	1.26	1.23
Ap	0.16	0.17	0.17	0.16	0.18	0.21	0.22	0.20	0.25	0.25

*major oxide composition from Scruggs & Putirka (2018)

Table 4. Trace Element Abundances and Isotopic Compositions of Mafic Enclaves.

Sample	CC-A-I-13 core	CC-A-I-13 inner rim	CC-A-I-13 outer rim	CC-A-I-14 core	CC-A-I-14 rim	CC-A-I-16 inner core	CC-A-I-16 outer core	CC-A-I-16 rim	CC-UPF-I-1 core
Rb	18.2	23.1	27.1	9.9	12.2	16.3	15.2	16.7	9.1
Ba	202	264	311	188	195	220	228	242	173
Zr	54	63	72	54	57	56	58	61	47
Sr	559	525	512	574	563	552	555	533	575
Y	12.9	13.8	15.0	15.1	13.8	13.9	13.9	13.7	13.7
Ni	42.8	33.5	33.9	51.9	41.4	37.2	37.8	33.1	35.3
Sc	32.1	29.8	27.6	32.5	31.6	30.9	30.5	29.6	32.4
Cr	46.7	39.5	33.3	31.2	41.6	32.2	31.2	33.7	37.0
Cs	0.7	1.0	1.3	0.4	0.6	0.7	0.7	0.8	0.4
Hf	1.5	1.6	2.0	1.6	1.7	1.6	1.6	1.6	1.5
Th	1.5	2.5	3.6	1.4	1.8	1.9	1.9	2.3	1.2
U	0.6	1.0	1.3	0.5	0.5	0.7	0.7	0.9	0.4
La	5.5	7.5	9.2	5.9	6.0	6.3	6.7	7.1	5.0
Ce	13.6	16.9	19.5	13.7	12.5	15.0	15.0	16.5	12.2
Pb	2.2	4.1	3.8	2.6	2.5	2.7	2.8	3.1	1.8
Pr	1.8	2.1	2.4	1.9	1.8	1.9	2.0	2.1	1.7
Nd	8.3	9.1	10.2	8.6	8.7	8.6	8.7	9.2	7.9
Sm	2.1	2.3	2.3	2.3	2.3	2.2	2.2	2.2	2.1
Eu	0.8	0.8	0.8	0.8	0.9	0.8	0.8	0.8	0.8
Gd	2.2	2.1	2.4	2.5	2.4	2.2	2.4	2.5	2.3
Tb	0.4	0.4	0.4	0.4	0.4	0.4	0.4	0.4	0.3
Dy	2.2	2.3	2.5	2.6	2.7	2.5	2.4	2.6	2.3
Ho	0.5	0.5	0.5	0.5	0.5	0.5	0.5	0.5	0.5
Er	1.4	1.4	1.4	1.6	1.7	1.5	1.5	1.5	1.5
Tm	0.2	0.2	0.2	0.3	0.3	0.2	0.2	0.2	0.2
Yb	1.4	1.4	1.4	1.6	1.7	1.5	1.5	1.5	1.3
Lu	0.2	0.2	0.2	0.2	0.2	0.2	0.2	0.2	0.2
$^{87}Sr/^{86}Sr$	0.703664	0.703704	0.703724	--	--	--	--	--	0.703637
$^{143}Nd/^{144}Nd$	0.512810	0.512816	0.512792	--	--	--	--	--	0.512812

Table 4, cont'd. Trace Element Abundances and Isotopic Compositions of Mafic Enclaves.

Sample	CC-UPF-I-1 rim	CC-B-I-11 core	CC-B-I-11 rim	CC-B-I-17 core	CC-B-I-17 rim	CC-B-I-9 inner core	CC-B-I-9 outer core	CC-B-I-9 inner rim	CC-B-I-9 middle rim
Rb	12.0	28.5	34.0	23.2	23.2	11.1	14.6	15.2	19.8
Ba	189	224	276	203	204	185	191	181	191
Zr	50	55	57	56	56	53	56	52	50
Sr	571	541	523	548	548	573	567	542	559
Y	14.5	14.1	13.4	14.1	14.0	13.9	13.5	13.3	14.0
Ni	39.1	38.0	38.1	34.0	32.9	31.5	41.8	32.5	41.0
Sc	32.8	32.6	30.0	33.3	34.0	32.0	31.1	29.8	32.4
Cr	32.8	40.2	40.8	44.6	45.4	32.4	35.3	25.5	34.1
Cs	0.5	0.9	1.3	0.7	0.7	0.5	0.6	0.6	0.7
Hf	1.5	1.5	1.7	1.6	1.6	1.6	1.5	1.4	1.4
Th	1.5	1.6	2.3	1.7	1.7	1.4	1.4	1.6	1.5
U	0.5	0.6	0.9	0.6	0.6	0.5	0.6	0.6	0.6
La	5.7	5.8	7.1	6.0	6.0	5.7	5.5	5.3	5.6
Ce	13.4	14.1	16.0	14.3	14.2	13.2	13.9	12.9	13.4
Pb	3.0	4.1	4.6	3.2	3.2	2.7	3.0	2.5	3.0
Pr	1.9	1.9	2.0	1.9	1.9	1.8	1.8	1.8	1.8
Nd	8.5	8.4	8.8	8.5	8.6	8.3	8.6	7.7	8.2
Sm	2.2	2.2	2.2	2.3	2.2	2.1	2.1	2.1	2.3
Eu	0.8	0.8	0.7	0.8	0.8	0.8	0.8	0.8	0.8
Gd	2.3	2.2	2.3	2.4	2.4	2.3	2.2	2.1	2.5
Tb	0.4	0.4	0.4	0.4	0.4	0.4	0.4	0.3	0.4
Dy	2.4	2.5	2.3	2.3	2.4	2.3	2.4	2.4	2.4
Ho	0.5	0.5	0.5	0.5	0.5	0.6	0.5	0.5	0.5
Er	1.6	1.5	1.4	1.6	1.6	1.5	1.5	1.4	1.5
Tm	0.2	0.2	0.2	0.2	0.2	0.2	0.2	0.2	0.2
Yb	1.5	1.5	1.5	1.4	1.5	1.5	1.5	1.4	1.6
Lu	0.3	0.2	0.2	0.3	0.2	0.2	0.2	0.2	0.2
$^{87}Sr/^{86}Sr$	0.703685	0.703701	0.703701	--	--	0.703659	0.703655	0.703661	0.703701
$^{143}Nd/^{144}Nd$	0.512812	0.512804	0.512794	--	--	0.512803	0.512808	0.512817	0.512805

Table 4, cont'd. Trace Element Abundances and Isotopic Compositions of Mafic Enclaves.

Sample	CC-B-I-9 outer rim	LHCC-B-6 core	LHCC-B-6 rim	CC-C-I-1 core	CC-C-I-1 rim	CC-C-I-11 inner core	CC-C-I-11 core	CC-C-I-11 rim	CC-C-I-13 core
Rb	26.2	12.7	16.1	19.2	24.0	16.5	19.1	42.4	21.2
Ba	268	208	227	259	28	202	238	465	281
Zr	55	59	60	59	59	54	60	82	71
Sr	542	551	541	532	526	565	542	478	526
Y	13.1	14.2	14.0	15.7	15.0	14.0	14.3	16.6	15.2
Ni	39.5	30.8	27.6	43.0	40.3	54.2	56.4	35.9	44.0
Sc	27.6	30.2	29.1	30.6	29.0	31.9	30.1	28.3	27.6
Cr	30.3	36.3	41.4	19.9	29.6	47.7	39.6	37.5	31.4
Cs	1.3	0.6	0.8	1.1	1.4	1.7	0.9	2.7	2.5
Hf	1.6	1.7	1.5	2.0	1.9	1.6	1.7	2.6	1.9
Th	2.4	1.8	1.7	2.7	2.8	1.5	2.2	5.7	2.2
U	1.0	0.6	0.7	0.7	1.0	0.7	0.9	2.1	0.9
La	7.1	6.3	6.7	8.1	8.3	7.0	8.0	13.8	8.0
Ce	16.3	14.4	15.3	15.2	18.2	14.3	16.6	27.1	18.2
Pb	4.7	2.7	3.3	3.5	3.2	3.2	3.0	6.0	3.6
Pr	2.1	1.9	2.0	2.1	2.3	2.2	2.4	3.3	2.3
Nd	8.6	8.6	8.7	9.5	9.8	8.8	10.0	12.9	10.1
Sm	2.2	2.1	2.3	2.4	2.6	2.3	2.4	2.9	2.5
Eu	0.8	0.7	0.8	0.8	0.8	0.8	0.8	0.9	0.8
Gd	2.3	2.4	2.5	2.6	2.5	2.3	2.4	2.8	2.6
Tb	0.3	0.4	0.4	0.4	0.4	0.4	0.4	0.4	0.4
Dy	2.5	2.4	2.4	2.7	2.5	2.4	2.3	2.6	2.5
Ho	0.5	0.5	0.5	0.6	0.5	0.5	0.5	0.6	0.6
Er	1.4	1.6	1.6	1.7	1.6	1.5	1.4	1.8	1.7
Tm	0.2	0.2	0.2	0.2	0.2	0.2	0.2	0.3	0.2
Yb	1.4	1.6	1.5	1.7	1.6	1.5	1.5	1.8	1.6
Lu	0.2	0.2	0.2	0.3	0.3	0.2	0.2	0.3	0.3
$^{87}Sr/^{86}Sr$	0.703691	--	--	--	--	0.703697	0.703697	0.703747	--
$^{143}Nd/^{144}Nd$	0.512818	--	--	--	--	0.512802	0.512809	0.512807	--

Table 4, cont'd. Trace Element Abundances and Isotopic Compositions of Mafic Enclaves.

Sample	CC-C-I-13 rim	CHCC-0921 core	CHCC-0921 inner rim	CHCC-0921 outer rim	CC-D-I-1 core	CC-D-I-1 rim	CC-D-I-2 core	CC-D-I-2 rim	CC-D-I-4 core
Rb	29.7	29.2	28.1	39.3	14.0	27.8	34.3	34.8	8.6
Ba	298	247	256	339	214	269	331	379	210
Zr	76	59	55	57	54	64	73	79	57
Sr	514	500	495	467	568	525	512	505	573
Y	14.8	13.9	13.4	13.2	13.0	11.9	13.1	12.0	15.8
Ni	51.9	60.6	46.3	66.9	24.8	26.8	40.1	23.7	56.9
Sc	26.5	33.9	32.8	29.0	32.6	28.7	26.0	24.8	32.3
Cr	34.0	42.8	47.4	40.9	47.6	50.9	32.2	41.6	31.9
Cs	3.3	1.7	1.3	2.4	1.1	1.9	1.5	2.1	1.7
Hf	2.0	1.7	1.6	1.6	1.5	1.7	1.9	2.1	1.7
Th	2.5	2.0	2.0	5.0	1.7	2.4	3.0	3.7	2.1
U	1.0	0.7	0.7	1.8	0.7	1.0	1.4	1.7	0.7
La	8.4	6.5	6.5	10.5	6.0	7.2	8.5	9.6	7.0
Ce	19.2	14.1	14.6	21.7	13.7	16.9	20.1	21.8	17.3
Pb	4.4	3.8	3.5	5.4	2.2	3.8	4.5	4.3	2.3
Pr	2.5	1.9	1.9	2.6	1.8	2.1	2.5	2.5	2.3
Nd	10.2	8.5	8.4	9.8	7.9	8.6	9.8	9.4	10.0
Sm	2.3	2.2	2.0	2.3	1.9	2.0	2.3	2.1	2.5
Eu	0.9	0.7	0.8	0.8	0.8	0.8	0.8	0.8	0.9
Gd	2.5	2.3	2.1	2.1	2.0	2.1	2.4	2.2	2.7
Tb	0.4	0.4	0.3	0.4	0.4	0.3	0.4	0.3	0.4
Dy	2.5	2.3	2.3	2.2	2.2	2.3	2.3	2.2	2.9
Ho	0.5	0.5	0.5	0.5	0.5	0.4	0.5	0.4	0.6
Er	1.5	1.4	1.5	1.4	1.4	1.4	1.4	1.3	1.7
Tm	0.2	0.2	0.2	0.2	0.2	0.2	0.2	0.2	0.2
Yb	1.5	1.5	1.5	1.3	1.3	1.4	1.4	1.3	1.6
Lu	0.2	0.2	0.2	0.2	0.2	0.2	0.2	0.2	0.2
$^{87}Sr/^{86}Sr$	--	--	--	--	0.703708	0.703729	--	--	--
$^{143}Nd/^{144}Nd$	--	--	--	--	0.512792	0.512794	--	--	--

Table 4, cont'd. Trace Element Abundances and Isotopic Compositions of Mafic Enclaves.

Sample	CC-D-I-4 rim	CC-D-I-5 core	CC-D-I-5 rim	CC-E-I-10 core	CC-E-I-10 rim	CC-E-I-12 core	CC-E-I-12 inner rim
Rb	10.8	14.7	14.9	50.0	49.4	27.5	26.4
Ba	219	238	247	647	549	354	309
Zr	59	63	62	116	79	73	66
Sr	562	538	553	416	464	513	498
Y	15.3	16.3	16.5	22.8	19.7	12.5	12.9
Ni	57.3	65.3	58.2	24.0	25.8	25.5	35.1
Sc	32.0	32.5	30.3	18.7	22.7	25.6	26.8
Cr	34.1	14.3	11.8	65.2	54.5	39.3	39.3
Cs	3.0	0.7	1.2	2.2	2.4	1.6	1.2
Hf	1.8	1.7	1.8	3.0	2.1	2.1	1.8
Th	2.6	1.9	1.9	6.0	5.0	3.6	2.8
U	1.0	0.7	0.7	2.2	2.2	1.4	1.1
La	7.3	7.1	7.4	20.6	16.5	9.5	8.3
Ce	17.5	16.8	16.9	45.6	37.8	19.9	18.3
Pb	2.0	2.7	3.2	7.6	7.5	4.0	4.0
Pr	2.4	2.2	2.3	5.6	4.7	2.3	2.2
Nd	10.4	10.0	10.4	22.3	17.7	9.1	8.8
Sm	2.6	2.6	2.6	4.7	1.2	2.0	2.1
Eu	0.9	0.9	0.9	1.2	1.0	0.8	0.7
Gd	2.6	2.7	2.8	4.0	3.5	2.1	2.1
Tb	0.4	0.4	0.4	0.6	0.5	0.3	0.3
Dy	2.6	2.9	2.8	3.8	3.5	2.2	2.0
Ho	0.6	0.6	0.6	0.8	0.6	0.4	0.4
Er	1.7	1.8	1.8	2.3	2.1	1.3	1.4
Tm	0.3	0.2	0.3	0.4	0.3	0.2	0.2
Yb	1.5	1.7	1.7	2.3	1.8	1.3	1.5
Lu	0.3	0.3	0.3	0.4	0.3	0.2	0.2
$^{87}Sr/^{86}Sr$	--	0.703708	0.703703	0.704085	0.703966	--	--
$^{143}Nd/^{144}Nd$	--	0.512809	0.512791	0.512771	0.512780	--	--

Table 4, cont'd. Trace Element Abundances and Isotopic Compositions of Mafic Enclaves.

Sample	CC-E-I-12 outer rim	CC-E-I-16 core	CC-E-I-16 rim	CHCC-0813 core	CHCC-0813 rim	CC-F-I-10 core	CC-F-I-10 rim
Rb	32.5	20.6	23.7	27.1	21.3	23.7	25.5
Ba	361	284	276	335	199	300	299
Zr	75	71	64	80	55	69	71
Sr	492	537	527	509	554	530	526
Y	12.9	14.3	12.2	13.6	13.3	13.6	14.0
Ni	21.6	44.0	38.8	26.7	25.7	43.1	38.9
Sc	25.0	29.1	27.2	26.5	30.7	26.3	27.4
Cr	35.8	29.6	40.8	32.7	38.8	77.2	82.8
Cs	1.5	1.0	1.0	1.3	1.2	1.2	1.2
Hf	1.9	2.0	1.6	2.0	1.5	1.7	1.8
Th	3.8	2.7	2.4	3.2	1.3	2.6	2.8
U	1.4	1.0	1.0	1.3	0.5	1.1	1.0
La	9.4	8.4	7.6	9.0	5.3	8.3	8.6
Ce	20.0	17.6	17.1	20.2	13.2	18.8	18.4
Pb	4.3	3.7	3.8	4.6	4.2	4.0	3.8
Pr	2.5	2.3	2.1	2.5	1.8	2.3	2.3
Nd	9.3	9.1	8.8	9.8	8.0	9.3	9.6
Sm	2.3	2.3	2.0	2.4	2.2	2.3	2.2
Eu	0.8	0.8	0.8	0.8	0.8	0.8	0.8
Gd	2.2	2.3	2.0	2.2	2.2	2.3	2.3
Tb	0.4	0.4	0.3	0.4	0.4	0.4	0.4
Dy	2.2	2.5	2.0	2.3	2.4	2.5	2.4
Ho	0.5	0.5	0.5	0.5	0.5	0.5	0.5
Er	1.3	1.6	1.3	1.6	1.6	1.3	1.5
Tm	0.2	0.3	0.2	0.2	0.2	0.2	0.2
Yb	1.4	1.5	1.3	1.5	1.3	1.4	1.4
Lu	0.2	0.2	0.2	0.2	0.2	0.2	0.2
$^{87}Sr/^{86}Sr$	--	--	--	--	--	0.703738	0.703743
$^{143}Nd/^{144}Nd$	--	--	--	--	--	0.512780	0.512784

E. Discussion

At the level of exposure, field relations, petrography, and mineral compositions provide unequivocal evidence for open-system magmatic processes—namely, magma mixing—operating at Chaos Crags (Heiken & Eichelberger, 1980; Tepley *et al*., 1999; Underwood *et al.,* 2012; Scruggs & Putirka, 2018). It is the aim of this study to test the hypothesis that an earlier episode of AFC affected the mafic magmas before shallow level magma mixing, without contesting the occurrence of mixing between rhyodacitic and mafic recharge magmas at this locality.

1. Geochemical Evidence of Upper Crustal Assimilation Processes Operating at Chaos Crags

A magma body is never completely isolated from its surroundings, so there is always the potential for assimilation. We show here that some enclaves bear clear evidence that Chaos Crags mafic endmember magmas intermittently assimilated a Sierra Nevada-like contaminant prior to their mixing with an already-emplaced rhyodacitic crystalline mush underlying the LVC (Klemetti & Clynne, 2014). The variegated nature of this contamination is consistent with wallrock meltback (Bruce & Huppert, 1990) in the middle to upper crust—a likely spatially and temporally variable process (Philpotts & Asher, 1993; Petcovic & Grunder, 2003; Acosta-Vigil *et al.*, 2006; Karlstrom *et al*., 2019).

a. The Anomalous Isotopic Signature of Enclave CC-E-I-10

Enclave CC-E-I-10 is macroscopically and petrographically similar to other basaltic-andesitic enclaves at Chaos Crags, and exhibits no distinct textural or mineralogical differences from core to rim. Moreover, major oxide concentrations of CC-E-I-10 are not

remarkably different from those of other enclaves at Chaos Crags (Fig. 3; Tepley *et al*., 1999; Scruggs & Putirka, 2018). Although on the basis of *major* elements, enclave CC-E-I-10 does not exhibit an unambiguous assimilation signal, trace elements and especially Sr and Nd isotopic ratios tell a different story (Figs. 3-5). $^{87}Sr/^{86}Sr$ and $^{143}Nd/^{144}Nd$ ratios of CC-E-I-10 are respectively higher and lower than $^{87}Sr/^{86}Sr$ and $^{143}Nd/^{144}Nd$ ratios of other mafic enclaves with similar SiO_2 contents; CC-E-I-10 core is especially isotopically evolved, more so than any other sample—*including host rhyodacites*—analyzed in this study (Fig. 7). Similarly, the measured isotopic compositions of CC-E-I-10 lie demonstrably off a constructed mixing line between our most mafic enclave (CC-UPF-I-1core) and the least contaminated host lava sample, as illustrated by the red lines in Figures 5 and 7a– highly inconsistent with two-endmember mixing of parental mafic and rhyodacitic magmas.

Lassen-area mafic enclaves with anomalous trace element and isotopic compositions have been previously reported by Tepley *et al*. (1999) and Feeley *et al*. (2008b). Tepley *et al*. (1999) report major oxide compositions for mafic enclaves that have highly radiogenic $^{87}Sr/^{86}Sr$ compared to others found within Chaos Crags eruptive products (Fig 7). Feeley *et al*. (2008b) report one mafic enclave from the Mt. Helen dome that is texturally and mineralogically similar to other mafic enclaves at Mt. Helen, but has much more enriched trace element concentrations compared to other mafic enclaves at Mt. Helen. In both of these instances, anomalous compositions of the selected mafic enclaves were attributed to mixing between host lavas and some *additional* mafic endmember component—one with a different isotopic composition (Tepley *et al*., 1999), and another derived from low-degree partial melting of a low-wt.% H_2O mantle source (Feeley *et al*., 2008b). Although such hypotheses cannot be eliminated, because mafic magmas ascended through 30-40 km of Sierra Nevada granitoids

(SNG) crust before encountering the shallow-level rhyodacite storage reservoir, we apply the principle of parsimony and argue that AFC of these granitoid rocks is a more likely causative process leading to the observed isotopic variability.

As CC-E-I-10 core is *more* radiogenic than rhyodacitic host magmas, Occam's razor would suggest some degree of interaction with a magma, partial melt, or wallrock much more evolved than the Chaos Crags magma body. Sierra Nevada granitoids (SNG) are quite heterogeneous and isotopically evolved, with a wide variety of major, trace element, and isotopic compositions (Borg & Clynne, 1998; Cecil *et al.,* 2012). SNG underlie the LVC (Berge & Stauber, 1987; Guffanti *et al*., 1990; Feeley *et al.* 2008a), and rare crustal xenoliths with relict granitoid textures have been recovered from Cinder Cone Volcano (Bullen & Clynne, 1990; Borg & Clynne, 1998). Although no SNG crop out within the LVC, SNG compositions in the surrounding area are reported by Borg & Clynne (1998) and Cecil *et al.* (2012), and almost certainly lie within the crustal column at LVC (Berge & Stauber, 1987; Guffanti *et al.*, 1990; Feeley *et al.*, 2008a). A series of mixing lines between the most mafic enclave examined (CC-UPF-I-1) and SNG (Borg & Clynne, 1998; Cecil *et al.* 2012) compositions were constructed to constrain the isotopic composition of a potential assimilant (Fig. 5a). *The isotopic signature of enclave CC-E-I-10 lies almost perfectly along two calculated mixing curves as illustrated in Figure 5a: one between the most mafic measured enclave, CC-UPF-I-1, and SNG composition G01 from Cecil et al. (2012), and the other between CC-UPF-I-1 and SNG composition LB92-155 from Borg & Clynne (1998)*. This evidence strongly suggests that the mafic magma interacted with SNG crust as it made its way to the surface.

2. Phase Equilibria Modeling of Open-System Processes

As noted previously, there is extensive field and geochemical evidence for magma mixing at Chaos Crags (Heiken & Eichelberger, 1980; Tepley *et al.*, 1999; Scruggs & Putirka, 2018). Taking into consideration the isotopic results of Tepley *et al.* (1999) and those presented here, reconciliation necessitates a two-stage petrogenesis (Fig. 8) where some parental mafic melts become variably contaminated by wallrock (WR) during ascent through the mid-to-upper crust (**AFC**). These newly contaminated magmas then mix (**R**) with resident rhyodacitic crystalline mush (Klemetti & Clynne, 2014) to form variably quenched and hybridized mafic enclaves, modifying the composition of the rhyodacitic host magma in the process (Scruggs & Putirka, 2018; Ruprecht *et al.* 2020; Weinberg *et al.*, 2021). To test whether the major and trace element compositions of CC-E-I-10 core can be approximated by assimilating any of the aforementioned SNG compositions, we used phase equilibria models generated by the MCS code (Bohrson *et al.,* 2020*;* Heinonen *et al*., 2020) to model the effects of AFC on the evolution of a single parental mafic magma, prior to its recharge into rhyodacitic magma and enclave formation. The descriptions of and motivations behind our specific modeling techniques are described below.

a. Modeling Contamination of Mafic Magma at Depth (AFC)

Assimilation of WR by mafic magmas is a spatially and temporally irregular process that can produce large variations in trace element and isotope compositions, while not significantly altering the major oxide chemistries of a magma (Taylor, 1980; Reiners *et al.*, 1995; Heinonen *et al.*, 2020; Weinberg *et al.*, 2021). Furthermore, the diversity of dike emplacement histories is consistent with the 'spotty' nature of contamination (Philpotts & Asher, 1993; Karlstrom *et al*., 2019). As SNG (*sensu lato*) compositions vary widely in major and trace elements,

isotopes, and modal mineralogy (Borg & Clynne, 1998; Feeley *et al.*, 2008a; Cecil *et al.* 2012), an attempt to identify the *exact* contaminant is specious. However, after considering crustal xenoliths recovered from the Lassen region (Borg & Clynne, 1998; Feeley *et al.*, 2008b) and the petrologic variability of SNG exposed in the Northern Sierra Nevada (Borg & Clynne, 1998; Cecil *et al.*, 2012), a plausible ensemble of wallrock compositions was used to test the two-stage contamination and mixing (AFC→R) hypothesis by forward modeling. In consideration of the isotopic and elemental diversity of potential assimilants, AFC phase-equilibria (AFC-PhaseEQ) models were generated using the most mafic composition in our data set (CC-UPF-I-1 core) and five WR compositions representative of northern SNG lithic heterogeneity (Table 5; see also Methods). As illustrated in Fig. 8, the modeling approach is a two-step process, wherein the results of AFC-PhaseEQ models (i.e., assimilation of SNG by parental mafic melts, modeled at P = 4 kbar) are the now-contaminated mafic magmas (cM) that serve as starting melt compositions for the shallow (P = 1.45 kbar) R models of cM mixing with host rhyodacite. We present abridged results of the best-fit AFC-PhaseEQ models in Table 7 that constrain F_{mix} by major oxides, trace elements, *and* isotopes; full results of AFC models for all WR tested are provided in Appendix D. AFC-PhaseEQ results should not be directly compared to enclave compositions since enclaves are the end result of the two-stage process of AFC+R. Rather, the AFC results provide estimates for the mafic endmember in subsequent magma mixing models.

Our forward models attempt to replicate different mechanisms by which contamination might have occurred—the assimilation of WR partial melts (**AFC**) in both energetically-constrained and decoupled proportions, isotopically-incongruent melting during crustal anatexis, and also the complete melting and/or reaction of stoped WR blocks (**SFC**). Although

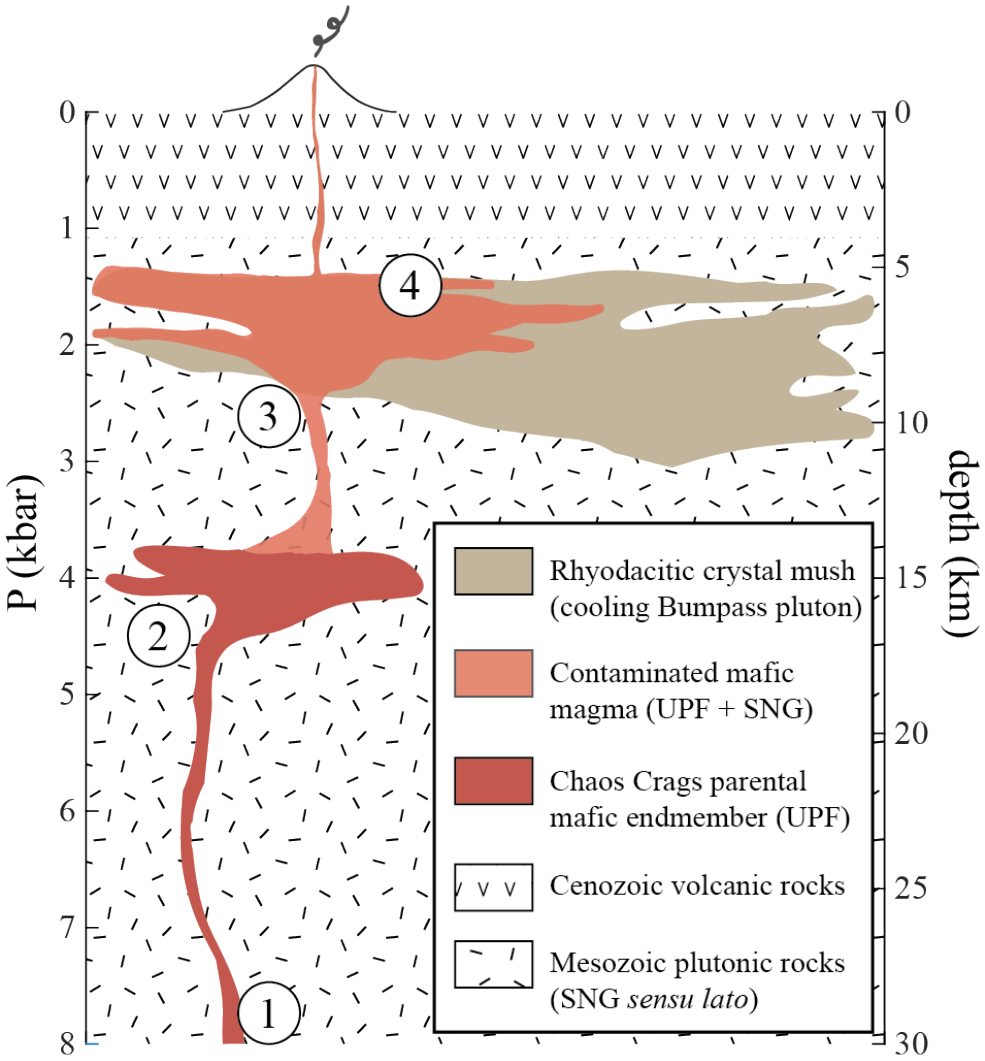

Figure 8. Cartoon cross-section of magma plumbing system [modified from Tavarez (2015)] beneath Chaos Crags. (1) Chaos Crags mafic magma (represented in this study as CCUPFi1core) is generated at depth >30 km (upper mantle or lower crust), and rises upwards through the middle and upper crust. (2) As mafic magma ascends through the crust as a plexus of dikes (but simply represented here), heat is transferred to the surrounding wallrock and the surrounding Sierra Nevada granite (*sensu lato*; SNG) undergoes partial melting, eventually triggering assimilation. (3) *Melt* (cM) from the now-contaminated mafic magma ascends upwards, where it encounters the cooled, partially molten pluton left over from Bumpass volcanism. (4) cM recharges a portion of the Bumpass Pluton, mixing with rhyodacitic host magmas to form basalt-andesitic mafic enclaves, and erupting as the partially hybridized tephra deposits and lava domes of Chaos Crags. Much like the bifurcated plumbing system in this cartoon, our Magma Chamber Simulator (MCS) forward models were constructed as a two-step process. AFC of SNG (#2) by mafic magma UPFi1core was modeled at $P = 4$ kbar. cM is then allowed to rise isentropically (#3) from $P = 4$ *kbar* to $P = 1.45$ *kbar*, undergoing a negligible amount of fractionation. At $P = 1.45$ *kbar*, R is modeled to simulate the now-contaminated mafic melt cM mixing and mingling with Chaos Crags host rhyodacite magma, producing mafic enclaves that have been variably mixed and mingled. Figure is horizontally exaggerated; depth was calculated using crustal $\rho = 2.67$ g/cm^3 (Tavarez (2015).

Table 5. Starting compositions for MCS phase-equilibria, trace element, and isotope AFC models.

	Mafic EM[1]	Host Rhyodacite[2]	SNG WR 1[3]	SNG WR 2[4]	SNG WR 3[5]	SNG WR 4[6]	SNG WR 5[7]
SiO_2 (wt.%)	51.56	67.07	71.32	67.52	59.88	78.78	76.07
TiO_2 (wt.%)	0.66	0.43	0.25	0.28	0.93	0.06	0.16
Al_2O_3 (wt.%)	18.44	14.74	15.05	16.56	19.38	12.06	13.16
Fe_2O_3 (wt.%)	1.23	0.49	0.67	0.52	0.62	0.10	0.34
FeO (wt.%)	6.97	2.13	1.56	2.94	3.53	0.40	1.87
MnO (wt.%)	0.14	*o.m.*	*o.m.*	0.09	0.09	*o.m.*	0.04
MgO (wt.%)	5.67	1.35	0.92	1.25	1.33	0.07	0.14
CaO (wt.%)	10.25	3.09	2.80	4.10	2.80	0.43	1.97
Na_2O (wt.%)	2.72	3.89	4.31	4.15	5.27	3.29	2.91
K_2O (wt.%)	0.78	2.55	2.75	2.15	5.57	4.54	3.32
P_2O_5 (wt.%)	0.08	*o.m.*	*o.m.*	0.09	0.26	0.01	0.03
H_2O (wt.%)	1.49	4.28	0.25	0.25	0.25	0.25	0.25
CO_2 (wt.%)	0.20	*o.m.*	0.10	0.10	0.10	*o.m.*	0.10
Ni (ppm)	35.30	8.15	3	0	0	0	0
Rb (ppm)	9.13	82.7	53	47.87	45.73	244.6	114.2
Sr (ppm)	574.90	335.25	442	405.2	415.8	34.86	187
Y (ppm)	13.72	11.42	16	9.47	13.33	14.44	33.39
Ba (ppm)	172.70	776	983	753.1	1630	97.46	720.3
La (ppm)	5.01	20.53	17	11.47	56.02	13.65	44.57
Nd (ppm)	7.90	14.33	11.5	9.35	4.21	9.14	36.89
Sm (ppm)	4.33	4.5	2.18	2.02	2.02	2.00	7.25
Yb (ppm)	1.33	1.34	0.54	0.98	0.27	1.75	2.45
$^{87}Sr/^{86}Sr$	0.703637	0.704039	0.70469	0.70448	0.70545	0.73463	0.70568
$^{143}Nd/^{144}Nd$	0.512812	0.512780	0.512736	0.51275	0.51243	0.51266	0.51261
$\delta^{18}O$	5.8	7.9	8.9	8.9	8.9	8.9	8.9

[1] Composition calculated by adding 1.5 wt.% H_2O & 0.1 wt.% CO_2 to the composition of the least radiogenic mafic enclave (CC-UPF-I-1core) composition reported this study, then renormalizing to 100 wt.%. $\delta^{18}O$ value from Walowski *et al.* (2016).

[2] Composition calculated by adding 4.5 wt.% H_2O & 0.1 wt.% CO_2 to Sample CC-B-H-2 from this study, then renormalizing to 100 wt.%. $\delta^{18}O$ value from Feeley *et al.* (2008).

[3] Composition calculated by adding 0.25 wt.% H_2O & 0.1 wt.% CO_2 to Sample LB92-155 from Borg & Clynne (1998), then renormalizing to 100 wt.%. $\delta^{18}O$ value after Taylor (1980).

[4] Composition calculated by adding 0.25 wt.% H_2O & 0.1 wt.% CO_2 to Sample G01 from Cecil *et al.* (2012), then renormalizing to 100 wt.%. $\delta^{18}O$ value after Taylor (1980).

[5] Composition calculated by adding 0.25 wt.% H_2O & 0.1 wt.% CO_2 to Sample G04 from Cecil *et al.* (2012), then renormalizing to 100 wt.%. $\delta^{18}O$ value after Taylor (1980).

[6] Composition calculated by adding 0.25 wt.% H_2O to Sample G05 from Cecil *et al.* (2012), then renormalizing to 100 wt.%. $\delta^{18}O$ value after Taylor (1980).

[7] Composition calculated by adding 0.25 wt.% H_2O to Sample G08 from Cecil *et al.* (2012), then renormalizing to 100 wt.%. $\delta^{18}O$ value after Taylor (1980).

n.r. = not reported in the literature; *o.m.* = omitted in model [oxide was set at 0 wt.% in MCS model to stabilize composition]

there is no way to conclusively determine the exact mechanism of assimilation (Weinberg *et al.*, 2021), our models run the gamut of geologically-plausible AFC scenarios.

To simulate 'traditional' assimilation of wallrock partial melts by intrusion of a basalt, MCS was used to construct a series of AFC models performed at P = 4 kbar—corresponding to ~15 km depth (Fig. 8) as constrained by *P-T* estimates from Scruggs & Putirka (2018). Initial run conditions for each AFC model are given in Table 6, and our best model results (*AFC 21SepF*) illustrated in Figure 9. In our AFC models, as the wallrock (purple triangles in Fig. 9) undergoes partial melting, the compositional evolution of produced anatecitc melts (asterisks in Fig. 9) is dictated by the stoichiometric melting relationships of that wallrock. Within MCS, the mass of anatectic liquid generated within the WR subsystem depends upon many factors set by the user, most notably M_0^{WR} / M_0^{M}, T_0^{WR}, and T^{M} (Table 1). Further, any mass of generated melt above the user-set $f^{WR}_{crit,}$ value (Table 1) is transferred to the M subsystem, producing the new, contaminated magma (cM) composition. Hence, the cM produced in phase-equilibria AFC models (purple crosses in Fig. 9) represents an idealized situation where assimilation is energetically-restricted, and isotopic equilibrium is maintained in the WR subsystem as anatectic reactions occur (Bohrson *et al.* 2014, 2020; Heinonen *et al.* 2020). A low f^{WR}_{crit} value will maximize the transfer of anatectic melt into M, further contaminating cM as the run progresses. Despite our low selected thresholds (f^{WR}_{crit} = 0.025), the energetically-constrained mass of anatectic melt generated using MCS is insufficient to reproduce the geochemical compositions of the most radiogenic enclave (Fig. 9;).

While the energy constrained models fail to reproduce the isotopic composition of CC-E-I-10core, partially melted crustal xenoliths preserved in various systems worldwide (Grove *et al.*, 1988; Dumond *et al.*, 2005; Arjmandzadeh *et al.*, 2011) demonstrate that assimilation need

not always be an energetically-constrained process (Weinberg *et al.*, 2021). Although AFC is not a simple linear process, it may be deconstructed into a sequence of mixing phenomena—perhaps as a series of anatectic liquids mixing with an ascending primary melt (DePaolo & Wasserburg, 1976; Turner & Langmuir, 2015), or as a multi-component mixture of ascending magma, anatectic liquids, and cumulates (Taylor, 1980). We therefore relax the energetic constraints of our phase-equilibria models such that the degree of WR melting and mass of generated partial melt are still controlled by enthalpic relations, but the generated partial melt compositions are mixed with the ascending mafic magma in not-energetically-restricted proportions, analogous to how some enclaves might have been more contaminated at depth than others—i.e., the crustal melt likely mixed with a relatively small volume of the mafic magma, rather than the entire volume of basaltic magma that provided the energy to heat and melt the wallrock (Grove *et al.*, 1988; Dumond *et al.*, 2005; Arjmandzadeh *et al.*, 2011; Weinberg *et al.*, 2021). Our methods for constraining the best mass-decoupled F_{mix} for each wallrock composition are given in Appendix B, and we use these F_{mix} values (Table 7) to calculate new bulk compositions of contaminated magmas where mass-decoupled contamination occurs by complete homogenization of whole blocks of stoped wallrock (Fig. 9, "S of SNG bulk WR"), and also by assimilation of wallrock partial melts under isotopic equilibrium (Fig. 9, "A of EQ anatectic melt") and isotopic disequilibrium conditions (Fig. 9, “A of DisEQ anatectic melt).

Our mass-decoupled assimilation models adequately reproduce the $^{143}Nd/^{144}Nd$ variations observed in mafic enclaves, but do not reproduce the $^{87}Sr/^{86}Sr$ composition of CC-E-I-10core (Fig. 9e-g; Table 7), for the specific Sierra Nevada granodiorite compositions modeled in this study (Table 5; see also Appendix D).Given the wide range of potential wallrock compositions

(white triangles on Figs. 3, 5, 7 and 9), similar modeling of a different composition could likely reproduce a suitable mafic endmember to explain the CC-E-I-10 compositions. However, we also note that phase equilibria models intrinsically maintain isotopic equilibrium during partial melting of wallrock. If one considers that heating of wallrock was localized and short-lived as mafic magmas travelled through the crust via a crack network, it is possible that partial melting in the country rock took place under isotopic disequilibrium conditions (Knesel & Davidson, 1996; Petcovic & Grunder, 2003; Acosta-Vigil *et al.*, 2006; Farina & Stevens, 2011). Incongruent melting of granitoids (*sensu lato*) has been documented in both the laboratory (Knesel & Davidson, 1996; Acosta-Vigil *et al.*, 2006) and in the field (Petcovic & Grunder, 2003; Arjmandzadeh *et al.*, 2011; Farina & Stevens, 2011), and explored through numerical modeling (Iles *et al.*, 2018) to produce an extensive array of isotopic variability in the restite and partial melt products. The assumption of isotopic equilibrium in a rock is reasonable at magmatic temperatures when diffusion can keep up with in-growth (Faure, 2001; Acosta-Vigil *et al.*, 2006), or over long timescales where melt generation rates do not exceed the time required for its segregation and/or removal (Knesel & Davidson, 1996). However, as the isotopic variability of partial melts is controlled by the stoichiometric relationships between anatectic melts and peritectic phases, in environments where partial melts are removed before recrystallization and growth of new peritectic phases can occur, melting will lead to a series of isotopically heterogeneous melts (Knesel & Davidson 1996; Acosta-Vigil *et al.*, 2006; Farina & Stevens, 2011)—providing another geologically reasonable avenue to explore.

In a typical SNG, the K-feldspar and biotite have especially radiogenic Sr since Rb is a compatible element in these phases (Knesel & Davidson 1996). Considering that biotite and

K-feldspar (Tables 5 & 6) copiously contribute to the first increments of partial melts, it is expected that the $^{87}Sr/^{86}Sr$ of wallrock anatectic melts would vary during disequilibrium partial melting (Knesel & Davidson, 1996; Acosta-Vigil *et al.*, 2006; Farina & Stevens, 2011; Iles *et al.*, 2018). The variation of $^{87}Sr/^{86}Sr$ during progressive disequilibrium partial melting (from high to lower values) is a function of both the age of the wallrock and the stoichiometric reactions which take place as it melts (Knesel & Davidson, 1996; Faure, 2001; Acosta-Vigil *et al.*, 2006). For Mesozoic SNG, K-feldspar and biotite are quite radiogenic (Cecil *et al*., 2012), and contribute most to the first fraction of partial melt (Knesel & Davidson, 1996). Of the five WR compositions tested (Table 5) in our forward models, two produced melt compositions which, when assimilated by the parental mafic melt, satisfied our F_{mix} requirement for major oxides, trace elements, and isotopes (see Table 7, with full results for all AFC models presented in Appendix D).

Partial melting experiments of H_2O-saturated leucogranite have demonstrated that: (1) biotite is more readily consumed during anatexis than K-feldspar, which is, in turn, consumed earlier during progressive partial fusion than plagioclase (Knelsen & Davidson, 1996); (2) back-reactions occur between the anatectic melt and the wallrock restite, perhaps even crystallizing new mineral phases or adding to the mass of preexisting WR phases (Acosta-Vigil *et al.*, 2006); and (3) anatectic melts are isotopically homogeneous, but are *not* in equilibrium with the WR residue (Acosta-Vigil *et al.*, 2006). Our model results show that while biotite is completely consumed, the growth of restite mineral phases, particularly oxides, pyroxenes and feldspars, occurs in response to partial melting (Tables 5 & 6). The initial increments of partial melts generated by isotopic disequilibrium partial fusion in the best-fit AFC model results are therefore *extremely* enriched ($^{87}Sr/^{86}Sr$=0.722062 and

$^{143}Nd/^{144}Nd$=0.512764). By allowing for low degrees (<3%) of isotopic disequilibrium partial melting, the first increments of anatectic melt are *highly* radiogenic—even exceeding $^{87}Sr/^{86}Sr$ values of the most radiogenic Chaos Crags enclaves (Figs. 9e & 9g).

Table 6. Initial Run Conditions for Magma Chamber Simulator Best-Fit AFC Model Results.

AFC Model	WR	fO_2:	ΔT (°C)	Initial WR Mineralogy (m^{WR}_{Φ})
21SepF	LB92-155	(buffer absent) Fe^{2+}/Fe_{tot} = 0.78 (as reported)	5 °C	bt (2.18), cpx (0.71), fl (0.26), il (0.89), kfs (15.99), mt (1.26), opx (2.48), pl (48.39), qtz (28.65)
21SepZ	G01	(buffer absent) Fe2+/Fetot = 0.85	5 °C	ap (0.21), bt (1.09), fl (0.30), gt (0.20), il (0.47), kfs (11.86), mt (0.81), ol (0.47), opx (6.52), pl (54.79), qtz (23.28)
22SepB	G04	(buffer absent) Fe2+/Fetot = 0.85	5 °C	ap (0.61), bt (2.68), fl (0.22), il (1.70), kfs (39.32), mt (1.03), ol (0.77), opx (5.10), pl (48.54)
22SepA	G05	(buffer absent) Fe2+/Fetot = 0.85	5 °C	gt (0.85), il (0.12), kfs (38.45), leuc (3.31), mt (0.16), pl (14.28), qtz (41.47), sill (1.24)
No DisEQ AFC Model	G08	(buffer absent) Fe2+/Fetot = 0.85	5 °C	Subsolidus WR composition not equilibrated
All models run at: P = 4 kbar, f^{WR}_{crit} = 0.025, T_0^{WR} = 700°C, M_0^{WR} / M_0^{M} = 1				

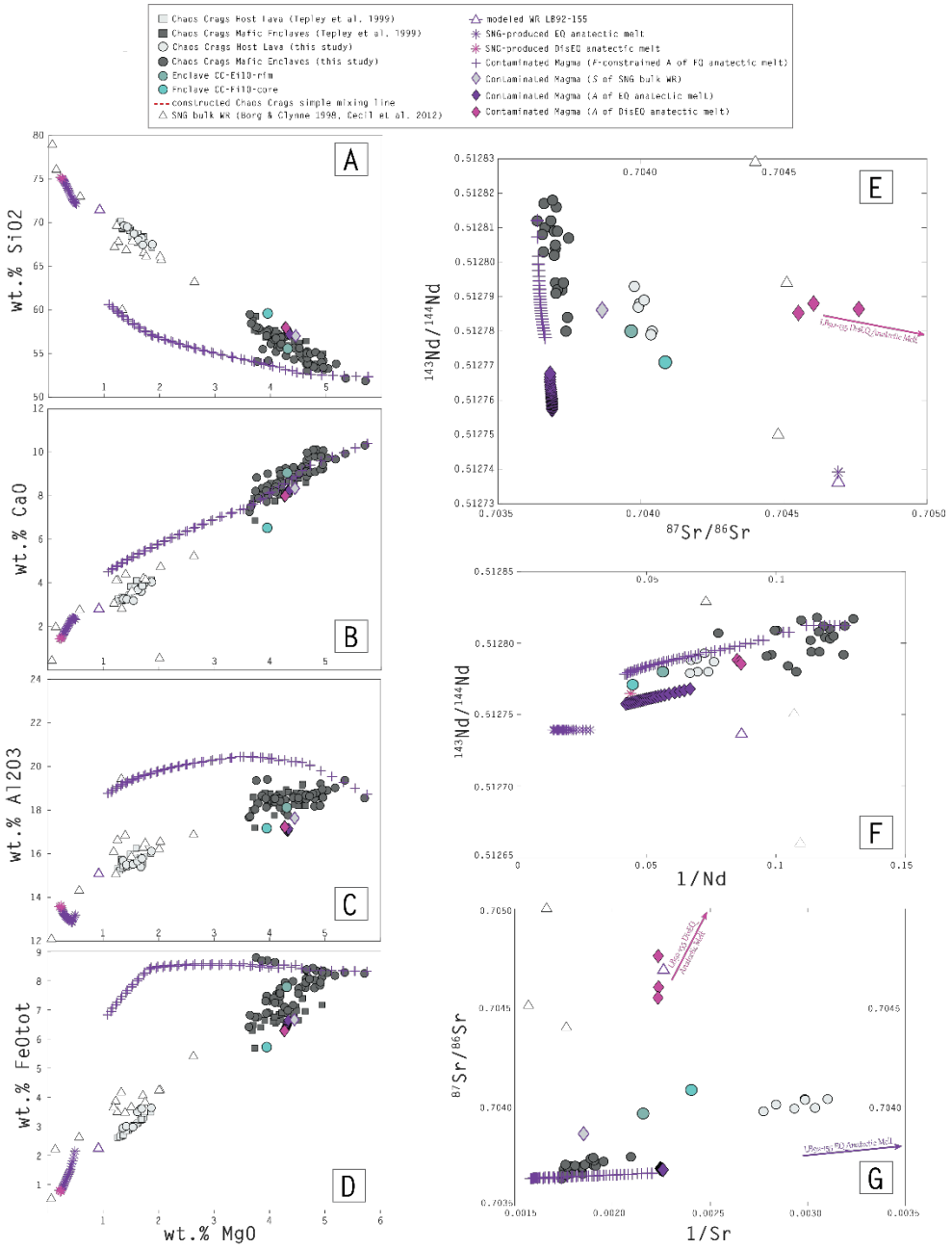

Figure 9. Major oxide compositions (a-d) and Sr-Nd isotope systematics (e-g) of Chaos Crags mafic eruptive products (circles and squares), and reported northern Sierra Nevada granitoid (*sensu lato*) wallrock compositions (triangles). Measured lava compositions are overlain with our best AFC model results, produced by assimilation of partial melts from wallrock LB92-155 (Borg & Clynne, 1998). Anatectic melt produced under *both* isotopic equilibrium *and* disequilibrium conditions (asterisks), and bulk wallrock compositions (colored triangles) are used as the 'contaminant' compositions. Energetically-constrained AFC produces a line of melt evolution (crosses) that bounds Chaos Crags mafic enclaves and contributes to the *pre-recharge* compositional diversity of mafic magmas, but cannot account for the composition of CC-E-I-10core. Relaxing the energy constraint and allowing anatectic melts or bulk SNG to mix in greater proportions (F_{mix} given in Table 4) produces contaminated melts (diamonds) which *approach* the composition of CC-E-I-10core. Mixing of mafic recharge magmas with resident rhyodacitic magmas at Chaos Crags is indisputable, so the results of our AFC models should *not* match CC-E-I-10core directly, as our AFC model results serve as the starting composition in our later AFC+R models. Full results for all AFC models are presented in Appendix D.

Table 7. Abridged Results of MCS-PhaseEQ AFC Runs & Disequilibrium Isotope Calculations

	AFC 21SepF [base for LB Mixes]	AFC 21SepZ [base for G01 Mixes]	AFC 22SepB [*'fails' F_{mix} test*]	AFC 22SepA [*'fails' F_{mix} test*]
$T_{solidus}^{WR}$ (°C)	780 °C	757 °C	862 °C	705 °C
Degree of WR partial melting at t_R:	2.43%	0.69%	0.84%	1.98%
$T^{M}t_R$ (°C)	1131 °C	1150 °C	1105 °C	1146 °C
$T^{WR}t_R$ (°C)	800 °C	756 °C	871 °C	714 °C
Restite Phases at t_R ($m^{WR}{}_{\Phi}$)	cpx (0.26), fl (0.13), il (0.31), kfs (14.99), mt (1.10), opx (4.06), pl (48.30), qtz (25.99)	ap (0.13), cpx (0.15), fl (0.17), il (0.47), kfs (11.43), mt (0.76), ol (0.04), opx (7.88), pl (54.12), qtz (21.69)	ap (0.48), fl (0.11), il (1.07), kfs (41.87), mt (1.69), ol (1.98), opx (3.05), pl (43.78)	gt (0.92), il (0.09), kfs (16.89), mt (0.15), pl (37.98), qtz (38.88), sill (0.60)
SiO_2 (wt.%) WR_{liq}	71.86	66.89	59.46	65.88
TiO_2 (wt.%) WR_{liq}	0.39	0.22	0.35	0.20
Al_2O_3 (wt.%) WR_{liq}	12.96	13.61	17.78	20.88
FeO (wt.%) WR_{liq}	0.51	0.64	2.48	0.32
Fe_2O_3 (wt.%) WR_{liq}	0.24	0.19	0.15	0.18
MgO (wt.%) WR_{liq}	0.24	0.16	0.32	0.07
CaO (wt.%) WR_{liq}	1.43	2.81	1.99	0.41
Na_2O (wt.%) WR_{liq}	2.29	1.63	5.22	1.50
K_2O (wt.%) WR_{liq}	5.81	5.25	6.39	4.77
H_2O (wt.%) WR_{liq}	4.11	5.43	4.63	5.58
CO_2 (wt.%) WR_{liq}	0.16	0.14	0.13	*omitted*
EQ Nd (ppm) WR_{liq}	64.77	39.00	7.51	68.04
EQ Sr (ppm) WR_{liq}	83.14	68.55	77.35	7.91
***DisEQ* Nd (ppm) WR_{liq}**	*91.39*	*83.27*	*5.98*	*8.16*
***DisEQ* Sr (ppm) WR_{liq}**	*72.01*	*172.32*	*423.02*	*3.29*
EQ $^{143}Nd/^{144}Nd$ M_{liq}	0.512739	0.512750	0.512430	0.512660
EQ $^{87}Sr/^{86}Sr$ M_{liq}	0.70469	0.704480	0.705450	0.734630
***DisEQ* $^{143}Nd/^{144}Nd$ M_{liq}**	*0.512758*	*0.512783*	*0.512477*	*0.512626*
***DisEQ* $^{87}Sr/^{86}Sr$ M_{liq}**	*0.720644*	*0.710606*	*0.706465*	*0.783873*
Constrained F_{mix} Mafic:	0.7369 ± 0.04	0.7157 ± 0.09	0.7141 ± 0.03	0.6909 ± 0.04

b. Modeling of Open-System Magma Mixing (R) Processes

Magma mixing is a significant petrogenetic process at Chaos Crags and must be accounted for in the phase equilibria models. Due to funding and sample preservation issues, the exact degree of mixing experienced by enclave *CC-E-I-10* could not be quantified, but we recognize that our model of enclave petrogenesis is incomplete without a shallow-mixing component. Our AFC models described above demonstrate it is possible to approach the composition of *CC-E-I-10* by assimilation of ~30% of a low-degree partial melt into a mafic recharge magma, and we construct a series of models to estimate the final enclave composition after mixing with 5%, 10%, and 15% of host rhyodacite (Table 8). We constructed a series of magma mixing models for F_{mix} = 0.01, 0.05, and 0.10, where F_{mix} is the fraction of rhyodacitic host magma mixed with the now-contaminated mafic recharge (cM; see Table 7) to produce the bimodal lavas erupted at Chaos Crags. Traditional MCS runs that involve mixing and assimilation are generally referred to as RAFC models, but here we refer to our Chaos Crags forward models as AFC+R, because our model is serial and we allow for crystallization but no removal of newly crystallized hybrid phases after recharge. The bulk composition of the newly hybridized magma is therefore set *a priori*. To accompany bulk magma mixing calculations, phase-equilibria models of mixing were performed at P = 1.45 kbar (~5-6 km; see Fig. 8), as constrained by the experiments of Quinn (2014) and *P-T* estimates from Scruggs & Putirka (2018), with initial FeO/FeO_{total} = 0.85 and no further external (buffer) restriction of f_{O2} during R. Abridged results of our best AFC+R forward models are presented in Table 7; full results for our mixing models may be found in Appendix E.

The hybrid lavas produced by our mixing calculations (Table 9) are analogous to the variably contaminated mafic enclaves erupted at Chaos Crags. in Figure 10, closed binary

mixing between our most mafic enclave and least contaminated host lava is represented by the red dashed line; if mixing was the *only* magmatic process occurring at Chaos Crags and there was no separation of crystals from melts, one would expect all eruptive products to lie along this curve (the curvature of which is a function of the concentrations of Nd and Sr in each endmember composition). AFC+R models take the *not-energetically-constrained* results of our AFC calculations (diamonds) and mix those contaminated melts with host rhyodacitic magmas in increments of 5%, 10%, and 15%, producing hybrid lavas (stars). Dashed black lines connect the model results for each amount of host lava added to cM (as contamination by a stoped block, or by either isotopic equilibrium or diequilibrium partial melts). The mixed compositions (stars) do not exactly match the composition of CC-E-I-10core. Instead, *our model results demonstrate that the isotopic signature of CC-E-I-10core is bound by a mixture of 10-15% host lavas with a mafic melt that has been contaminated by low-degrees of partial fusion under isotopic equilibrium conditions, and a mixture of 10-15% host lavas with a mafic melt that has been contaminated by low-degrees of partial fusion under isotopic disequilibrium conditions. These models also successfully approximate the major oxide composition (with the exception of Na_2O) of that enclave.* Of course, we do not expect that wallrock LB92-155 (Borg & Clynne, 1998) is the *exact* contaminant to affect the geochemical signature of CC-E-I-10—and our model results are not *exactly* a match for the composition of CC-E-I-10core. However, we have demonstrated that multiple wallrock compositions are capable of generating melts under conditions ranging between isotopic equilibrium and disequilibrium that, when mixed with mafic magmas and resident host lavas, are very near or surround the measured composition of CC-E-I-10core.

Table 8. Initial MCS run conditions for RFC models, conducted at P = 1.45 kbar. For MCS Phase-EQ runs, major oxides are renormalized to 100 wt.%, and f_{O2} was not restricted along a buffer.

	Base WR LB92-155	Base WR G01	Host Rhyodacite
Percent of WR contamination at t_R:	26.31%	28.43%	*n/a*
$T^M t_R$ (°C)	1131 °C	1150 °C	1146 °C
$T^R t_R$ (°C)	785 °C	785 °C	785 °C
SiO_2 (wt.%) M_{liq}	57.98	57.27	67.06
TiO_2 (wt.%) M_{liq}	0.59	0.54	0.43
Al_2O_3 (wt.%) M_{liq}	17.23	17.38	14.72
FeO (wt.%) M_{liq}	5.34	5.22	2.13
Fe_2O_3 (wt.%) M_{liq}	0.94	0.92	0.49
MgO (wt.%) M_{liq}	4.27	4.13	1.35
CaO (wt.%) M_{liq}	7.99	8.23	3.09
Na_2O (wt.%) M_{liq}	2.65	2.45	3.89
K_2O (wt.%) M_{liq}	2.17	2.14	2.55
H_2O (wt.%) M_{liq}	2.5	2.50	4.28
CO_2 (wt.%) M_{liq}	0.10	0.10	*omitted*
EQ Nd (ppm) M_{liq}	22.86	16.74	14.33
EQ Sr (ppm) M_{liq}	445.52	430.93	335.25
***DisEQ* Nd (ppm) M_{liq}**	*11.52*	*11.57*	*n/a*
***DisEQ* Sr (ppm) M_{liq}**	*447.69*	*435.11*	*n/a*
EQ $^{143}Nd/^{144}Nd$ M_{liq}	0.512758	0.512771	0.512780
EQ $^{87}Sr/^{86}Sr$ M_{liq}	0.703687	0.703675	0.704039
***DisEQ* $^{143}Nd/^{144}Nd$ M_{liq}**	*0.512785*	*0.512797*	*n/a*
***DisEQ* $^{87}Sr/^{86}Sr$ M_{liq}**	*0.704550*	*0.704016*	*n/a*

Note also that the *rim* of enclave CC-E-I-10 is *less* radiogenic and less contaminated than the core of the enclave, necessitating back-mixing with mafic magmas after core formation to produce the composition of CC-E-I-10rim. Mixing lines between the core and rim of this enclave (dashed blue arrows in Figs. 10 & 11) point towards the energy-constrained cM compositions as the other endmember, which may be expected; as AFC is essentially a sequence of miniature mixing lines between two magmas (Taylor, 1980). It is highly unlikely that CC-E-I-10 is the only enclave produced by such complex, open-system magmatic

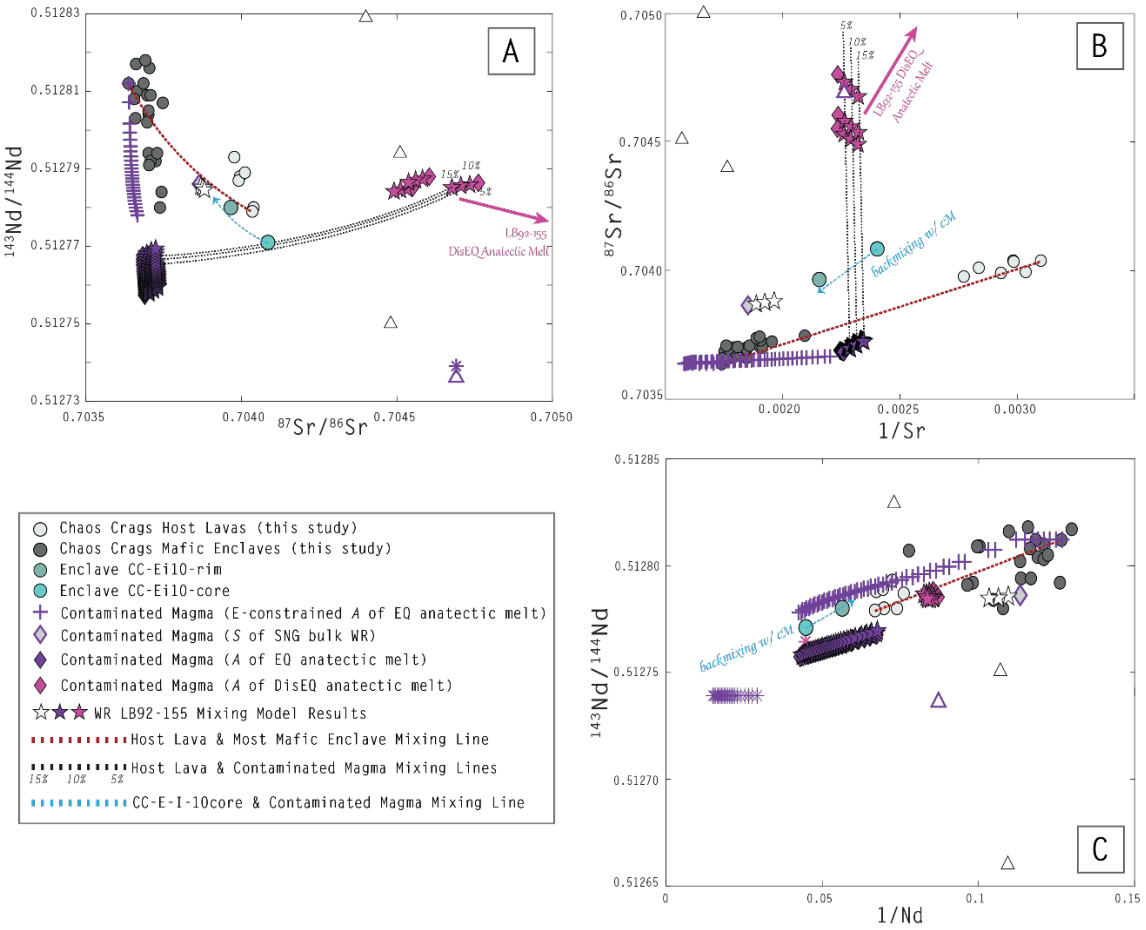

Figure 10. Sr-Nd isotope systematics of Chaos Crags mafic enclaves overlain with our best mixing (R) model results. Closed binary mixing between the most mafic enclave and least contaminated host lava is represented by the red dashed line; if mixing was the *only* magmatic process occurring at Chaos Crags and there was no separation of crystals from melts, we would expect all eruptive products to correlate along this curve (the curvature of which is a function of the concentrations of Nd and Sr in each endmember composition). AFC+R models take the *not-energetically-constrained* results of our AFC calculations (diamonds) and mix those contaminated melts with host rhyodacitic magmas in increments of 5%, 10%, and 15%, producing hybrid lavas (stars) that reasonably approach the most radiogenic enclave composition of CC-E-I-10core. Dashed black lines connect the model results for each amount of host lava added to cM (as contamination by partial melts under isotopic equilibrium, isotopic disequilibrium, and by stoping). *Model results demonstrate that the isotopic signature of CC-E-I-10core can be bound by a mixture of 10-15% host lavas with a melt that has been contaminated by low-degrees of partial fusion under isotopic equilibrium conditions, or a mixture of 10-15% host lavas with a melt that has been contaminated by low-degrees of partial fusion under isotopic disequilibrium conditions, that <u>also</u> successfully approximates the major oxide composition of that enclave.* Note also that the *rim* of enclave CC-E-I-10 is *LESS* radiogenic and contaminated than the core of the enclave, necessitating back-mixing (represented by blue dashed arrow) with cM after core formation to produce the geochemical composition of CC-E-I-10rim. It is highly unlikely that CC-E-I-10 is the only enclave subjected to such complex, open-system magmatic processes, and the geochemical and isotopic compositions of many Chaos Crags mafic enclaves may be reproduced by mixing host lavas with magmas that have been variably contaminated by partial melt (crosses), suggesting that assimilation of wallrock at depth—*prior to mixing with rhyodacitic host magmas*—is a plausible petrogenetic scenario for those more radiogenic mafic enclaves examined.

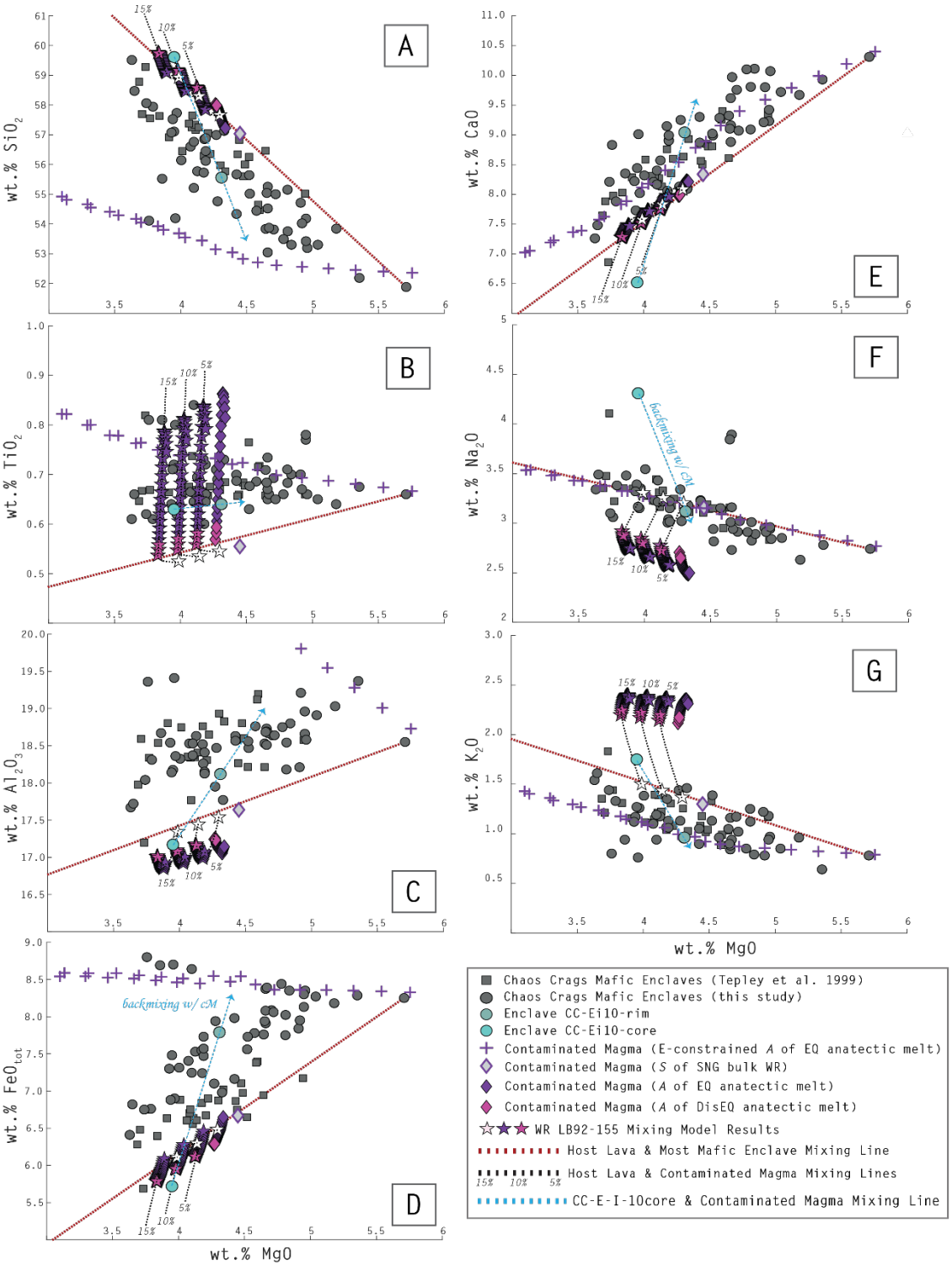

Figure 11. Zoomed-in major oxide compositions of Chaos Crags mafic enclaves overlain with our best mixing (R) model results. All symbols are the same as in Figure 10; see Figure 10 caption and text for details of model results.

Table 9. Abridged results of best-fit AFC+R Models using WR LB92-155 (Borg & Clynne, 1998)

	5% Host Magma	10% Host Magma	15% Host Magma	CC-E-I-10 core
T_0^R (°C)*	785 °C	785 °C	785 °C	
$T^M t_R$ (°C)*	1092 °C	1092 °C	1092 °C	
T_f^{Hybrid} (°C)*	1080 °C	1065 °C	1051 °C	1041 °C+
Phases in Hybrid Magma (m^{Hyb}_{Φ})*	fl (0.01) opx (0.32) cpx (1.70)	fl (0.01) opx (0.65) cpx (3.39)	fl (0.01) opx (0.98) cpx (5.10)	fl pl cpx/amph
SiO_2 (wt.%) Hyb_{bulk}	58.56	59.15	59.73	59.61
TiO_2 (wt.%) Hyb_{bulk}	0.58	0.57	0.56	0.63
MgO (wt.%) Hyb_{bulk}	4.13	3.98	3.84	3.95
Al_2O_3 (wt.%) Hyb_{bulk}	17.15	17.08	17.00	17.17
FeO_{tot} (wt.%) Hyb_{bulk}	6.12	5.95	5.79	5.72
CaO (wt.%) Hyb_{bulk}	7.75	7.52	7.28	6.52
Na_2O (wt.%) Hyb_{bulk}	2.72	2.78	2.87	4.31
K_2O (wt.%) Hyb_{bulk}	2.20	2.22	2.25	1.75
H_2O (wt.%) Hyb_{bulk}*	2.60	2.74	2.88	*n.m.*
CO_2 (wt.%) Hyb_{bulk}*	0.04	0.04	0.04	*n.m.*
RSS (wt.% majors^{Þ})	5.54	3.79	2.97	
RSS (wt.% majors†)	3.02	1.51	0.90	
Sr (ppm) EQ Hyb_{bulk}	440.01	434.49	428.98	416.11
Nd (ppm) EQ Hyb_{bulk}	22.43	22.01	21.58	22.33
$^{87}Sr/^{86}Sr$ EQ Hyb_{bulk}	0.703702	0.703716	0.703730	
$^{143}Nd/^{144}Nd$ EQ Hyb_{bulk}	0.512758	0.512759	0.512760	
Sr (ppm) DisEQ Hyb_{bulk}	442.07	436.45	430.83	
Nd (ppm) DisEQ Hyb_{bulk}	11.66	11.80	11.95	
$^{87}Sr/^{86}Sr$ DisEQ Hyb_{bulk}	0.704531	0.704511	0.704491	0.704085
$^{143}Nd/^{144}Nd$ DisEQ Hyb_{bulk}	0.512785	0.512785	0.512784	0.512771

*MCS phase-equilibria model result
+estimated crystallization *T* from Scruggs & Putirka (2018)
ÞRSS including Na_2O
†RSS excluding Na_2O

processes, and the geochemical and isotopic compositions of many Chaos Crags mafic enclaves can be reproduced by mixing host lavas with magmas that have been variably contaminated by crustal melts (crosses in Figs. 10-11), suggesting that assimilation of wallrock at depth—*prior to mixing with rhyodacitic host magmas*—is a plausible petrogenetic scenario for a number of mafic enclaves.

3. A Broader Role for Assimilation in Chaos Crags Magma Evolution

As noted above, CC-E-I-10 is not the first mafic enclave found at Chaos Crags that displays unusually enriched $^{87}Sr/^{86}Sr$ (Fig. 7); bulk compositions for five highly radiogenic enclaves were presented by Tepley *et al.* (1999), and their elevated $^{87}Sr/^{86}Sr$ signature attributed to an enriched secondary mafic endmember magma. As $^{143}Nd/^{144}Nd$ and trace elements of Chaos Crags eruptive products have not been previously reported, we are unable to directly compare the Chaos Crags enclaves from Tepley *et al.* (1999) to our AFC+R models presented in Figure 10. We can, however, directly compare the $^{87}Sr/^{86}Sr$ and major oxide signatures of Chaos Crags enclaves provided by Tepley *et al.* (1999) with those presented in this study. The highly radiogenic mafic enclaves examined by Tepley *et al.* (1999) are quite similar in isotopic (Fig. 7) and major oxide composition (Fig. 11) to enclave CC-E-I-10, suggesting that they could also have been affected by assimilation of a similar SNG component as CC-E-I-10.

These highly radiogenic mafic enclaves are few in number, and we note that they have only been found (to date) in the latter half of the eruptive sequence (Domes D—F; Fig. 7b). Although sampling bias cannot be discounted, a simple explanation for the population of high $^{87}Sr/^{86}Sr$ enclaves in Domes D—F may be that the increased advective heating from mafic magmas over the duration of the eruptive sequence resulted in higher magma conduit wall

temperatures and hence a higher proclivity for partial melting of surrounding SNG wallrock (Bruce & Huppert, 1990; Petcovic & Grunder, 2003).

In addition to this small population of highly radiogenic mafic enclaves, approximately half of the enclaves analyzed in this study do not plot along the mixing line defined by the least radiogenic mafic enclave and most radiogenic host lava (red dashed lines in Figs. 10 & 11). Samples pulled off the mixing line however, do lie between the mixing line and the composition of contaminated basaltic melt (cM, crosses in Figs. 10a & 11) as produced by the AFC models. Enclave compositions are then likely two-component mixures of rhyodacitic host lava and a mafic endmember magma that becomes progressively more contaminated over the duration of the eruption sequence. Hence, the majority of enclaves studied herein display evidence suggesting an open-system process other than binary mixing of parental mafic melts with a resident rhyodacitic magma body.

Initially, Bullen & Clynne (1990) rejected assimilation of an SNG-like crustal component as contributing to the isotopic variation of mafic magmas at the LVC, explicitly stating that to reproduce such variation by assimilation of Mesozoic granitoid rocks, a granitoid composition with $^{87}Sr/^{86}Sr > 0.7046$ would be necessary. Not only have nearby SNG have been recorded with $^{87}Sr/^{86}Sr > 0.7046$ (Borg & Clynne, 1998; Cecil *et al.*, 2012), but the data presented herein and the results of our phase equilibria modeling confirm that requirement and successfully demonstrate that assimilation of granitoid partial melts can reproduce the geochemical anomalies addressed in this study. Additionally, Chaos Crags is located on the northern flank of the now-eroded Brokeoff Volcano (Clynne & Muffler, 2010), the center of which is inferred to be Diamond Peak (Fig. 2; Feeley *et al.*, 2008a). Prolonged intrusion of mantle-derived mafic magmas into the magma reservoir during the construction of the

Rockland Caldera Complex and Brokeoff Volcano likely served to homogenize the upper crust in the immediate vicinity, obscuring the compositional contrasts generally associated with assimilation processes (Marsh & Kantha, 1978; Feeley *et al.*, 2008a). This prolonged mafic magmatism, likely combined with extreme hydrothermal alteration of the Brokeoff Volcano core, has resulted in a positive correlation between $\delta^{18}O$ of LVC lavas and increasing distance from Diamond Peak (Feeley *et al.*, 2008a). Chaos Crags lies ~7 km north of Diamond Peak (Fig. 2)—the distance at which Feeley *et al.* (2008a) noted a distinct increase in $^{87}Sr/^{86}Sr$ and $\delta^{18}O$ in eruptive products, suggestive of an increased SNG-like upper crustal component in those lavas. Although we have no $\delta^{18}O$ measurements for our samples, MCS model results of $\delta^{18}O$ (Appendix E) lie within the range of Chaos Crags $\delta^{18}O$ previously reported by Taylor (1980) and Feeley *et al.* (2008a).

By examining the geochemical data in the context of the petrogenetic findings of Feeley *et al.* (2008a) and considering the thermal effects of assimilation (Bruce & Huppert, 1990; Reiners *et al.*, 1995), we can construct a magma evolution model for Chaos Crags mafic magmas that accounts for the wide range in isotopic diversity exhibited by mafic enclaves throughout the eruptive sequence (Fig. 8):

(1) The mafic parental magma for Chaos Crags was initially relatively uniform in composition, as indicated by the positive correlation between $^{87}Sr/^{86}Sr$ and major oxide compositions of mafic enclaves (Fig. 7a).

(2) The newly emplaced dike plexus of mafic parental magma of the same (or very similar) initial composition propagated through upper-to-middle crust of SNG-like composition. As it ascended, magma in the boundary layers along the dike walls initially solidified, creating a thermal and chemical barrier against the wallrock.

(3) Continued supply of mafic magma thermomechanically erodes the solidified dike margins, allowing access to the now-warmed wallrock.

(4) Advection of heat from continuing magma ascent melts the solidified barrier, and partially melts the wallrock under conditions of variable isotopic disequilibrium conditions, generating highly radiogenic anatectic melts (Fig. 9e-g).

(5) Varying proportions of anatectic liquids contaminate mafic recharge magmas as they ascend towards the resident Chaos Crags magma body. Mass-decoupled assimilation of partial melts variably contaminates recharge magmas, producing an isotopically diverse mafic endmember. CC-E-I-10core, being a mixture of ~25% anatectic liquid and ~75% mafic melt, represents an extreme example of contamination, with the majority of recharge magmas being subject to much smaller degrees of assimilation (Fig. 9).

(6) Contaminated recharge magmas—now of varying isotopic composition (Fig. 10)—intrude into the underlying Chaos Crags magma body, mingling with host rhyodacite magmas to form the enclave-bearing lava domes of Chaos Crags (Figs. 10 & 11; Heiken & Eichelberger, 1980; Tepley *et al.*, 1999; Clynne & Muffler, 2010).

(7) A decrease in magma flux allows for cooling, initiating crystallization of dikes. Dikes die a viscous death, eventually ceasing the supply of mafic magma to the Chaos Crags magma reservoir.

F. Conclusions

Evidence presented here suggests that Chaos Crags mafic endmember magmas likely assimilated Sierra Nevada granitoids, and that temporally and spatially heterogeneous

assimilation of this underlying country rock by mafic magmas, prior to their mixing with rhyodacitic host lavas, is partially responsible for the geochemical variations seen within mafic enclaves at Chaos Crags. Previously, major oxide variation diagrams, as well as field and petrographic evidence convinced many investigators that magma mixing is the sole petrogenetic process responsible for the compositional variations within Chaos Crags mafic enclaves (Figs. 3 & 5; see also Heiken & Eichelberger, 1980; Tepley *et al.*, 1999; Scruggs & Putirka, 2018). *However, the isotopic signature of some mafic enclaves cannot be produced by mixing between the mafic endmember and rhyodacitic host magmas (dashed red line in Figs. 5 & 10).*

This study attempts to explain, in-depth, the complex pre-eruptive processes of *one* mafic enclave. Although it is one of a few extreme samples (Fig. 7), reconciling the petrogenesis of this small population of enclaves with the geochemical compositions of the majority of mafic enclaves necessitates the existence of a second magmatic process—in addition to magma mixing—at Chaos Crags. Variable amounts of assimilation of SNG wallrock (Figs. 9-11) plays a more important role in contributing to the compositional diversity of Chaos Crags' mafic magmas than previously thought, as mass-decoupled assimilation of granitoid partial melts by recharge magmas can explain the highly radiogenic population of enclaves, whereas simple mixing between recharge and host magmas cannot.

G. Acknowledgements

Thank you to Mike Tappa, Ryan Mills, and Drew Coleman for their assistance in completing isotopic analyses, Andrew Kylander-Clark and Gareth Seward for their assistance with trace element analyses, and Jade Star-Lackey for use of the XRF facilities at Pomona College. Additional thanks to Allison Price and Matt Jackson for their many productive

discussions regarding isotope geochemistry, and Matt Rioux and Roberta Rudnick for their thoughtful comments and assistance in concluding this project.

H. Electronic Supplemental Materials

This manuscript has not yet been submitted for publication. The following Electronic Appendices and Supplemental Materials have been uploaded to ProQuest to accompany this dissertation chapter:

Appendix A. Partition coefficients used in MCS trace element calculations.

(1) Excel file with partition coefficients used in this study, and references for the same.

(2) Folder containing PAR files used in MCS-TracesIsotope calculations.

Appendix B. Calculating geochemically-constrained mixing proportions for energy-decoupled mass transfer of wallrock partial melts.

Appendix C. Isotopic disequilibrium from incongruent melting during crustal anataxis.

(1) Figure C1, depicting steps involved in isotopic disequilibrium calculations.

(2) Table C1, containing the reported trace element and isotopic compositions of reported Sierra Nevada granitoid (*sensu lato*) near Lassen Volcanic National Park.

(3) Table C2, containing the initial state of each WR examined. Because the subsolidus state of wallrock G08 (Cecil *et al.*, 2012) was unable to be equilibrated, no isotopic disequilibrium calculations were done for that composition.

(4) Table C3, containing the final state of each WR examined.

(5) Folder “WR Phase Compositions”, containing the full results of our isotopic disequilibrium calculations at each increment of AFC.

Appendix D. Complete results of MCS-PhaseEQ and MCS-TracesIsotope AFC forward models.

(1) Folder “Partial Melting Models”, containing all MCS-PhaseEQ AFC forward models organized by WR composition.

   a. Folder “Input Files”, containing all MES_ input files for the AFC forward models.

(2) Folder “AFC Best Results wrG01”, containing full AFC model results for that wallrock composition.

(3) Folder “AFC Best Results wrG04”, containing full AFC model results for that wallrock composition.

(4) Folder “AFC Best Results wrG05”, containing full AFC model results for that wallrock composition.

(5) Folder “AFC Best Results wrG08”, containing full AFC model results for that wallrock composition.

(6) Folder “AFC Best Results wrLB92-155”, containing full AFC model results for that wallrock composition.

(7) Figure D1, illustrating the major oxide results of ALL MCS-PhaseEQ AFC forward models.

(8) Figure D2, illustrating the major oxide, trace element, and isotope results of ALL MCS-PhaseEQ AFC forward models.

Appendix E. Complete results of MCS-PhaseEQ best-fit AFC+R Models

(1) Folder “RFC_cM_wrG01”, containing all mixing models organized by condition of assimilation, as well as output file for MCS PhaseEQ RFC model.

(2) Folder “RFC_cM_wrLB92-155”, containing all mixing models organized by condition of assimilation, as well as output file for MCS PhaseEQ RFC model.

(3) Figure E1, illustrating the major oxide results of AFC→R models using cM as contaminated by WR G01 (Cecil *et al.*, 2012).

(4) Figure E2, illustrating the major oxide results of AFC→R models using cM as contaminated by WR G01 (Cecil *et al.*, 2012).

(5) Figure E3, illustrating Sr-Nd isotope systematics, trace element, and major oxide results of AFC→R models using cM as contaminated by WR G01 (Cecil *et al.*, 2012).

(6) Figure E4, illustrating the major oxide results of AFC→R models using cM as contaminated by WR LB92-155 (Borg & Clynne 1998).

(7) Figure E5, illustrating Sr-Nd isotope systematics, trace element, and major oxide results of AFC→R models using cM as contaminated by WR LB92-155 (Borg & Clynne 1998).

I. References

Acosta-Vigil, A., London, D., & Morgan, G.B. (2006) Experiments on the kinetics of partial melting of a leucogranite at 200 MPa H_2O and 690-800°C: compositional variability of melts during the onset of H_2O-saturated crustal anatexis. *Contributions to Mineralogy and Petrology*, **151**, 539-557.

Anderson, D.L. (1982) Isotopic evolution of the mantle: the role of magma mixing. *Earth and Planetary Science Letters*, **57(1)**, 1-12.

Andrews, B.J. & Manga, M. (2014) Thermal and rheological controls on the formation of mafic enclaves or banded pumice. *Contributions to Mineralogy and Petrology*, **167**, 961, doi: 10.1007/s00410-013-0961-7.

Arjmandzadeh, R., Karimpour, M.H., Mazaheri, S.A., Santos, J.F., Medina, J.M., & Homam, S.M. (2011) Sr-Nd isotope geochemistry and petrogenesis of the Chah-Shaljami granitoids (Lut Block, Eastern Iran). *Journal of Asian Earth Sciences*, **41**, 283-296.

Arvin, M., Dargahi, S., & Babaei, A.A. (2004) Mafic microgranular enclave swarms in the Chenar granitoid stock, NW of Kerman, Iran: evidence for magma mingling. *Journal of Asian Earth Sciences*, **24**, 105-113.

Bacon, C.R. (1986) Magmatic inclusions in silicic and intermediate volcanic rocks. *Journal of Geophysical Research*, **91(B6)**, 6091-6112.

Bacon, C.R., Bruggman, P.E., Christiansen, R.L., Clynne, M.A., Donnelly-Nolan, J.M., & Hildreth, W. (1997) Primitive magmas at five Cascade volcanic fields: melts from hot, heterogeneous sub-arc mantle. *The Canadian Mineralogist*, **35**, 397-423.

Beard, J.S., Ragland, P.C., & Rushmer, T. (2004) Hydration crystallization reactions between anhydrous minerals and hydrous melt to yield amphibole and biotite in igneous rocks: description and implications. *The Journal of Geology*, **112**, 617-621.

Berge, P.A. & Stauber, D.A. (1987) Seismic refraction study of upper crustal structure in the Lassen Peak area, northern California. *Journal of Geophysical Research*, **92(B10)**, 10571-10579.

Bohrson, W.A., Spera, F.J., Ghiorso, M.S., Brown, G.A., Creamer, J.B. & Mayfield, A. (2014) Thermodynamic model for energy-constrained open-system evolution of crustal magma bodies undergoing simultaneous recharge, assimilation, and crystallization: the Magma Chamber Simulator. *Journal of Petrology*, **55(9)**, 1685-1717.

Bohrson, W.A., Spera, F.J., Heinonen, J.S., Brown, G.A., Scruggs, M.A., Adams, J.V., Zeff, G. & Suikkanen, E. (2020) Diagnosing open-system magmatic processes using the Magma Chamber Simulator (MCS): part I – major elements and phase equilibria. *Contributions to Mineralogy and Petrology*, **175**, 104. doi: 10.1007/s00410-020-01722-z.

Borg, Lars E., Clynne, Michael A., & Bullen, Thomas D. (1997) The variable role of slab-derived fluids in the generation of a suite of primitive calc-alkaline lavas from the southernmost Cascades, California. *The Canadian Mineralogist*, **35**, 425-452.

Borg, L.E. & Clynne, M.A. (1998) The petrogenesis of felsic calc-alkaline magmas from the southernmost Cascades, California: origin by partial melting of basaltic lower crust. *Journal of Petrology*, **39(6)**, 1197-1222.

Bowen, N.L. (1915) The later stages of the evolution of the igneous rocks. *The Journal of Geology*, **23(8)**, Supplement, 91 p.

Bowen, N.L. (1928) *Evolution of the igneous rocks*. Princeton.

Browne, B.L., Eichelberger, J.C., Patino, L.C., Vogel, T.A., Dehn, J., Uto, K. & Hoshizumi, H. (2006) Generation of porphyritic and equigranular mafic enclaves during magma recharge events at Unzen Volcano, Japan. *Journal of Petrology*, **47(2)**, 301-328.

Bruce, Paul M. & Huppert, Herbert E. (1990) Solidification and melting along dykes by the laminar flow of basaltic magma. In: Ryan, M.P. (ed.). *Magma Transport and Storage*. Wiley, 420 p.

Bullen, T.D. & Clynne, M.A. (1990) Trace element and isotopic constraints on magmatic evolution at Lassen Volcanic Center. *Journal of Geophysical Research*, **95(B12)**, 19,671-19,691.

Burgisser A. & Bergantz, G. W., 2011, A rapid mechanism to remobilize and homogenize highly crystalline magma bodies: Nature, v. 471, p. 212–216.

Carslaw, H.S. & Jaeger, J.C. (1959) *Conduction of Heat in Solids, 2n^{d} Ed.* Oxford University Press.

Carter, S.R., Evensen, N.M., Hamilton, P.J., & O'Nions, R.K. (1978) Neodymium and strontium isotopic evidence for crustal contamination of continental volcanics. *Science*, **202(4369)**, 743-747.

Cecil, M.R., Rotberg, G.L., Ducea, M.N., Saleeby, J.B., & Gehrels, G.E. (2012) Magmatic growth and batholithic root development in the northern Sierra Nevada, California. Geosphere, **8(3)**, 592-606.

Christiansen, R.L., Clynne, M.A. & Muffler, L.J.P. (2002) Geologic Map of the Lassen Peak, Chaos Crags, and Upper Hat Creek area, California. U.S. Geological Survey Geologic Investigations Series I-2723.

Clynne, M.A. (1990) Stratigraphic, lithologic, and major element geochemical constraints on magmatic evolution at Lassen Volcanic Center, California. *Journal of Geophysical Research*, **95(B12)**, 19651-19669.

Clynne, M.A. (1999) A complex magma mixing origin for rocks erupted in 1915, Lassen Peak, California. *Journal of Petrology*, **40(1)**, 105-132.

Clynne, M.A., Christiansen, R.L., Trimble, D.A. & McGeehin, J.P. (2008) Radiocarbon dates from volcanic deposits of the Chaos Crags and Cinder Cone eruptive sequences and other deposits, Lassen Volcanic National Park and vicinity, California: U.S. Geological Survey Open-file Report 02-290, 18 p.

Clynne, M.A. & Muffler, L.J.P. (2010) Geologic map of Lassen Volcanic National Park and vicinity, California: U.S. Geological Survey Scientific Investigations Map 2899, scale 1:50 000, 1 sheet, 101 p.

Clynne, M.A., Muffler, L.J.P., Siems, D.F., Taggart, J.E. Jr. & Bruggman, P. (2008) Major and EDXRF trace element chemical analyses of volcanic rocks from Lassen Volcanic National Park and vicinity, California. U.S. Geological Survey Open-File Report 2008-1091, 10 p.

Clynne, M.A., Robinson, J.E., Nathenson, M. & Muffler, L.J.P. (2012) Volcano hazards assessment for the Lassen Region, northern California: U.S. Geological Survey Scientific Investigations Report 2012-5176-A, 47 p.

Collins, Sarah J., Davidson, Jon P., Morgan, Daniel J., and Llewellin, Edward W. (2012) Crystals, melt inclusions and magma mingling. *Mineralogical Magazine*, **76(6)**, Goldschmidt 2012, Montreal, Canada.

Cooper, G.F., Blundy, J.D., Macpherson, C.G., Humphreys, M.C.S., and Davidson, J.P. (2019) Evidence from plutonic xenoliths for magma differentiation, mixing and storage in a volatile-rich crystal mush beneath St. Eustatius, Lesser Antilles. *Contributions to Mineralogy and Petrology*, **174**, 39. doi: 10.1007/s00410-019-1576-4.

Cooper, K. M. & Kent, A. J. R. (2014) Rapid remobilization of magmatic crystals kept in cold storage: *Nature*, **506**, 480 – 483.

DePaolo, D.J. & Wasserburg, G.J. (1979) Petrogenetic mixing models and Nd-Sr isotopic patterns. *Geochimica et Cosmochimica Acta*, **43**, 615-627.

De Paolo, D.J. (1981) Trace Element and Isotopic Effects of Combined Wallrock Assimilation and Fractional Crystallization. *Earth and Planetary Science Letters*, **53**, 189-202.

Dumond, G., Yoshinobu, A., & Barnes, C.G. (2005) Midcrustal emplacement of the Sausfjellet pluton, central Norway: ductile flow, stoping, and in situ assimilation. *GSA Bulletin*, **117(3/4)**, 383-395.

Eberz, G.W. & Nicholls, I.A. (1990) Chemical modification of enclave magma by post-emplacement crystal fractionation, diffusion and metasomatism. *Contributions to Mineralogy and Petrology*, **104**, 47-55.

Eichelberger, J.C. (1975) Origin of andesite and dacite: Evidence of mixing at Glass Mountain in California and at other circum-Pacific volcanoes. *Geological Society of America Bulletin*, **86**, 1381-1391.

Eichelberger, J.C. (1978) Andesitic volcanism and crustal evolution. *Nature*, **275**, 21-27.

Eichelberger, J.C., Izbekov, P.E. & Browne, B.L. (2006) Bulk chemical trends at arc volcanoes are not liquid lines of descent. *Lithos*, **87**, 135-154.

Ericksen, S.M., Miller, J.S., Miller, C.F., Harper, B.E., & Aggarwal, J.K. (2004) Isotopic constraints on the evolution of felsic magma in the Aztec Walsh pluton, Eldorado

Mountains, Nevada. Geological Society of America *Abstracts with Programs*, **36(4)**, 8.

Farina, F., & Stevens, G. (2011) Source controlled $^{87}Sr/^{86}Sr$ isotope variability in granitic magmas: The inevitable consequence of mineral-scale isotopic disequilibrium in the protolith. *Lithos*, **122**, 189-200.

Faure, G. (2001) *Origin of igneous rocks: the isotopic evidence*. Springer.

Faure, G., & Mensing, T.M. (2005) *Isotopes: Principles and Applications, 3rd Ed.* John Wiley & Sons.

Feeley, T.C., Clynne, M.A., Winer, G.S. & Grice, W.C. (2008a) Oxygen isotope geochemistry of the Lassen Volcanic Center, California: resolving crustal and mantle contributions to continental arc magmatism. *Journal of Petrology*, **49(5)**, 971-997.

Feeley, T.C., Wilson, L.F. & Underwood, S.J. (2008b) Distribution and compositions of magmatic inclusions in the Mount Helen dome, Lassen Volcanic Center, California: Insights into magma chamber processes. *Lithos*, **106**, 173-189.

Furman, T. & Spera, F.J. (1985) Co-mingling of acid and basic magma with implications for the origins of mafic I-type xenoliths: field and petrochemical relations of an unusual dike complex at Eagle Lake, Sequoia National Park, California, U.S.A. *Journal of Volcanology and Geothermal Research*, **24(1-2)**, 151-178.

Gale, A., Dalton, C.A., Langmuir, C.H., Su, Y. & Schilling, J. (2013) The mean composition of ocean ridge basalts. *Geochemistry, Geophysics, Geosystems*, **14(3)**, 489-518.

Gençalioğlu-Kuşcu, G. & Floyd, P.A. (2001) Mineral compositional and textural evidence for magma mingling in the Saraykent volcanics. *Lithos*, **56**, 207-230.

Ghiorso, M.A. & Gualda, G.A.R. (2015) An H_2O-CO_2 mixed fluid saturation model compatible with rhyolite-MELTS. *Contributions to Mineralogy and Petrology*, **169**, 53, doi: 10.1007/s00410-015-1141-8.

Gonnermann, H.M., Manga, M., and Jellinek, A.M. (2002) Dynamics and longevity of an initially stratified mantle. *Geophysical Research Letters*, **29**, 1399, doi: 10.1029/2002GL014851.

Guffanti, M., Clynne, M.A., Smith, J.G., Muffler, L.J.P. & Bullen, T.D. (1990) Late Cenozoic volcanism, subduction, and extension in the Lassen Region of California, southern Cascade Range. *Journal of Geophysical Research*, **95(B12)**, 19453-19464.

Guffanti, M., Clynne, M.A., & Muffler, L.J.P. (1996) Thermal and mass implications of magmatic evolution in the Lassen volcanic region, California, and minimum constraints on basalt influx to the lower crust. *Journal of Geophysical Research*, **101(B2)**, 3003-3013.

Gualda, G.A.R., Ghiorso, M.S., Lemons, R.V. & Carley, T.L. (2012) Rhyolite-MELTS: a modified calibration of MELTS optimized for silica-rich, fluid-bearing magmatic systems. *Journal of Petrology*, **53(5)**, 875-890.

Harvey, J. & Baxter, E.F. (2009) An improved method for TIMS high precision neodymium isotope analysis of very small aliquots (1-10 ng). *Chemical Geology*, **258**, 251-257.

Hedman, K.M., Curry, B.B., Johnson, T.M., Fullager, P.D. & Emerson, T.E. (2009) Variation in strontium isotope ratios of archaeological fauna in the Midwestern United States: a preliminary study. *Journal of Archaeological Science*, **36**, 64-73.

Heiken, G. & Eichelberger, J.C. (1980) Eruptions at Chaos Crags, Lassen Volcanic National Park, California. *Journal of Volcanology and Geothermal Research*, **7**, 443-481.

Heinonen, J.S., Bohrson, W.A., Spera, F.J., Brown, G.A., Scruggs, M.A. & Adams, J.V. (2020) Diagnosing open-system magmatic processes using the Magma Chamber Simulator (MCS): part II—trace elements and isotopes. *Contributions to Mineralogy and Petrology*, **175**, 105, doi: 10.1007/s00410-020-01718-9.

Heinonen, J.S., Luttinen, A.V., Spera, F.J., & Bohrson, W.A. (2019) Deep open storage and shallow closed transport system for a continental flood basalt sequence revealed with Magma Chamber Simulator. *Contributions to Mineralogy and Petrology*, **174**, 87.

Huber, C., Bachmann, O., & Dufek, J. (2011) Thermo-mechanical reactivation of locked crystal mushes: Melting-induced internal fracturing and assimilation processes in magmas. *Earth and Planetary Science Letters*, **304(34)**, 443– 454.

Ingebritsen, S.E., & Gleeson, T. (2015) Crustal permeability: introduction to the special issue. *Geofluids*, **15(1-2)**, 1-10, doi: 10.1111/gfl/12118.

Jackson, M.G., Price, A.A., Blichert-Toft, J., Kurz, M.D. & Reinhard, A.A. (2016) Geochemistry of lavas from the Caroline hotspot, Micronesia: Evidence for primitive and recycled components in the mantle sources of lavas with moderately elevated $^{3}He/^{4}He$. *Chemical Geology*. https://doi.org/10.1016/j.chemgeo.2016.10.038.

Johnson, D.M., Hooper, P.R. & Conrey, R.M. (1999) XRF analysis of rocks and minerals for major and trace elements on a single low dilution Li-tetraborate fused bead. *Advances in X-ray Analysis*, **41**, 843-867.

Karlstrom, L., Murray, K.E., & Reiners, P. W. (2019) Bayesian Markov-Chain Monte Carlo inversion of low-temperature thermochronology around two 8-10 m wide Columbia River Flood Basalt dikes. *Frontiers in Earth Science*, **7**, 90.

Kent, A.J.R., Darr, C., Koleszar, A.M., Salisbury, M.J., & Cooper, K.M. (2010) Preferential eruption of andesitic magmas through recharge filtering. *Nature Geoscience*, **3**, 631-636.

Klemetti, E.W. & Clynne, M.A. (2014) Localized rejuvenation of a crystal mush recorded in zircon temporal and compositional variation at the Lassen Volcanic Center, northern California. *PLoS ONE*, **9(12)**, e113157.

Knesel, K.M. & Davidson, J.P. (1996) Isotopic disequilibrium during melting of granite and implications for crustal contamination of magmas. *Geology*, **24(3)**, 243-246.

Kovalenko, V.I., Kozlovsky, A.M., & Yarmolyuk, V.V. (2009) Trace element ratios as indicators of source mixing and magma differentiation of alkali granitoids and basites of the Haldzan-Buregtey Massif and the Haldzan-Buregtey Rare-Metal Deposit, Western Mongolia. *Petrology*, **17(2)**, 158-177.

Kumar, S. (2014) *Magmatic processes: Review of some concepts and models*. In: Kumar, S. and Singh, R.N. (eds.). *Modelling of Magmatic and Allied Processes*. Society of Earth Scientists Series, 1-22.

Lackey, J.S., Cecil, M.R., Windham, C.J., Frazer, R.E., Bindeman, I.N. & Gehrels, G.E. (2012) The Fine Gold Intrusive Suite: The roles of basement terranes and magma source development in the Early Cretaceous Sierra Nevada Batholith. *Geosphere*, **8(2)**, 292-313.

Langmuir, C.H., Vocke, Jr., R.D., Hanson, G.N., & Hart, S.R. (1978) A general mixing equation with applications to Icelandic basalts. *Earth and Planetary Science Letters*, **37**, 380-392.

LeBas, M.J., LeMaitre, R.W., Streckeisen, A., & Zanettin, B. (1986) A chemical classification of volcanic rocks based on the total alkali-silica diagram. *Journal of Petrology*, **27**, 745-750.

Lesher, C.E. (1994) Kinetics of Sr and Nd exchange in silicate liquids: Theory, experiments, and applications to uphill diffusion, isotopic equilibration, and irreversible mixing of magmas. *Journal of Geophysical Research*, **99(B5)**, 9585-9604.

Lesher, C.E., & Spera, F.J. (2015) *Thermodynamic and transport properties of silicate melts and magma*. In: Sigurdsson, H., Houghton, B., Rymer, H., Stix, J., McNutt, S. (eds.), *The Encyclopedia of Volcanoes*. Elsevier, 113-141.

MacCaskie, D.R. (1984) Identification of petrogenetic processes using covariance plots of trace-element data. *Chemical Geology*, **42**, 325-341.

Martin, V.M., Holness, M.B. & Pyle, D.M. (2006) Textural analysis of magmatic enclaves from the Kameni Islands, Santorini, Greece. *Journal of Volcanology and Geothermal Research*, **154**, 89-102.

Marsh, B.D. (1982) On the mechanics of igneous diapirism, stoping, and zone melting. *American Journal of Science*, **282**, 808-855.

Marsh, B.D. & Kantha, L.H. (1978) On the heat and mass transfer from an ascending magma. *Earth and Planetary Science Letters*, **39**, 435-443.

McDonough, W.F. & Sun, S.-s. (1995) The composition of the Earth. *Chemical Geology*, **120**, 223-253.

Muffler, L.J.P. & Clynne, M.A. (2015) Geologic field-trip guide to Lassen Volcanic National Park and vicinity, California: U.S. Geological Survey Scientific Investigations Report 2015-5067, 67 p.

Nicholson, H., Condomines, M., Fitton, J.G., Fallick, A.E., Gronvöld, K., & Rogers, G. (1991) Geochemical and isotopic evidence for crustal assimilation beneath Krafla, Iceland. *Journal of Petrology*, **32(5)**, 1005-1020.

Nielsen, R.L. (1989) Phase equilibria constraints on liquid lines of descent generated by paired assimilation and fractional crystallization: Trace elements and Sr and Nd isotopes. *Journal of Geophysical Research*, **94(B1)**, 787-794.

Oldenburg, C., Spera, F. J., Yuen, D., & Sewell, G. (1989) Dynamic mixing in magma bodies: Theory, simulations and implications. *Journal of Geophysical Research*, **94(B7)**, 9215-9236.

Paton, C., Hellstron, J., Paul, B., Woodhead, J. & Hergt, J. (2011) Iolite: freeware for the visualisation and processing of mass spectrometric data. *Journal of Analytical Atomic Spectrometry*, **26**, 2508-2518.

Petcovic, H.L. & Dufek, J.D. (2005) Modeling magma flow and cooling in dikes: Implications for emplacement of Columbia River flood basalts. *Journal of Geophysical Research*, **110(B10201)** 1-15. doi: 10.1029/2004JB003432.

Petcovic, H.L. & Grunder, A.L. (2003) Textural and thermal history of partial melting in tonalitic wallrock at the margin of a basaltic dike, Wallowa Mountains, Oregon. *Journal of Petrology*, **44(12)**, 2287-2312.

Philpotts, A.R. & Asher, P.M. (1993) Wallrock melting and reaction effects along the Higganum Diabase Dike in Connecticut: contamination of a continental flood basalt feeder. *Journal of Petrology*, **34(5)**, 1029-1058.

Poletti, J.E., Cottle, J.M., Hagen-Peter, G.A. & Lackey, J.S. (2016) Petrochronological constraints on the origin of the Mountain Pass Ultrapotassic and Carbonatite Intrusive Suite, California. *Journal of Petrology*, **57(8)**, 1555-1598.

Quinn, Erin T. (2014) Experimental determination of pre-eruptive storage conditions and continuous decompression of rhyodacite magma erupted from Chaos Crags, Lassen Volcanic Center, California, 179 p. M.S. thesis, Humboldt State University.

Reiners, P.W., Nelson, B.K. & Ghiorso, M.S. (1995) Assimilation of felsic crust by basaltic magma: Thermal limits and extents of crustal contamination of mantle-derived magmas. *Geology*, **23(6)**, 563-566.

Rhodes, J.M., Dungan, M.A., Blanchard, J.P. & Long, P.E. (1979) Magma mixing at mid-ocean ridges: Evidence from basalts drilled near 22° N on the Mid-Atlantic Ridge. *Tectonophysics*, **55(1-2)**, 35—61.

Richer, M., Mann, C.P. & Stix, J. (2004) Mafic magma injection triggers eruption at Ilopango Caldera, El Salvador, Central America. In: Rose, W.I., Bommer, J.J., López, D.L., Carr, M.J. & Major, J.J. (eds.). *Natural hazards in El Salvador*. Geological Society of America Special Paper 375, 175-189.

Ruprecht, P., Simon, A.C. & Fiege, A. (2020) The survival of mafic magmatic enclaves and the timing of mafic recharge. *Geophysical Research Letters*, **47**, e2020GL087186. https://doi.org/10.1029/2020GL087186.

Ryan, A.G., Heap, M.J., Russell, J.K., Kennedy, L.A. & Clynne, M.A. (2020) Cyclic shear zone cataclasis and sintering during lava dome extrusion: insights from Chaos Crags, Lassen Volcanic Center (USA). *Journal of Volcanology and Geothermal Research*, **401**, 106935.

Sato, H., Holtz, F., Botcharnikov, R.E. & Nakada, S. (2017) Intermittent generation of mafic enclaves in the 1991-1995 dacite of Unzen Volcano recorded in mineral chemistry. *Contributions to Mineralogy and Petrology*, **172**, doi: 10.1007/s00410-017-1335-3.

Saito, G., Stimac, J.A., Kawanabe, Y. & Goff, F. (2002) Mafic-felsic magma interaction at Satsuma-Iwojima volcano, Japan: Evidence from mafic inclusions in rhyolites. *Earth Planets Space*, **54**, 303-325.

Scaillet, B., Whittington, A., Martel, C., & Pichavant, M. (2000) Phase equilibrium constraints on the viscosity of silicic magmas II: implications for mafic-silicic mixing processes. *Earth and Environmental Science Transactions of the Royal Society of Edinburgh*, **91**, 61-72.

Schmidt, M.E., Grunder, A.L. & Rowe, M.C. (2008) Segmentation of the Cascade Arc as indicated by Sr and Nd isotopic variation among diverse primitive basalts. *Earth and Planetary Science Letters*, **266**, 166-181.

Scruggs, M.A. & Putirka, K.D. (2018) Eruption triggering by partial crystallization of mafic enclaves at Chaos Crags, Lassen Volcanic Center, California. *American Mineralogist*, **103**, 1575-1590.

Sparks, R.S.J. & Marshall L.A. (1986) Thermal and mechanical constraints on mixing between mafic and silicic magmas. *Journal of Volcanology and Geothermal Research*, **29**, 99-124.

Spera, F.J. & Bohrson, W.E. (2002) Energy-constrained open-system magmatic processes 3. Energy-Constrained Recharge, Assimilation, and Fractional Crystallization (EC-RAFC). *Geochemistry, Geophysics, Geosystems*, **3(12)**, doi: 10.1029/2002GC000315.

Spera, F.J. & Bohrson, W.E. (2018) Rejuvenation of Crustal Magma Mush: Tale of Multiply Nested Processes and Timescales. *American Journal of Science*, **318**, 90-140.

Spera, Frank J., Bohrson, Wendy E., Till, Christy B., & Ghiorso, Mark S. (2007) Partitioning of trace elements among coexisting crystals, melt, and supercritical fluid during isobaric crystallization and melting. *American Mineralogist*, **92**, 1881-1898.

Spera, F.J., Schmidt, J.S., Bohrson, W.A. & Brown, G.A. (2016) Dynamics and thermodynamics of magma mixing: Insights from a simple exploratory model. *American Mineralogist*, **101**, 627-643.

Sykes, M.L. & Holloway, J.R. (1987) Evolution of granitic magmas during ascent: a phase equilibrium model. In: Mysen, B.O. (ed.), Magmatic Processes: Physicochemical Principles, Special Publication No. 1, 447-461.

Tavarez, Samantha C. (2015) Geophysical evidence for mid-crustal magma reservoirs in the Lassen volcanic region, California, 75 p. M.S. thesis, University of South Florida.

Taylor, H.P., Jr. (1968) The oxygen isotope geochemistry of igneous rocks. *Contributions to Mineralogy and Petrology*, **19**, 1-71.

Taylor, H.P., Jr. (1980) The effects of assimilation of country rocks by magmas on $^{18}O/^{16}O$ and $^{87}Sr/^{86}Sr$ systematics in igneous rocks. *Earth and Planetary Science Letters*, **47**, 243-254.

Tepley, F.J. III, Davidson, J.P. & Clynne, M.A. (1999) Magmatic interactions as recorded in plagioclase phenocrysts of Chaos Crags, Lassen Volcanic Center, California. *Journal of Petrology*, **40(5)**, 787-806.

Turner, S.J. & Langmuir, C.H. (2015) The global systematics of arc front stratovolcanoes: evaluating the role of crustal processes. *Earth and Planetary Science Letters*, **422**, 182-193.

Underwood, S.J., Feeley, T.C., & Clynne, M.A. (2012) Hydrogen isotope investigation of amphibole and biotite phenocrysts in silicic magmas erupted at Lassen Volcanic Center, California. *Journal of Volcanology and Geothermal Research*, **227-228**, 32-49.

Vogel, T.A., Hidalgo, P.J., Patino, L., & Tefend, K.S. (2008) Evaluation of magma mixing and fractional crystallization using whole-rock chemical analyses: Polytopic vector analyses. *Geochemistry, Geophysics, Geosystems*, **9(4)**, doi: 10.1029/2007GC001790.

Vollmer, R. (1976) Rb-Sr and U-Th-Pb systematics of alkaline rocks: the alkaline rocks from Italy. *Geochimica et Cosmochimica Acta*, **40**, 283-295.

von Engelhardt, W. (1989) Remarks on “ratio plots” and “mixing lines”. *Geochimica et Cosmochimica Acta*, **53**, 2443-2444.

Voth, G.A., Haller, G.H., & Gollub, J.P. (2002) Experimental measurements of stretching fields in fluid mixing. *Physical Review Letters*, **88**, 254501, doi: 10.1103/PhysRevLett.88.254501.

Walowski, K.J., Wallace, P.J., Cashman, K.V., Marks, J.K., Clynne, M.A., & Ruprecht, P. (2019) Understanding melt evolution and eruption dynamics of the 1666 C.E. eruption of Cinder Cone, Lassen Volcanic National Park, California: Insights from olivine-hosted melt inclusions. *Journal of Volcanology and Geothermal Research*, doi: 10.1016/j.jvolgeores.2019.106665.

Walowski, K.J., Wallace, P.J., Clynne, M.A., Rasmussen, D.J., & Weis, D. (2016) Slab melting and magma formation beneath the southern Cascade arc. *Earth and Planetary Science Letters*, **446**, 100-112.

Waters, L.E. & Lange, R.A. (2015) An updated calibration of the plagioclase-liquid hygrometer-thermometer applicable to basalts through rhyolites. *American Mineralogist*, **100**, 2172-2184.

Weinberg, R.F., Vernon, R.H., & Schmeling, H. (2021) Processes in mushes and their role in the differentiation of granitic rocks. *Earth Science Reviews*, **220**, 103665.

Wilcox, R.E. (1999) The idea of magma mixing: History of a struggle for acceptance. *The Journal of Geology*, **107(4)**, 421-432.

Wright, T.L., & Doherty, P.C. (1970) A linear programming and least squares computer method for solving petrologic mixing problems. *GSA Bulletin*, **81(7)**, 1995-2008.

Zheng, Y. (2019) Subduction zone geochemistry. *Geoscience Frontiers*, **10**, 1223-1254, doi: 10.1016/j.gsf.2019.02.003.